MONASH University

Shared Aperture Planar Array Antenna for Soil Moisture Radiometer

Muhsiul Hassan

A thesis submitted for the degree of Doctor of Philosophy at

Monash University in 2019

The department of Electrical and Computer Systems Engineering,

Faculty of Engineering

Statement of Authorship

I hereby declare that,

• To the best of my knowledge, this thesis contains no material that has been previously published or written by another person except where explicit reference is made in the context of the thesis.

• This thesis contains no material which has been accepted for the award of any other degree or diploma at any university or equivalent institution and that, to the best of my knowledge and belief, this thesis contains no material previously published or written by another person, except where due reference is made in the text of the thesis.

Signature:…….

Print Name: Muhsiul Hassan

Date: 31 August 2019

Copyright Notices

Notice 1

Notice 2

Abstract

Water is one of the most important elements of our ecosystem. The agricultural sector is the largest user of the total water resource in Australia. A 10% water saving in agriculture sector will save up to one-third of the total water use by all capital cities combined. Due to limited manpower and high cost, the most practical way to provide high resolution soil moisture data is using remote sensing. A number of techniques have been attempted for remote sensing of soil moisture, of which, microwave remote sensing has the best response. Remote sensing of soil moisture is possible using ground or airborne sensors using visible, thermal-infrared or active/passive microwave electromagnetic radiation. Microwave sensing has some definite advantage over these other techniques with its all-weather capability and less interference. Both active and passive sensing techniques have been demonstrated in order to increase the resolution of soil moisture mapping but yield complex and expensive system. In passive sensing technique, radiometer antenna detects and measure from soil/ocean radiation and measures brightness temperature which works in L-band (1.4 GHz) spectrum with low resolution. In addition to passive L-band radiometer, active radar is now used to increase the data resolution. A compact shared aperture multifrequency radiometer can be the answer for the quest of cheap, lightweight and high-resolution soil moisture sensing. Along with L-band antenna, two other high frequency bands (Ku- (18.7 GHz) and Ka-bands (37 GHz)) can exploit their high frequency property for better resolution keeping the same penetration and sensing of original L-band. Higher frequency results in more power hence increasing resolution will share the same physical aperture as the lower L-band, and also will generate more data for better approximation. The primary object of this research is to build a fully planar radiometer antenna for airborne facility which will lead to spacecraft. A systematic approach is discussed in this thesis in the endeavour to build a system in a modular approach. The major challenges of this

study would be organization, design and integration of different module to work harmoniously. Many novel concepts and designs must be implemented to solve very stringent conditions required for the research. Mainly antenna design for the radiometer system is the scope of this thesis. Designing arrays of three different bands of antenna array sharing the same physical aperture is a huge task. To break down this, the task is divided into smaller tasks and discussed throughout the chapters of this thesis. Starting with single element antenna designing, this thesis discusses array synthesis, beamforming and multi-band structure. Successful completion of this research will open a new horizon to water management in agriculture system. A more detailed and accurate data can be estimated which will help conserve water in the agriculture sector. Also, this research can help designing antenna system working in different bands working with minimum coupling and interference for future reference. The main challenge of the antenna designing part has been the consideration to make the antenna smaller to fit in the aircraft or spacecraft requirement. Smaller size often leads to complex design and inter-element coupling which in this thesis have been analysed thoroughly.

List of Publications

Journal Papers

1. M. Hassan and N. C. Karmakar, "8 × 8 Ku- and Ka- multi-band antenna array for soil moisture radiometer," in IEEE Access (Under review).
2. M. Hassan and N. C. Karmakar, "8 × 8 Ka-band array for soil moisture radiometer," in IEEE Transactions on Antenna and Propagation (Under review).
3. M. Hassan and N. C. Karmakar, "Design of 8 × 8 Ku-band array antenna with beamforming for soil moisture radiometer" in Progress In Electromagnetics Research (PIER) (Under review).

Conference Proceedings

4. M. Hassan and N. C. Karmakar, "Soil moisture measurement using smart antennas," in Electrical and Computer Engineering (ICECE), 2014 International Conference on, 2014, pp. 192-195.
5. M. Hassan, S. Dey and N. C. Karmakar, "Ka-band complementary reflector backed slot antenna array for soil moisture radiometer," *2015 International Symposium on Antennas and Propagation (ISAP)*, Hobart, TAS, 2015, pp. 1-4.
6. M. Hassan and N. C. Karmakar, "Comparative study of different power distribution methods for array antenna beamforming for soil moisture radiometer" *2017 The 11th International Conference on Sensing Technology*, Sydney, NSW, 2017
7. Shahriar Hasan Shehab, M. Hassan and N. C. Karmakar, “SIW slot antenna at Ka-band for soil moisture radiometer system” *2017 The 11th International Conference on Sensing Technology*, Sydney, NSW, 2017

8. M. Hassan and N. C. Karmakar, “Design Considerations of DP ACPA with Higher Isolation at Ku-band for Soil Moisture Radiometer” *2017 IEEE Asia Pacific Microwave Conference (APMC),* Kuala Lumpur, Malaysia, 2017

Acknowledgement

I would like to express my utmost gratitude to my supervisor, Associate Professor Nemai Chandra Karmakar for his supervision and guidance during my PhD research life. His direction and support helped me in improving the quality of my research work. I am truly grateful to him for his continuous support and patience during my ups and downs of my PhD life. I would also like to thank my co-supervisor, Professor Jeff Walker for his kind directions and invaluable inputs and support.

The project is part of an Australian Research Council (ARC) project: DP150102487 – 'Shared aperture smart antenna for soil moisture monitoring radiometer'. I am truly grateful to ARC for their support for my research.

I would like to take the opportunity to thank Dr. Md Shakil Bhuiyan, Dr. Aminul Islam and Dr. Emran Amin, Dr. Shuvashis Dey, Dr. Rubayet-E-Azim, Mr. Shahriar Shehab, Mr. Wan Wan Mohd Zamri, Mr. Mazyar Forouzandeh, Ms. Anushani Bibile, Ms. Sika Srestha, and the list goes on for their valuable support and direction in my research.

I also acknowledge the support given by every faculty and staff members in the faculty of ECSE, without whom my life would have been more difficult.

Finally, I must acknowledge the most two important people in my life, my mother and my wife, who always supported me in rain or shine. This work would not have been completed if you were not so helpful and supportive.

Dedicated to

My mother Syeda Akhtar Banu and my wife Amrin Naher Asha

Table of Contents

Table of figures

List of Tables

List of Abbreviations

3-d	Three Dimensional
ACMSA	Aperture Coupled Microstrip Antenna
ALOS	Advance Land Observing Satellite
AMSR-E	Advanced Microwave Scanning Radiometer of the Earth
ARC	Australian Research Council
ASAR	Advanced Synthetic Aperture Radar
BE	Beam Efficiency
CAD	Computer Aided Design
CPW	Coplanar Waveguide
CST	Computer Simulation Technology
dB	Decibel
DBDP	Dual Band Dual Polarized
DP	Dual Polarized
EM	Electromagnetic
ENVISAT	Environmental Satellite
ESA	European Space Agency
ESTAR	Electronically Scanned Thinned Array Radiometer
GHz	Gigahertz
LP	Linear Polarized
MHz	Megahertz
MIRAS	Microwave Imaging Radiometer using Aperture Synthesis
MSLL	Maximum Side Lobe Level
MW	Microwave

NASA	National Aeronautics and Space Administration
PALSAR	Phased Array type L-band SAR
PLIS	Polarimetric L-band Imaging Scatterometer
PLMR	Polarimetric L-band Multibeam Radiometer
PSKR	Polarimetric Scanning Ka/Ku-band Radiometer
RF	Radio Frequency
SAR	Synthetic Aperture Radar
SIR	Spaceborne Imaging Radar
SMAP	Soil Moisture Active Passive
SMOS	Soil Moisture and Ocean Salinity
TRMM-TMI	Tropical Rainfall Measuring Mission (TRMM) Microwave Imager (TMI)
VNA	Vector Network Analyser
WIMAX	Worldwide Interoperability for Microwave Access
Wind Sat	Wind Satellite
WLAN	Wireless Local Area Network

List of Symbols

A	Magnetic vector potential / Amplitude
AF	Array factor
d	Inter-element distance
d_x	Inter-element distance along the x-axis
d_y	Inter-element distance along the y-axis
e_p	Emissivity
f_c	Cut-off/resonate frequency
I_0	Magnitude
j	Unit imaginary number
k	Free space wave number
l	Substrate length
$l1$	Feed length from the port
$l2$	Arm length of the feed
$l3$	Length of dual offset of the feed line
$l4$	Stub length
lp	Patch length
ls	Slot length
T	Physical temperature in Kelvin
TB_p	Brightness temperature
w	Substrate width
wp	Patch width

ws	Slot width
$w50$	Width of a 50 Ω microstrip line
$w70$	Width of a 70 Ω microstrip line
x_0	Mean position along the x-axis
y_0	Mean position along the y-axis
Z_T	Impedance of the transformer
Z_0	impedance of the tee junction
Z_L	Impedance of the feed line
β	Phase difference
β_x	Phase difference along the x-axis
β_y	Phase difference along the y-axis
θ	Incident angle along x-axis
δ_n	Amplitude of the Nth element
λ	Wavelength
λ_g	Guided wavelength
ϕ	Incident angle along z-axis
σ	Standard variation
σ_{x}	Standard variation along the x-axis
σ_y	Standard variation along the y-axis
σ_p	Taylor parameter
μ	Mean position
$\bar{n}$	Boundary of the region of uniform side lobes

1 Introduction

1.1 Microwave sensing of soil moisture

Water is the basis of all lives in the earth. About 71% of earth is water but 97% of them is not drinkable or usable for irrigation. Here comes the importance of water conservation. For agriculture, soil moisture is one of the deciding factors, so it is very important to maintain and monitor soil moisture in soil. The source of soil moisture can be understood by water or hydrologic cycle. The heat from the sun causes to evaporate water from water storage in the oceans. Evapotranspiration causes water to be evaporated through transpiration from trees and from soil. In the process of sublimation, precipitation water comes back in water storage in oceans and ground. In the form of rain, snow, hail etc. some precipitations infiltrate through land and becomes groundwater. Unsaturated ground water in the soil pores is called moisture.

Soil moisture plays vital role in plant growth as it serves as nutrient element for plants, regulates soil temperature overall most important element for photosynthesis. It is a variable parameter for runoff and infiltration [1] [2]. Energy fluxes are also a function of soil moisture that plays vital role in energy cycle [3] [4]. Moreover, climate change and forecasting can be improved if a data set of previous soil moisture is measured for a specific region [5]. Not all part of soil is same in different regions. The deciding factor of a region's ecosystem is mainly how much water that system has. Depending on the soil; habitat, food, lifecycle of animals and plants vary. Agriculture is totally dependent on the soil type, sunlight and temperature of a certain region. If soil moisture of a land can be monitored and maintained, it would significantly change the current cultivation schemes.

Remote sensing of soil moisture is possible using ground or airborne sensors using visible, thermal-infrared or active/passive microwave electromagnetic radiation. Among these

techniques microwave serves the best. Soil moisture remote sensing using microwave approach [6, 7] has been investigated for several decades. Detection is possible in almost all-weather conditions for microwave remote sensing. It is a definite advantage which is not possible using visible or infrared remote sensing. The sun is the primary source of electromagnetic radiation. The earth receives, transmits and absorbs to maintain thermal equilibrium. Transmission of electromagnetic (EM) radiation is different from different parts of earth depending on the dielectric constant of the radiating surface. Dry and moist soils have different dielectric constants [8] which results different radiation pattern. The real part of the dielectric constants of water is 80.4 and dry soil is about 3.5 which yields the dielectric constant of wet soil about 40 [9] at 50% humidity. Microwave remote sensors can be classified in two types: active and passive. Active means the back-scattering from the earth surface which is reflected from transmitted microwave from some active source. Passive sensors receive emission from soil and calculate radiation from emissivity and brightness temperature. Both emissivity and brightness temperatures are function of dielectric properties, surface roughness, physical temperature of soil and frequency, angle of observation and polarization etc. of measurement [10]. Microwave radiometer is an example of passive sensors that measures the radiation from a body in the microwave range (300MHz-300GHz) [11].

1.2 Different frequency bands for the soil moisture radiometer

The frequency bands that are currently being used for radiometer are P(0.3-0.4GHz)-, L(1-2GHz)-, C(4-8GHz)-, X(8-12GHz)-, Ku(12-18GHz)-, Ka(26.5-40GHz)- and W(75-110GHz)-bands. As the frequency increases, the penetration into soil property deteriorates but accuracy increases because of higher associated power. Among these bands L-band is the optimal choice because of its less sensitivity from soil roughness, vegetation and atmospheric condition. Natural properties of this frequency such as deep penetration capability and less prone to radio frequency interference make it most used frequency band for soil moisture sensing. Though P-

band has more penetrability in soil, it suffers more from spatial resolution and radio frequency interference. Since the size of antenna will be larger for small frequency, it becomes big and bulky for airborne facility. On the other hand, as frequency increases, penetration capability decreases which makes the C-, X-, Ka-, Ku- etc. bands poor candidates. With higher frequency of operation, accuracy increases due to more power, but less sensing properties of these bands make it impossible to measure soil moisture correctly. Now, L-band radiometer requirements for high spatial resolution result in a very large, bulky and heavy sensor. Contrary to this, radiometer design in the Ku- and Ka-bands can provide the high-resolution imaging of scanned plane with a much lighter, smaller and compact antenna size compared to that for L-band. Thus, if these microwave bands can be combined to a single radiation aperture, and can be made planar and conformal, it will bring significant advancement in the field that will allow the technology to be demonstrated from a small inexpensive platform such as that of a small airborne [12]. Therefore, the antenna configuration must be a light weight and planar, conformal phased array.

1.3 Advantages of microwave sensing to measure soil moisture

Microwave energy can penetrate clouds and rains and can be an all-weather remote sensing unit. This is one of the main advantages of using microwave sensing. Microwave sensing is not dependent on weather and can work in adverse weather conditions.

Synoptic view of large area is possible. It is possible to monitor data of a large area. Depending on the altitude of the radiometer, it is possible to have a wide swath for the radiometer. For active and passive system, the resolution can be different as the active system suffers more from scattering and other losses.

The coverage can be obtained at interval specified by the user and system requirement. Space satellite held radiometers generally have 3-4 days of interval for mapping. It depends on the trade-off between spatial and temporal resolution.

Microwave wavelengths are outside the visible and infrared regions of the electromagnetic spectrum, providing information on moisture content, soil roughness, dielectric properties.

Higher resolution data can be obtained by using higher frequency radiometer, though the sensitivity can be sacrificed. SMAP (Soil Moisture Active Passive) satellite has one active L-band radar system which is active microwave sensing and one passive L-band radiometer system which is passive. For the active system the resolution is as big as a 1 km by 1 km grid whereas the passive system resolution is around 40 km by 40 km grid. This grid or footprint depends on the beamwidth of the antenna, the height of the radiometer and the operating band or frequency. For higher frequency radiometers such as Ku- or Ka-bands the resolution for the passive system can be as small as a 1 km by 1 km or even less area grid.

By using dual polarized antenna, different polarization data can be obtained which can be used to calculate the Stokes parameter leading to the calculation of brightness temperature which has a direct relationship with soil moisture and emissivity. There are many different algorithms of soil moisture retrieval, but the most advanced methods require to solve four Stoke's parameter. Radiometer antenna can provide two polarizations to solve for the four parameters.

Microwave sensing can produce overlapping images and interferometric operation using multiple antennas for 3-D mapping.

1.4 Research incentive

The goal of this thesis is to develop an antenna system for a soil moisture radiometer antenna system. Soil moisture, being one of the key elements in nature, is a primary state variable of the water cycle over land and hydrology. In many earth and science models, soil moisture is a boundary condition making soil moisture a very significant parameter. Moreover, the soil moisture distribution data are required to various applications such as weather forecast, skilful modelling of climate variability and change, water management [13-15], agricultural productivity modelling [16-20], flood area prediction [21], drought prediction and so on. Thus, soil moisture data has impact on the ecology and relationship of human and ecosystem. The simplest way to monitor the soil moisture variation is to establish a network for soil moisture measurement data. This method is however very expensive and require huge human power and resources. Different remote sensing techniques such as using visible, thermal infrared, active and passive microwave are used to measure and map soil moisture to some extent. All these sensing methods are based on the change in soil moisture content and their respective electromagnetic radiation [22, 23]. Visible/infrared observation techniques have been reported in few experiments [24-27], but they suffer from a narrow beam width, hence the coverage footprint is too narrow to satisfy the temporal and spatial coverage requirements, which are around 3 days and global coverage. The approximate spatial and temporal coverage frequency is around 1 km and 2 hours respectively. For microwave sensing, the temporal and spatial coverage can be meet but microwave spectrum is huge and not every band has the same sensitivity over the soil moisture variation. Also, depending on active or passive sensing, the sensitivity to soil surface roughness and vegetation scattering of soil moisture can be different in radar (active sensing) than radiometers (passive sensing). Generally, in active sensing or using radar, results in less certainty of the soil moisture retrievals [28, 29]. L-band radiometer is considered to be the most promising above all other bands due to its penetration through

cloud, less sensitivity to the surface roughness and direct relationship with soil moisture through the soil dielectric constant [30-33]. In the microwave spectrum, though L-band radiometers are the most sensitive to moisture variation but other radiometers such as operating at C-band (i.e. Wind-Sat ,AMSR-E, AMSR2), or X-band (i.e. TRMM-TMI) are also sensitive to soil moisture though the soil layer is significantly affected in these bands by the attenuation from the land vegetation canopy and earth scattering by the atmosphere [34, 35]. At these higher frequencies (C- and X-bands) the penetration depth in the vegetation in soil is typically ~1 cm [36]. At higher frequencies, microwave radiometers can be limited to areas where the water content of vegetation is less than 1.5 kg/m^2 [37].

After launching the SkyLab mission in the 1970s, the most recent space missions to map soil moisture data are Soil Moisture and Ocean Salinity (SMOS) led by European Space Agency (ESA), and Soil Moisture Active and Passive (SMAP) mission developed by NASA. There are other space missions carrying radiometers, but these two missions are dedicated to soil moisture monitoring. In the SMOS, a passive radiometer operating at L-band is used to measure the natural emission of the earth to map soil moisture. In the SMAP, along with an L-band passive radiometer, an active L-band radar is also used. The L-band active radar improves the resolution of the measurement. For the passive L-band radiometer the footprint of the satellite is 40 km by 40 km whereas the active L-band radar has a significantly smaller footprint of 1 km by 1 km. In order to use the soil moisture data to successfully model and plan agriculture as well as weather forecast, flood/drought prediction, the footprint should be smaller than the passive radiometer footprint. There are currently two techniques that are being used to downscale this footprint. The first one is using the active radar, but the active radar is expensive and using the same L-band antenna to feed the radar and radiometer takes complex and expensive designing and the results are inaccurate. The other option is to use higher frequencies along with the L-band to get higher resolution data or in other words downscaling the footprint.

The problem is using different bands require designing different antennas and separate radiometer systems in a limited physical aperture as space is crucial and must be minimized in satellites or aircrafts. Here comes the motivation of this thesis, if it is possible to incorporate multiple higher frequency bands in the same aperture as the L-band radiometer and the system remains fully passive, there will be less impact of the surface roughness and higher resolution will be still achievable.

This research will focus on the development on a radiometer system for soil moisture measurement. Antenna development part which is the heart of the radiometer system is studied in this research. Starting from the L-band, two other bands (Ku- and Ka- bands) are chosen to be fitted in the same shared aperture with L-band antenna. Starting from a single element antenna, array synthesis, beam shaping and multiband operation are the scopes of this research which are discussed in the next chapters.

1.5 Impact of the research

Soil moisture is an important parameter to monitor rainfall infiltration and runoff [38], evapotranspiration, soil micro-organism activities [39] and so on. The radiometer antenna will make the soil moisture mapping and monitoring cheaper and accurate. It will also bring about many benefits in the field of –

1. Agriculture water management – Monitoring soil moisture can help controlling the irrigation in the agriculture sector. It is possible to design the automated sprinklers so that it checks the data for current moisture content of the soil and find the requirement before watering the field [40-43]. The long-term prediction of the soil moisture from history data can assist farmers to decide the suitable time and crop to plant, and suitable irrigation to provide.

2. Weather forecasting and monitoring – Weather forecasting and monitoring requires accurate modelling of the water cycle, energy balance and carbon exchange and soil moisture being one of the boundary parameters of these models, plays huge role [44-46]. Forecasting, including short-term prediction [47], long-term water cycle trends [48], carbon cycle [49], climate variability [50] will be improved if the moisture measurement can be accurate.
3. Natural calamities forecasting – The prediction of natural calamities such as flood, drought [51], landslides can be approximated better with the help of soil moisture data. Also, better documentation of soil quality, erosion [40, 52] is possible which play role in these extreme events.
4. Other impacts such as in the defence sector to help with the foggy condition or dust presence or in health sector to predict few virus spreading in wet or dry soil are also few applications of this research.

1.6 Thesis objectives

The main objective of this thesis is to build the antenna system for the soil moisture radiometer. The antenna system is a gigantic project and only the multiband antenna development has been the scope of this thesis. The design is started from a single element antenna and array synthesis, beam shaping algorithm, multiband techniques are applied on that. The main objective is divided into smaller objectives and discussed in the following:

1.6.1 Element antenna designing with the most suitable feeding

Antennas in L- (1.4 GHz), Ku- (18.7 GHz) and Ka-(37 GHz) bands are going to be used in the shared aperture radiometer antenna as the literature discussed in chapter 2. In past experiments and missions different feeding techniques have been applied to feed the antenna. In this thesis, before designing the array multiband antenna, single antenna working in a single frequency is

discussed. Different feeding techniques and their advantage, complications are analysed from literature and a suitable feeding technique is applied to design a single element radiometer antenna. The radiometer antennas need to have two orthogonal polarizations to obtain data from two independent polarizations. Also, it is important that these two polarizations are isolated from each other so that radiation from one polarization does not affect polarization from another. After designing and analysing single polarized antenna, a dual-polarized antenna for each frequency is designed, fabricated and measure before moving on to array synthesis.

1.6.2 Array synthesis for better gain

For the radiometer to be fully planar, it is important to design the antenna fully planar and the best choice for this is microstrip patch antenna. Aperture-coupled feeding is chosen for the element antenna but for a single element the gain is very low. To enhance the gain of the antenna, array structure is necessary. Also, the antenna beam for a single element is very wide, which needs to be narrowed down in order to obtain higher spatial frequency. Hence 8 by 8 element array antenna is synthesized for all three frequency bands. The feed network designing is very challenging as the frequency increases, the size of the patch and all other dimensions decrease.

It is important to plan the design so that the antenna gain is about 25 dBi to be able to sense moisture content from a high altitude. If a single element exhibits 7 dBi gain by its own, then 8×8 or 2^6 element should have ideally $7 + 6 \times 3 = 25$ dBi gain which does not have the coupling or matching losses associated with the elements. In this case, as the gain is already 7.7 dBi, it is practical to assume, after designing 8×8 array configuration, subtracting all losses, the antenna will radiate more than 25 dBi which is the goal.

1.6.3 Beam shaping to shape the main-lobe of the array

Beam shaping is the technique to shape the main-lobe of an antenna array by tuning the excitation received by the antenna elements. For designing the radiometer, the antenna beam

pattern should have most of its power in the main-lobe and suppressed side-lobes. The side-lobes must be suppressed because radiation from other direction should not have similar power level as radiation from the desired direction or main-lobe. To suppress the side lobe there are many algorithms that can be adopted such as the Gaussian distribution, Taylor's distribution, Staircase power distribution, Chebyshev's method. Implementing these methods can be challenging as well as expensive to fabricate as the larger power ratio between the centre and corner elements the thinner the feed lines become. A detailed analysis on different technique must be discussed before implementing. Rigorous simulation and optimization is also required before fabrication and measurement.

1.6.4 Multi-band antenna array in the same antenna aperture

The multiband soil moisture radiometer will have multiple frequency bands in the same physical aperture. Designing an array antenna for multiple bands require a greater number of substrate layers for feed lines. Also, in aperture coupled structure, the slots in the ground plane need to be exactly in line with the feed lines and patches, but more than one frequency band is present. If the feed lines of one band passes over or under the slots of another band, it will affect the radiation pattern. The feed lines should be designed in such a way that they do not overlap and do not affect the radiation pattern, gain or add to mutual coupling.

1.6.5 Measurement of soil moisture using developed antenna

An experimental set up will be established to measure the soil moisture variation using spectrum analyser. The reason for this is to prove the antenna performance and validity of the design as well as get an overview of how these antennas are going to perform in the field. The sensitivity of these antennas depends on the frequency and surrounding environment, soil type and so on but for the sake of simplicity it is enough to show if other parameters are constant then only then change in the moisture content should change the emission and hence the received power to the spectrum analyser.

1.7 Original contributions

After the successful completion of this research work the following original contributions are expected to be achieved:

- A shared aperture dual polarized antenna element that can receive both vertical (EV) and horizontal (EH) polarized signals working in Ku- and Ka-bands.
- A single antenna array with low profile, low-cost, and high gain capability for L-, Ku- and Ka-band radiometers. Their excitation mechanism (feeding techniques), matching, and finally, optimized mutual coupling and suppression of higher order harmonics.
- A Ku- and Ka- multi-layered structure to provide the same physical aperture ready to be fitted in a smaller drone or aircraft system as soon as the receiver module is ready to process data from the antenna. This Ku- and Ka- multi-layer structure can augment the data from the L-band array which is designed in this thesis for an inexpensive planar system and also readily available in commercial radiometers.
- Beam shaping network and fixed beam shape design for this multi-frequency antennas to keep the antenna system simpler. Most suitable beam shaping technique will be applied to achieve the system requirements.

1.8 Thesis outline

This thesis has 8 chapters. Each chapter is dedicated to a part of the radiometer antenna development. A brief description of the chapters in this thesis is outlined below-

Chapter 1: Introduction

A brief introduction of microwave remote sensing, advantages of remote sensing for soil moisture measurement is discussed. Then the incentive of the research followed by impact of the research is then described. Thesis objectives along with original contributions are finally proposed.

Chapter 2: Literature Review

Starting with review of microwave remote sensing, this chapter discusses soil moisture measurement related space missions their critical analysis and radiometer structures. Then review of linear and dual-polarized antenna, array synthesis, beam shaping algorithm and multi-band structure of antenna are discussed one by one. Soil moisture retrieval method where dielectric property of soil, soil roughness effect and algorithm to measure soil moisture is discussed next. Finally, an analysis, research gap, research motivation and research aims are discussed before the conclusions.

Chapter 3: Linear Polarized Antenna

After a brief overview and theory of radiation, L-, Ku- and Ka-band antenna are designed for linear polarization. An element antenna of these three frequencies are designed, before fabrication and only Ku-band antenna is measured. A brief discussion of challenges of choosing the feeding method and result analysis and discrepancies are discussed. Effects of changing different parameters while designing the single element antenna is then documented and a generic flow chart is developed for designing antennas in this frequency range (from L-band to Ka- band and more).

Chapter 4: Dual Polarized Antenna

Similar to the linear polarized antenna, design of a single element for L-, Ku- and Ka-band antenna is performed for dual polarizations. Isolation, gain and radiation pattern were considered for the design process in all three bands. Measurement was carried out for Ku-band element and results were compared with the simulations. Again, effect of changing different parameters and a flow chart for designing dual-polarized antenna in this frequency range is developed before the conclusions.

Chapter 5: Array Antenna Design

In this chapter, starting with the theory of array factor, this chapter is dedicated to array antenna design. Starting with 2 × 2 array for L-, Ku- and Ka-bands, this chapter continues the design of 4 × 4 and finally 8 × 8 array for all three bands. After designing, 2 × 2 L-band, and 8 × 8 Ku- and Ka-band array antenna is fabricated and then measured before further analysis. This chapter also describes the effect of back-reflector to suppress the back-lobe radiation.

Chapter 6: Array Analysis

In this chapter, after a brief overview and theory different beam shaping methods such as uniform, Gaussian, Taylor's, staircase power, Chebyshev's distributions are discussed. A complete analysis of different parameters such as beam efficiency, 3 dB beamwidth and maximum side-lobe level for these distributions are compared and analysed. The staircase power distribution is then chosen to apply on the 8 × 8 Ku- and Ka-band antenna. After fabrication, results are compared with the simulation and discrepancies are discussed before conclusion.

Chapter 7: Multiband Antenna

Completing the array antenna and beam shaping algorithm in the chapter 5 and 6, Ku- and Ka-bands are designed in the same shared aperture in this chapter. Starting with one Ku- with 2 × 2 Ka-band structure, step-by-step design is performed to obtain 8 × 8 Ku- with 8 × 8 Ka-band. The feeding technique is the aperture-coupled design but due to the multiband structure, the number of feed layers is increased. The new feed layers being further from the ground require power divider network different than that discussed in the array synthesis chapter. Measurement result is provided along with the simulation result before a brief conclusion.

Chapter 8: Conclusions and Future Work

The final chapter of this thesis is the conclusions and future work discussion. A brief overview of the motivation of this work followed by the fulfilment of the goal of this thesis, contribution and future work is discussed.

2 Literature Review

2.1 Overview

In Chapter 1, a brief introduction about the soil moisture is provided along with microwave sensing and antenna system to sense the natural emission from the earth. This chapter presents an in-depth analysis on the shared aperture smart antenna to accommodate multiple frequencies in the same physical aperture. A comprehensive review on soil moisture measurement technique using microwave approach is then discussed. It also caters for a detailed study on the basics of microwave sensing followed by soil moisture retrieval algorithm and finally the motivation and research scopes of this study.

At first, a basic structure along with different feeding techniques of microstrip patch antenna is discussed in detail. Few novel designs of the microstrip patch antennas are discussed next. Array synthesis, beam shaping algorithms, and multifrequency operations are discussed next. After the antenna part, soil moisture retrieval related topics such as soil dielectric properties, soil roughness, stokes parameter to retrieve the soil moisture is discussed. Finally, research aims, and scope of this research is discussed.

It is important to establish that the focus of this thesis is to explore more on the antenna design parts than soil moisture measuring technique.

2.2 Review of antenna system for Radiometer

2.2.1 Microwave remote sensing overview

Remote sensing is the technique to acquire information from distance without physically touching. Among other remote sensing techniques such as using visible light or infrared lights, microwave remote sensing is the most effective and of more recent interest. Microwave remote sensing technique uses reflected or emitted energy having wavelengths ranges from about one

millimetre to a few tens of centimetres. It can identify, sense and measure the target of interest at all weather conditions. For example, low frequency microwaves have longer wavelengths that can penetrate clouds most of the time [53]. They can also penetrate through rain to some extent [54]. Microwave radiation can even penetrate ground and vegetation [55]. It can provide information about wind over the sea surface which can be extracted from the sea surface radiation, backscattering, polarization [56, 57]

Depending on the target's dielectric constant, the amount of radiation varies a lot. For example, the dielectric constant of dry soil is 3.5 whereas wet, saturated soil is approximately 40 [58], and water is 80. This difference in dielectric constant for different moisture content is the basis of this study. The soil dielectric constant increases with soil water content, with the exact relationship dictated by the soil particle distribution [58]. Based on the sources of radiation, microwave sensing can be categorized into two categories, active and passive.

The active remote sensing sensor emits microwave radiation towards the target of interest, and detects the radiation scattered back from the target. The most popular active microwave sensing configuration is the Synthetic Aperture Radar (SAR). The SAR can provide from tens of meters to over a swath of 50 to 500 km of spatial resolution. Among many other applications in various microwave sensing, five space-borne SAR systems are available for soil moisture observations. They are ESA's ERS-1/2 C-band SAR, ESA's ENVISAT (ERS-3) C-band ASAR (Advanced SAR), the Canadian C-band RADARSAR-1/2, the Japanese L-band ALOS (Advance Land Observing Satellite) PALSAR (Phased Array type L-band SAR), and the German X-band TerraSAR. The radars can be polarised either horizontally (H) or vertically (V), and therefore depending on which polarisation to send and to receive, there can be up to four polarisation combinations horizontal-horizontal (HH), vertical-vertical (VV), horizontal-vertical (HV) and vertical-horizontal (VH).

The passive remote sensing sensor doesn't use an illumination source but uses the thermal motion of atoms, any objects at a physical temperature above absolute zero (~-273 Cº or 0 K). A radiometer is used to measure this radiation. To elaborate the relationship between physical temperature and microwave emission, the black-body concept can be used. The black body radiation was introduced by Planck in his quantum theory in 1901. A black-body is a hypothetical ideal material that absorbs all radiation and reflects none. Therefore, for a black-body in thermodynamic equilibrium, it emits all absorbed energy outward. It is possible to quantify the intensity of electromagnetic emission using the term brightness temperature. The brightness temperature is defined as the physical temperature of a black-body emitting the same amount of energy. Similar to the black-body, a hypothetical white-body is a perfect reflector that reflects all energy and therefore absorbs none. Most of the practical life objects are grey body which is a mixture of black-body and white-body objects, when thermodynamic equilibrium is reached. Using the emissivity (ep) to describe the ability of materials to emit electromagnetic energy, the brightness temperature (TBp) of the material is expressed as

$$TB_p = e_p.T$$

where T is the physical temperature of the material in Kelvin, and the subscript ‘p’ is for the polarisation, which can be either horizontal or vertical. This equation is achieved from the Planck’s black-body radiation law using the Rayleigh-Jeans approximation for microwave frequencies [55, 59]. For soil, the emissivity varies from around 0.95 for dry soil (with moisture content of 0.05 m3 /m3) to around 0.6 for saturated wet soil (with moisture content of 0.4 m3 /m3), depending on electromagnetic wavelength, surface roughness, incidence angle, and soil properties [59, 60]. If the soil temperature can be considered as 300 K, then a change from dry soil to wet soil is seen as 90 K difference because of different brightness temperature [59], whereas actual difference in temperature is very small (approximately 1 K).

2.2.2 Radiometer antennas and satellite missions

Theoretically any antenna can be considered as a radiometer antenna but in practice, they differ depending on the application. In most of the cases, the sensitivity of the antenna or the brightness temperature is in the order of the noise of the receiving system, meaning the antenna system must have minimum transmission loss. As most of the applications in the microwave radiometry is basically imaging, the element antenna is usually part of a scanning mechanism generally but not limited to either mechanic, electronic, or a hybrid of both. Many aircraft missions have been carried out before launching satellites into the space. Radiometers working in different bands such as X-, Ku-, Ka-, C- bands [61-64] are used along with L-band or independently to compare and justify the choice of frequency for the radiometer.

SMOS: The first space mission dedicated to soil moisture was launched on November 2nd 2009 after 36 years of the first attempt to retrieve soil moisture from space (Skylab L-band

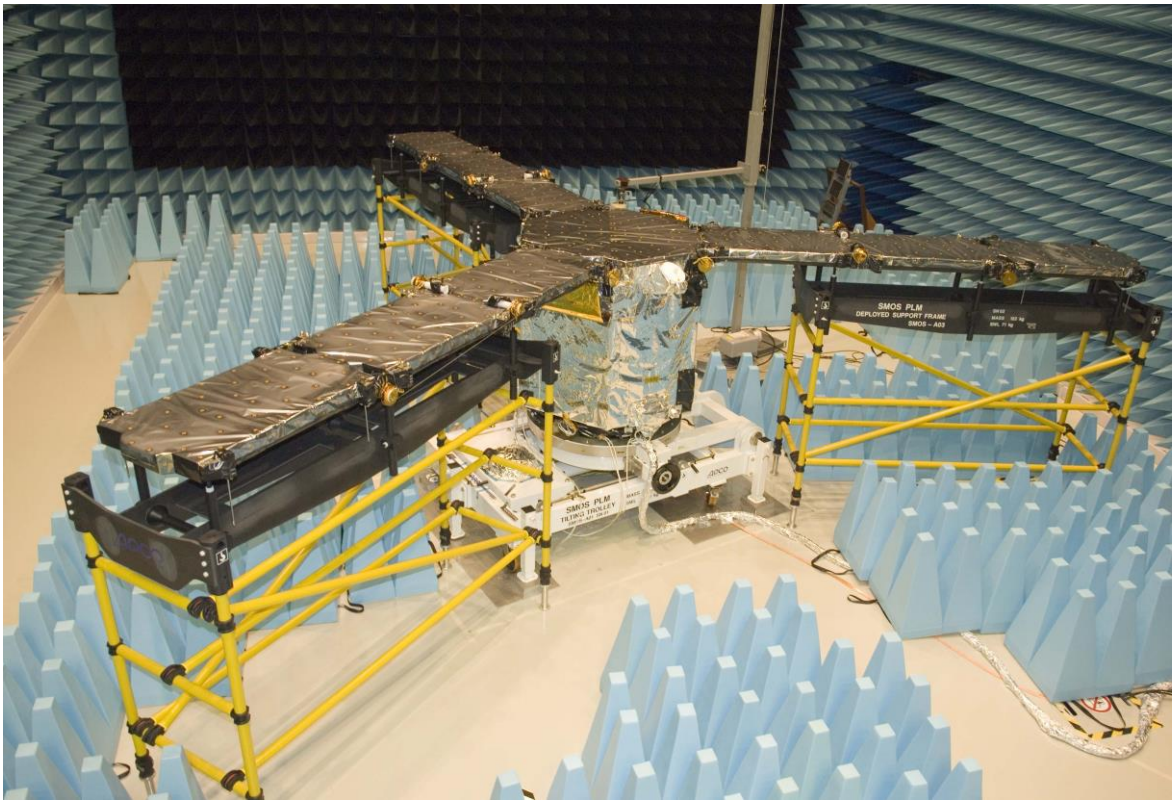

Figure 2. 1 SMOS MIRAS antenna load testing in ESA-ESTEC lab. Image credit: ESA

radiometer experiment in 1973, referred to as S-194) by the European Space Agency (ESA). The Soil Moisture and Ocean Salinity (SMOS) mission, led by the ESA in collaboration with the Centre National d'Etudes Spatiales (CNES) in France and the Centro para el Desarrollo Tecnologico Industrial (CDTI) in Spain, using a 2-D interferometric radiometer operating at L-band (1.413 GHz; Microwave Imaging Radiometer using Aperture Synthesis: MIRAS, shown in Figure 2. 1) [65] is designed to measure near surface (top 5 cm) soil moisture and ocean salinity. MIRAS, the only payload of the SMOS is a novel two-dimensional synthetic aperture radiometer with dual-/full-polarimetric imaging capabilities. This unique design makes brightness temperature observation possible within the SMOS field-of-view at different incidence angles. MIRAS is a Y-shaped aperture synthesis radiometer, operated in a protected band for radio-astronomical observations at a centre frequency of 1.413 GHz using a bandwidth of about 20 MHz. The single-element antenna is a dual-polarized aperture-coupled microstrip patch antenna. The diameter is 165 mm with an integrated feed network. Part of the L-band is in a protected frequency spectrum, also it provides sufficient sensitivity for both soil moisture and ocean salinity. The configuration of the SMOS MIRAS has sparse array consists of 69 receiver elements. Among them, 18 elements are in equidistance of 0.875λ on each arm of the Y, which makes 54 elements on the arms. The rest 15 elements are located in the hub and each arm length is 4.5 m. The maximum distance between two corner antenna elements is about 7.8 m, thus the boresight angular resolution, depending on the weighting function used for the sampled spatial frequency spectrum is in the order of just under 2 degrees. The useful swath on the ground is about 1,050 km for a satellite altitude of 758 km. temperature resolution is in the order of about 2 - 4 K. The main disadvantage of this mission is the radio frequency interference (RFI) produced by human seen from the space affecting the natural emission.

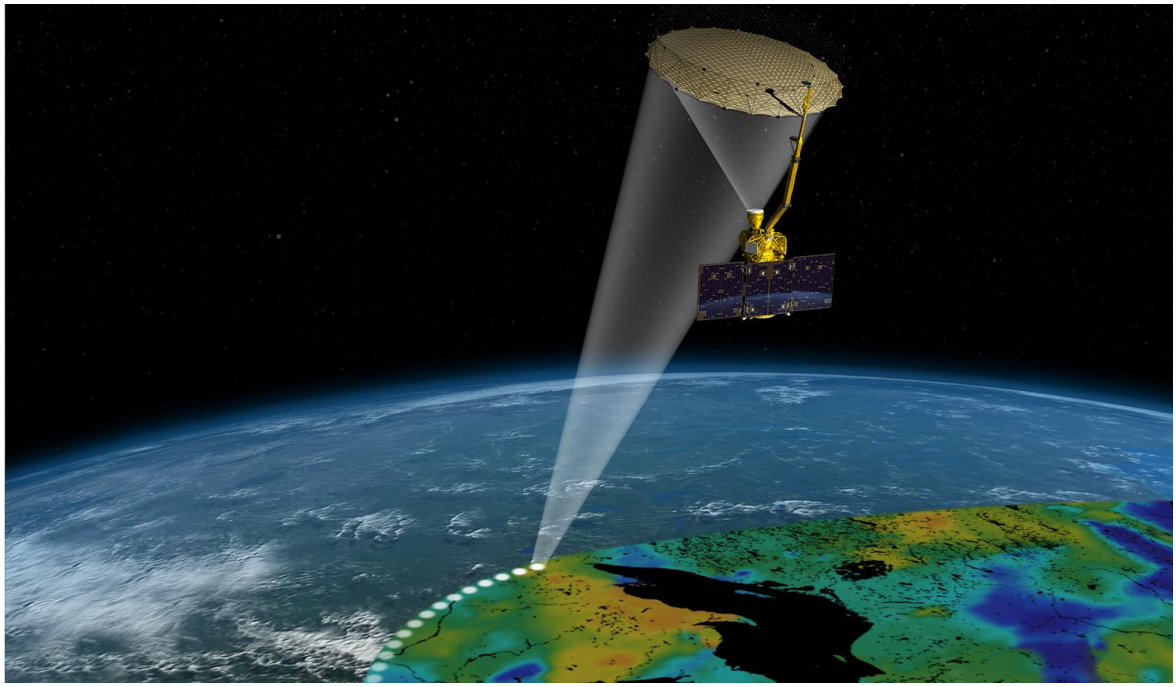

Figure 2. 2 Artist's rendering of the SMAP instrument. Image credit: NASA/JPL-Caltech

SMAP: The National Aeronautics and Space Administration (NASA) Soil Moisture Active Passive (SMAP) observatory, launched in January 2015, is designed to provide global mapping of high-resolution soil moisture and freeze-thaw state. This mission provides a unique remote sensing technique to measure soil moisture with advanced accuracy, resolution, and coverage [66] . The SMAP mission uses both active (using a radar) and passive (using a radiometer) microwave sensing to map soil moisture. The SMAP payload consists of a radar and a radiometer operating at L-band frequencies and is supposed to provide data in every two to three days [67]. For the antenna system in the SMAP architecture, a 6-m conically-scanning reflector antenna and a common L-band feed are shared by both the radar and radiometer. The reflector antenna can be set to produce a conically scanning antenna beam with an approximately 40-km, 3-dB footprint at the surface at as earth incidence angle of approximately 40º. The feed assembly employs an orthomode, single-horn transducer, with vertical (V) and horizontal (H) polarizations that are aligned with the Earth's surface polarization basis for both the radiometer and the radar. The artist's view on the SMAP satellite is shown in Figure 2. 2.

The radiometer uses 24 MHz of bandwidth centred at 1.4135 GHz. The radar and radiometer signals are separated by frequency diplexers and sent to the appropriate circuit for detection [68]. The spatial resolution of 1 to 10 km is required in hydrological modelling. The radiometer offers a resolution of 40 km which can be augmented by higher resolution radar system. The disadvantage of using a solo radar system is that they are significantly affected by the vegetation coverage and surface roughness. It was expected that by combining SMAP radar and radiometer data, accurate soil moisture with a high spatial resolution can be obtained but after the launch the radar failed irreparably and only the radiometer is functioning. The RFI mitigating filter is installed and functions properly offering filtered data without man-made RFI noise.

ESTAR: The Electronically Scanned Thinned Array Radiometer for Remote Sensing Measurement of Soil Moisture and Ocean Salinity. It is an L band radiometer operating at a wavelength of 21 cm with a capability of providing the equivalent of up to 7 beam position within its +/-45 degree field of view. This system was installed on the NASA C-130 aircraft operated by the NASA Ames Flight Center many times [69]. Similar to the SMOS, aperture synthesis – a concept to achieve high-resolution measurements, an interferometric technique is used in the ESTAR. The complex correlation of the output voltage from pairs of antennas is measured at many different baselines [70], which offers a practical way of putting such structures in space. Apart from the MIRAS system used in the SMOS, another example is the very large array [71] which uses a "Y" configuration of elements to achieve the resolution of a filled array whose diameter is equal to that of the circle that encloses the “Y”.

For an airborne L-band prototype the system uses five "stick" antennas, each consisting of a linear array of eight dipoles, developed at the University of Massachusetts and NASA/Goddard Space Flight Center, and flown several times on a NASA P-3 aircraft. The sticks provide

resolution in the direction of aircraft motion, and resolution across track is obtained "synthetically" from the correlated output of pairs of sticks [72]. For satellite, the antennas are designed as slotted waveguides. The primary frequency is 1.4 GHz, which requires slotted waveguide antennas 9.4 meters in length. Additional thinned array radiometers operating at 2.65 GHz and 5.0 GHz is nested within the L-band array in order to provide secondary channels to augment data to mitigate effects due to the vegetation canopy [72]. Above water the L- and S-band channels together provide an estimate of ocean salinity and temperature [73, 74] . L-band with the C-band channel provides information such as ocean-surface windspeed. The S- and C-band are of higher frequency hence the sizes of these antennas are smaller than the L-band.

Aquarius: Aquarius is the first NASA satellite to observe the sea surface salinity (SSS) over the global ocean. This mission successfully collected data from 25 August 2011 to 7 June 2015. The Aquarius is a combination radiometer and scatterometer (radar) operating at combined passive/active L-band (1.413 GHz for the radiometer and 1.26 GHz for the scatterometer). The primary objective of the Aquarius is to provide global [67] observations of surface sea salinity once every 7 days. However, Aquarius has also potential [68] capabilities to monitor soil moisture at global scales [75, 76]. The antenna of this satellite is a 2.5-m offset parabolic reflector with three feed horns. The three beams are arranged roughly 90 degrees with respect to the spacecraft heading at incidence angles 25.8, 33.8 and 40.3 degrees with respect to the satellite nadir. Similar to the SMAP, each feed is shared by both the radiometer and scatterometer. Each feed has a dedicated radiometer but, there is only one scatterometer that switches among the three feeds. The resolution of the three beams provide coverage of a swath of about 390 km. The radiometers are Dicke radiometers with noise injection for internal calibration [77]. The radiometer switching sequence between antenna, Dicke load, and noise

diode has been optimized to maximize antenna observations. The radiometers measure power at both polarizations and also the sum and difference of the fields (voltages) at the two polarizations from which the third Stoke's parameter can be obtained [78].

2.2.3 Critical analysis on space mission and radiometer system

The satellite missions over the decades set the standard for the antenna system. The antenna system can be active or passive (SMOS, ESTAR) or both active and passive (SMAP, Aquarius). The active system resembles a radar system, whereas the passive system is what radiometer resembles. The advantage of only passive system is the simplicity and less back scattering of the radiation as there is no incident radiation. The disadvantage of the passive system is the advantage of the active system, which is the resolution. Where the passive system generates a footprint of 40 km, an active system can generate around 1 km (SMAP footprints). The other way to achieve higher resolution with passive system is to incorporate multiple frequencies, such as in the Aquarius mission. The choice of other frequencies must be higher than the L-band to offer higher resolution. For the antenna system designing, the element antenna must be of dual polarizations to offer vertical and horizontal polarizations. Data from both polarizations are important to find Stokes' parameters to measure the brightness temperature. The gain of the antenna array must be very high (at least 25 dBi) which is possible by designing array antenna. The choice of antenna structure depends on the feeding structure of an element antenna; hence it is important to choose the right feeding technique of a single element antenna. For the SMOS mission, the choice of antenna is dual polarized aperture coupled microstrip patch antenna, whereas in the SMAP, the choice was horn antenna. For the ESTAR the antenna was dipole for the aircraft and slotted waveguide for the spacecraft and for the Aquarius, the antenna was reflector antenna.

2.3 Antenna Design

In today's modern communication industry, antennas are the most important components required to create a communication link. Microstrip antennas are the most suited for aerospace and mobile applications because of their low profile, light weight and low power handling capacity. They can be designed in a variety of shapes in order to obtain enhanced gain and bandwidth, dual band and circular polarization to even ultra-wideband operation. Microstrip antennas are attractive due to their light weight, conformability and low cost [79]. These antennas can be integrated with printed strip-line feed networks and active devices. The radiation properties of micro strip structures have been known since the mid 1950's [79]. The application of this type of antennas started in early 1970's when conformal antennas were required for missiles. Rectangular and circular micro strip resonant patches have been used extensively in a variety of array configurations.

2.3.1 Linear and dual polarized antenna

A detailed study of few selected linear and dual polarized antennas are discussed in the following. The choice of antennas discussed are based on the antennas used in the radiometers in the space missions discussed in the previous section and are good candidates for a potential multiband radiometer system.

Monopole Antenna: Generally, monopole antennas have a simple design, low-cost fabrication and low gain. They can be of wider bandwidth and can be designed for different frequencies covering L-, Ku- and Ka-bands [80-83] which are the concern of this research. Linear polarized coplanar waveguide (CPW) fed with trapezoidal ground planes with circular disc antennas are proposed in [84, 85]. The problem with these designs is their negative gain in most of the spectrum and beam not fixed in all frequencies. Similar designs with elliptical and arrow-like disks with CPW lines are discussed in [86] and [87]. Transfiguration of the monopole antenna

is proposed in [88] where more focus is given on increasing the bandwidth. A printed monopole antenna with reconfigurable polarization designed for WLAN applications is proposed in [89]. Monopole antenna with slots of different shapes (such as L- and U-shape) for WLAN/WiMAX application is discussed in [90]. Three planar monopole antennas (different shapes such as circular, triangular, strip loaded) are presented in [91]. All these monopole configurations have a very low gain. Other configurations such as planar polygonal monopoles in [92], circular ring monopole in [93], broadband monopole array in [94] also have a very low gain. Summarising these findings infers that monopole antennas generally have wider bandwidth and almost omnidirectional radiation pattern but very low gain. Therefore, monopole antennas are not a suitable option to be used in the radiometer antenna.

Dipole Antenna: Linear polarized printed dipole antenna with wideband and integrated balun feed is optimized to widen the bandwidth at L-band in [95]. Dual-band dipole antenna for WLAN purpose is discussed in [96, 97] and many other types of research. These both works lack the gain which is less than 2 dB in all cases. A novel Yagi-like printed dipole array antenna fed by a microstrip-to-coplanar strip transition and truncated microstrip ground plane as its reflecting element operating in X-band (at 12 GHz) is proposed in [98] which has a very complex design to implement in a range of different frequencies. Similarly, a planar microstrip-fed quasi-Yagi antenna with fair front to back ratio and bandwidth radiation characteristics around C-band (4 GHz - 8 GHz) is presented in [99] which also lack gain and simplicity in design. A planar elliptical dipole configuration, fed by coplanar stripline antenna is presented in [100], which suffered from beam splitting problem at different frequencies. Four planar dipoles and their comparison results are presented in [101] with a gain of only 7 – 8 dBi. Other dipole antennas such as with bow-tie configuration [102], the bottom fed elliptical dipole is presented in [103]. All these dipoles are omnidirectional with a lower gain value of around 0-3 dB, which would not be a good choice for the radiometer antenna. To increase the gain of the

antenna system, arrays can be formed for the dipole antennas. A leaf dipole array with balun feed is proposed in [104], a double-sided printed dipole array of thirty-two elements with twin lead transmission line presented in [105], another printable dipole with integrated balun is proposed in [106] and an 'H' shaped dipole array in [107], where, all of them used a metal reflector to improve the gains. But these types of antennas are end fire and have longer length with low gain required in the required frequency band with unnecessary wide bandwidth, therefore, cannot be used in radiometers. For dual polarization configuration, a broadband dual-polarized dipole antenna is presented in [108], but this type of design is non-planar. The operating frequency is 1.6 GHz and 3.55 GHz but designing for Ka-band will be a big challenge due to the smaller size of the feed lines. Similar designs are also presented in [109-111]. Dipole antennas with high isolation for base station applications is presented in [112, 113]. The isolation is ranging around 20 dB to 35 dB in these cases with decent gain of 7 dBi to 9 dBi. Problems with these structures are, even if they are printed, their configuration is not planar hence unsuitable for multi-layered structures and they are exclusively suitable for baseband applications only. A wideband DP antenna is proposed in [114], which is also used later for imaging system in [115] as well as for impulse radio (IR) UWB (ultra-wide band) application in [94].

Horn and Bi-conical: Horn antennas are large and bulky. They are mostly used for proving design concepts. With higher gain and beamwidth their electrical properties are suitable for this research, but the non-planar structure has made horn antennas unsuitable for this research. Similar limitations are also true for bi-conical design. Wideband, wide-angle basic bi-conical antenna in a single linear polarization is presented in [116]. Other variations of bi-conical antennas are discussed in [117, 118]. For the dual polarized structures, a novel horn antenna working between 2 and to 26.5 GHz with a coaxial line to improve the transition for better return loss is presented in [119], which has lower isolation between ports (21 dB). Similar

design with similar low isolation is also presented in [120]. Another DP array of horn antenna working at 92 GHz is presented in [121]. A DP probe for near-field application is presented in [122]. Unlike other antennas mentioned before, it has the required isolation (>40 dB), however, this design suffers from narrow bandwidth and heavier structure. Their size and structure are not suitable for this research.

Aperture coupled microstrip patch antennas (ACMSA): Aperture coupled configuration was first proposed by Pozar in [123]. Since then, a modified version of apertures, ground slots, patches have been explored by many researchers. Optimising stubs to increase performance such as bandwidth and reflection is reported in [124]. Among the research within single linear polarization domain, making the aperture shaped as 'dogbone' to improve bandwidth is discussed in [125]. Stacking patch layers on top of each other to increase bandwidth is discussed in [126-128]. Other modifications such as defective ground structure (DGS) is also implemented to improve back radiation problem and resonate in two different frequencies discussed in [129, 130]. Along with DGS, a parasitic structure in the patch layer is also explored to improve back radiation problem in [131]. Design with circular polarization is discussed in some studies such as [132-137]. Other designs such as with LTCC (low temperature cofired ceramic) which has metallic via holes can become an issue because of the space constraint discussed in [138]. For the dual polarized structure, Aperture coupled microstrip antenna are the preferred feeding technique suitable for this research which requires high gain, wide bandwidth and high port-to-port isolation [123]. For the aperture coupled design, two orthogonal non-overlapping slots are first presented in [139]. After that another model with a cross shaped slot is presented in [140]. Later, several other design such as with dog-bone shaped slot [141], shared aperture slot antenna [142], with defected ground structure (DGS) [129, 131], extended stub in the feedline [124] are proposed having improved isolation and gain but lacking the wide bandwidth which is vital for the Ka-band in the radiometer antenna.

Another DP ACMSA suitable for X-band SAR applications with a wide bandwidth of 2 GHz is presented in [143]. It possesses very high gain and 25 dB isolation between ports which is the marginal requirement. This design has a centre-fed slot configuration, symmetric radiation pattern and matched return loss. The relatively low bandwidth is improved by adding multiple resonant patch to the slot near its matched frequency [144]. This technique induces a quite high back-radiation, which is overcome by choosing the resonance of the slot as far as possible away from the operating band of the patch [127] and placing a cross-shaped reflector patch behind the antenna to increase the front-to-back ratio [145]. Stacked multilayer patches can also be used to increase the bandwidth further [146]. Furthermore, separate feed layer technique is used in [145] and [147] to improve the isolation.

After studying overall performance from the literature, it can be concluded that the aperture-coupled structure are the most suitable for their planar and conformal structure along with multiple layered feeding structure to accommodate more than one frequency in the future.

2.3.2 Array Antenna Design

The way to enlarge antenna dimensions without increasing size of individual elements is an array system. Array of antenna represents an assembly of radiating elements in an electrical and geometrical configuration. In most cases elements of array are identical but not necessary to be identical all the time. For identical cases, to provide beam shaping and scanning in any direction in space, arrays are phased arrays [148]. In the mid 1960's, array technology was dominated by open ended waveguide and dipole arrays fed by waveguide or coaxial transmission lines. As the need for lightweight antennas for missile and warfare increased, stripline transmission circuitry and slot elements development emerged [149, 150]. There were several unique array antennas used for spacecraft and missiles in 1950's to 1970's. Classic monolithic microstrip array proposed by Munson [151], the etched broadside and endfire arrays

of Fubini et al. [152, 153], the narrow line radiators of James and Wilson [154] are some notable research. These arrays have different characteristics. Their bandwidths and power levels are unique, and they point to different future research direction.

Some development in the array design, including arrays using non-contacting feeds, the problem of spurious feed radiation, and the monolithic phased array has been discussed in [155]. Photolithography allows a very easy fabrication method for series-fed array as both feed network and radiating patches/elements can be made without any soldering. Though this technique limits to fixed-beam or frequency-scanned arrays but linear or planar arrays can be fabricated in both mono and dual polarization feature. The best way to design these types of antenna array is using computer aided design (CAD). Using CAD models some progress have been made in series-fed linear arrays for proximity coupled dipoles [156, 157] and aperture coupled patches [158]. More control can be provided by the corporate-fed arrays as excitation of individual array elements are possible in this feeding. Phased arrays, multi-beam arrays, or shaped-beam array are usually fed by corporate-fed design. Proximity and aperture coupled elements are considered for such arrays. CAD models for arrays of this type [159] have been discussed in this regard.

An elaborate discussion about arrays, linear and planar array can be found in [79, 160-162] etc. most popular references. For this proposal, only planar array is point of interest in this research study. In the planar array, to get required beam-scanning and directivity, amplitude and phase distribution for the radiating elements are required. Fourier transform of this complex distribution is required to be measured in this purpose. To provide distribution for this complex distribution some algorithms [148, 163, 164] have been discussed in literature. The most common power divider for designing the feed network is the Wilkinson's power divider [165]. Designing the Wilkinson's divider requires diodes to be soldered between arms of the divider which makes the power divider complex in higher frequencies. A simpler quarter-wave

transformer power divider [79] can also provide very good matching and wideband return loss and is suitable for this study. In this case, to meet the requirement of the antenna array, some design constraints as side-lobe level, beamwidth etc. are the main challenge and for that reason different synthesis technique of planar array have to be analysed. In the next section different method of beam shaping algorithm and their benefits are discussed.

2.3.3 Array Analysis

Array analysis includes beam shaping, which is one of the properties of smart antennas, which allows antenna to receive energy from a specific direction while simultaneously blocking it from other directions [79, 166-168]. Beam shaping techniques can be divided into two general categories: conventional (fixed beam) beamformers and adaptive beamformers or phased array. Generally, with the fixed-beam antennas it is not possible to achieve higher gain. On the other hand, with a phased array antenna, the direction of the transmitted beam can be controlled by carefully adjusting the amplitudes and phase shift of the antenna elements [169]. Different kind of conventional beam shaping techniques have been discussed in literature. In the Chebyshev method, current distribution of this array has been first discussed by Dolph [170] which discusses the broadside array of a linear distribution. Some other studies have been made in [171-173]. Some modifications have been made to expand in planar arrays in the next few years [174]. In the next few studies some modifications in order to control the beamwidth have been discussed in [175-177]. The advantage of Chebyshev's method is that it allows having a constant side-lobe level. The beamwidth is the parameter that is sacrificed. Depending on the application, for this proposal Chebyshev can be very promising. Some other methods as uniform power distribution, gaussian power distribution are very common which offers easy understanding of the theory. Some modifications of these methods (Gaussian, Chebyshev) are recently discussed in [169, 178-180] where isosceles trapezoidal distribution and staircase

power distribution have been proposed and comparison with conventional Gaussian method has been showed.

2.3.4 Multi frequency operation

In conventional microstrip patch antennas, dual- or multi-frequency operation can be obtained by employing multiple radiating elements [181] or reactively loaded patch antennas [182] or multi-frequency dielectric resonator antennas [183]. Of them, multiple radiating element is promising because of its straightforward design procedure. Multiband synthetic aperture radar (SAR) antennas offer several advantages for spaceborne remote sensing satellite applications [184]. Dual-polarization enhances the information content by providing two co-polar and two

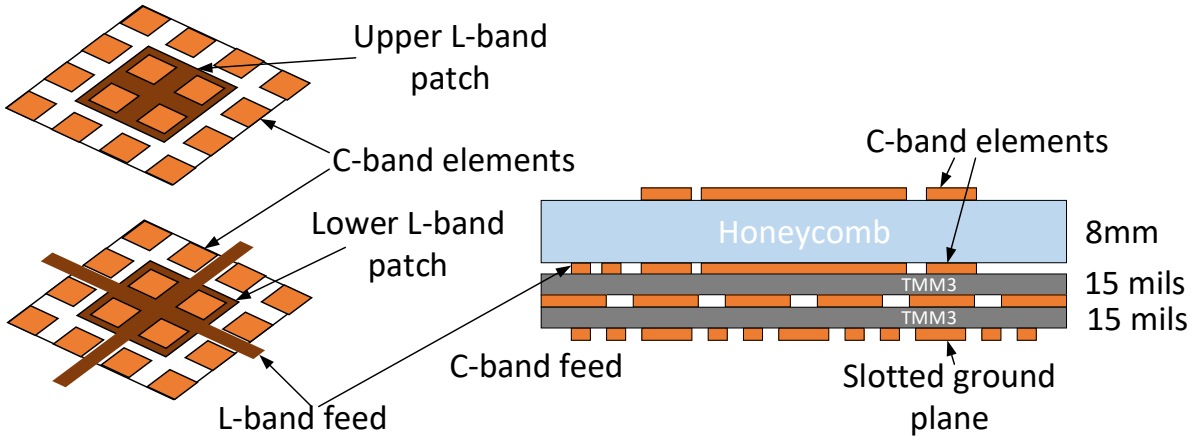

Figure 2. 3 L- and C-bandn antenna in the same shared aperture from Shafai et al 2000.

cross-polar scattering data. The cross- polarization Synthetic Aperture Radar (SAR) imagery is important at high-incidence angles. The multiband operation, on the other hand, can provide a finer resolution scanning and better penetration and reflection data from various scatterers [185]. This type of configuration have been reported by [186-193] and other many research works. Both L-band and C-band in the same aperture has been discussed by [185] shown in Figure 2. 3. A stacked configuration is used. The lower L-band antenna is etched on its TMM3 feed substrate, is thus a transmission- line-fed square patch. The upper patch is on a honeycomb substrate of about 8-mm thickness and is electromagnetically coupled to the lower patch. Both

these patches are perforated, symmetrically so that the induced currents are symmetric and cross polarization is kept to a minimum.

In the antenna design, four of the C-band patches had to be placed within the L-band ones. This resulted in a perforated L-band element surrounded by 16 C-band patches, forming a unit cell. To meet the bandwidth requirements with a low-profile lightweight design, a stacked configuration was utilized. The lower elements were placed on a thin 15-mil TMM3 substrate, which also contained the feed network of the L-band array directly coupled to its elements. The upper elements were placed on a honeycomb or foam substrate. The C-band elements were slot-coupled fed from a lower 15 mil TMM3 substrate. Thus, the entire array in both bands used electromagnetic coupling eliminating vertical connections.

2.3.5 Increasing gain, sensitivity and efficiency of operation

Recently, research work has focused on frequency reuse and polarization diversity involving the use of two orthogonal polarizations. Dual-polarized microstrip antennas have been studied and developed extensively [194]. And arrays of antenna are a very good way to increase gain of the antenna. An approach to use dual polarized arrays of microstrip antenna has been reported by [195]. Coaxial feeding has been used and horizontal/vertical dual polarization has been used shown in Figure 2. 4 where feeds touch the patch beneath the patch layer. The result of this approach was improved directivity gain, lower cross polarization. A number of dual polarization design has been reported in [185, 187-196]

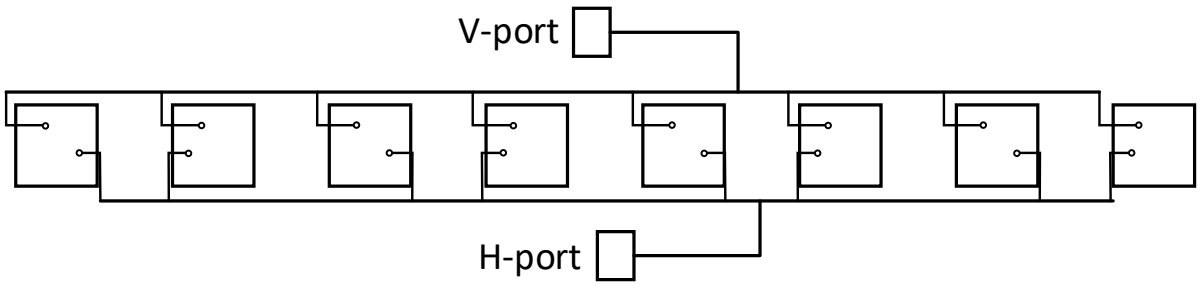

Figure 2. 4 Patch feed network for dual polarized antenna array.

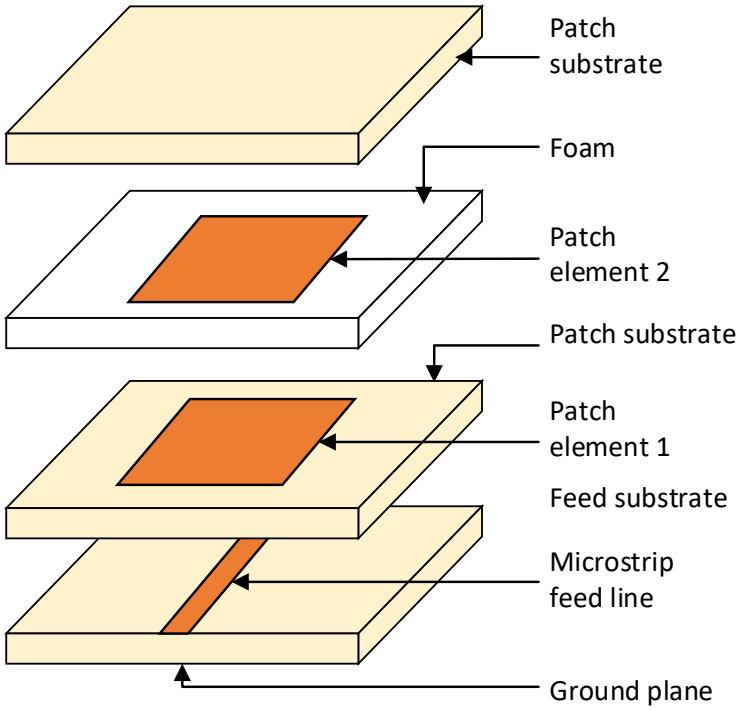

Figure 2. 5 Stacked patch proximity coupled antenna

Another novel design is to use stacked patch design to accommodate multiple patch in the same physical aperture. One design of this configuration is reported in [197] shown in Figure 2. 5. This investigation is a single polarized structure directly related to the results presented in [198], where it was shown that good bandwidth and efficient radiation could be achieved for the case of a proximity coupled stacked patch mounted on a high feed dielectric constant if the next layer was of similar dielectric constant value.

2.4 Soil Moisture Retrieval Method

2.4.1 Soil Dielectric Properties

The dielectric constant of dry soils is almost independent of temperature [199] and frequency. On the contrary, wet soils show a complex behaviour depending on the interaction between soil, water, and air particles. A series of dielectric constant measurements of five soils with

different texture composition at frequencies between 1.4 and 18 GHz was performed [200] and found out that texture has a strong effect on the dielectric behaviour. Models that use a semi-empirical was followed by two widely used models presented [201, 202].

2.4.2 Soil Roughness Effects

Several attempts have been made to account for the effect of surface roughness on the observed brightness temperature because when a radar wave impinges on a smooth surface at a specific incident angle, some energy is scattered in all directions, some of which returns to the sensor as backscatter, and the rest is reflected in the specular direction [6, 203-207]. Physical models [208] are generally driven by surface characteristics derived from measurements of surface height profiles [209]. Using only the coherent term of the scattered field, [203] proposed a simple model for the reflectivity.

2.4.3 Retrieval Algorithm

Retrieval algorithms can be different based on active or passive sensing. For SMAP, methods such as single channel algorithm [210], dual channel algorithm [210], land parameter retrieval model [211-213] can be used. Based on the experimental relationship between the geophysical variables and the radiative transfer equation using a regression technique moisture component of soil can be measured for passive sensing [214, 215]. Another approach can be based on the use of neural networks. These algorithms have been used with satisfactory results in the retrieval of agricultural parameters from radiometric data [216]. Another approach is widely used and is based on the inversion of radiative transfer models. Obviously, this approach has also some disadvantages, since errors of the model lead to errors in the retrieval. The soil moisture models are used as forward models, and the geophysical variables are retrieved by minimization of a cost function [217]. Estimates can be constrained to be close to the initial value by choosing low values, or they can be left as a free parameter by selecting.

2.5 Analysis and discussion

This article provides a detailed overview of previous works on soil moisture retrieval work as well as smart antennas. As water is one of the most valuable elements in nature, soil moisture plays a vital role determining the climate and vegetation of a certain area. Combining the soil moisture algorithm with multiband antenna design concept, the present research can be enriched with new technologies. As discussed in the soil moisture retrieval algorithm section, L-band is considered the frequency band which is most likely to be used in remote sensing of soil moisture. But though L-band penetrates 1-5 cm which is impressive, lacks the sensitivity or details in information. That is why multiband structure could be very novel and effective in remote sensing. Active radar sensing at L-band has shown some positive results for soil moisture retrieval, passive microwave measurements have a reduced sensitivity to land surface roughness and vegetation cover. The ESA (European Space Agency) has launched SMOS (Soil Moisture and Ocean Salinity) which is the first dedicated soil moisture mission based on L-band passive microwave radiometry. Another mission is SMAP (by NASA in 2015) working in the same study. Aquaris (June 2011) is another mission that is to bridge the previous two missions by ensuring harmonious soil moisture product with consistent characteristics. The scientific basis of operational algorithm for high resolution mapping of near-surface soil moisture content is yet to be explored. Until now, there has been no way to undertake such a comprehensive and integrated study anywhere in the world due to no access to the appropriate combination of airborne sensor systems to be flown simultaneously.

To summarize, it is possible to measure soil moisture using radiometer because the amount of soil moisture has direct effect on dielectric constant. Using only L-band data can determine soil moisture but with only small sensitivity and less accuracy. Other high frequency bands Ku and Ka can provide the required sensitivity. Different antennas for those three bands will require more physical space and will be a bulky system. A shared aperture multiband antenna operating

these frequencies could be a good choice for this operation. Also, the brightness temperature for single L-band system is currently present using the Polarimetric L-band Multibeam Radiometer (PLMR) which can effectively calculate from L-band radiation but combining multiband and decipher the data will be a rigorous work. Also phase shifters, beam shaping networks and RF switches design would be specialized for this system.

2.6 Research gap

The space missions can provide the data for the soil moisture and ocean salinity, but every system has its own drawbacks. It is clear that though active system gives higher resolution, it is expensive, and it lacks the sensitivity. Hence a fully passive system is needed for the viability and practicality. SMOS is a fully passive system but it lacks the resolution as it has only L-band radiometer. To achieve higher resolution, multi-band radiometer is required. Currently Department of Civil Engineering at Monash University is working with NASA for SMAP data collection and validation using Polarimetric L-band Multibeam Radiometer (PLMR), Polarimetric Scanning Ka/Ku-band Radiometer (PSKR) and Polarimetric L-band Imaging Scatterometer (PLIS) from Prosensing Inc and it is a natural choice to use Ku – and Ka-band antenna as a supplement to the L-band antenna for the multiband radiometer. There is no single module commercially available in the market that can measure soil moisture and be planar, cheap and portable to be used in the agriculture sector where resolution of few tens of metres are more realizable than a 40 km by 40 km grid. Ku- and Ka-band antennas alone as airborne radiometer can also help estimate the moisture information which can be helpful in the agriculture sector.

2.7 Research Motivation

The present situation allows to measure soil moisture from remote in a very complicated way which lacks viability by some margin. Both active and passive leads to a complicated and

expensive way of soil moisture mapping. A number of satellite missions have already been launched in endeavour to measure soil moisture which no wonder are some very expensive missions. Here arises a cheap, viable way of determining soil moisture. In the microwave approach that has been discussed in the literature, only L-band is currently being used to monitor the brightness temperature which cannot be downscaled for higher resolution. In search for feasible method to downscale L-band data a novel conception must be developed. In order to solve this research problem, other high frequency bands (e.g. Ka-, Ku- bands) can be incorporated in the same aperture to make the design compact, cheap and enriched in terms of information. Along with L-band antenna, these high frequency bands (Ku- and Ka-bands) can exploit their high frequency property for better resolution keeping the same penetration and sensing of original L-band. The primary target will be a fully planar compact module for aircraft which in future can be used in spacecraft and satellites.

2.8 Research Aims

The core aim of this research is to build a shared aperture radiometer antenna for measuring soil moisture. The specific targets of the projects are following-

- Developing compact shared aperture antennas for multi-band operations in L-, Ku- and Ka-bands.
- Implementing novel array synthesis and analysis for uniform antenna performance in multiple bands.
- Novel beam forming algorithm to shape the beam in multiple frequencies.

The system of this research endeavour is presented in Figure 2. 6 (a) defining all three bands' beamwidth, approximate altitude of the aircraft and tentative covering area. The expected higher resolution footprint of the Ku- and Ka-bands are shown in Figure 2. 6 (b). The requirement specifications (Table 2. 1) of the space-borne/airborne radiometer are very

demanding in terms of antenna beamwidth, pattern efficiency and beam steering capabilities. New mathematics and sciences in the field will enhance the knowledge bases of antenna design and advance the field.

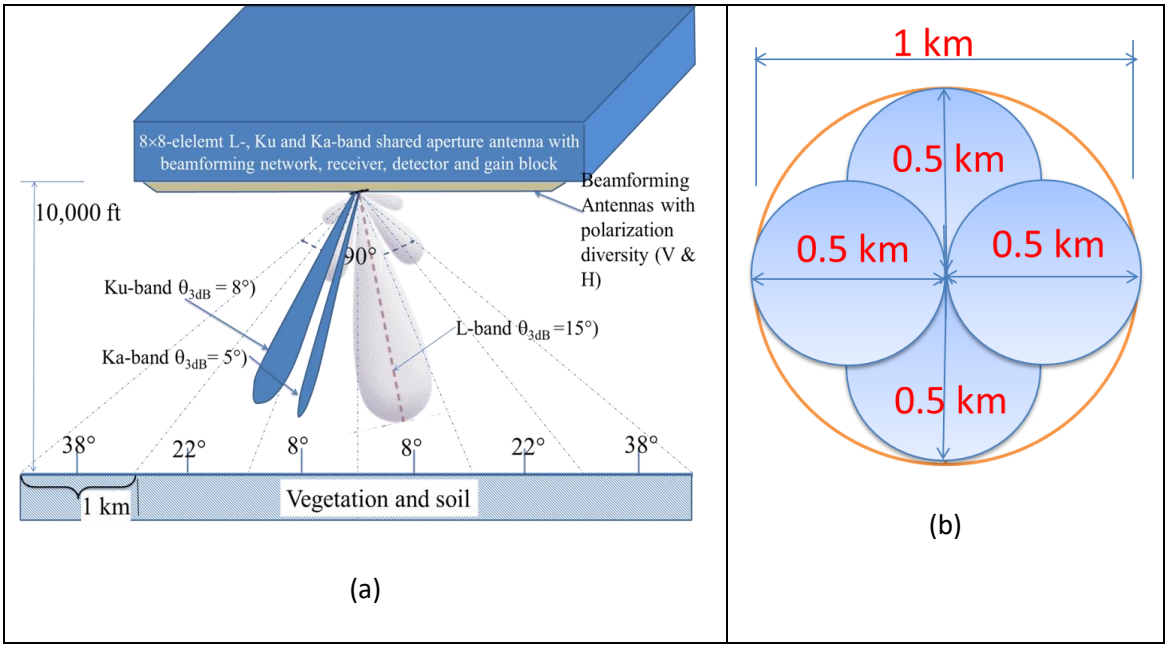

Figure 2. 6 (a) Proposed shared aperture multi-beam multi-band radiometer planar antenna and scan zone for aircraft, (b) Ku- and Ka-band footprint inside an L-band footprint from 10000 feet altitude.

In brief, the main aim is to design a universal smart polarimetric antenna system that can be used for multiple-bands covering sparsely located L-, Ku and Ka-bands. The ultimate objectives that can be fulfilled are: L-band for more accurate mapping and Ku- and Ka-bands for higher resolution. However, it is not a trivial task to design an antenna that covers multiple bands in a compact and shared aperture configuration and still be light weight. Another aim is to use the developed antenna universally without any modification of existing facility to fit the antenna on board an aircraft for demonstrating the technology and developing the downscaling approach with the provision to use with commercially equipped satellite radiometers in near future. So far, such an antenna system has not been reported.

Table 2. 1 Specifications of shared aperture multi-band multi-beam antenna

Specifications			
Design Parameters	**L-Band**	**Ku-band**	**Ka-band**
Design Frequency	1.4 GHz	18.7 GHz	37 GHz
10 dB return loss (RL) Bandwidth (%)	25 MHz (1.8%)	200 MHz (1%)	1.5 GHz (4.1%)
No. of antenna elements (M×N)	8 × 8	8 × 8	8 × 8
Max. aperture size (mm × mm)	1,200 × 1,200	90 ×90	50 × 50
Beamwidth (BW°)	**8°**	**8°**	8°
Beam efficiency	**90%**	**90%**	**90%**
3 dB BW footprint diameter (km)	1	0.5	0.5
Peak gain	22 dBi	22 dBi	22 dBi
Sidelobe level (SLL)	25 dB	25 dB	25 dB
Cross-polar isolation	≥ 25 dB	≥ 25 dB	≥ 25 dB
Weight	Less than 20 kg (including radome)		
Dimensions (mm)	1,200 × 1,200 × 100 mm		

2.9 Conclusions

This chapter presents a comprehensive review on soil moisture measurements and antenna structures. Soil moisture, being one of the key elements in hydrology, weather science and agriculture sector, can be measured using microwave remote sensing. Passive sensing senses the natural emission from the earth to measure the soil moisture content. Several space missions along with a lot of aircraft and ground missions are carried out by researchers to measure the soil moisture accurately. The spatial, temporal and polarization diversities exploited from smart antennas have added new and unique dimensions in wireless communications. The advantages of smart antennas (especially polarization diversity) have been exploited in PMR to capture the natural emission (also called brightness temperature) for soil moisture measurement. For remote sensing radiometer smart antennas, it is preferable to have shared aperture multiple band multi-beam and polarization diversity antenna so that the weight can be reduced, and the antenna can be made compact and light weight. From the literature, aperture coupled feeding technique is found to be a suitable method of feeding the antenna. Array antenna design, array analysis and multi-band structure are few stages of the radiometer design discussed in this chapter. After a thorough review, research gap is found, and research goal is established. The system requirements for the radiometer antenna to be used commercially is set to the standard of the ARC project requirements.

The previous chapter and this chapter lay the foundation of the motivation and aim for this research. The next chapters discuss technical work performed to achieve the goal of this research.

3 Linear Polarized Antenna

3.1 Overview

A number of techniques for the development of the radiometer LP antennas are analysed in the previous chapter and the aperture coupled microstrip antenna (ACMSA) is chosen because of the simultaneous presence of all prerequisite properties for a radiometer antenna, such as lower cost, smaller size, lighter weight and higher gain, when compared with other antennas. A radiometer antenna has a very demanding gain, reflection, linearity, isolation requirements so it is important to choose the antenna element and design and/or optimize before implementing array configuration.

On the process to develop a multi-band radiometer array, the first step is to design an element antenna for each frequency band. In this chapter, the development of the LP ACMSA antennas in three different microwave frequency bands, namely L-, Ku- and Ka-bands are presented in detail, which is suitable for radiometers, and the flow of the chapter contents are as follows:

First, a brief review is carried out to discuss the advantages of the aperture coupled feeding for radiometer requirements. Then, upon finding the aperture coupled microstrip patch antennas to be suitable, the theory of radiation is discussed. Then, three single element LP antennas are designed for three different bands. In the measurement section, a single element Ku-band element is fabricated, assembled and measured to compare with the simulation result. Finally, a parametric study is shown in detail to explain and understand the design procedure and optimization given the different frequencies and requirements.

Chapter Outline

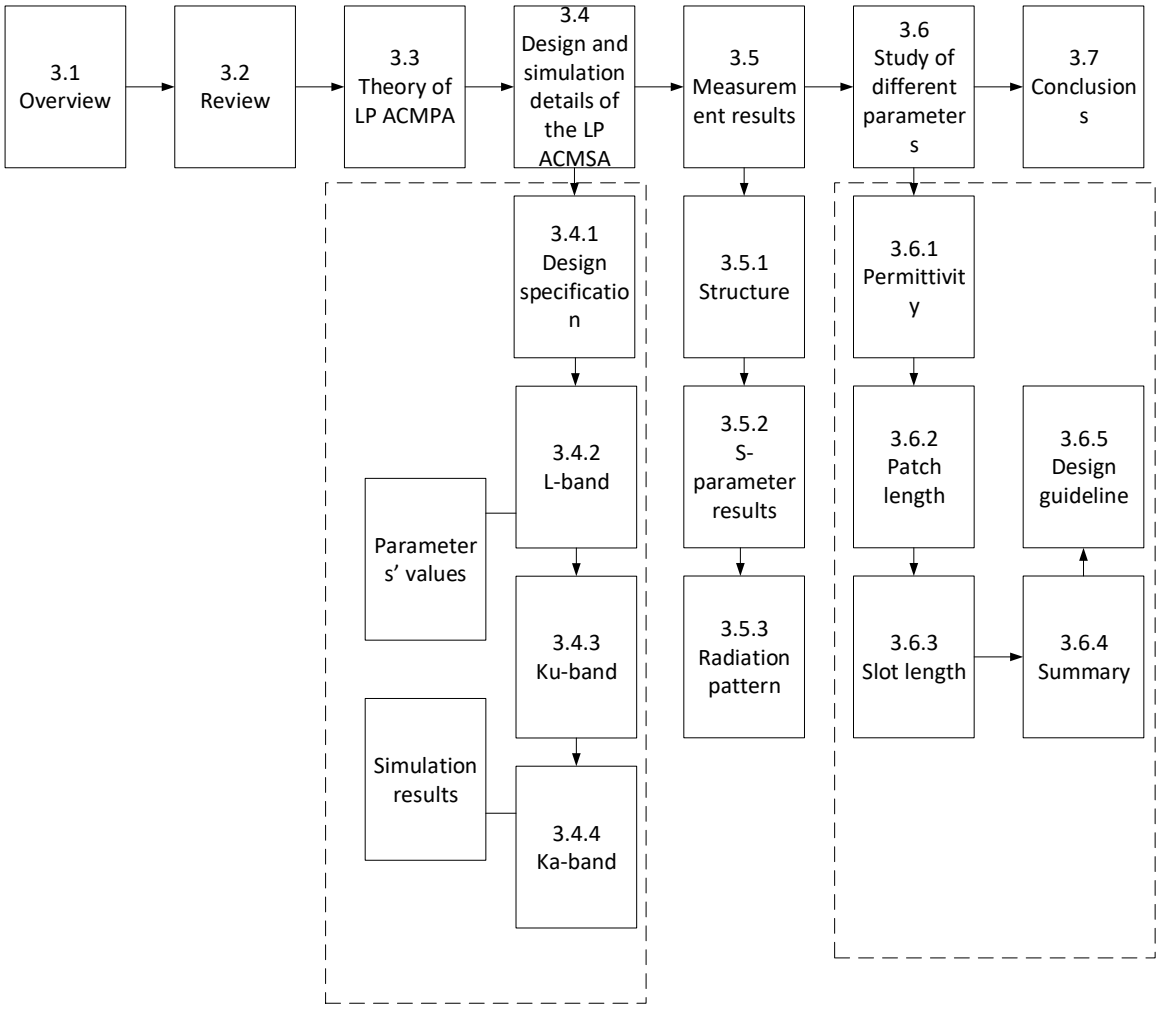

3.2 Review

The goal of this chapter is to develop linearly polarized (LP) radiometer antennas for all three bands, which are L- band at 1.4 GHz, Ku-band at 18.7 GHz and Ka-band at 37 GHz. The typical properties of an LP antenna element are - (i) higher gain, so that it can scan from some distance, (ii) smaller in size to be easily placed in the radiometer frame, (iii) lower manufacturing cost, since the system needs to be cheap, (iv) lighter weight, so that it can be fitted in an aircraft, UVA or even satellite. Among many feeding techniques discussed in Chapter 2, some of them have a very large profile, some other have a too narrow bandwidth, some have higher weight

and manufacturing cost, and some other have lower gain and beam-widths. Upon considering all the facts available from the literature discussed in the previous chapter, aperture coupled design is chosen to be the suitable feeding technique for the element antenna design for this chapter and the future chapters.

Advantages of LP ACMSA over other designs make it suitable for it to be used in radiometer antenna in all three frequencies together. Here are few advantages to summarise them-

- LP ACMSA is a low-profile design than the most other wideband antennas (horn, dipole, LPDA).
- Manufacturing cost is also lower than horns, dipoles and bi-conical antennas.
- Planar configuration is possible which gives this technique an edge over horn, bi-conical, Vivaldi notch and other non-planar designs.
- Weight and size are relatively smaller than horn, bi-conical and Vivaldi notch antennas.
- Gain is quite high, and it has symmetric and similar electric and magnetic field.
- For multi-band design, a stacked layered structure is possible.

3.3 Theory of LP ACMSA

LP ACMSA is a low profile, low cost, lightweight, wideband, high gain and wide beam antenna. Unlike regular patch antenna, where patch size and the excitation point of the feed lines are optimized, in the LP ACMSA antennas, aperture size, stub length and in some cases air gap between patch layer and feed layer and/or multilayer stack patches are optimized. Increased number of variables for optimization also means an increased degree of freedom for designers. Due to the structure, where the feed layer, the ground layer and the patch layer are isolated, it is easier to design an array later using this structure than any other structures up to an extent. For LP antenna, the top layer is the patch layer shown in Figure 3. 1, the ground is the next

layer and the feed line is the bottom layer. Plan view with all the design parameters is also shown in the figure. This antenna has two substrate layers of length, l, and width, w. One layer is in between the patch and the ground, and the other layer is in between the ground and the feed line layer. A rectangular patch with length, lp, and width, wp, is etched from the top substrate layer. The ground plane consists just a rectangular slot of length, ls, and width, ws. The feed layer is the most complicated part in this design. A 50 Ohm line is etched from the bottom layer of length, l1. This feed line is a dual offset feedline meaning it divides into two parts, each part identical to the other. Each part consists of an L-shaped 100 Ohm line orthogonal to the 50 Ohm line so that it passes under the aperture on the ground layer and continues a bit longer. The distance between two arms of 100 Ohm lines is, l2, and the length of the individual arm is, l3. The extended or continued part from the aperture is of, l4, length and called stub length which is a very important parameter for the impedance matching.

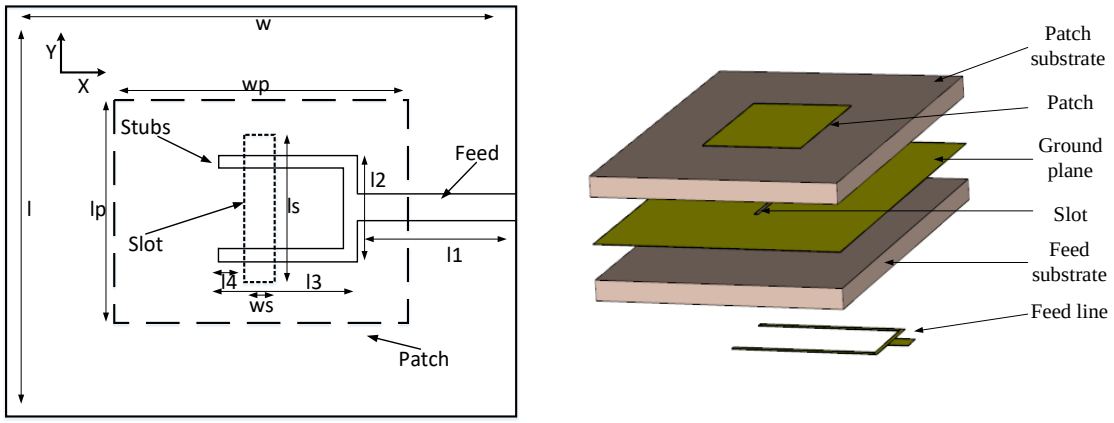

(a) (b)

Figure 3. 1 Layout of the single element LP ACMSA (a) plan view and (b) expanded 3-D view

The widths (not shown in the figure) of the 50 Ohm and 100 Ohm lines depend on the substrate thickness and the dielectric properties of the substrate. The widths are very important to be accurate as there will be mismatch otherwise hence high reflection and low gain will result from this mismatch. The transition from the 100 Ohm to 50 Ohm is the place where it is likely

to have the most mismatch as it is impossible to directly transit from two different impedances. Several intermediate stages or impedances are not designed to avoid the design complexity. Two substrates are aligned one top of the other without any airgap and the centre of the patch, ground and feed line are also aligned. The substrate thickness has direct impact on the bandwidth and the feed width calculation. Thinner feed lines are generally preferable because it is easier to design the feed lines for a large array. Also, thinner feed lines couple with the slot better which makes the design more ideal. To ensure less spurious radiation with minimal copper loss or radiation from the feed lines, substrate with permittivity between 2 and 10 is a good choice and thickness of the substrate should also be approximately $0.01\ \lambda$. The size of the patch which are the patch length and patch width determine the radiation from the patch. The patch length, lp, determines the resonant frequency of the antenna, whereas, patch width, wp, controls the resonant impedance. To achieve lower cross polarization level and impedance the patch width wp should be bigger than the patch length, lp. In the ground plane, slot width, ws, and slot length ls also play important part on the radiation coming from the ground plane. The size of the slot determines the amount of radiation coming through. The length of the slot, ls, is responsible for coupling and radiation contributing to the back lobe, and the width of the slot, ws, also play a role in the coupling. At the bottom layer, the feed line has many design parameters and each of them plays part determining the coupling and tuning to the resonant frequency. Tuning stub, l4, is tuned to mitigate the excess reactance. Other parameters such as, l1, l2 and l3 are also optimized to tune to the resonant frequency. This configuration is for only one polarization and can be either horizontal or vertical polarization which will be discussed in details in the next chapter.

3.4 Design and simulation details of LP ACMSA

Computer Simulation Technology (CST) Microwave Studio 2017 is used for the design, simulation and optimization of the single element LP ACMSA. First, a commercially available

substrate is chosen for developing the antenna, in this case it is TLX-8 with dielectric constant of 2.55 and thickness of 0.127 mm. Then, the antenna parameters and feed line widths on that substrate are calculated for the centre frequency. After that, the slot is matched with the dual offset feed lines over the entire bandwidth in simulation. Next, the radiating patch is matched with the slot and feed line. Finally, the single element LP ACMSA design is optimized further for fabrication.

3.4.1 LP ACMSA design specification for the radiometer antenna

Following specifications are initially set for developing a single element linear polarized antenna for L-, Ku- and Ka-bands. These specifications will ensure that when designing the array antenna in dual-polarized polarization is completed, the design requirements are satisfied.

- Gain: Gain for a single element LP antenna should be more than 6.5 dBi in all three bands. This is set to ensure that the array antenna after beam shaping has a high gain which is essential for the radiometer antenna.
- Bandwidth: Bandwidth is one of the most important properties of an antenna. In general, radiometer antennas are narrow band with high quality factor. The design requirement is set to have 25 MHz (1.8%) for the L-band, 200 MHz (1%) for the Ku-band and 2 GHz (5.4%) for the Ka-band. The reason is purely to focus the antenna beam onto the area of interest.
- Cross-polar isolation: Cross-polar isolation is to be set as high as possible. The requirement is set to have less than -25 dB
- Weight and size: The weight and size of a single element LP ACMSA will be multiplied by a factor depending on the array size, so a single element must be as compact as possible.

- Beamwidth: The beamwidth of a single element and an array will be different as increasing the number of elements in an array will narrow the beamwidth. For a single element LP ACMSA, the beamwidth is set to have around 65°.

Table 3. 1 Design target for LP ACMSA

Antenna parameter	Target value for single LP ACMSA	Target value for 8 × 8 array after beamforming
Gain	6.5 dBi	22 dBi
Bandwidth	25 MHz (L-), 200 MHz (Ku-), 1.5 GHz (Ka-band)	25 MHz (L-), 200 MHz (Ku-), 1.5 GHz (Ka-band)
Beamwidth	~ 65°	~ 10°
Cross-polarization	< -25 dB	< -25 dB

These design specifications are summarised in the Table 3. 1 below

3.4.2 L-band LP ACMSA design simulation and results

L-band antenna operates at 1.4 GHz as the centre frequency. The feed network of this antenna is selected as aperture coupled and the polarization is linear as discussed.

3.4.2.1 Parameter values for L-band LP ACMSA

As mentioned earlier, only linear polarization is discussed in this chapter. The aperture coupled configuration of the L-band antenna is similar to what is shown in Figure 3. 1. In this study the values of the parameters are as follows. The substrate is TLX-8 with a thickness of 0.127 mm. The length and width of the patch are the same, lp = wp = 62 mm though in the theory section it is mentioned that the width should be longer than the length. This symmetry will be used for dual-polarized structure in the next chapter. The feed length l1 = 60 mm. Feed line width is the

same as 50 Ω line and not set as a variable. The extension of the dual offset or the Y branch of the feed is l2 = 18 mm. The arms of the feed lines are l3 = 48 mm. The stub is l4 = 4 mm. Substrate length and width are also the same l = w = 120 mm. The slot length is ls = 23 mm and slot width ws = 5mm. These variables are obtained from the simulation using CST 2013.

3.4.3 Simulation results

Simulation shows the S-parameter, which in this case only S11 against frequency in Figure 3. 2. In this figure it can be seen that the antenna is very well matched centred at 1.4 GHz. The reflection loss is very minimum at approximately 35 dB which results in only 0.03% power loss due to reflection. Also, the bandwidth is from around 1.33 GHz to 1.48 GHz resulting around 150 MHz which is way above than the requirement (25 MHz).

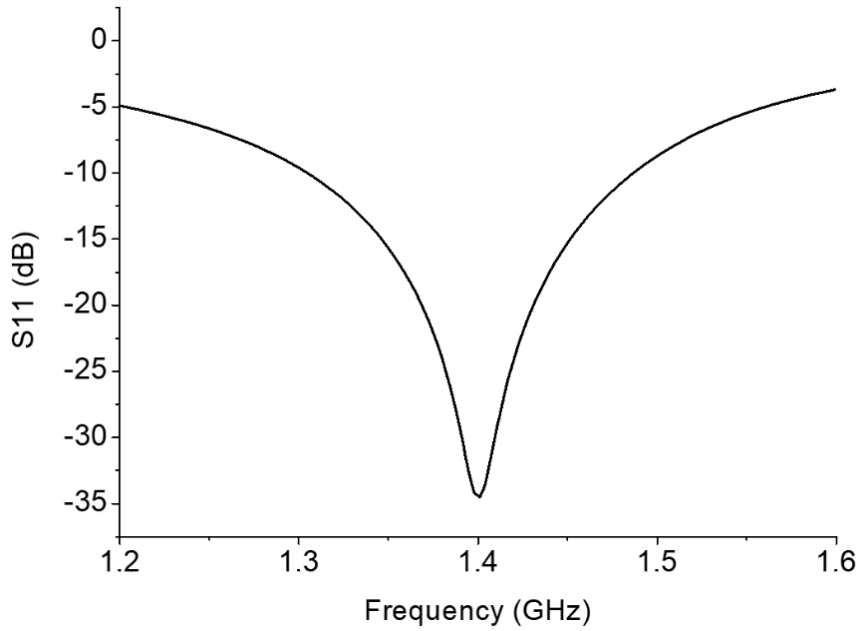

Figure 3. 2 S-parameter for L-band LP ACMSA

The radiation patterns for the electric and magnetic fields are shown in Figure 3. 3 (a) and (b) respectively. For the electric field the co-polar magnitude of the antenna is around 7.7 dBi and that is at 0º. The cross-polar level is below -30 dBi and at 0º that is minimum with -63 dBi which is 70 dB below the co-polar main lobe. The shape of both the co-polar and cross-polar

pattern are symmetric along 0º and 180º line. For the magnetic field, again the co-polar magnitude of the antenna is around 7.4 dBi and that is at 0º. The cross-polar level is below -40 dBi this time and at 0º that is minimum with -72 dBi which is around 80 dB below the co-polar main lobe. The shape of both the co-polar and cross-polar patterns are again symmetric along 0º and 180º line.

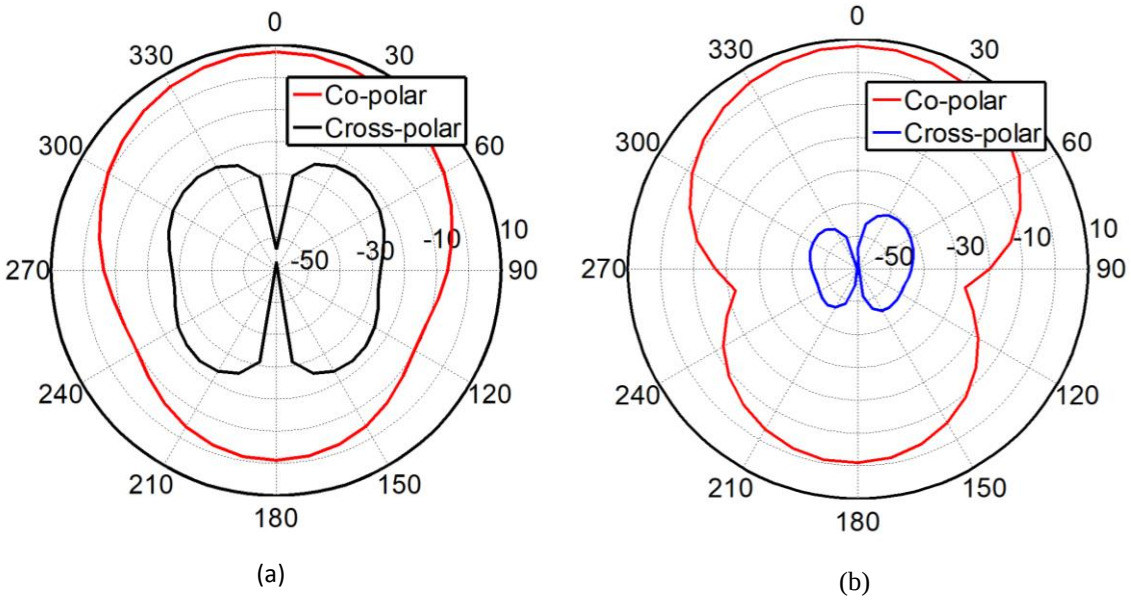

Figure 3. 3 Radiation pattern of (a) E- and (b) H- plane for co polar and cross polar of single element L-band LP ACMSA antenna

3.4.4 Ku-band LP ACMSA design simulation and results

Ku-band antenna in this case operates at 18.7 GHz as the centre frequency. The feed network of this antenna is also selected as aperture coupled and the polarization is linear as discussed.

3.4.4.1 Parameter values for Ku-band LP ACMSA

The aperture coupled configuration of the Ku-band antenna is again similar to what is shown in Figure 3. 1. In this study, the values of the parameters are as follows. The substrate is TLX-8 with a thickness of 0.127 mm. The length and width of the patch are the same, lp = wp = 4.8

mm. The feed length l1 = 4.1 mm. Feed line width is the same as 50 Ω line and is a constant for a given substrate of fixed thickness. The extension of the Y branch of the feed is l2 = 1.5 mm. The arms of the feed lines are l3 = 3 mm. The stub is l4 = 1.1 mm. Substrate length and width are also the same l = w = 8 mm. The slot length is ls = 3 mm and slot width ws = 0.3 mm.

3.4.4.2 Simulation results

Simulation shows the S-parameter, which in this case only S11 against frequency in Figure 3. 4. In this figure, the antenna is very well matched at 18.7 GHz. The reflection loss is very minimum at approximately 25 dB which results in only 0.32% power loss due to reflection. Also, the bandwidth is from around 18.5 GHz to 18.8 GHz resulting around 300 MHz which is above than the requirement (200 MHz).

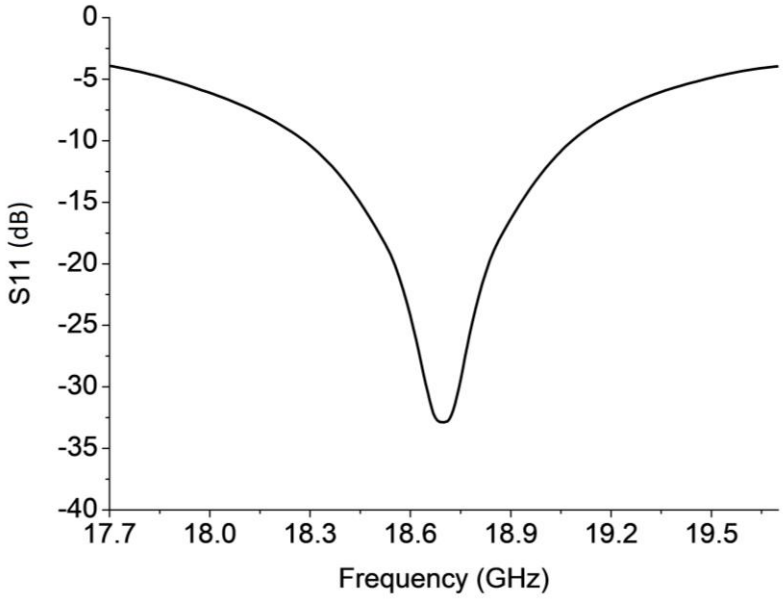

Figure 3. 4 S-parameter for Ku-band LP ACMSA

The radiation patterns for the electric and magnetic fields are shown in Figure 3. 5 (a) and (b) respectively. For the electric field the co-polar magnitude of the antenna is around 8.3 dBi and that is at 0º. The cross-polar level is below -50 dBi and at 0º that is minimum with -75 dBi

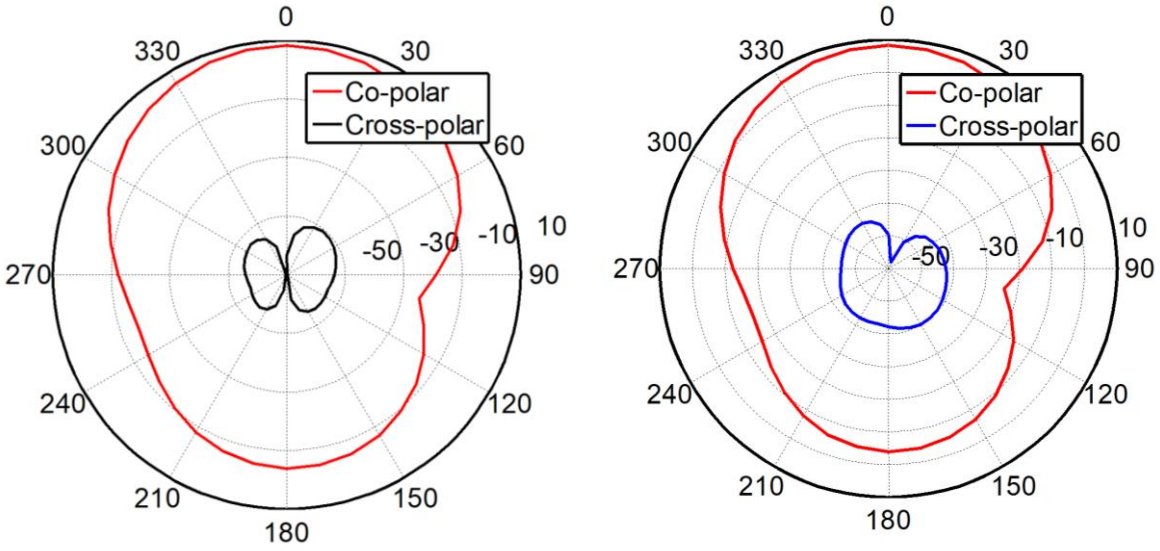

Figure 3. 5 Radiation pattern of (a) E- and (b) H-plane for co polar and cross polar of single element Ku-band LP ACMSA antenna

which is approximately 85 dB below the co-polar main lobe. The shape of both the co-polar and cross-polar pattern are symmetric along 0º and 180º line. For the magnetic field, again the co-polar magnitude of the antenna is around 8.0 dBi and that is at 0º. The cross-polar level is below -50 dBi this time and at 0º that is minimum with -70 dBi which is approximately 80 dB below the co-polar main lobe. The shape of both the co-polar and cross-polar patterns are again symmetric along 0º and 180º line.

3.4.5 Ka-band LP ACMSA design simulation and results

Ka-band antenna operates at 37 GHz. The feed network of this antenna is again selected as the aperture coupled feeding and the polarization is linear.

3.4.5.1 Parameter values for Ka-band LP ACMSA

The aperture coupled configuration of the Ka-band antenna is similar to what is shown in Figure 3. 1. In this study the values of the parameters are as follows. The substrate is TLX-8

with a thickness of 0.127mm. The length and width of the patch are the same but smaller than that of the Ku- and L-bands. The patch length and width, lp = wp = 2.4 mm. The feed length l1 = 1.92 mm. Feed line width is the same as 50 Ω line and not set as a variable. The extension of the Y branch of the feed is l2 = 0.82 mm. The arms of the feed lines are l3 = 1.3 mm. The stub is l4 = 0.7 mm. Substrate length and width are also the same l = w = 4 mm. The slot length is ls = 2 mm and slot width ws = 0.2 mm.

3.4.5.2 Simulation results

Simulation shows the S-parameter, which in this case only S11 against frequency in Figure 3. 6. In this figure, the antenna is very well matched at 37 GHz. The reflection loss is very minimum at approximately 34 dB which results in only 0.033% power loss due to reflection. Also, the bandwidth is from around 35.9 GHz to 37.9 GHz resulting around 2 GHz which is above the requirement (1.5 GHz).

The radiation patterns for the electric and magnetic fields are shown in Figure 3. 7 (a) and (b) respectively. For the electric field the co-polar magnitude of the antenna is around 8 dBi and that is at 0º. The cross-polar level is below -45 dBi and at 0º that is minimum with -65 dBi

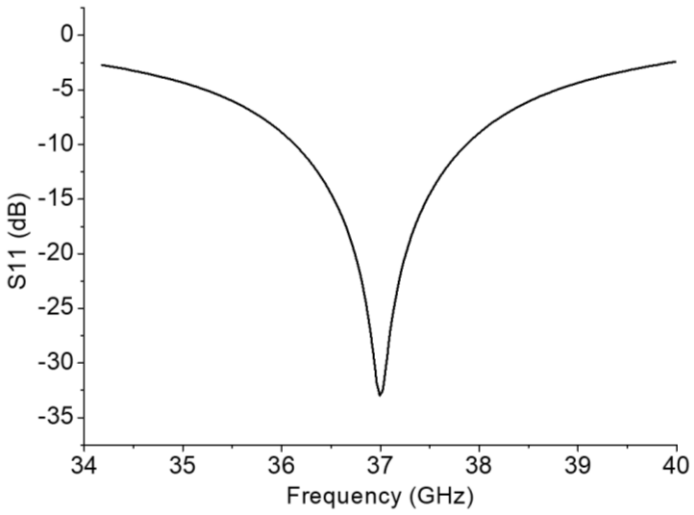

Figure 3. 6 S-parameter for Ka-band LP ACMSA

which is approximately 75 dB below the co-polar main lobe. The shape of both the co-polar and cross-polar pattern are symmetric along 0º and 180º line. For the magnetic field, again the

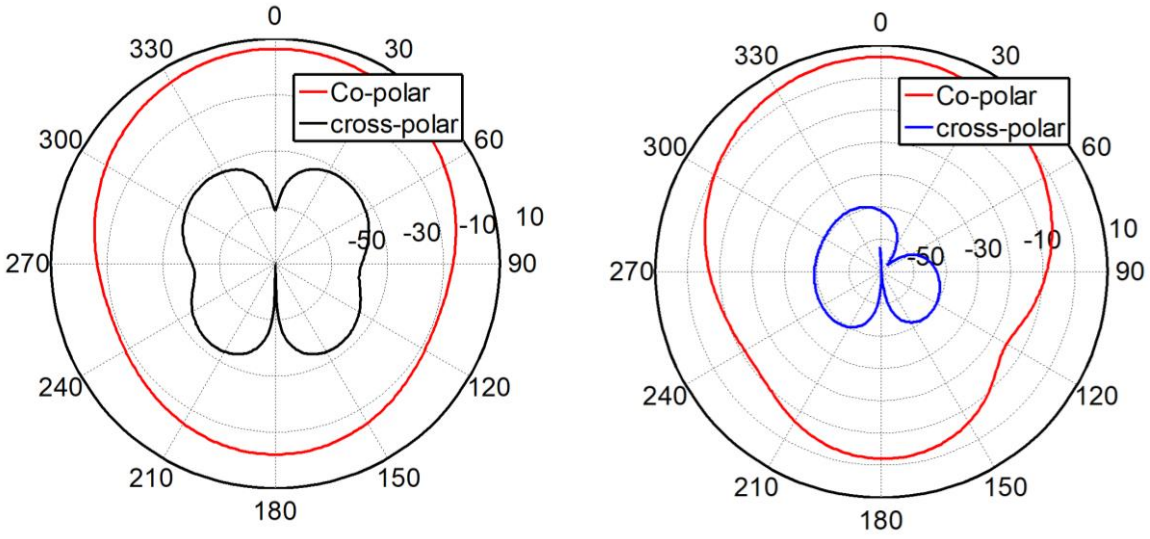

Figure 3. 7 Radiation pattern of (a) E- and (b) H-plane for co polar and cross polar of single element Ka-band LP ACMSA antenna

co-polar magnitude of the antenna is around 8.0 dBi and that is at 0º. The cross-polar level is below -45 dBi this time and at 0º that is minimum with -65 dBi which is approximately 75 dB below the co-polar main lobe. The shape of both the co-polar and cross-polar pattern are again symmetric along 0º and 180º line.

3.5 Measurement results

In this study a LP Ku-band antenna was fabricated and measured as the proof of concept. Details of the structure and measurement results are discussed in the next sections.

3.5.1 Structure

The structure of the Ku-band LP ACMSA is the same as shown in Figure 3. 1. The substrate is TLX-8 with a thickness of 0.127 mm. Similar to the simulation the length and width of the patch are kept, lp = wp = 4.8 mm. The feed length l1 = 4.1 mm. Feed line width is the same as 50 Ω line and is 0.35 mm for a given substrate of fixed thickness. The extension of the Y branch

of the feed is l2 = 1.5 mm. The arms of the feed lines are l3 = 3 mm. The stub is l4 = 1.1 mm. Substrate length and width are also the same l = w = 8 mm. The slot length is ls = 3 mm and slot width ws = 0.3 mm. The designed antenna is then fabricated and is shown in Figure 3. 8.

3.5.2 S-parameter result

The antenna was fabricated by a commercial PCB design company using photolithography process in all cases. The fabricated antenna is measured using a vector network analyser (VNA) from Agilent's programmable network analyser (PNA) E8361A series. The results of S-parameter are shown in Figure 3. 9. The deviation between the simulated and the measured result is due to the fabrication precision and assembly error. Otherwise a well-matched condition is found at the resonant frequency 18.7 GHz.

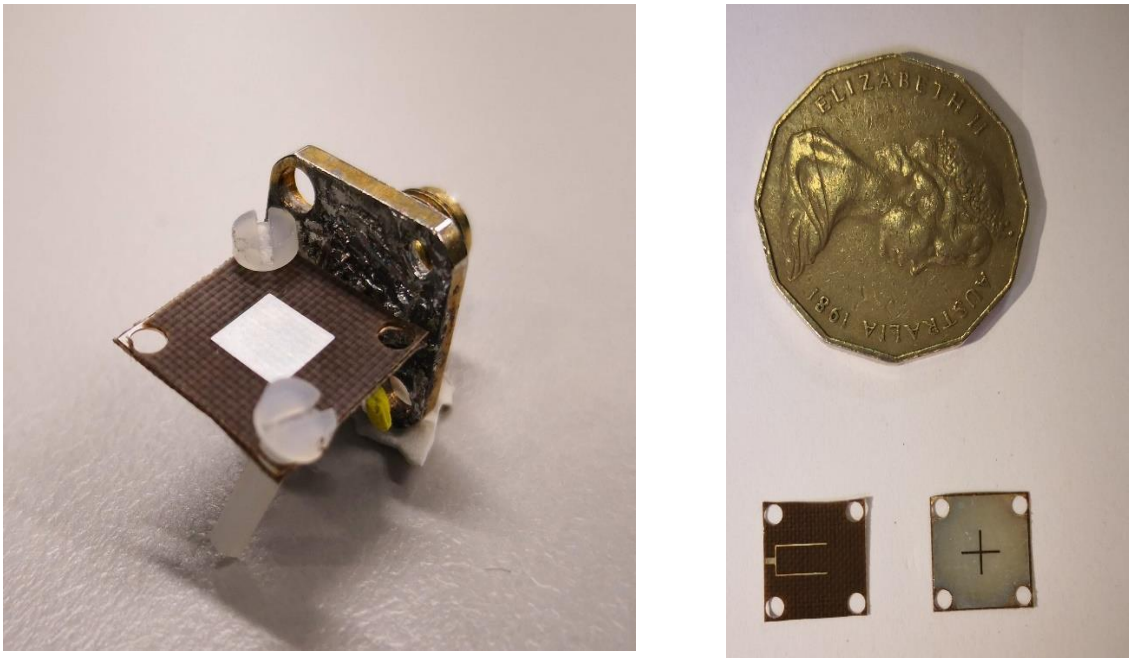

(a) (b)

Figure 3. 8 (a) Fabricated LP ACMSA antenna at Ku-band (18.7 GHz), (b) ground and feed layer size comparison with a 50 cent AUD

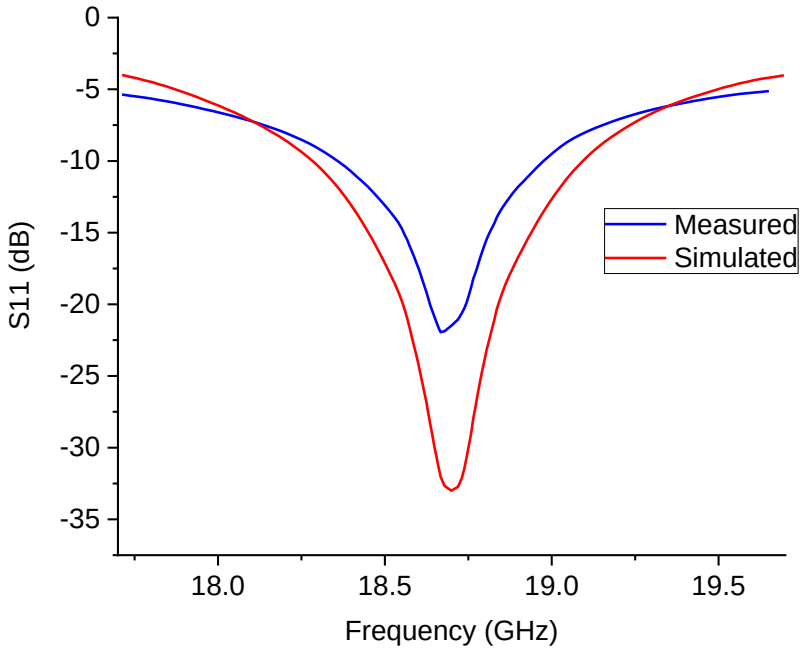

Figure 3. 9 Simulation and measured S11 of Ku-band LP ACMSA antenna

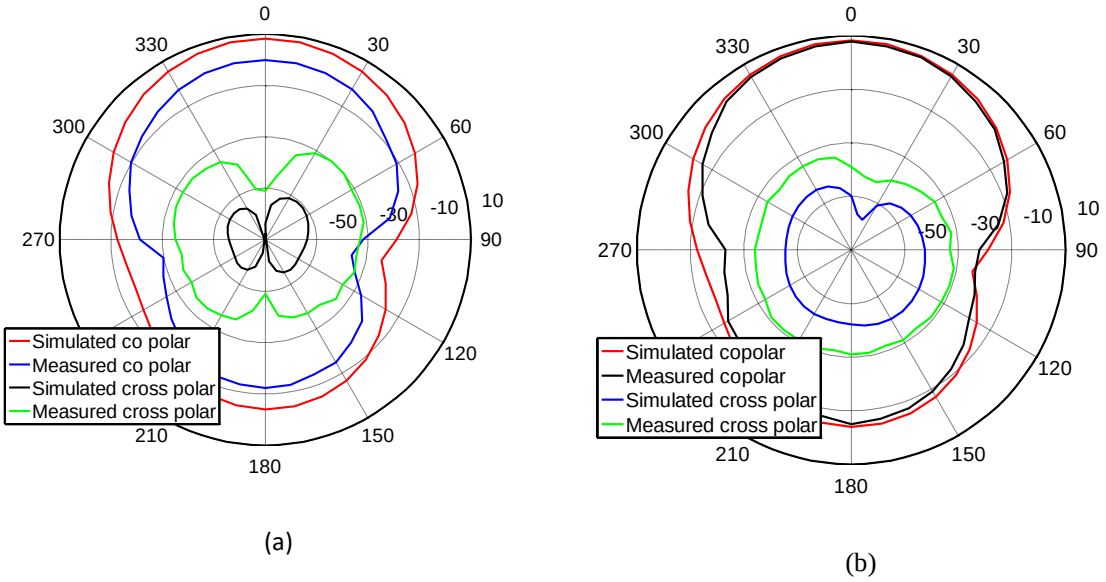

Figure 3. 10 Radiation pattern of (a) E- and (b) H-plane for co polar and cross polar of single element Ku-band LP ACMSA antenna in both simulation and measured.

3.5.3 Radiation pattern

Radiation pattern of both the simulated and measured LP ACMSA Ku-band is shown in Figure 3. 10. From the figure it can be said that the measured and simulated patterns have similar shape. The gain for both the co-polar and cross-polar measured result have a maximum

magnitude of 6.97 dBi and 6.9 dBi. The mismatches are due to some fabrication and assemble issues which are very normal given the tiny size, connector losses, soldering losses etc.

3.6 Study of different parameters' effect and design guideline for LP ACMSA

All three frequency bands will be in a multilayered structure which is only possible if there are multiple substrate layers in the design. Initially all antennas were designed using the simplest substrate and ground structure which is two substrate layers on either sides of the ground and a patch on the top.

3.6.1 Substrate permittivity

Permittivity of the substrate plays vital role on the radiation efficiency and bandwidth. Also, for the array structure thickness of the substrate determines the width of the power divider which becomes important and critical because of the minimal spaces between multiple slots in the ground layer. Lower permittivity of the substrate makes wider bandwidth.

In Figure 3. 11, S11 or equivalent to reflection coefficient is plotted against different values of permittivity for all L-, Ku- and Ka-bands. All three bands show a resonant situation where best matching occurs. Sharpness of the dip shows bandwidth variation in this case. Also, the level of matching is another factor which might be dependent on the substrate permittivity. For very low permittivity matching was harder and not as the same as of higher permittivity. In this simulation, a material was created with similar loss tangent as of TLX-8 lossy and the permittivity was set variable to be swept. Also, the realized gain is a function of permittivity shown in Figure 3. 12.. For lower and higher value of permittivity gain were found very low as matching and other losses were very prominent.

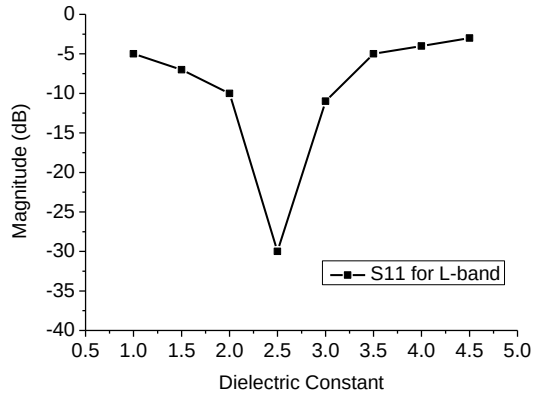

(a)

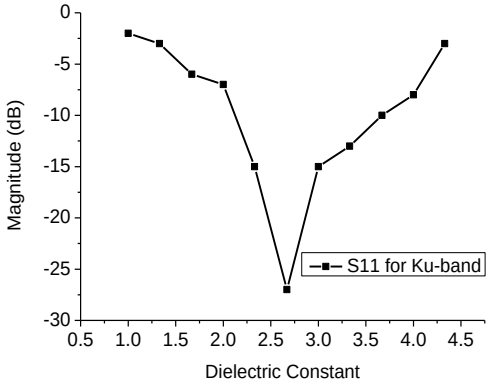

(b)

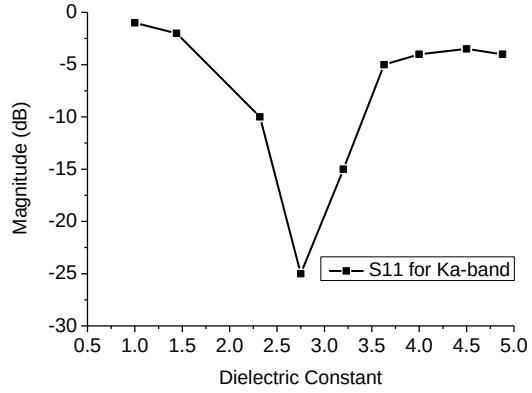

(c)

Figure 3. 11 Effect of dielectric constant on S11 for (a) L-, (b) Ku- and (c) Ka-band

This is because the design was done for a commercially available substrate (TLX-8) and thus it matches for its permittivity (which is 2.55) only and other values yield larger mismatch and loss.

3.6.2 Effect of Patch Length

The resonant frequency of operation is determined by the length of radiating edge of the patch or in another word patch length and width. In this case this is a dual polarized antenna which makes it a square patch having same length as width. From literature and numerous available equation and physical explanation it is known that the resonant frequency is inversely proportional to the patch length. The patch is physically placed over the slot in the ground plane for maximum coupling. E-plane has more influence than H-plane on the alignment [218].

To understand the effect of patch length over reflection coefficient, and realized gain, patch length is varied, and the effects are shown in Figure 3. 13, and Figure 3. 14. In Figure 3. 13, S11 variation is shown which is the measure of reflection coefficient or matching is. Changing the patch length from its optimum value makes shift S11 upward or poorer direction in all three frequencies. Realized gain shows similar trend as Figure 3. 12 here as well and it is shown in Figure 3. 14.

It can be concluded that realized gain, S11 has optimized value where they show resonant kind behaviour and at other values, they show poor responses depending on their frequency range and bandwidth.

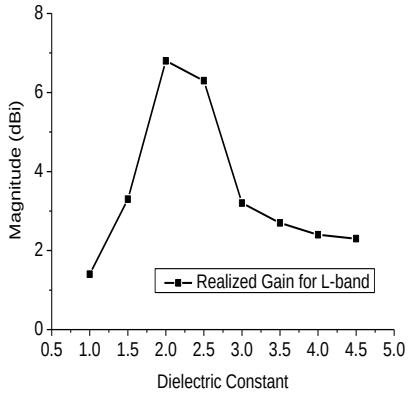

(a)

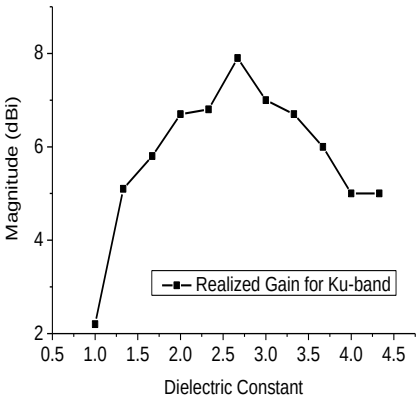

(b)

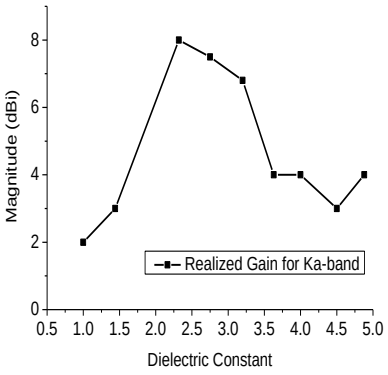

(c)

Figure 3. 12 Effect of dielectric constant on realized gain for (a) L-, (b) Ku- and (c) Ka-band

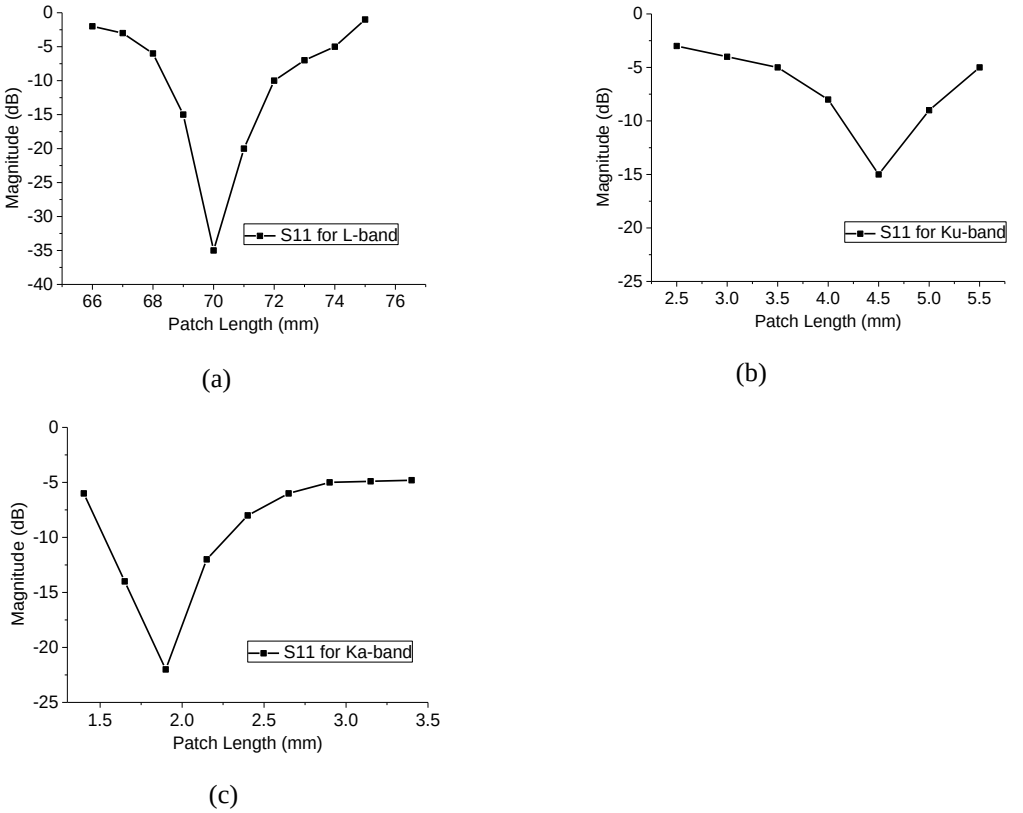

Figure 3. 13 Effect of patch length on S11 for (a) L-, (b) Ku- and (c) Ka-band

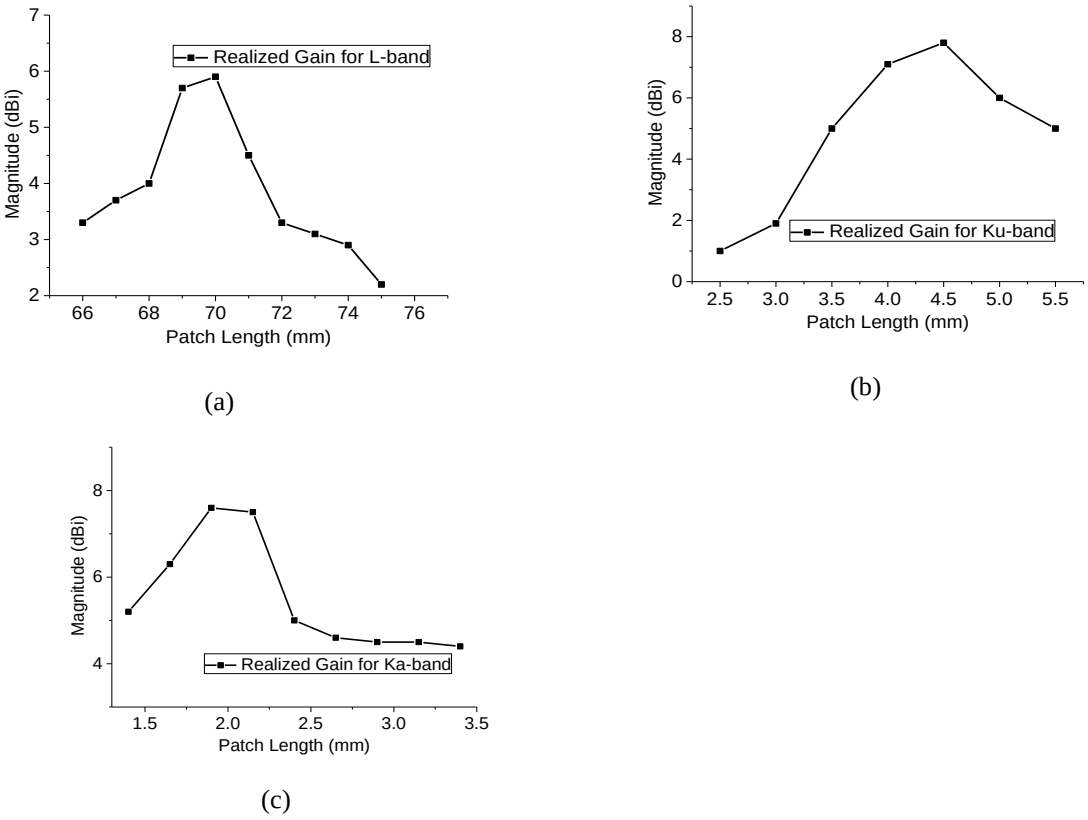

Figure 3. 14 Effect of patch length on realized gain for (a) L-, (b) Ku- and (c) Ka-band

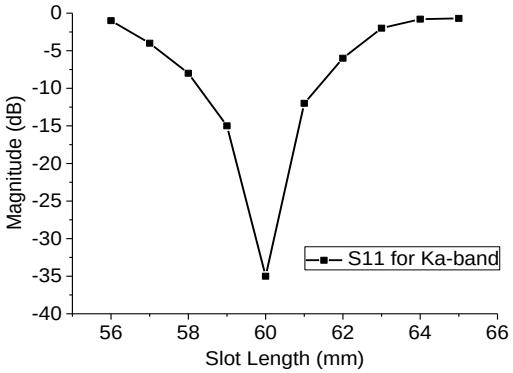

(a)

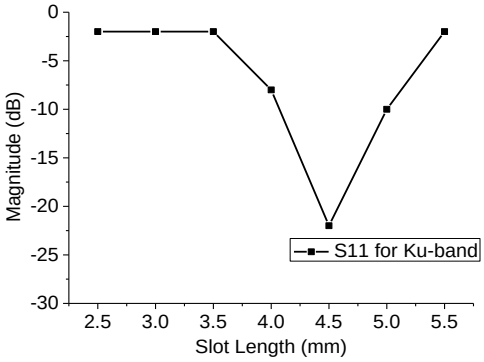

(b)

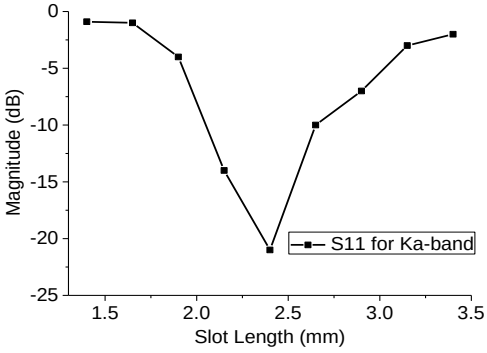

(c)

Figure 3. 15 Effect of slot length on S11 for (a) L-, (b) Ku- and (c) Ka-band

3.6.3 Effect of Slot length

The coupling between the feed line and the patch is the primary reason for radiation and it depends on the slot length. Also, it determines the radiation level. Instead of using the traditional rectangular slot, improved shapes of slots may improve performance for different requirements. In this case a cross coupling slot is studied and feed lines were 'Y' shaped for better coupling. Length and position of the slot determines the point where the patch is being excited and thus it plays vital role for matching. Figure 3. 15 shows the effect of slot length over S11 or reflection coefficient. As expected, slot lengths have matching or resonant length for each frequency. Effect of slot length over bandwidth can also be realized from this study or at least can get a general pattern from it.

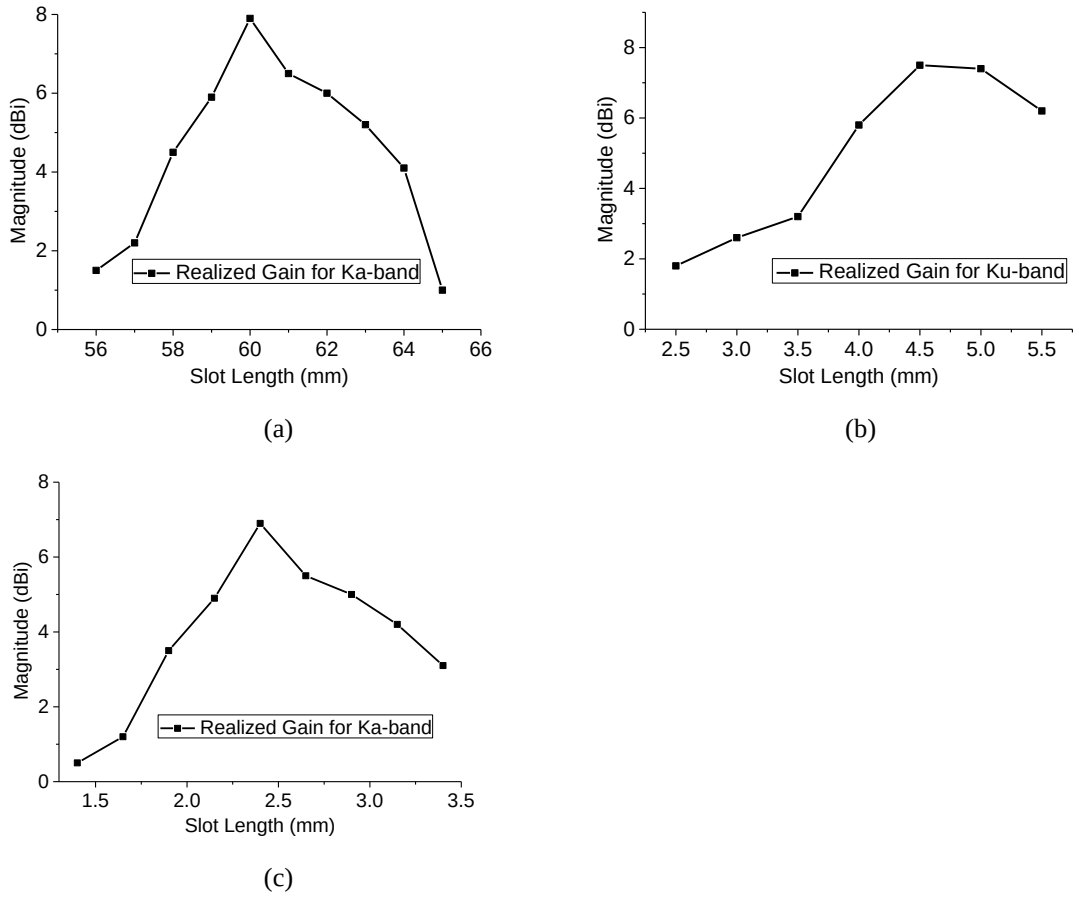

Figure 3. 16 Effect of realized gain vs slot length for (a) L-, (b) Ku- and (c) Ka-band

Realized gain shows similar matching or optimized length for each of the frequency. Other lengths except the optimized result low realized gain as mismatch occurs. This effect of slot length over realized gain is shown in Figure 3. 16.

3.6.4 Summary of parametric study

In this study, all the important parameters for designing the LP ACMSA are varied and results are analysed. Independent of the frequency bands the reflection loss and realized gain pattern show very similar trends. Later, a design guideline is provided for designing antennas in these frequencies.

In Table 3. 2, the effects of few parameters such as substrate dielectric constant (Ɛr), length of the patch (lp), width of the patch (wp), feed length (l1), stub length (l4), slot length (ls), slot width (ws), substrate width (w) and substrate length (l) are shown.

Table 3. 2 Summary of the effect of different parameter changes

Parameter names	Effect on the S11	Realized Gain	Comments
ε_r	U	D	S11 and Realized gain change moderately
h	U	D	Significant change in both S11 and realized gain
lp	DU	UD	S11 and Realized gain change abruptly
wp	D	-	S11 changes but realized gain not so
l1	UDU	DUD	Matching is affected so are S11 and gain
l4	UDU	DUD	Stub is crucial to matching, S11 and gain change abruptly
ls	UDU	DUD	Amount of excitation affects S11 and gain
ws	U	D	S11 and Realized gain change moderately
w	-	-	Not much effect
l	-	-	Not much effect

* U = upwards

* D = downwards

It is observed that the effect of changing the substrate permittivity (ε_r) and substrate thickness (h) have a significant effect on the antenna performance. Also, for any practical design it is ideal to choose to select the substrate material and thickness beforehand otherwise it is very difficult to change later. So, throughout the design process of LP ACMSA these parameters are unchanged. The next parameter that should be fixed is the patch length (lp). The length has a direct proportional relationship with the centre frequency of operation. Hence increasing the length increases the radiation edge and hence the centre frequency. The length of patch should be chosen in such a way that the antenna resonates in the required frequency. The change in the realized gain is due to matching as at a certain frequency, the antenna radiates the most only at a certain matching condition. The length of the patch is hence to be fixed as well for a certain frequency of operation. All the other parameters can be varied up to a limit except these three parameters. The substrate permittivity and height/thickness must be fixed for practicality of the design and the patch length is found from the theory hence cannot be changed. The other dominant parameters that result in larger variation are the slot length (ls), stub length (l4), width

of the slot (ws) and few others. The slot length variation varies the point of excitation on the patch and has similar effect of changing feeding position of the coaxial cable in coaxially fed antenna. At the right slot length, the S11 or the reflection coefficient hits the optimum point and change abruptly with further change in this parameter. Next, the stub length (l4) is vital obtaining the matching of impedance. Changing the stub length changes the reactance of the impedance hence changes the matching condition. Again, at a certain frequency, the stub length must be fixed at a certain value and just a little variation in that length results huge variation in the S11 of reflection coefficient. The slot width (sw) controls the amount of excitation going through the ground plane and hence vital designing the antenna. The feed length (l1) also has impact as this controls the feed position and hence the matching. There are also other parameters that change the performance of the antenna such as the width of the 'Y' arm of the feed and width of the patch (wp) but they are changed to tune the matching circuit only after fixing other important parameters beforehand. There is also another very important parameter which is found theoretically and is fixed independent of the frequency and operation and that is the width of the feed which should be of 50 Ω always. In the next section a complete design guideline is presented after documenting these parameters variation.

3.6.5 Design guideline for LP ACMSA

After performing simulations and optimizations a design guideline is presented here to help future designers to start the optimization process step-by-step.

- The first step is to select the substrate material with right permittivity (ε_r) and thickness. As later for fabrication these properties will be unchangeable. Substrate thickness of about 0.01λ to 0.02λ is better for feed substrate and thicker substrate with lower permittivity is preferable for patch substrate. One important thing about designing in the higher frequency domains is that the patch size and feed lines become small and in an array, designing the feed network becomes very challenging. So, in order to design

an array antenna for future it is imperative that single element is designed using the right substrate permittivity and thickness.

- The next step is selecting the resonant frequency of operation, band-width (BW) and realized gain. These parameters are the goal functions and they are independent of each other. For this chapter, the requirements for LP ACMSA are different for different frequencies.
- The next step is to calculate the patch length (lp) for the required frequency. The equation for calculating the length is

$$lp = \frac{\lambda_g}{2} = \frac{300}{2 \times f_c \times \sqrt{\varepsilon_r}} \text{.....(1)}$$

For feed line width, the equation can be found from literature

- The next step is the approximation of other parameters. Patch width can be set as the 1.2 times the patch length ($wp = 1.2 \times lp$). Substrate length and width can also be the same and can be approximated as $w = l = 3.5 \times lp$. Slot length (ls) can be set as $ls = 0.8 \times lp$. Slot width (sw) can be $sw = lp/10$. Feed length (f1) can be set as $l1 = lp/3$ and the space between the 'Y' arms (l2) can be approximated as $l2 = 0.7 \times lp$. The stub length (l4) is also very important and sensitive parameter and that can be approximated as $l4 = 0.2 \times lp$.
- The next step is to set up the CST simulation environment and design the antenna using parameters. The E- and H-field boundary conditions were then set and results are then followed by the simulation and result analysis.
- After the simulation, it is checked if the reflection coefficient, bandwidth, radiation pattern and realized gain are satisfactory or need modification.
- If the required properties need modifications, it is optimized changing one parameter at a time and using the parameter sweep function in the CST MWS.

- The requirement of S11 is generally below -10 dB and is obtained by varying slot length (ls), stub length (l4), feed length (l1) and slot width (ws) one at a time. Generally, to move the resonant frequency, patch length (lp) is varied in the beginning and for further resonance slot length (ls) and stub length (l4) is varied. For even further matching condition other parameter such as feed length (l1), slot width (ws) etc. are optimized.

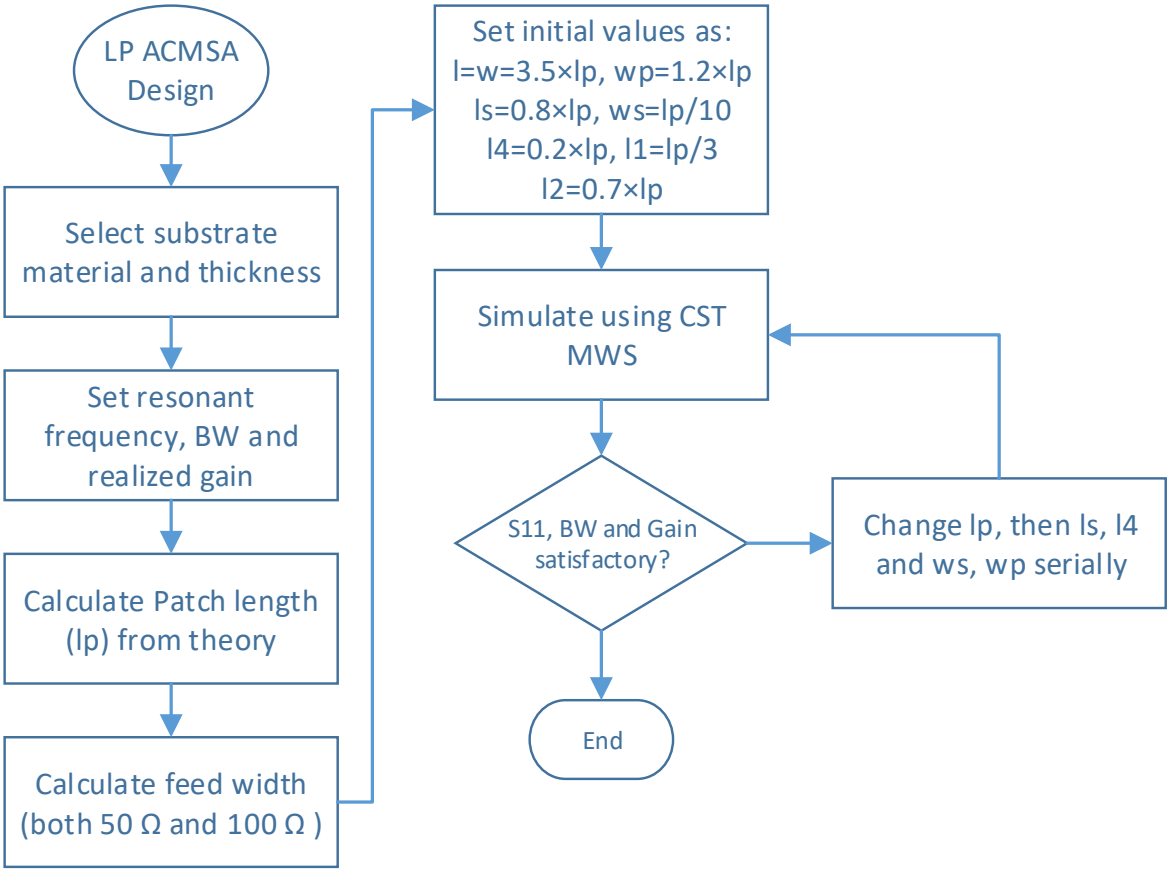

Figure 3. 17 Design guideline for LP ACMSA development

- The optimization process can be long depending on the mesh spacing and size of the antenna. Also, the simulation is basically iteration of different parameters sweep one at a time in the beginning then combination of different parameters sweeps at the same time until required result is obtained. The flow chart of the whole design process is summarized in the Figure 3. 17.

3.7 Conclusions

Three single element LP ACMSA antennas for three bands, L-, Ku- and Ka-bands, are developed in this chapter. This chapter starts with an overview of the LP ACMSA antenna design, then a review of the LP ACMSA antenna with its benefits, advantages over other feeding structures is discussed. Then design requirements and design procedures of L-, Ku- and Ka-band antennas are discussed elaborately. The reason for choosing linearly polarized antenna is to offer the radiometer system to have a separate or isolate polarization of either horizontal or vertical direction. Computing Stokes' parameter requires horizontal and vertical polarization separately to find the brightness temperature which is a key factor towards the approximation of the moisture content of the soil. The literature review part discusses and reasons the motivation of the research of LP ACMSA antenna. Simulation helps to design for three different band antennas and model them. Measurement part proves the concept and boosts the idea of having another polarization or in other words dual polarized (DP) antenna which is investigated in the next chapter. Finally, a thorough investigation of the parametric dependence or analysis to understand the design process which leads to a design guideline for future endeavours to design LP ACMSAs completes this chapter.

4 Dual Polarized Antenna

4.1 Overview

The next logical step after designing the LP ACMSA is to upgrade the design to dual polarized ACMSA (DP ACMSA). A detail study is conducted on DP ACMSA in this chapter. The goal to design radiometer antennas, that work in three different frequencies which are L-, Ku- and Ka-bands, that require two orthogonal polarizations in order to obtain radiation from both polarizations and finally calculate the Stoke's parameters to obtain the brightness temperature, a key variable to measure soil moisture. Theoretically, DP antennas can be sensitive of both horizontally and vertically polarized signals simultaneously. This way, both polarizations can be used to handle double data from two polarizations. It is also useful to compare between two polarizations.

A detail study is performed on the dual polarized antennas to explore literature to find the suitable match (high port-to-port isolation, low cost, low profile, lightweight, wideband, wide-beam). After thorough research conducted in the literature review chapter, the aperture coupled feeding technique is found to be a suitable technique to pursue for the radiometer antenna because of its planar structure, low profile and easier to fabricate features. Moreover, because of the configuration, two orthogonal feeds can be placed in different layers enabling a higher isolation between ports. A high isolation between ports is an essential requirement as signal received by one port should not interfere with the other. Hence, DP antennas are developed using DP ACMSA with separate feed layer design technique, which are comprehensively presented here. This chapter goes as follows-

- First, a literature review is performed on low profile, low cost dual polarized antenna

Chapter Outline

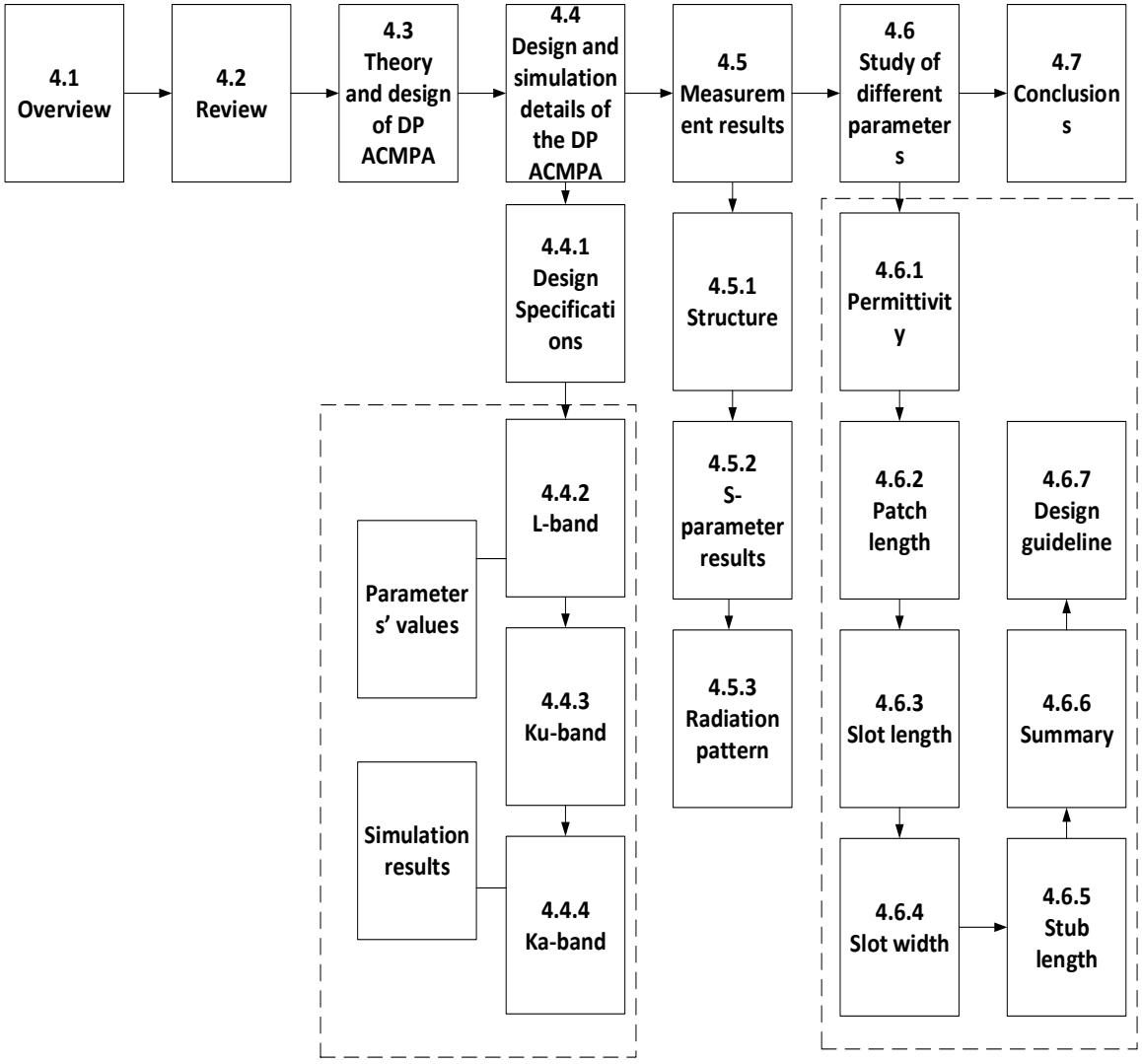

- Next, for higher port-to-port isolation, double feed layered design is chosen.
- Then, for L-band a single element DP ACMSA is designed
- After designing, optimization comes next of the design
- Next, similarly Ku- and Ka-band antenna are designed and optimized
- Parametric study of all three bands is then summarized.
- Lastly, a design guideline is presented for designing DP ACMSA in all three bands.

This development of the low profile, low cost, lightweight, high isolation and gain dual polarized antenna meets the requirement of a commercially realizable radiometer, which is capable of sensing soil moisture data from both polarizations.

4.2 Review

The goal of this chapter is to design a suitable DP element antenna that can be transformed into an array for the radiometer in three separate frequencies. From the literature review discussed in Chapter 2 it is observed that some of the designs lack port-to-port isolation, some of them have low gain, some of the are bulky and not planar, some of them operate at lower frequency and not found to be working at higher frequency. Upon considering all the factors, aperture coupled feeding technique is chosen for the dual polarized configuration similar to the linear polarized antenna discussed in the previous chapter.

The main advantages of the aperture coupled feeding for the dual polarized antenna are –

- Low profile design compared to horn antenna, dipole, bi-conical antenna etc.
- Less expensive than horns, dipoles and bi-conical antennas.
- Planar structure is an important advantage which is not present in other structures such as horn, dipole and bi-conical structure.
- High isolation is achievable due to the physical distance between the ports.
- Gain is quite high, and it has symmetric and similar electric and magnetic field.
- For multi-band feature, the feed layers can be placed in a stacked layer configuration making the design process less complicated and easy to fabricate.
- As this design is a continuation from the previous chapter, LP ACMSA, only a feed layer is modified along with the extra slot in the ground plane. The simulation and modification is easier for this structure.

4.3 Theory and design of DP ACMSA

In this section, the working principal of a dual polarized single element aperture coupled microstrip antenna is discussed. The configuration of the DP ACMSA is very much similar to the configuration of the LP ACMSA discussed in the last chapter. The main difference is that there is another feed line or port orthogonal to the LP ACMSA and the shape of the slot is 'cross' instead of 'rectangular'. The new feed line is etched in another layer of the substrate and is placed between the patch layer and ground layer. The idea behind placing this layer in between the patch and the ground layer is to ensure equal distant from the ground layer to the feed layer.

This DP ACMSA has the same planar, light-weight, high gain, wide beam feature. It also has two polarizations and a high isolation between ports. The reason for this high isolation requirement is to ensure two ports receive power without affecting each other. Plan view and expanded 3-d view is shown in Figure 4. 1.

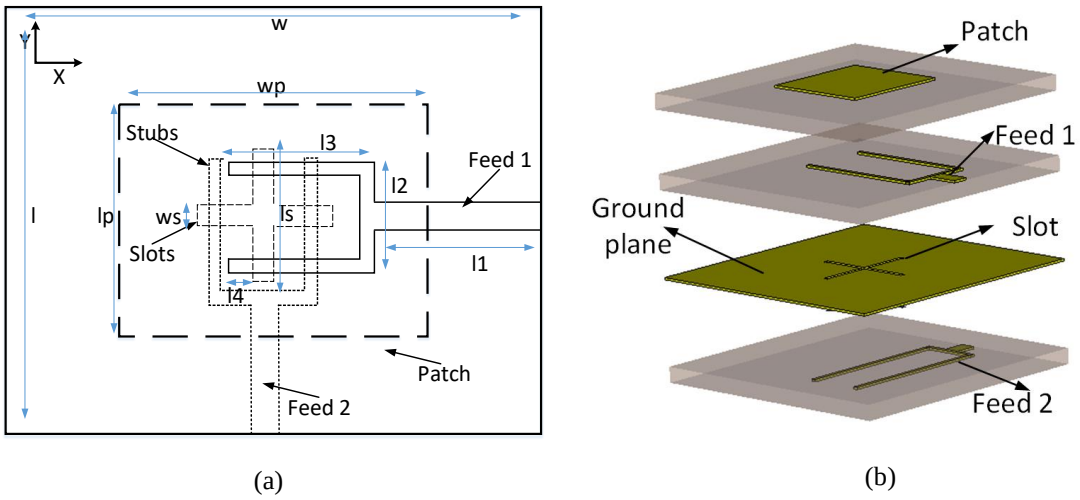

(a) (b)

Figure 4. 1 Layout of the single element DP ACMSA (a) plan view and (b) expanded 3-D view

This DP ACMSA has one extra substrate layer than the DP ACMSA for and extra feed line/network. The length and width of the substrate layers are identical as the operating

frequency for both polarizations are the same or $l = w$. The size of the patch is also a square to ensure the same radiating edge and this length should come from the same equation discussed in the previous chapter or mathematically $lp = lw$. The patch layer is in the top layer of substrate followed by one polarization (can be horizontal or vertical), then ground plane and finally the other feed layer (could be vertical or horizontal). The shape of the feed is similar to the DP ACMSA but just one extra layer of substrate at the middle. The shape of the slot in the ground plane is different than that of DP ACMSA. This is because the slots let the radiation through the slot edges to the patch layer. Logically for one feed line, a rectangular slot is required which is orthogonal to the direction of the feed, so for another polarization orthogonal to the existing one another slot orthogonal to the existing slot is needed. Thus, the shape of the slot is like a 'cross'. The feed line is 'Y' shaped with an extension for stub just as the same as DP ACMSA. Basically, the radiation occurs the same way as DP ACMSA but in this case from two different polarizations.

A similar design but with common orthogonal offset slots with straight feed line with orthogonal stub is explored and published in the author's one of the publications [219]. This cross-slot design surely gives additional isolation and better current distribution than any other aperture coupled structure.

4.4 Design and simulation details of the DP ACMSA

Commercially used designing software CST 2017 MW (Computer Simulation Technology) is used throughout in this designing process. Designing a multi-layer structure for three different frequencies is a challenging task and moreover practical aspect and availability and precision of material and fabrication techniques have to be considered before designing. To begin with, a commercially viable material TLX-8 with 0.127 mm of thickness is chosen as substrate. The patch length, width and 50 ohm line width are calculated from theoretical equations presented

in [79]. The ground plane has a cross shaped slot which needs to be matched with the patch's resonant frequency and the feed lines are also needed to be optimized for overall matching. In the following subsections, L-, Ku- and Ka-band antenna designing processes are discussed.

4.4.1 DP ACMSA design specification for the radiometer antenna

Following specifications are initially set for developing a single element dual polarized antenna for L-, Ku- and Ka-bands. These specifications will ensure that when designing the array antenna in dual-polarized polarization is completed, the design requirements are satisfied.

- Gain: Gain for a single element DP antenna should be more than 6.5 dBi in all three bands. This is set to ensure that the array antenna after beam shaping has a high gain which is essential for the radiometer antenna.

- Bandwidth: Bandwidth is one of the most important properties of an antenna. In general, radiometer antennas are narrow band with high quality factor. The design requirement is set to have 25 MHz (1.8%) for the L-band, 200 MHz (1%) for the Ku-band and 2 GHz (5.4%) for the Ka-band. The reason is purely to focus the antenna beam onto the area of interest.

- Cross-polar isolation: Cross-polar isolation is to be set as low as possible. The requirement is set to have less than 25 dB

- Port-to-isolation: port-to-isolation is to be set as high as possible. The requirement is set to have less than -25 dB

- Beamwidth: The beamwidth of a single element and an array will be different as increasing the number of elements in an array will narrow the beamwidth. For a single element DP ACMSA, the beamwidth is set to have around 65°.

These design specifications are summarised in the Table 4. 1 below:

Table 4. 1 Design target for DP ACMSA

Antenna parameter	Target value for single DP ACMSA	Target value for 8 × 8 array after beamforming
Gain	6.5 dBi	22 dBi
Bandwidth	25 MHz (L-), 200 MHz (Ku-), 1.5 GHz (Ka-band)	25 MHz (L-), 200 MHz (Ku-), 1.5 GHz (Ka-band)
Beamwidth	~ 65°	~ 10°
Cross-polarization	< -25 dB	< -25 dB
Isolation	< -25 dB	< -25 dB

4.4.2 L-band DP ACMSA

4.4.2.1 Parameter values

As mentioned earlier, a similar design to the previous chapter is presented. The configuration of the L-band antenna is shown in Figure 4. 1. The substrate is chosen to be TLX-8 with 0.127 mm thickness. The length and width of the patch are the same to ensure the same resonant frequency for both polarizations, lp = wp = 62 mm. The feed length of the layer between the patch and the ground plane, l1 = 60 mm. Feed line width is the same as 50 Ω line and is constant at 0.35 mm. The extension of the Y branch of this feed is l2 = 18 mm. The arms of the feed lines are l3 = 48 mm. The stub is l4 = 4 mm. Substrate is square shaped and the length and width are also the same l = w = 120 mm. The slot length is ls = 23 mm and slot width ws = 5 mm. For the feed below the ground plane, l1= 55mm, l3 = 50mm, and stub, l4 = 5mm.

4.4.2.2 Simulation Result

Simulation was run using the dimensions mentioned above but the values of the slot length, slot width, feed line dimensions were optimized to find the best result. Because this antenna is dual polarized that means in the S-parameter results S11, S12, S21 and S22 are present. Because S11 and S22 are the reflection coefficient for port 1 and port 2 or horizontal and vertical polarizations. Curve of the S11 and S22 are identical due to symmetry. Similarly, the S12 and S21 are also identical due to the symmetry.

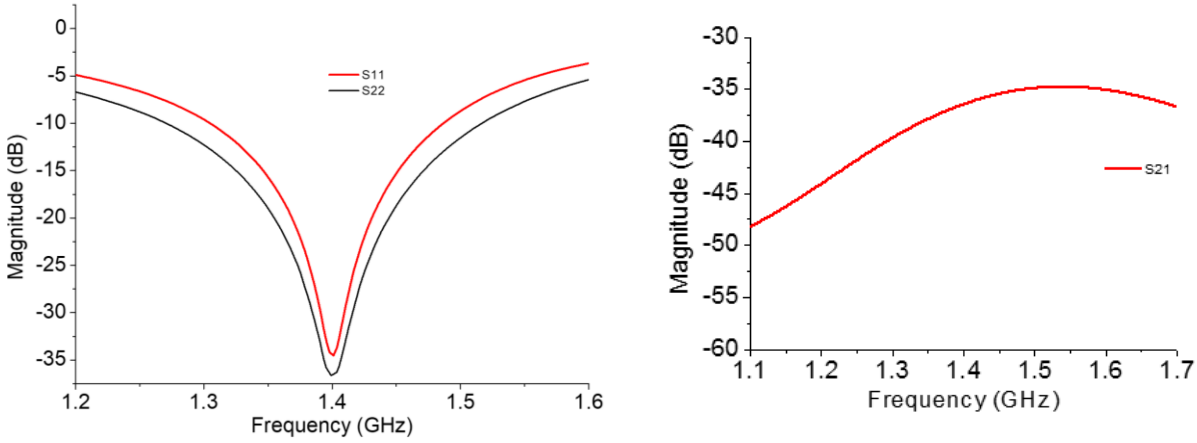

(a) (b)

Figure 4. 2 (a) S11 and S22 and (b) S21 for L-band DP ACMSA single element antenna

Figure 4. 2 shows S-parameter results at L-band at 1.4 GHz. Figure 4. 2 (a) shows the S11 and S22 which indicates the reflection loss of port 1 and port 2 respectively. Both S11 and S22 resonate at 1.4 GHz having a bandwidth of around 180 MHz which is larger than the 25 MHz requirement. The magnitude of S11 and S22 are both below -30dB indicating less than 0.1% reflection loss. S21 or S12 shows the power received by one port when the other is transmitting. A higher isolation means both ports are separated in such a way that only 0.01% power is being received by one port while another port is transmitting. A minimum interference is expected and is achieved in this case.

Figure 4. 3 shows the electric and magnetic field co and cross polar radiation patterns for both horizontal and vertical polarizations. Co-polar electric and magnetic field magnitude or both poles are approximately 7.7 dBi proving the validity of a high gain element. One thing is worth mentioning that, for doubling the element number, ideally 3 dB gain increase can be expected.

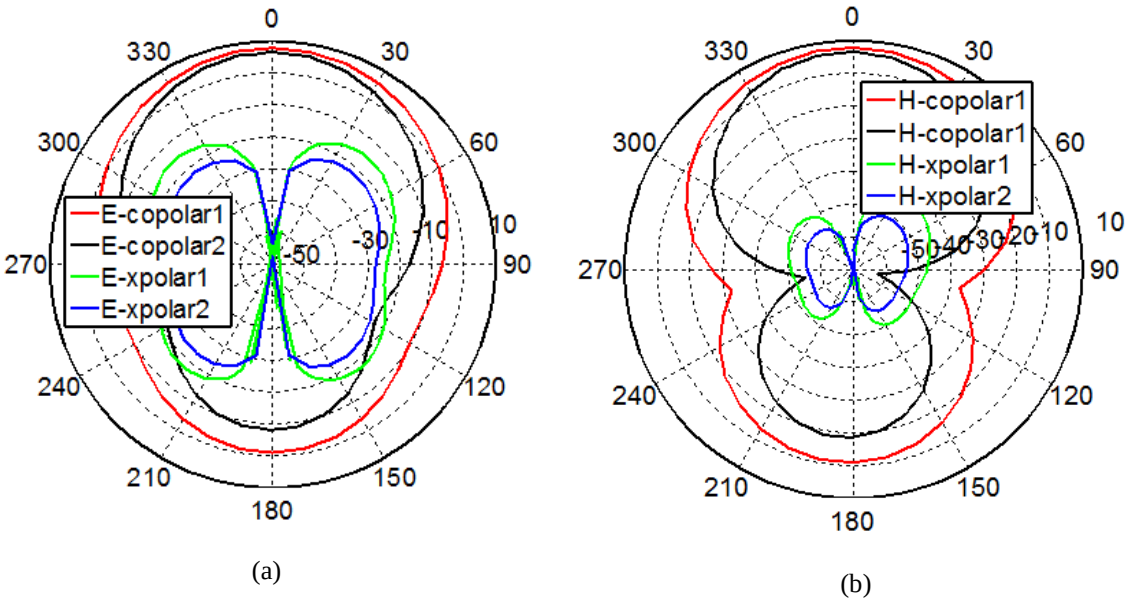

(a) (b)

Figure 4. 3 Radiation pattern for single element DP ACMSA L-band antenna. (a) E- and (b) H-plane

The cross-polarization can be defined as the ratio of the power coupled between the two polarization ports of a dual polarized antenna. The cross-polar level is below -30 dB overall and at 0°, it is below 70 dB of the main lobe for both electric and magnetic fields. Both co- and cross-polarization patterns are symmetrical around 0° and 180° axis.

4.4.3 Ku-band

Ku-band is designed to resonate at 18.7 GHz with a bandwidth of minimum 150 MHz, reflection coefficient or S11 below -10 dB, with 25 dB isolation between ports and a minimum gain of 6 dBi.

4.4.3.1 Parameter values for DP ACMSA

The antenna configuration is similar to that of the L-band antenna. The plan view and 3-d view are shown in Figure 4. 1. The parameters of the design are optimized after rigorous research and simulation and the final values are presented. The substrate was TLX-8 with a thickness of 0.127 mm for all layers. The length and width of the patch are the same as this is a square patch with, lp = wp = 4.8 mm. The feed length l1 = 4.1 mm. Feed line width is the same as 50 Ω line and not is not something optimized but fixed. The line width is set as 0.35 mm. The extension of the Y branch of the feed is l2 = 1.5 mm. The arms of the feed lines are l3 = 3 mm each. The stub length is l4 = 1.1 mm. Substrate length and width are also the same l = w = 8 mm. The slot length is ls = 3 mm and slot width ws = 0.3 mm.

4.4.3.2 Simulation Result

Simulation results are obtained using CST MW 2017 software. S-parameters and radiation pattern are generated after rigorous research and optimization.

Figure 4. 5 (a) shows the S11 and S22 of the designed Ku-band DP ACMSA antenna. Both S11 and S22 are resonated at 18.7 GHz meaning a well-matched condition is achieved at the desired frequency. The magnitude of the S11 and S22 are both below -25 dB meaning only less than 0.3% power being reflected. The bandwidth is also approximately 850 MHz which is above the requirement. In (b) of Figure 4. 5, isolation between ports or S21 is shown and it can be observed that the isolation is well below -40 dB throughout the spectrum.

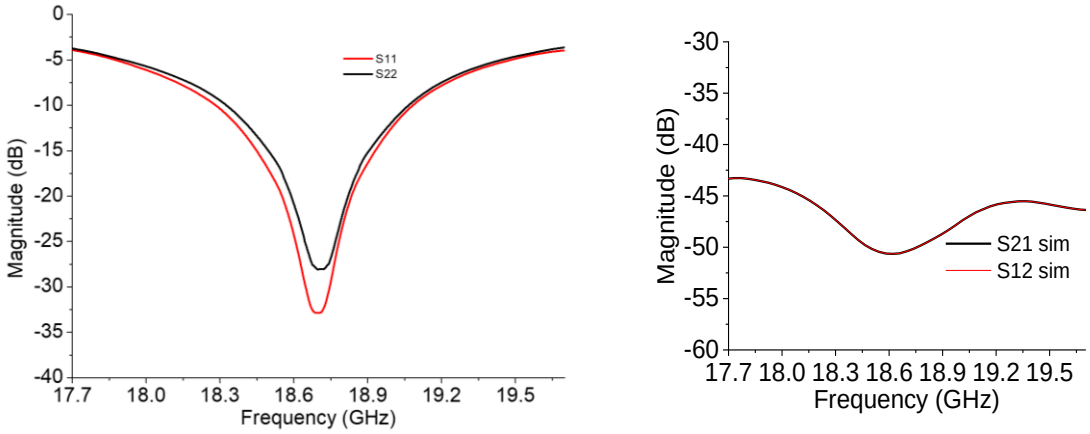

(a) (b)

Figure 4. 5 (a) S11 and S22 and (b) S21 for K-band DP ACMSA single element antenna

Figure 4. 4 (a) and (b) show the electrical and magnetic field radiation pattern of the designed Ku-band element DP ACMSA antenna. The gain for the electric field co-polar is 8.3 dBi making this a very good candidate for array implementation. The cross-polarization for electric field is also very small. At 0°, the cross-polarization level is around -75 dB from the main lobe. Magnetic field radiation pattern also follows similar result like the electric field. The co-polar gain is maximum at 0° and the magnitude of gain is 8.0 dBi. The cross-polar level is -70 dB

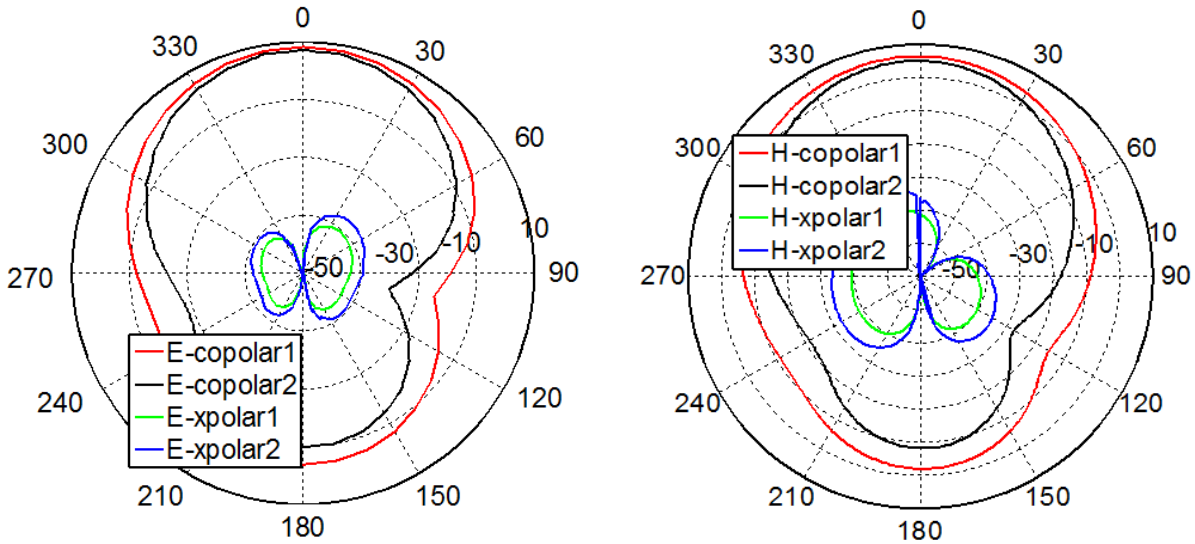

(a) (b)

Figure 4. 4 Radiation pattern for single element DP ACMSA K-band antenna. (a) E- and (b) H-plane

below the main lobe at 0°. Both the electrical and magnetic fields are symmetric along 0° and 180° axis.

4.4.4 Ka- band

Ku-band is designed to resonate at 37 GHz with a bandwidth of minimum 1 GHz, reflection coefficient or S11 below -10 dB, with 25 dB isolation between ports and a minimum gain of 6 dBi.

4.4.4.1 Parameter values for DP ACMSA

The aperture coupled configuration of the Ka-band antenna is similar to what is shown in Figure 4. 1. In this study the values of the parameters are as follows. The substrate was TLX-8 with a thickness of 0.127mm. The length and width of the patch are the same, lp = wp = 2.4 mm. The feed length l1 = 1.92 mm. Feed line width is the same as 50 Ω line and not set as a variable. The extension of the Y branch of the feed is l2 = 0.82 mm. The arms of the feed lines are l3 = 1.3 mm. The stub is l4 = 0.7 mm. Substrate length and width are also the same l = w = 4 mm. The slot length is ls = 2 mm and slot width ws = 0.2 mm.

4.4.4.2 Simulation Result

Simulation results are obtained using CST MW 2017 software. S-parameters and radiation pattern are generated after rigorous research and optimization. Figure 4. 7 (a) and (b) show the S-parameters of the Ka-band antenna. As the antenna is passive, S21 and S12 are identical. S11 and S22 show very well-matched behaviour at 37 GHz with around 2 GHz bandwidth. The magnitude of the reflection is less than 25 dB meaning only 0.3% or less reflection. S21 or isolation is shown in figure (b) where it is less than -40 dB in the overall spectrum. -40 dB accounts for 0.01% of power interference between ports and is a very negligible amount for this study.

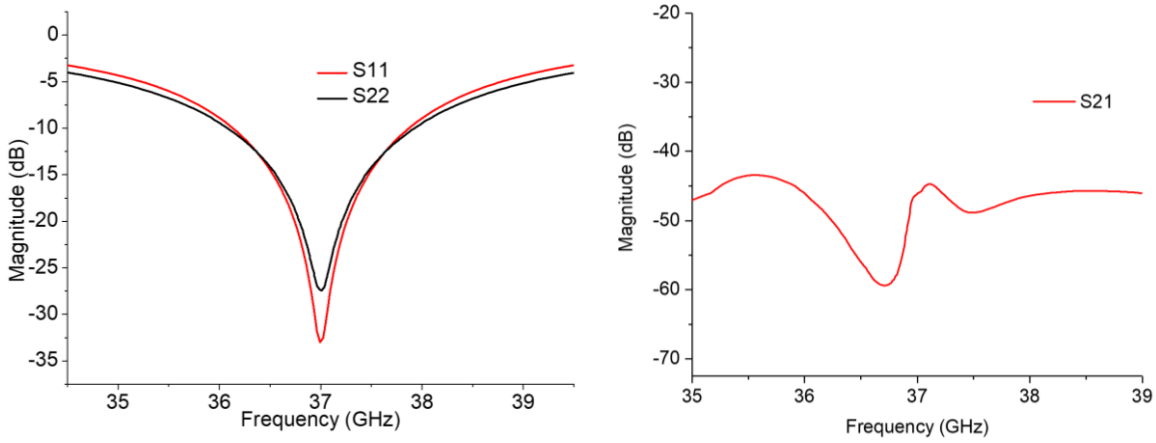

(a) (b)

Figure 4. 7 (a) S11 and S22 and (b) S21 for Ka-band DP ACMSA single element antenna

Figure 4. 6 (a) and (b) show the radiation pattern of the electric and magnetic field respectively. Electric field main lobe of the co-polar orientation shows a maximum gain of 8.2 dBi at 0° for port 1 and for port 2 it is around 8.15 dBi. Cross-polarization level is at least 50 dB less than the main lobe at 0°. Both co-polar and cross-polar pattern show symmetry around 0° and 180° axis. Similarly, magnetic field main lobe of the co-polar orientation shows a maximum gain of 8.7 dBi at 0° for port 1 and for port 2 it is around 8.69 dBi. Cross-polarization level is at least

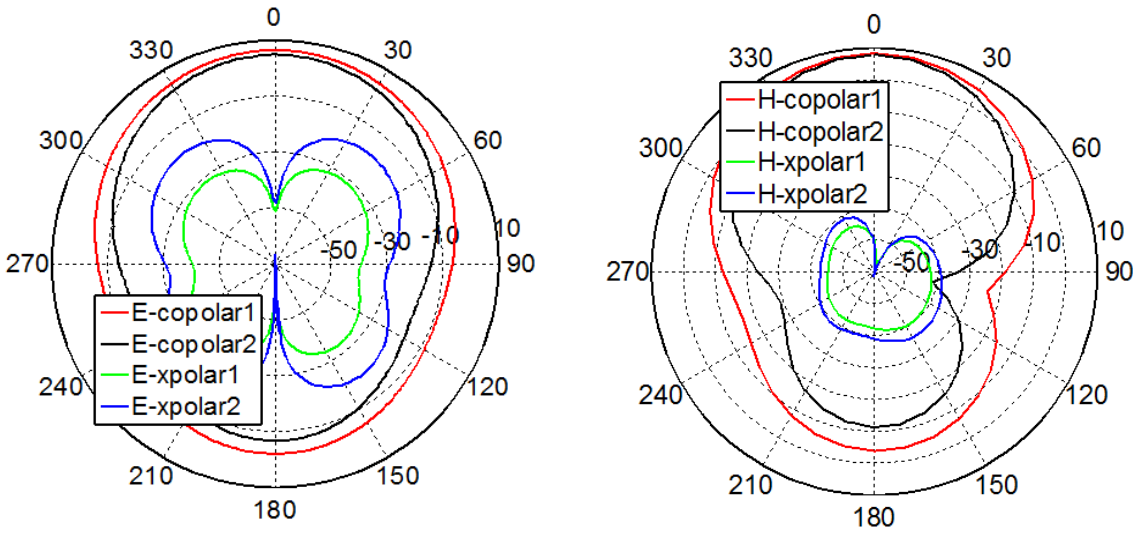

(a) (b)

Figure 4. 6 Radiation pattern for single element DP ACMSA Ka-band antenna. (a) E- and (b) H-plane

55 dB less than the main lobe at 0°. Both co-polar and cross-polar pattern show somewhat symmetry around 0° and 180° axis.

4.5 Measurement results

In this study a DP Ku-band antenna was fabricated and measured as the proof of concept. Details of the structure and measurement results are discussed in the next sections.

4.5.1 Structure

The structure of the Ku-band LP ACMSA is the same as shown in Figure 4. 1. The substrate is TLX-8 with a thickness of 0.127 mm. Similar to the simulation the length and width of the patch are kept, lp = wp = 4.8 mm. The feed length l1 = 4.1 mm. Feed line width is the same as 50 Ω line and is 0.35 mm for a given substrate of fixed thickness. The extension of the Y branch of the feed is l2 = 1.5 mm. The arms of the feed lines are l3 = 3 mm. The stub is l4 = 1.1 mm.

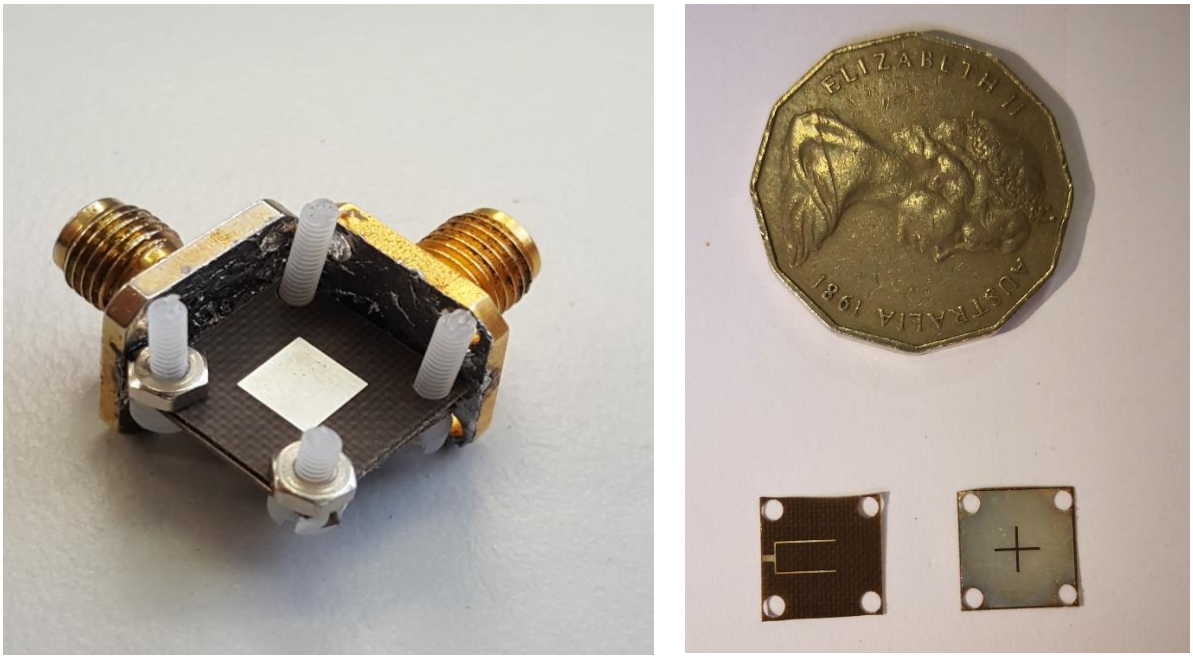

(a) (b)

Figure 4. 8 (a) Fabricated DP ACMSA antenna at Ku-band (18.7 GHz) (b) feed and ground layer size comparison

Substrate length and width are also the same l = w = 8 mm. The slot length is ls = 3 mm and slot width ws = 0.3 mm. The designed antenna is then fabricated and is shown in Figure 4. 8

4.5.2 S-parameter result

The fabricated antenna is measured using a vector network analyser (VNA) from Agilent's programmable network analyser (PNA) E8361A series. The results of S-parameter are shown in Figure 4. 9. The deviation between the simulated and the measured result is due to the fabrication precision and assembly error. Both the reflection coefficients (S11 and S22) resonate at 18.7 GHz. The S11 and S22 level for both measurements is below -20 dB showing

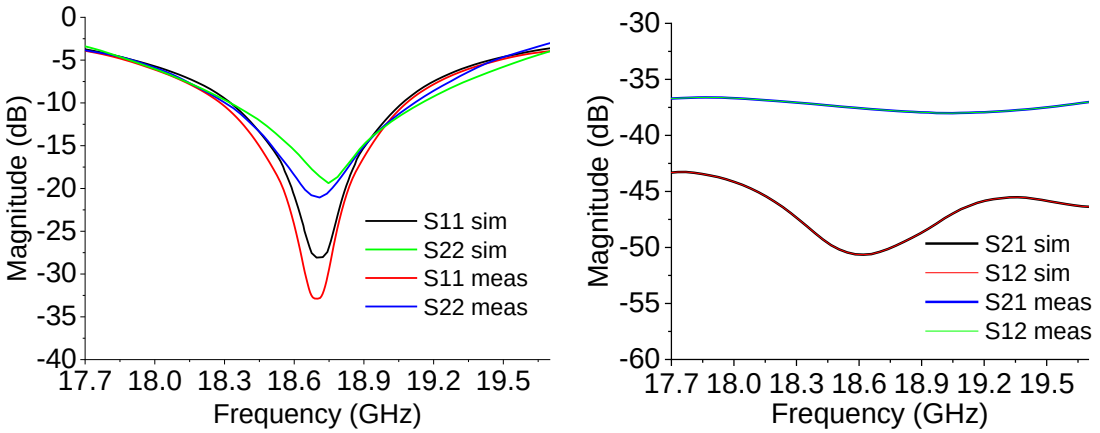

Figure 4. 9 Simulation and measured (a) reflection coefficient and (b) isolation of Ku-band DP ACMSA antenna

an excellent impedance matching. For the isolation, the measured isolation level is more than 35 dB. The mismatch between the simulation and measurement is due to the fabrication and assemble error.

4.5.3 Radiation pattern

Radiation pattern of both the simulated and measured DP ACMSA Ku-band is shown in Figure 4. 10. From the figure it can be observed that the measured and simulated patterns have similar shape. The main-lobe or co-polar level of the measure Ku-band DP antenna for

both electric and magnetic fields are around 7.2 dBi. The cross-polarization is less than -40 dB. The cross-polarization level of the measured result follows the simulation result with some mismatch.

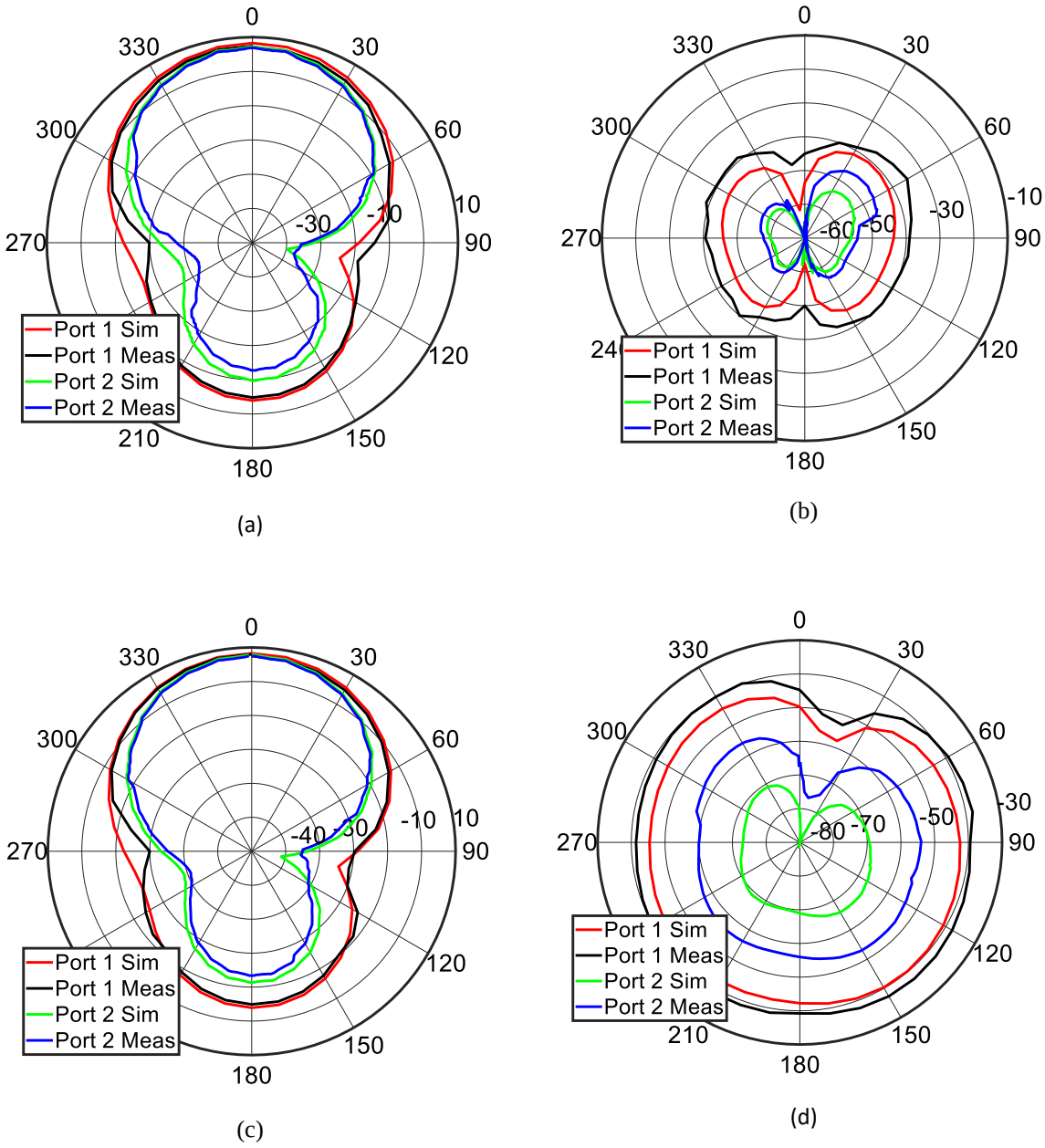

Figure 4. 10 Radiation pattern of (a) E- plane co polar, (b) E- plane cross polar, (c) H- plane co polar and (d) H- plane cross polar orientation of single element Ku-band DP ACMSA antenna in both simulation and measured

The mismatches are due to fabrication error and assemble issues which are very normal because of the tiny size, connector losses, soldering losses.

4.6 Study of different parameters

In this section, a detailed study is presented to document how different parameters play role in the design process.

4.6.1 Substrate permittivity

Permittivity of the substrate determines the electric field distribution in the substrate hence is an important parameter to study. In reality, substrates are found in sheets with pre-fabricated thicknesses. It is important to choose a substrate according to the requirement of the study, so upon deciding a fixed thickness which is 0.127 mm, a standard thickness, the permittivity was varied in CST MW Studio 2017 to observe the effect of permittivity in designing process.

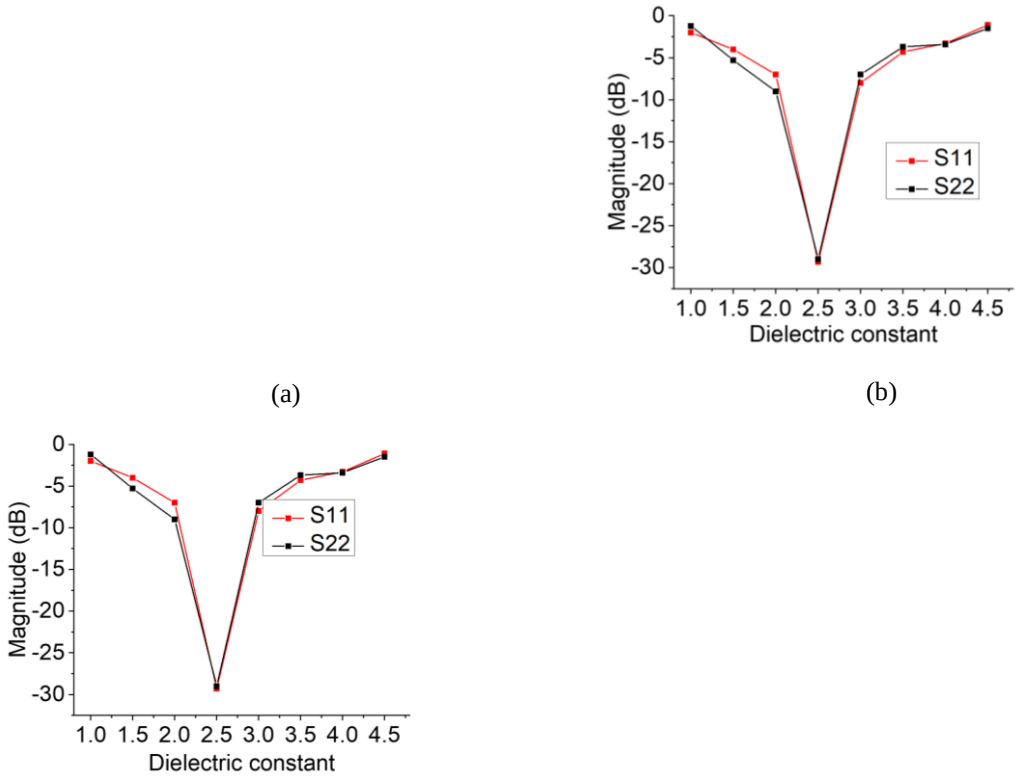

Figure 4. 11 Effect of dielectric constant on S11 and S22 for (a) L-, (b) Ku- and (c) Ka-band

In Figure 4. 11, S11 and S22 or reflection coefficient is plotted against different values of permittivity ranging from 1 to 4.5 for all L-, Ku- and Ka-bands. All three bands show a resonant

situation where best matching occurs. Sharpness of the dip shows bandwidth variation in this case. Also, the level of matching is another factor which might be dependent on the substrate permittivity. For very low permittivity matching was harder and not as the same as of higher permittivity. In this simulation, a material was created with similar loss tangent as of TLX-8 lossy and the permittivity was set variable to be swept. Also, the realized gain is a function of permittivity shown in Figure 4. 12. For lower and higher value of permittivity gain were found very low as matching and other losses were very prominent. This is because the design was designed for a commercially available substrate (TLX-8) and thus it matches for its permittivity (which is 2.55) only and other values yield larger mismatch and loss.

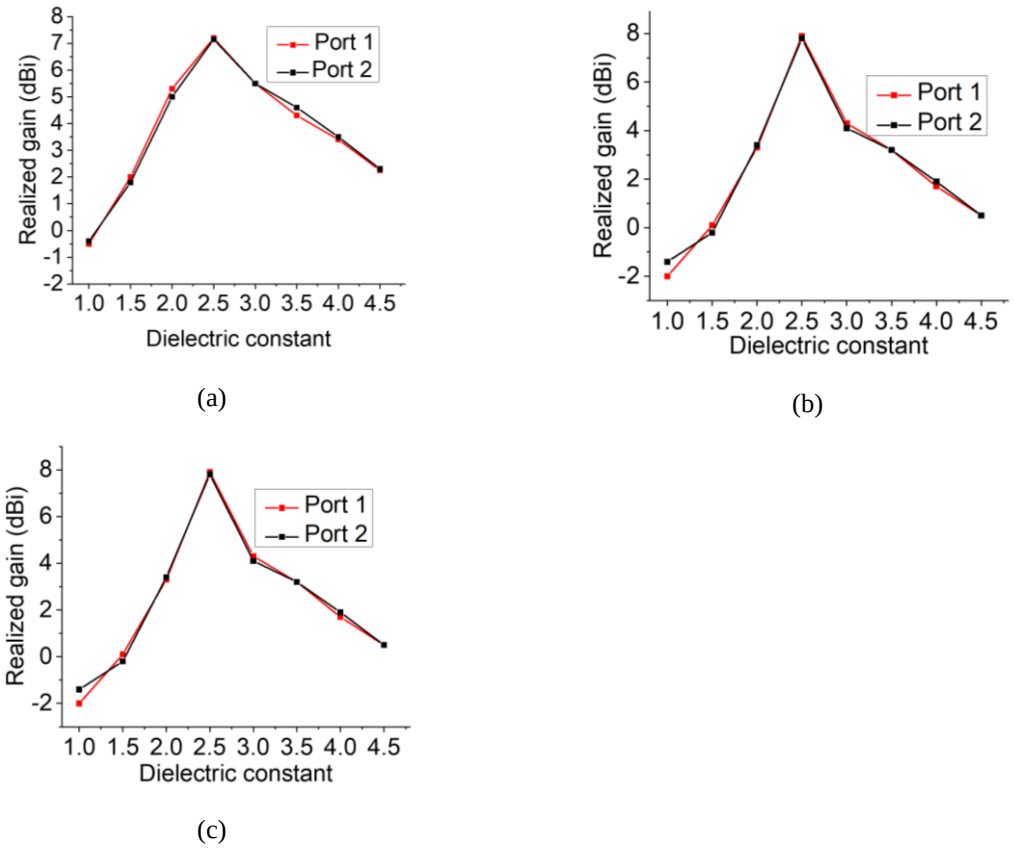

Figure 4. 12 Effect of dielectric constant on realized gain for (a) L-, (b) Ku- and (c) Ka-band

4.6.2 Effect of Patch Length

Patch length plays vital role determining the radiation edge. The longer the patch length is the more wavelength is radiated and hence lower frequency. In this study both horizontal and

vertical polarizations are designed hence the shape of the patch is square. The effect of patch length variation over reflection coefficient, and realized gain, the patch length is varied, and the results are summarised in Figure 4. 13 and Figure 4. 14. In Figure 4. 13 S11 and S22 variation is shown which is the measure of reflection coefficient or matching.

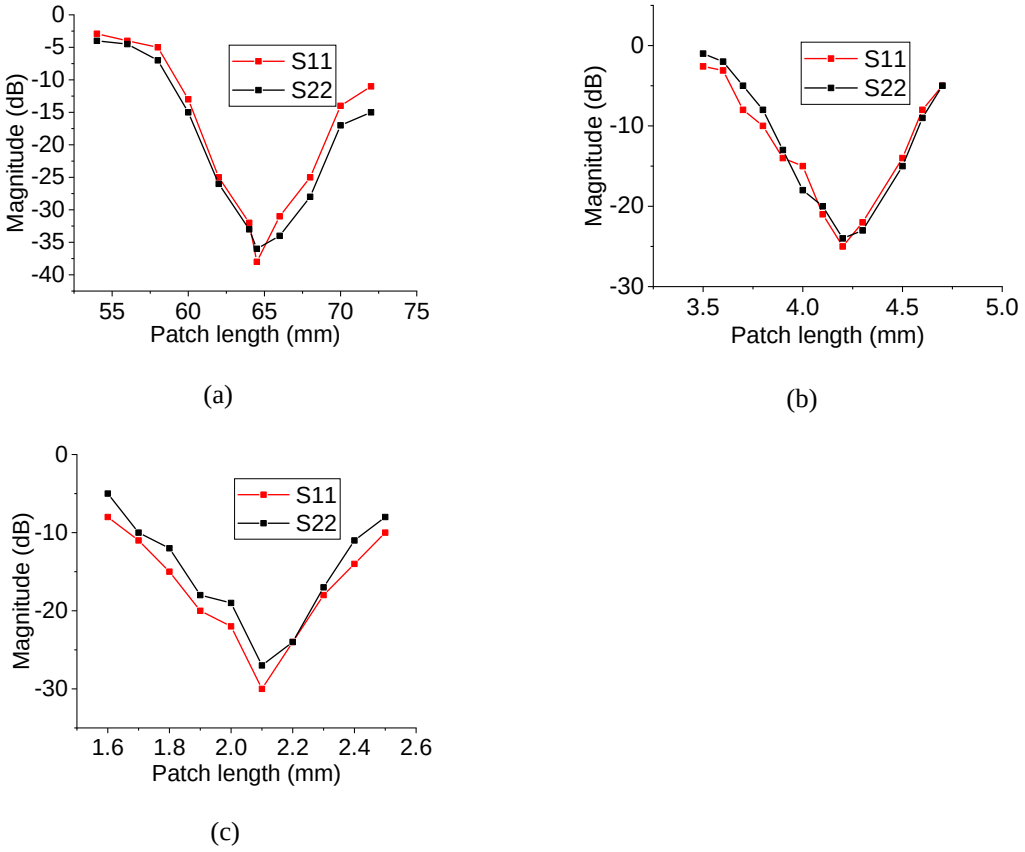

Figure 4. 13 Effect of patch length on S11 and S22 for (a) L-, (b) Ku- and (c) Ka-band

Changing the patch length from its optimum value results S11 and S22 shifting upward or poorer direction in all three frequencies but the rate of change is different for individual. In the higher frequencies the change is seen more abrupt in general. Realized gain shows similar trend as here as well and it is shown in Figure 4. 14. It can be concluded that realized gain, S11 has optimized value where they show resonance and at other values, they show poor responses depending on their frequency range and bandwidth.

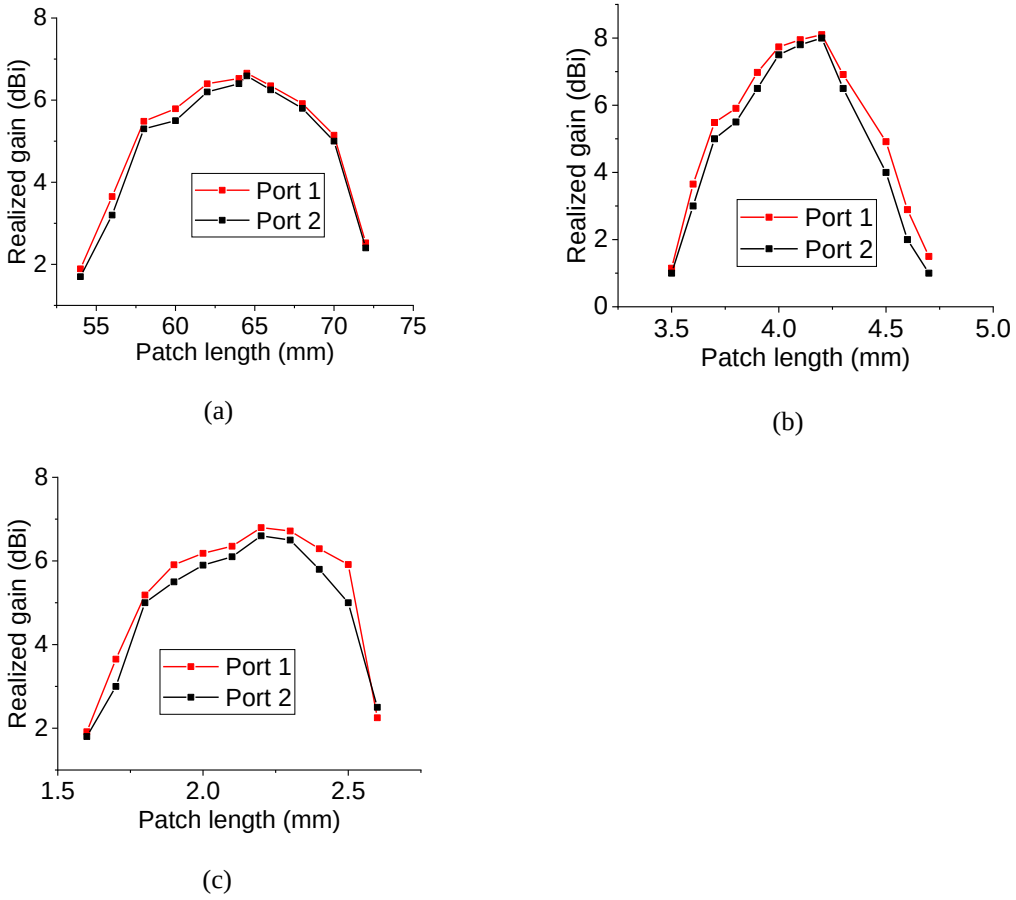

Figure 4. 14 Effect of patch length on realized gain for (a) L-, (b) Ku- and (c) Ka-band

4.6.3 Effect of Slot length

Slot length variation varies the amount of radiation going from the feed through the ground layer to the patch layer. Also, it varies the radiation level. Instead of using the traditional rectangular slot, improved shapes of slots may improve performance for different requirements. A cross shaped slot is designed in this design and the length of the slot is varied. Length and position of the slot determines the point where the patch is being excited and thus it plays vital role for matching. Figure 4. 16 shows the effect of slot length over S11 or reflection coefficient. As expected, slot lengths have matching or resonant length for each frequency. Effect of slot length over bandwidth can also be realized from this study or at least can get a general pattern from it. Realized gain shows similar matching or optimized length for each of the frequency. Other lengths except the optimized result low realized gain as mismatch occurs. This effect of slot length over realized gain is shown in Figure 4. 15.

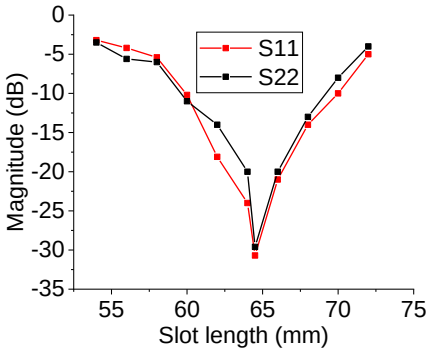

(a)

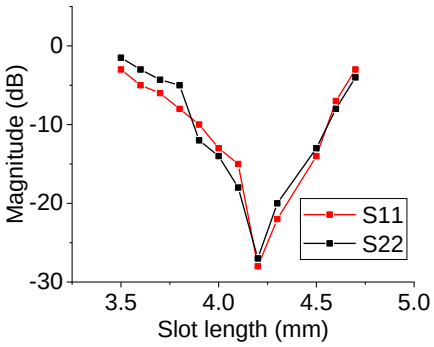

(b)

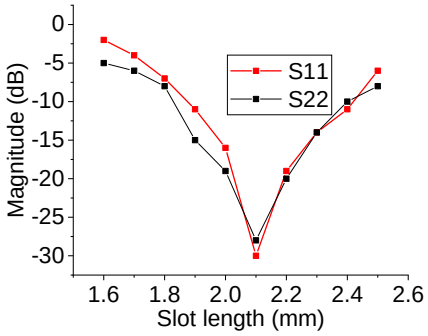

(c)

Figure 4. 16 Effect of slot length on S11 and S22 for (a) L-, (b) Ku- and (c) Ka-band

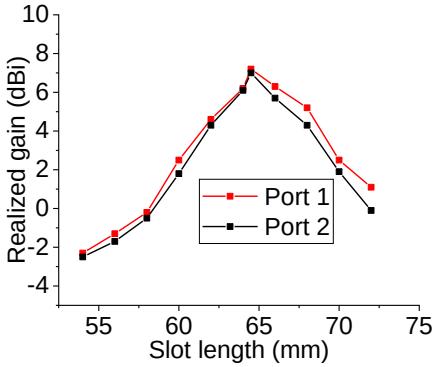

(a)

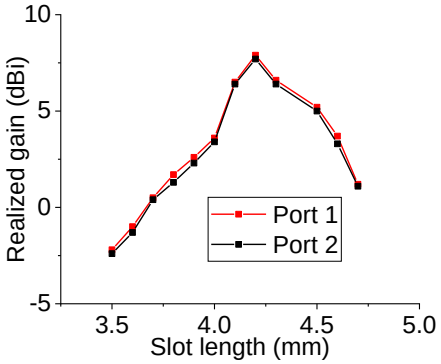

(b)

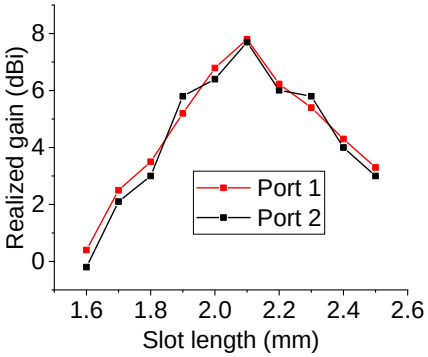

(c)

Figure 4. 15 Effect of slot length on realized gain for (a) L-, (b) Ku- and (c) Ka-band

4.6.4 Effect of slot width

Slot width also affects the coupling level from the feed layer through the ground layer to the patch layer. General size of the slot should be, where the length is about ten times the width. The wider the slot the more reactance it induces which can be cancelled adjusting the stub length. Figure 4. 17 and Figure 4. 18 show the S11/S22 and realized gain variation for the slot width variation. For S11 and S22 results, it can be seen that the variation of the slot width tends to shift the reflection coefficients from less matched to well matched and then again moving away towards less matched result. The change in the matching also has and impact of frequency. As frequency changes to higher frequency from lower frequency, the matching becomes very sensitive or in another words the matching becomes difficult. This is shown in Figure 4. 17. The slot width is one of the limiting dimensions when it comes to fabrication process as this becoming the smallest etched portion of the substrate. The realized gain variation also follows

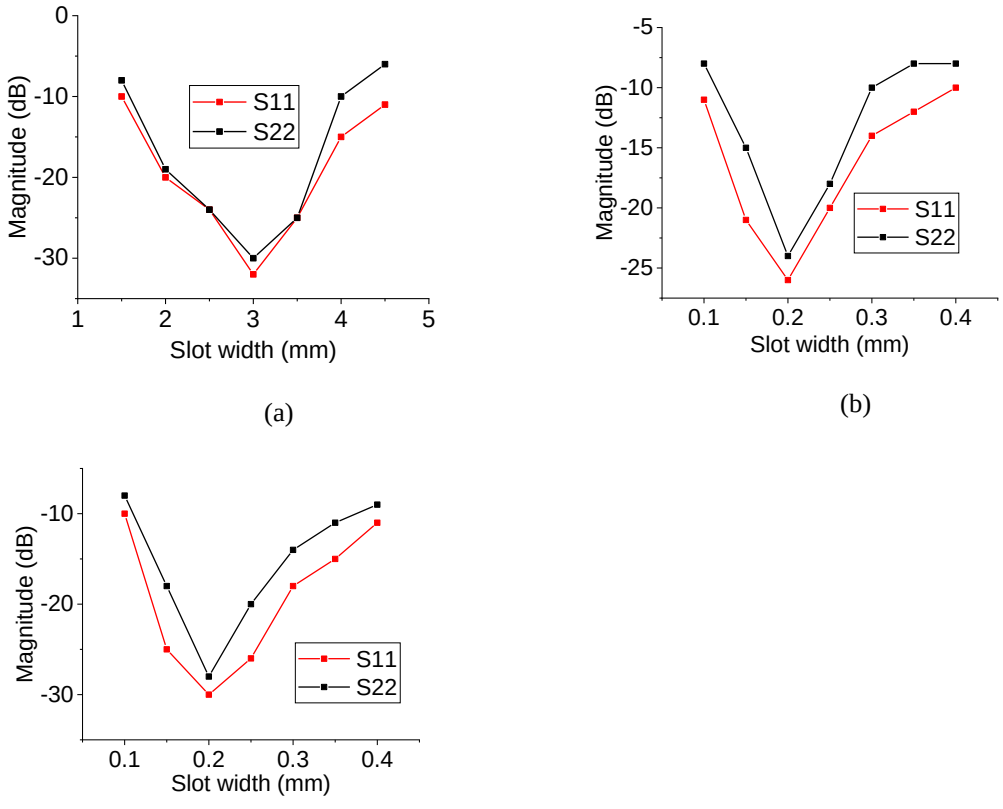

Figure 4. 17 Effect of slot width on S11 and S22 for (a) L-, (b) K- and (c) Ka-band

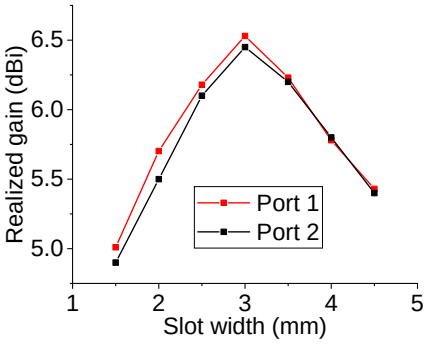

(a)

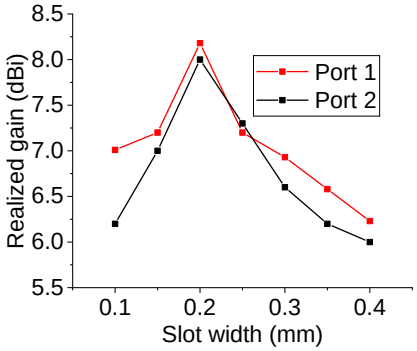

(b)

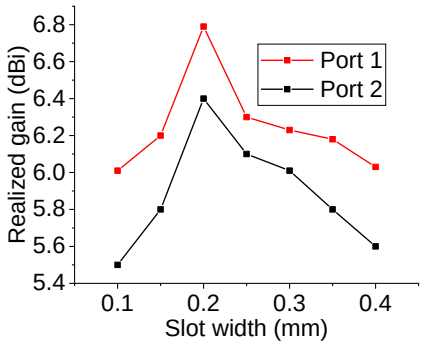

(c)

Figure 4. 18 Effect of slot width on realized gain for (a) L-, (b) K- and (c) Ka-band

similar trend as the reflection coefficient as it becomes very low magnitude at a less matched configuration. Again, it becomes difficult to design for the higher frequency than a relatively lower frequency. The change in the realized gain is shown in Figure 4. 18. In general, the effect of slot width is less compared to few of the other variables as the realized gain tends to shift within 30% to 35% of the maximum value.

4.6.5 Effect of stub length

Stub length is tuned to minimize the excess reactance of the slot. Tuning the stub length changes the reflection coefficient and also the realized gain of any ACMSA. It is very important that the matching between the port which has a fixed 50 Ω impedance and the antenna is very well matched so that the S11 and S22 lies on the unit circle on the x-axis of the smith chart.

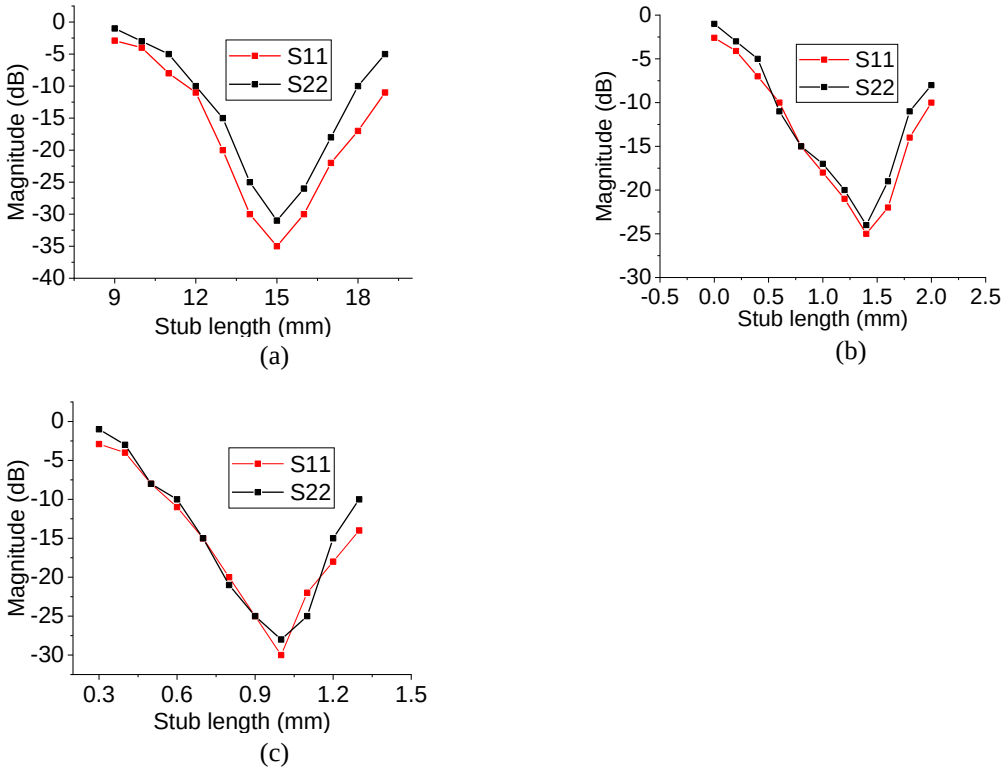

Figure 4. 19 Effect of stub length on S11 and S22 for (a) L-, (b) K- and (c) Ka-band

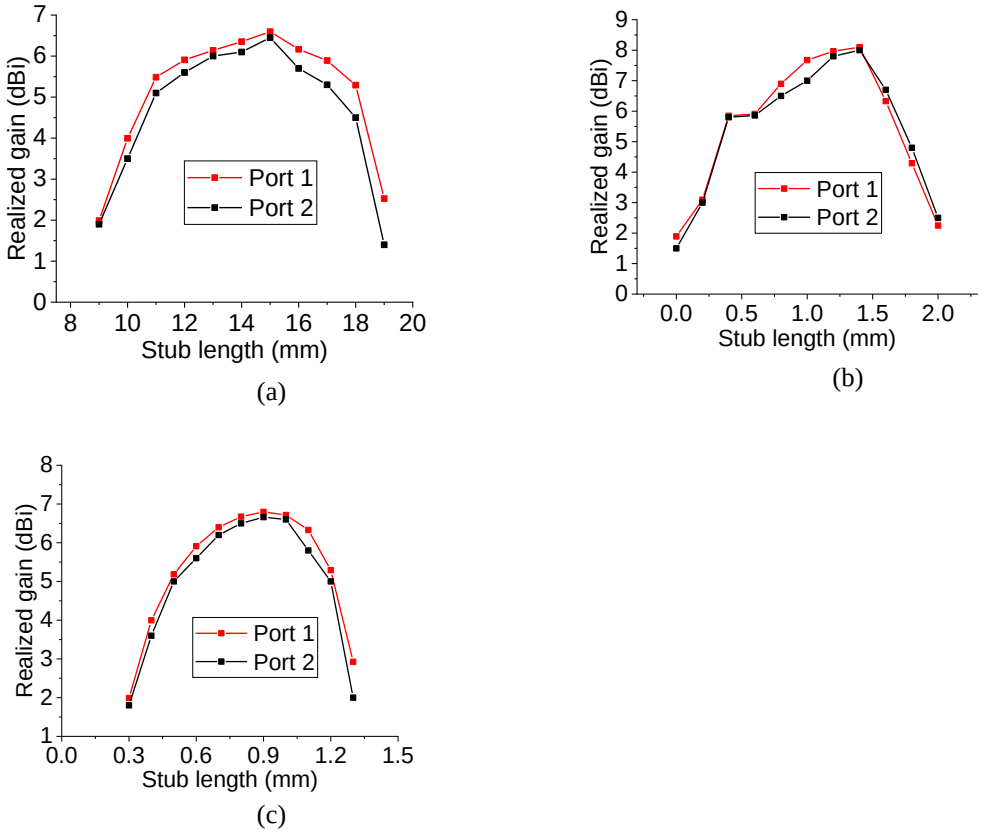

Figure 4. 20 Effect of stub length on realized gain for (a) L-, (b) K- and (c) Ka-band

In Figure 4. 19, variation in S11 and S22 is plotted against the stub length. Stub length adjustment shifts the reflection coefficient from not matched to well matched to not matched again. Again, as the frequency goes from L-band to Ka-band or lower to higher the change becomes more abrupt. Similarly, for the realized gain, changing the stub length, changes the realized gain. The change in the realized gain is around 5 dB meaning the realized gain is very much tuneable by stub length variation.

4.6.6 Summary of the parametric study

Designing DP ACMSA is a very challenging task in three different frequencies maintaining the same configuration. A number of factors or parameters play roles in designing the antenna such as the substrate, patch length, feed length, slot length and width, stub length and so on. In the previous section all these parameters were varied, and their effect was observed. In the next section a design guideline is presented.

In Table 4. 2 effect of few parameters such as substrate dielectric constant (Ɛr), length of the patch (lp), width of the patch (wp), feed length (l1), stub length (l4), slot length (ls), slot width (ws), substrate width (w) and substrate length (l) are summarized.

It is observed that the effect of changing the substrate permittivity (ε_r) and substrate thickness (h) have a significant effect on the antenna performance than other parameters. As not every substrate with every dielectric constant is available in the market, so a fixed substrate with fixed thickness is first selected. The next parameter that should be fixed is the patch length (lp). The length has a direct proportional relationship with the centre frequency of operation. Hence increasing the length increases the radiation edge and hence the centre frequency, the antenna radiates the most only at a certain matching condition. The length of the patch is hence to be fixed as well for a certain frequency of operation. Similarly, as the substrate and its thickness

Table 4. 2 Summary of the effect of different parameter changes

Parameter names	Effect on the S11 / S22	Realized Gain	Comments
ε_r	U	D	S11 / S22 and Realized gain change moderately
lp	DU	UD	S11 / S22 and Realized gain change abruptly
wp	D	-	S11 / S22 changes but realized gain not so
l1	UDU	DUD	Matching is affected so are S11 / S22 and gain
l4	UDU	DUD	Stub is crucial to matching, S11 / S22 and gain change abruptly
ls	UDU	DUD	Amount of excitation affects S11 / S22 and gain
ws	U	D	S11 / S22 and Realized gain change moderately
w	-	-	Not much effect
l	-	-	Not much effect

* U = upwards

* D = downwards

are fixed, a 50 Ω line will have a constant thickness which should not be varied while optimizing. All the other parameters can be varied up to a limit except these parameters. The substrate permittivity and height/thickness must be fixed for practicality of the design and the patch length is found from the theory hence cannot be changed. The other dominant parameters that result in larger variation are the slot length (ls), stub length (l4), width of the slot (ws) and few others. The slot length variation varies the point of excitation on the patch and has similar effect of changing feeding position of the coaxial cable in coaxially fed antenna. At the right slot length, the S11 / S22 or the reflection coefficient hits the optimum point and change abruptly with further change in this parameter. Next, the stub length (l4) is vital obtaining the matching of impedance. Changing the stub length changes the reactance of the impedance hence changes the matching condition. Again, at a certain frequency, the stub length must be fixed at a certain value and just a little variation in that length results huge variation in the S11 of reflection coefficient. The slot width (sw) controls the amount of excitation going through the ground plane and hence vital designing the antenna. The feed length (l1) also has impact as

this controls the feed position and hence the matching. There are also other parameters that change the performance of the antenna such as the width of the 'Y' arm of the feed and width of the patch (wp) but they are changed to tune the matching circuit only after fixing other important parameters beforehand. There is also another very important parameter which is found theoretically and is fixed independent of the frequency and operation and that is the width of the feed which should be of 50 Ω always. The isolation between the ports depend on the feeding technique and the physical distance between the ports. The configuration chosen in this study has a very high isolation between ports compared to some other designs. A cross shaped slot and different layered feed lines ensure this high isolation between ports so that a high isolation is maintained in all three frequencies. In the next section a complete design guideline is presented after documenting these parameters variation.

4.6.7 Design guideline for DP ACMSA

A brief design guideline is presented here for designing DP ACMSA for a frequency range between L-band (1.4 GHz) and Ka-band (37 GHz).

- The first task is to choose the substrate with a suitable permittivity (ε_r) and thickness. As commercially not every thickness is not available. Substrate thickness of about 0.01 λ to 0.02 λ is better for feed substrate. For patch substrate, thicker substrate with lower permittivity is preferable but the same substrate can be chosen for conformity and cheap price. As this design is going to be implemented in an array hence selecting the right substrate and thickness is very crucial.
- The next task is to select the resonant frequency and bandwidth of operation.
- The next step is to calculate the patch length (lp) for the required frequency. The equation for calculating the length is

$$lp = \frac{\lambda_g}{2} = \frac{300}{2 \times f_c \times \sqrt{\varepsilon_r}} \text{.....(1)}$$

Where, f_c is the resonant frequency and ε_r is the relative dielectric constant, and λ_g is the guided wavelength.

As this is a dual polarized configuration, hence the length and the width should be the same.

- Other parameters can be approximated as follows. Substrate length and width can also be the same and can be approximated as $w = l = 2 \times lp$. Slot length (ls) can be set as $ls = 0.9 \times lp$. Slot width (sw) can be $sw = lp/10$. Feed length (f1) can be set as $l1 = lp/3$ and the space between the 'Y' arms (l2) can be approximated as $l2 = 0.8 \times lp$. The stub length (l4) is also very important and sensitive parameter and that can be approximated as $l4 = 0.3 \times lp$.
- The next step is to set up the CST simulation environment and design the antenna using parameters. Setting up the boundary conditions and results are then followed by the simulation and result analysis.
- After the simulation, results are checked, and parameter sweep is prepared.
- If the required properties need modifications, it is optimized changing one parameter at a time and using the parameter sweep function in the CST MWS.
- The requirement of S11 is generally below -10 dB and is obtained by varying slot length (ls), stub length (l4), feed length (l1) and slot width (ws) one at a time. Generally, to move the resonant frequency, patch length (lp) is varied in the beginning and for further resonance slot length (ls) and stub length (l4) is varied. For even further matching condition other parameter such as feed length (l1), slot width (ws) etc. are optimized.

- The optimization process can be long depending on the mesh spacing and size of the antenna. Also, the simulation is basically iteration of different parameters sweep one at a time in the beginning then combination of different parameters sweeps at the same time until required result is obtained. The flow chart of the whole design process is summarized in the Figure 4. 21

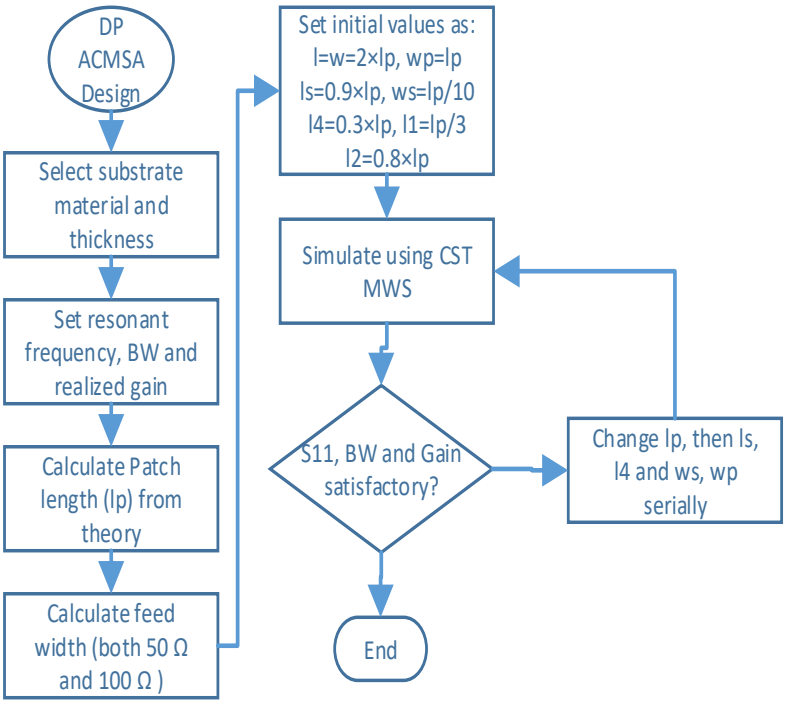

Figure 4. 21. Design guideline for DP ACMSA development

- This flow chart only helps to start the design with initial values. As the optimization continues, it might be required to tweak few parameters to achieve best optimization in terms of reflection coefficient, gain and isolation etc.

4.7 Conclusions

Three single element DP ACMSA antennas are designed and developed in this chapter. Three separate frequencies with specific bandwidth, isolation and gain were considered as the design requirements. A systematic approach is taken for designing these antennas. A brief theory of operation is discussed. Simulation results with all the parameter values are shown followed by a measurement result, then a detailed parametric study and finally a design guideline with step by step formula is presented. It is found more challenging to design and optimize Ku- and Ka-band antennas, compared to of L-band due to their small size and higher frequency characteristics.

The main challenge of this chapter was to select the DP ACMSA method for designing the antennas. Many other feeding techniques such as co-axial, microstrip line, slot on the ground plane were investigated and it was found that DP ACMSA suits the best for the radiometer with low profile and planar configuration. To maintain simplicity and symmetry this sacrifice is made. For the Ku- and Ka-band, the gain and the isolation are very high. Between the Ku- and Ka-bands, the Ka-band has the smaller size making it very difficult to fabricate and measure a single element thus no single element Ka-band antenna is fabricated and measured but an array is fabricated and discussed in the next chapters.

During this design, there are many parameters in the antenna that are tweaked to match the best. Finding the optimized dimensions of different parameters is a big challenge thus a systematic approach to optimize the antenna design to observe which parameter changes what parameter is then discussed. A flow chart is then documented to show the findings and a guide to design effectively for future.

This chapter works as a unit cell for the rest of the chapters, which are the array antenna, beam shaping algorithm and multi-band antenna are based on array antenna design and the single element from this chapter is used to build these arrays.

5 Array Antenna Design

5.1 Overview

Linearly polarized (LP) and dual polarized (DP) antennas radiating in L- (1.4 GHz), Ku- (18.7 GHz) and Ka- bands (37 GHz) are discussed in the previous two chapters. These antennas are the perfect candidate for radiometer antenna because of their planar design, high gain, high port-to-port isolation and simpler design. The requirement of radiometer antenna system cannot be met using a single element antenna as the radiometer system needs to have higher gain and low side-lobe levels. Hence an array system is essential to meet the requirement of the radiometer system. In this chapter, array antenna is designed, simulated and measured for all three L-, Ku-, and Ka-bands starting from 2 × 2 then 4 × 4 and finally 8 × 8 elements. The idea behind using three bands is to have the sensitivity of the lower frequency band to penetrate deeper into the soil and to have the higher resolution from the higher frequency. Combining these lower and higher frequency bands in the same compact aperture is the main challenge discussed in this research. For the array antenna development, it is important to design the feed network that operates in the corresponding frequency band, has relatively matched reflection coefficient or return loss. In this chapter, only uniform distribution of the array configuration is discussed so the feed network supplying excitation to the elements is symmetric. The feed network or power divider configuration depends on the feeding technique of the array. For the power divider network, basic quarter-wavelength transformer power dividers are used. The divider network can be sub-divided into two basic categories, (a) corporate of tree structure where 1-to-2 way structure is implemented and replicated to get 1-to-N way structure and (b) N-way structure where N-way from 1 is directly designed [220]. Groove feed structure for slotted array antenna is discussed in [221]. Based on the theory of traveling wave power divider

Chapter Outline

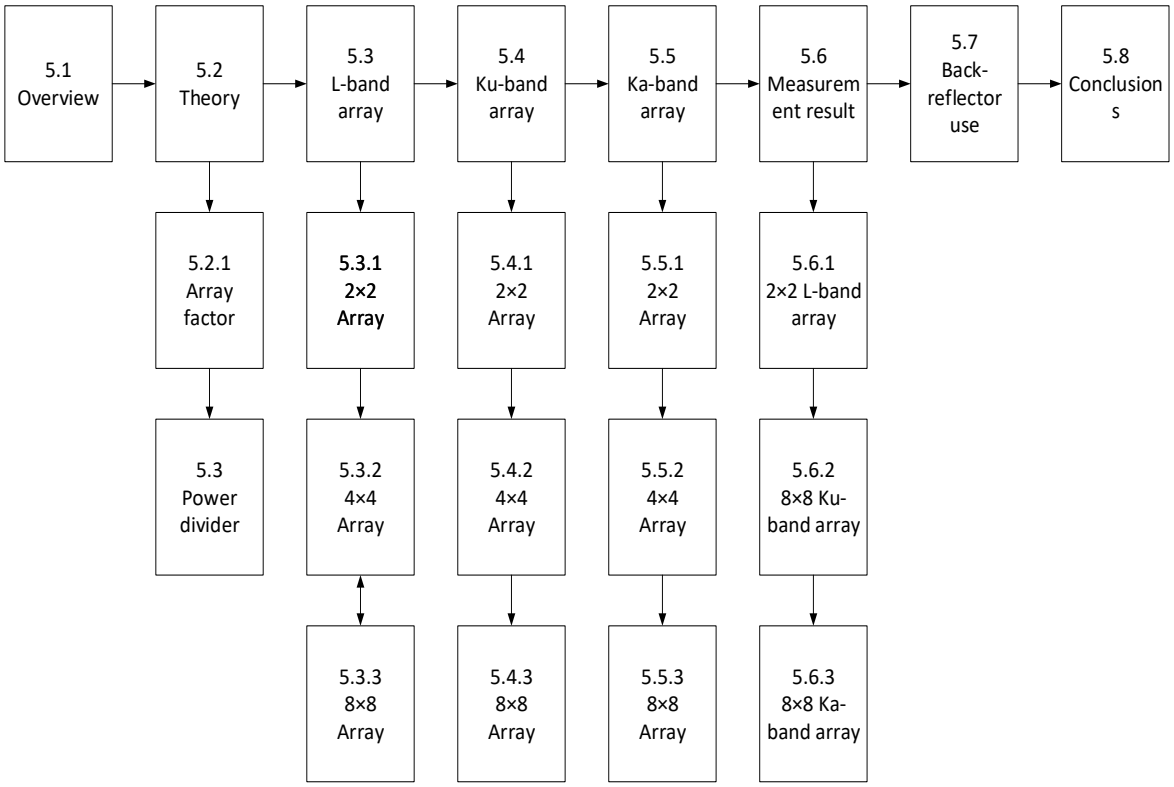

a 1-to-8 way Ka-band power divider is presented in [222]. The problems with such designs are the inclusions of the short walls and posts in the substrate for a multi-layered structure. Tapered and quarter-wave transformer power divider is discussed in [223] and is the most appropriate simpler technique to be adopted. Other popular techniques such as Wilkinson power divider [224, 225], hybrid power divider [165], split tee structure [226], multi-layer slot line [227] are discussed in many literatures but are not feasible due to the structure of the array.

If the development of the radiometer system can be divided into many parts and a step-by-step approach is taken, then the first step is to design a single element which is discussed in the previous chapters. This chapter is dedicated for the array development, and the next chapters are to shape the array radiation pattern or beam and retrieval of the moisture.

5.2 Theory

An array of antenna consists of a specific number of element antennas separated by a distance, arranged in a specific physical arrangement to achieve a certain radiation pattern. This antenna configuration provides a number of advantages such as higher gain than an element, directivity and shape of the radiating beam. In an antenna array, there are few parameters that play vital role determining the shape and performance of the radiation pattern [79]:

- The number of elements
- Shape or geometric arrangement of the array such as linear, rectangular, circular and so on.
- The radiation pattern of the single element antenna
- The amplitude of excitation of the single element antenna and
- The phase of excitation of the single element antenna.

The antenna array can be used to:

- increase the overall gain [228]
- provide diversity reception
- cancel out interference from a particular set of directions
- "steer" the array so that it is most sensitive in a particular direction
- determine the direction of arrival of the incoming signals
- to maximize the Signal to Interference Plus Noise Ratio (SINR)

5.2.1 Array factor

An array configuration with identical elements spaced uniformly can be characterized in a closed-form expression, function of the array geometry and of the excitation of its elements, called array factor (AF).

For N-element linear array with uniform amplitude and spacing the array factor can be found from [79]-

$$AF = 1 + e^{j(kdcos\theta+\beta)} + e^{j2(kdcos\theta+\beta)} + \cdots e^{j(N-1)(kdcos\theta+\beta)}$$

Where, $k = \frac{2\pi}{\lambda}, \lambda =$ wavelength, $d =$ inter-element distance between two elements, $\beta =$ phase difference of the excitation, $N =$ number of elements

Or, we can write in summation form in-

$$AF = \sum_{n=1}^{N} e^{j(n-1)(kdcos\theta+\beta)}$$

For this study, spacing between adjacent elements were chosen to be half of the wavelength. The new equation for array factor becomes

$$AF = \sum_{n=1}^{N} \delta_n e^{j(n-1)(kdcos\theta+\beta)}$$

Actually, the distance between two adjacent elements is decided to be 0.7λ as smaller than this creates space-proofing challenging. If the distance is over λ, then grating-lobe appears and that is avoided.

5.2.2 Power Divider

The feed network is the most important component in the design due to the following reasons. The first and most important is that this design should operate over a large bandwidth. There is more than one element in an array and the network has to supply power to all of them.

Supplying the same amount of equiphasic power to all of them requires on-trivial calculations and understanding of the transmission line theory. The transmission line width is represented by impedance.

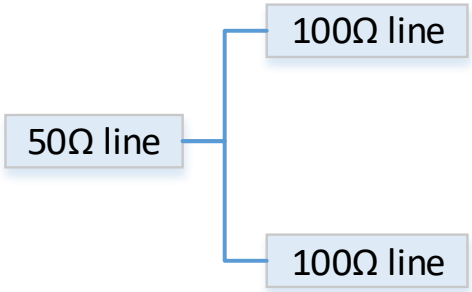

Figure 5. 1 A 1-to-2-way power divider.

A 1-to-2-way power divider would be made up of these impedances to keep balanced. The final feed network is a 1-to-8-way divider. The 2-way tee junction power divider is the heart of the design, shown in Figure 5. 1.

An alternative 1-to-4-way power divider would be made up of these impedances to keep it balanced as shown in Figure 5. 2

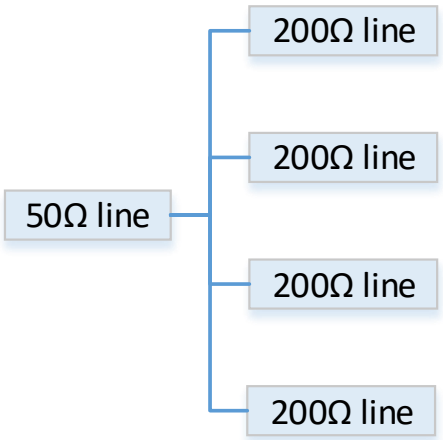

Figure 5. 2 A 1-to-4-way power divider.

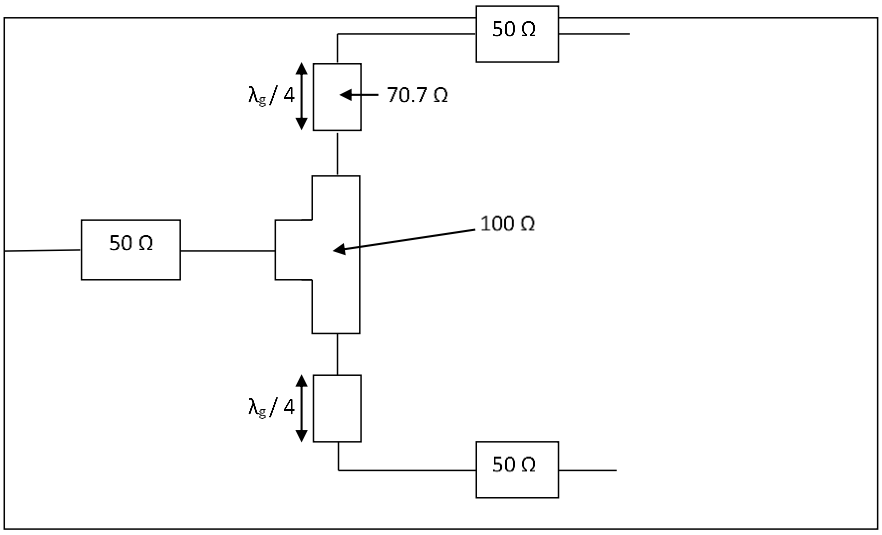

Figure 5. 4 A 2-way power divider with 2 quarter wavelength transformers.

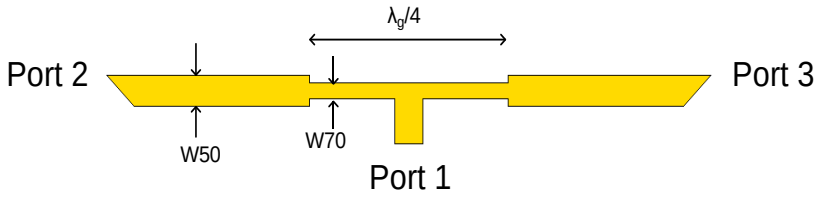

(a)

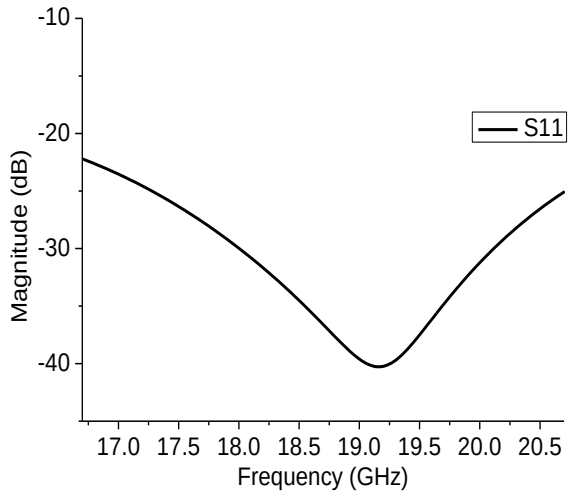

(b)

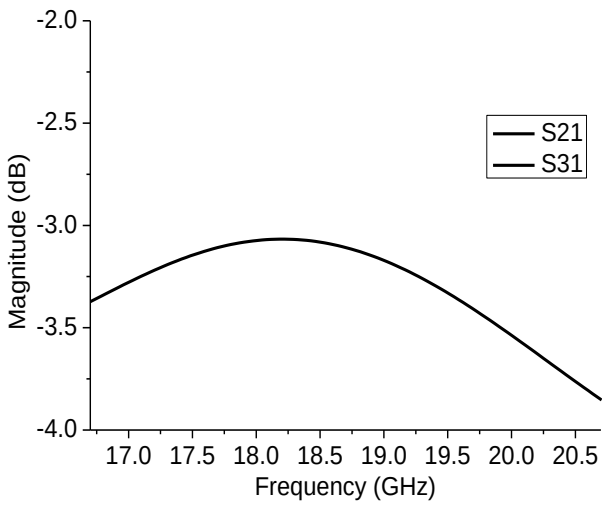

(c)

Figure 5. 3 (a) Schematic of quarter wavelength power divider for Ku-band, (b) S11 of power divider, (c) S21 and S31 of power divider in Ku-band

This means that the microstrip line width would be unrealizable. These small width lines are impossible to realize in physical dimensions, so a quarter wave length transformer can be used

to design the power divider. However, still 4-way power divider even when using quarter wavelength transformers is not a feasible option. Therefore, choosing the 2-way quarter wavelength power divider as the building block of the 8-way final beam shaping network is decided.

The Schematic of 1-to-2-way power divider using quarter wavelength transformation is shown in Figure 5. 4.

Quarter wavelength transformer impedance is calculated from [79] by:

$$Z_T = \sqrt{Z_0 \times Z_L}$$

Where Z_L is the impedance of the feed line = 50 Ω

Z_0 is the impedance of the tee junction = 100 Ω

Z_T = (50 * 100) ^ 0.5 = 70.7 Ω

Designing for Ku-band at 18.7 GHz result can be seen in Figure 5. 5, where Figure 5. 5 (a) shows the quarter wave transformer method of power divider. The substrate of the divider was chosen to be TLX-8, the same chosen for the antenna. Due to the fixed thickness of the substrate, which was 0.127 mm, the thickness of the 50Ω line was 0.35 mm and for 70.7Ω line it is 0.25 mm. The simulation result of such divider is shown in Figure 5. 5 (b) and (c) where it is evident that at the resonant frequency, the divider network is well matched, and almost half of the power is being transferred from port 1 to port 2 and 3 individually.

5.3 L-band antenna

L-band antenna requirement is to resonate at 1.4 GHz with a very narrow bandwidth of 25 MHz and with port-to-port isolation of over 25 dB. First, 2 × 2 array is designed, then 4 × 4 and finally 8 × 8.

5.3.1 2 × 2 Array

For the element cell of the array, DP ACMSA is selected as mentioned in the previous chapter. The design of the array is performed using CST MW 2017. First, a power divider for the 2 × 2 feed network is designed, which is shown in Figure 5. 5 (a). Then on top of the centre of the feed network, 2 × 2 patches are placed, shown in Figure 5. 5 (b) so that they are exactly above each feed line. Finally, a cross shaped slotted ground plane was designed in the middle of the

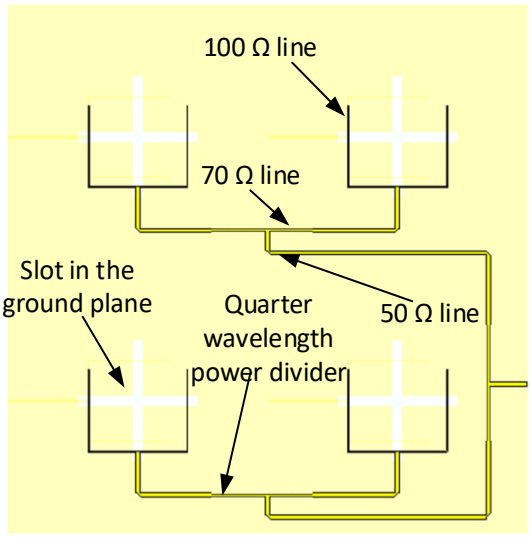

(a)

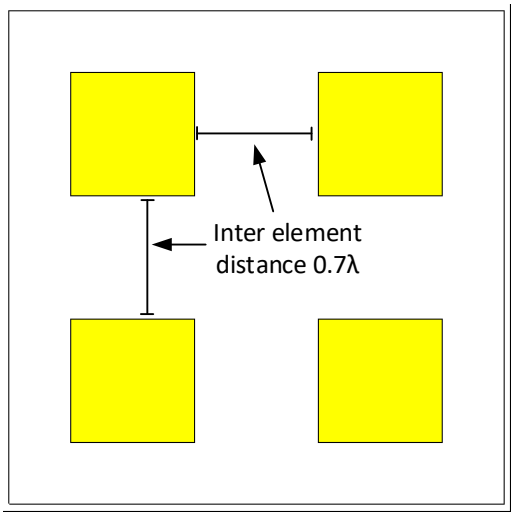

(b)

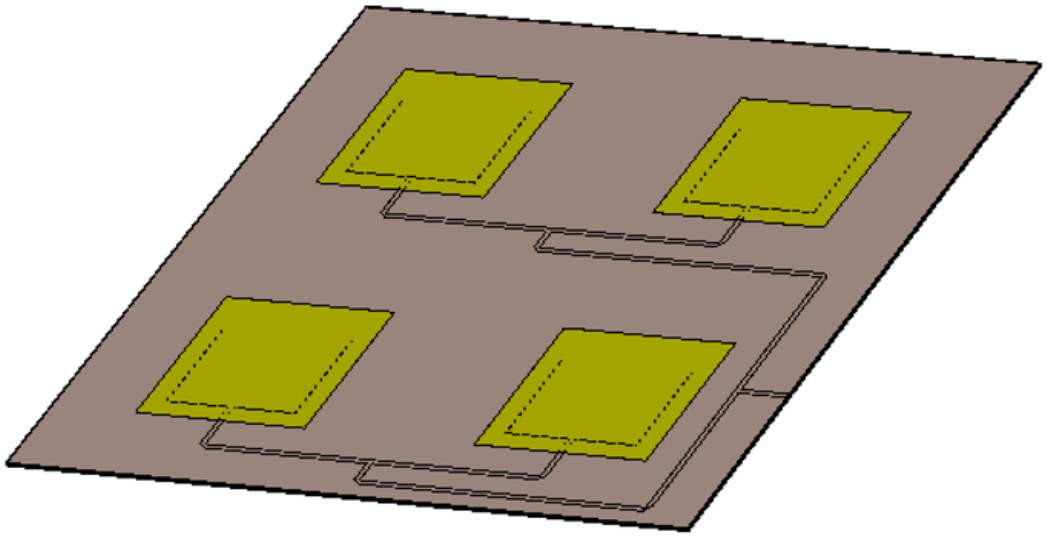

(c)

Figure 5. 5 (a) Power divider or feed network for the array, (b) patch configuration, (c) 3-d view of the 2 × 2 L-band array antenna.

2 feed line layers to complete the design shown in Figure 5. 5 (c). The distance between two adjacent elements is decided to be 0.7λ. If the distance is over λ, then grating-lobe appears. Optimal spacing is always a trade-off as smaller inter-element distance will cause strong coupling and vice versa bigger distance will cause grating-lobe [79].

5.3.1.1 Simulation result

Simulation was performed using CST MW Studio 2017 after optimizing the design by tweaking the feed network parameter. All the boundary condition was checked, and simulation environment was set to ideal. The result is presented in this section.

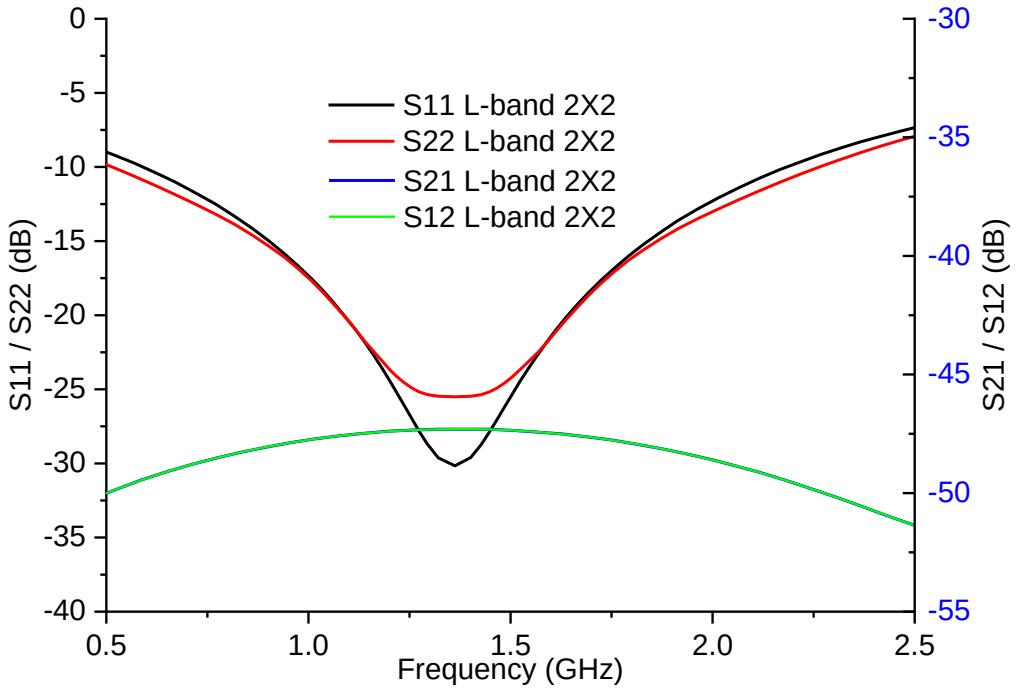

Figure 5. 6 S-parameter result for L-band 2 × 2 array antenna

In Figure 5. 6, S-parameter result is shown in the same figure. S11 and S22 result show very good return loss at the resonant frequency (1.4 GHz). Port-to-port isolation or S21 is also less than -45 dB throughout the spectrum. In all the cases from hereon, S21 and S12 are overlapped and in the figure they actually appear as a single line. The bandwidth is found around 1.6 GHz

ranging from 0.6 GHz to 2.2 GHz. S-parameter result overall shows very good matching and minimum coupling.

Figure 5. 7 (a) and (b) show electric and magnetic field radiation pattern for the L-band 2 × 2 array antenna. From the electric field radiation pattern, a maximum gain of 13.1 dBi is found with 55 dB cross polarization level at 0°. Similarly, for the magnetic field, a gain of 13.0 dBi is found at 0°, with a cross polarization level of around 60 dB. This antenna has a decent amount of back-lobe radiation which can be improved by implementing a back reflector which improves the front-to-back lobe ratio and is discussed in the later part of this chapter.

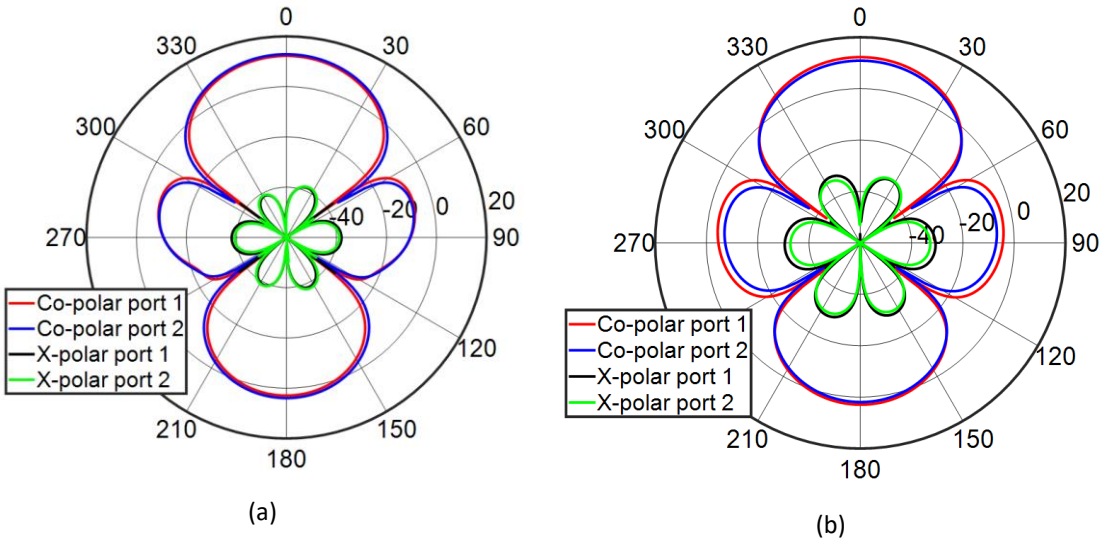

Figure 5. 7 (a) E- and (b) H-plane of 2 × 2 L-band array antenna

5.3.2 4 × 4 Array

The design of the 4 × 4 array is also performed using CST MW Studio 2017. Extending the 2 × 2 power divider network a power divider for the 4 × 4 feed network is designed, which is

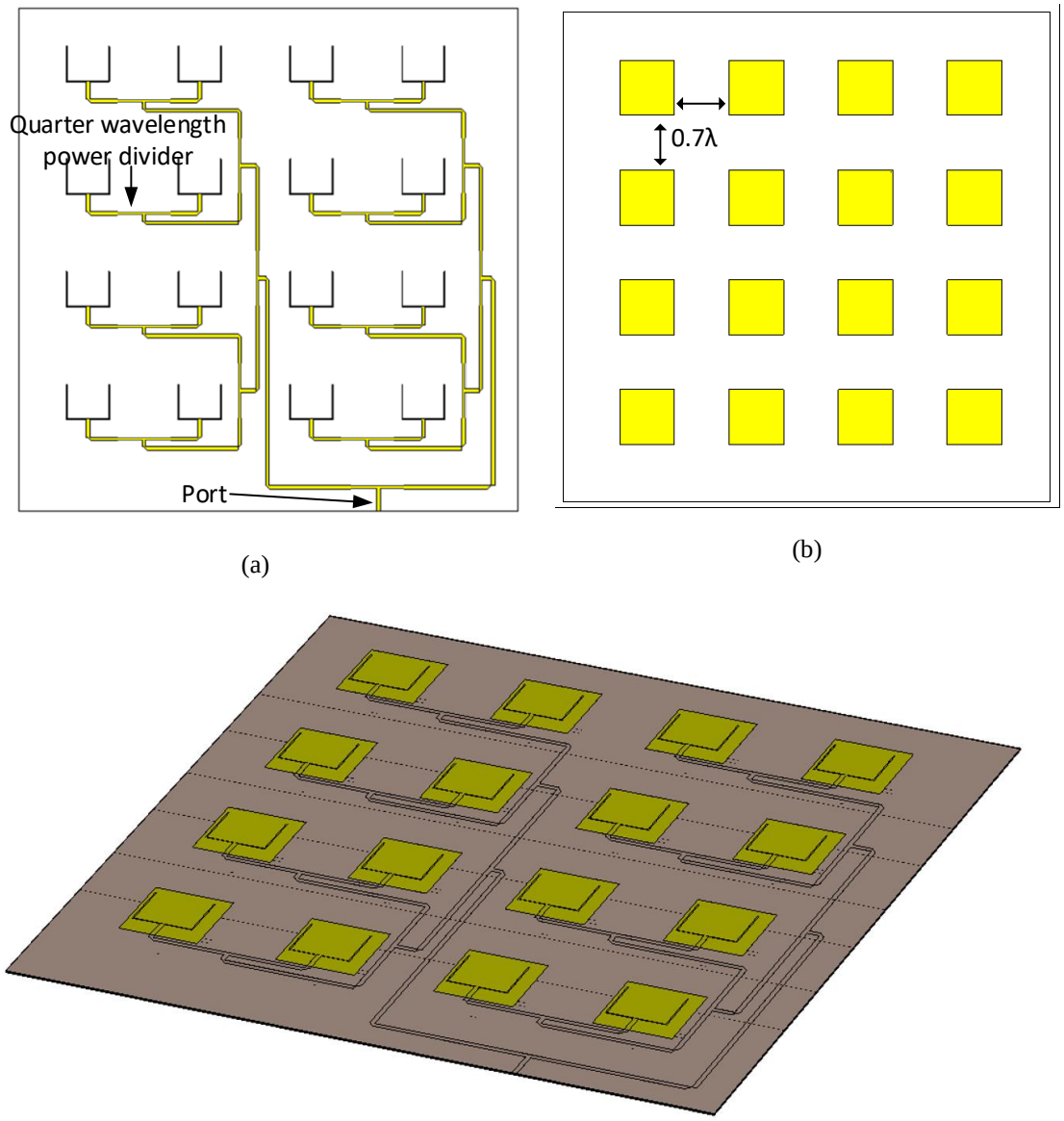

Figure 5. 8 (a) Power divider or feed network for the array, (b) patch configuration, (c) 3-d view of the 4 × 4 L-band array antenna.

shown in Figure 5. 8 (a). Then on top of the centre of the feed network, on the other side of the substrate, 4 × 4 patches are etched equidistantly, shown in Figure 5. 8 (b) so that they are exactly above the centre of each feed line. The ground plane has slots of 'cross' shape, so 4 × 4 'cross' shaped slots are etched and are shown in Figure 5. 8 (c). The distance between two adjacent elements is optimized to be 0.7λ to avoid grating-lobe.

5.3.2.1 Simulation result

Simulation was performed using CST MW Studio 2017 after optimizing the design by tweaking the feed network path and parameter. The result after setting the design environment is presented in this section.

In Figure 5. 9, S-parameter result is shown in the same figure. S11 and S22 result show very good return loss at the resonant frequency (1.4 GHz). Port-to-port isolation or S21 and S12 are also less than -45 dB throughout the spectrum. The bandwidth is found around 500 MHz ranging from 1.2 GHz to 1.7 GHz. S-parameter result overall shows very good matching and minimum coupling. Figure 5. 10 (a) and (b) show electric and magnetic field radiation pattern for the L-band 4 × 4 array antenna. From the electric field radiation pattern, a maximum gain of 18.6 dBi is found with 55 dB cross polarization level at 0°. Similarly, for the magnetic field, a gain of 18.7 dBi is found at 0°, with a cross polarization level of around 60 dB. This antenna

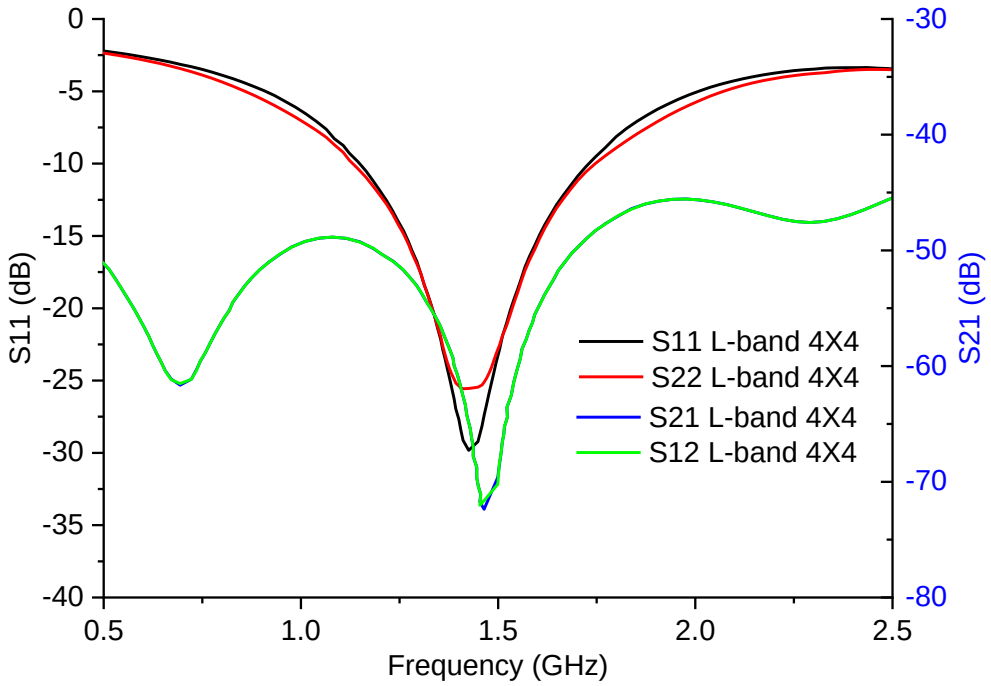

Figure 5. 9 S-parameter result for L-band 4 × 4 array antenna

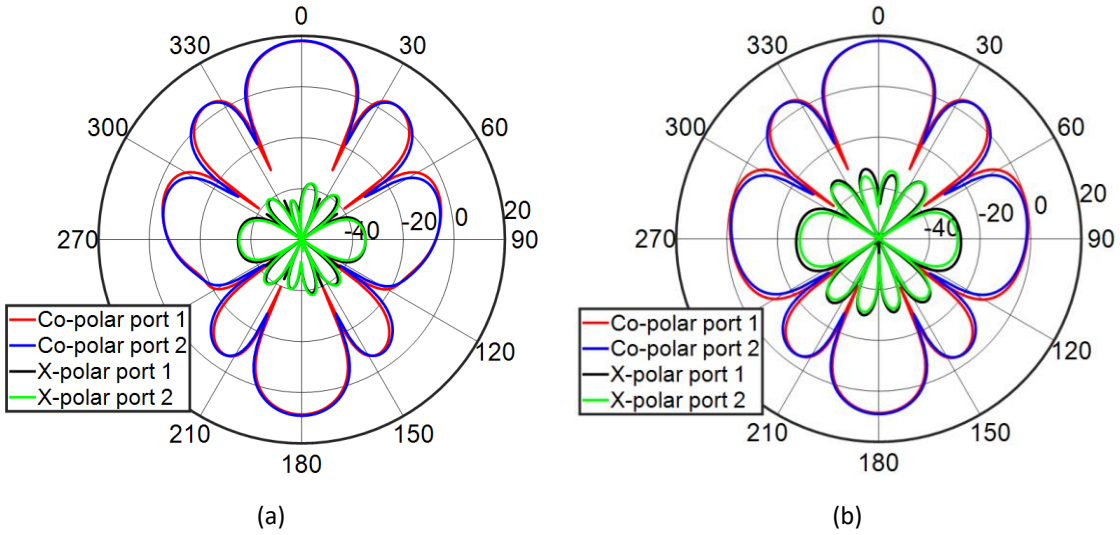

Figure 5. 10 (a) E- and (b) H-plane of 4 × 4 L-band array antenna

has a decent amount of back-lobe radiation which can be improved by implementing a back reflector which improves the front-to-back lobe ratio and is discussed in the later part of this chapter.

5.3.3 8X8 Array

The design of the 8 × 8 array is also performed using CST MW Studio 2017. The feed layer structure is the most complex and is shown in Figure 5. 11 (a). 8 × 8 patches are placed on top of the centre of the feed lines equidistantly, shown in Figure 5. 11 (b) so that they are exactly

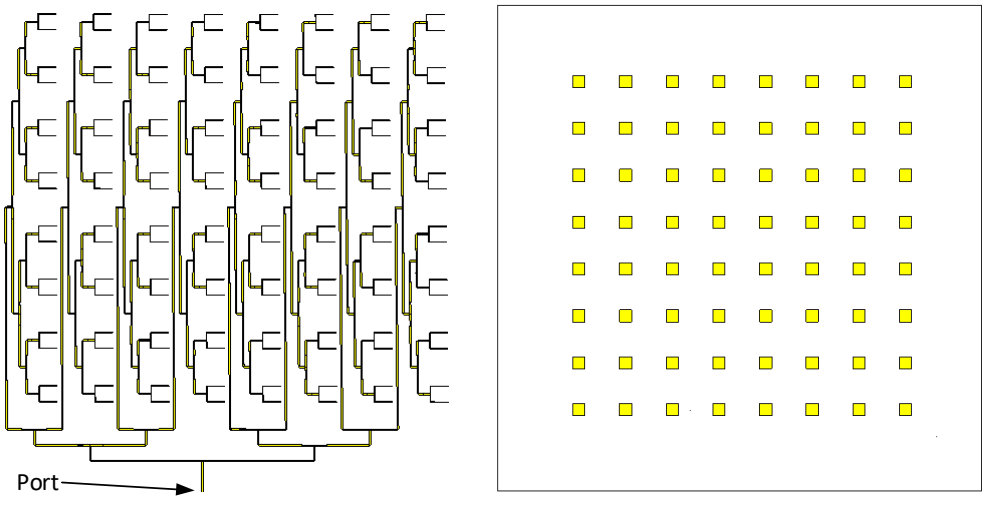

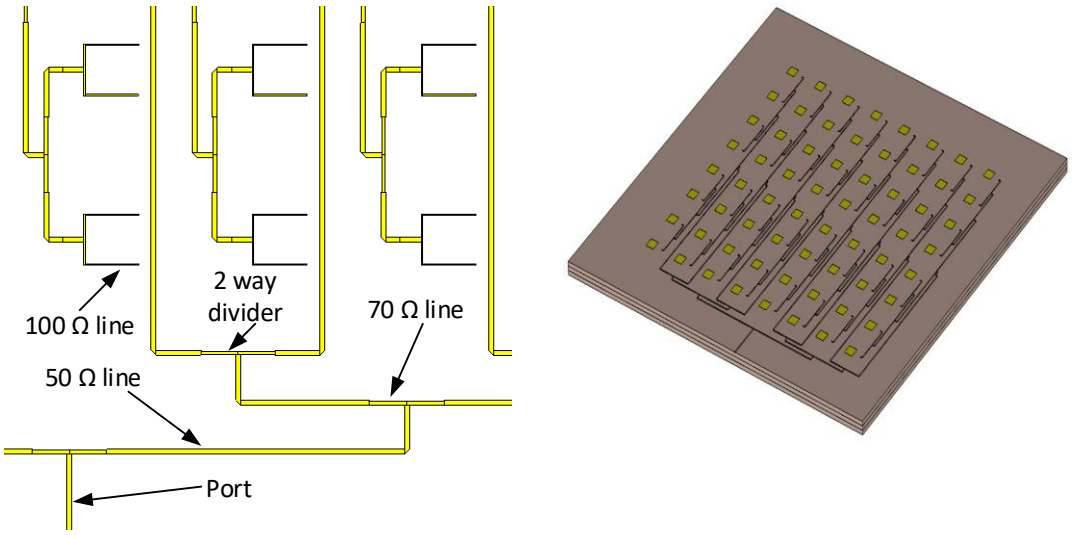

(c) (d)

Figure 5. 11 (a) Power divider or feed network for the array, (b) patch configuration, (c) expanded view of the power divider or feed network, and (d) 3-d view of the 8 × 8 L-band array antenna.

above the centre of each feed line. In Figure 5. 11 (c) an expanded view of the feed line is shown to explain and show the complexity of the design better. Finally, a cross shaped slotted ground plane was designed in the middle of the 2 feed line layers to complete the design shown in Figure 5. 11 (d). The distance between two adjacent elements is decided to be 0.7λ to avoid grating-lobe and optimization.

5.3.3.1 Simulation result

Simulation was run using CST MW Studio 2017 after optimizing the design by tweaking the feed network path and parameter. The result after setting the design environment is presented in this section.

In Figure 5. 13, all S-parameter results are shown in the same figure. S11 and S22 results show very good return loss at the resonant frequency (1.4 GHz). Port-to-port isolation or S21 and S12 are also less than -35 dB throughout the spectrum. The bandwidth is found around 500 MHz though S11 and S22 do not follow each other but covering the resonant frequency. S-parameter result overall shows very good matching and minimum coupling.

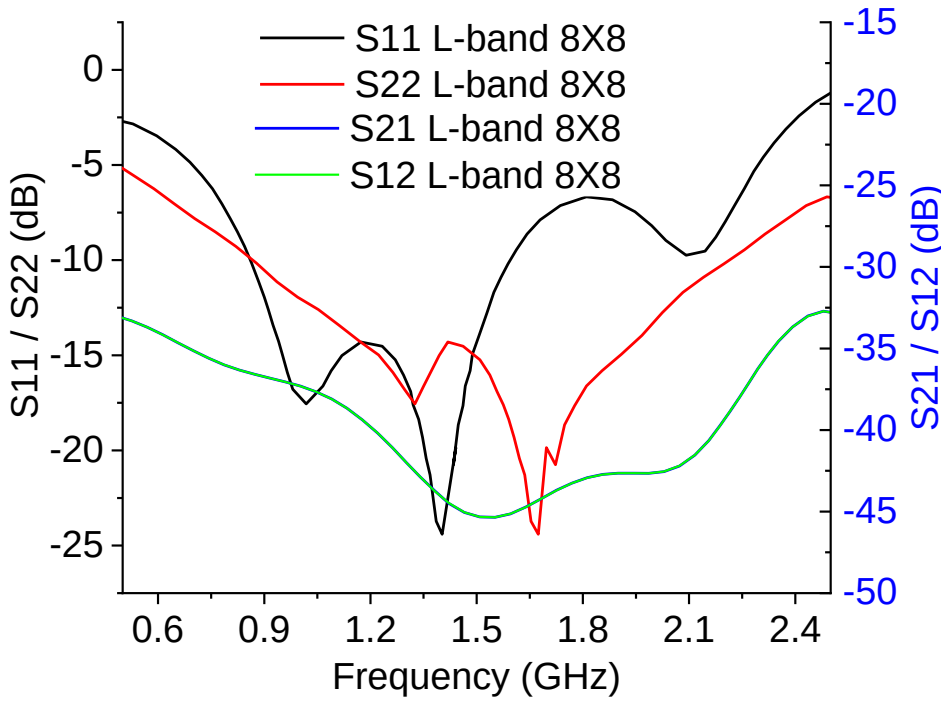

Figure 5. 13 S-parameter result for L-band 8 × 8 array antenna

Figure 5. 12 (a) and (b) show electric and magnetic field radiation pattern for the L-band 4 × 4 array antenna. From the electric field radiation pattern, a maximum gain of 23.9 dBi is found with 55 dB cross polarization level at 0°. Similarly, for the magnetic field, a gain of 24.0 dBi

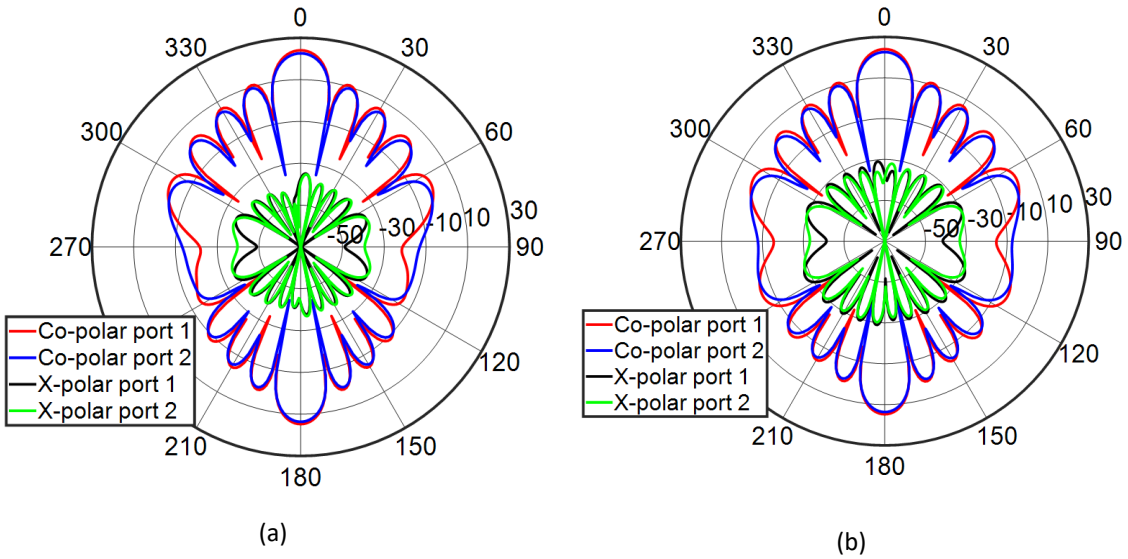

Figure 5. 12 (a) E- and (b) H-plane of 8 × 8 L-band array antenna

is found at 0°, with a cross polarization level of around 60 dB. Again back-lobe radiation is present, and it can be improved using a back-reflector.

5.4 Ku-band antenna

Ku-band antenna working requirement is the resonant frequency at 18.7 GHz with a bandwidth of 200 MHz and with port-to-port isolation of over 25 dB. First, 2 × 2 array is designed, then 4 × 4 and finally 8 × 8 designs are simulated and presented. It is important to show the 2 × 2 and 4 × 4 array design process to track the progress and maturity of the design.

5.4.1 2 × 2 Array

For the element cell of the Ku-band array, DP ACMSA is selected again as mentioned in the previous chapter. The design of the array is performed using CST MW 2017. Similar to the L-band, first, a power divider for the 2 × 2 feed network is designed, which is shown in Figure 5. 5 (a). Then on top of the centre of the feed network, 2 × 2 patches are placed, shown in Figure 5. 5 (b) so that they are exactly above each feed line. Finally, a cross shaped slotted ground plane was designed in the middle of the 2 feed line layers to complete the design shown in Figure 5. 5 (c). The distance between two adjacent elements is again decided to be 0.7λ which in this case is 11.23 mm. If the distance is over λ then grating-lobes appear. Optimal spacing is always a trade-off as smaller inter-element distance will cause strong coupling and vice versa bigger distance will cause grating-lobe.

5.4.1.1 Simulation result

Simulation was performed using CST MW Studio 2017 after optimizing the design by tweaking the feed network parameter. All the boundary condition was checked, and simulation environment was set to ideal. The result is presented in this section.

In Figure 5. 14, S-parameter result is shown in the same figure. S11 and S22 result show very good return loss at the resonant frequency (18.7 GHz). Port-to-port isolation or S21 is also less

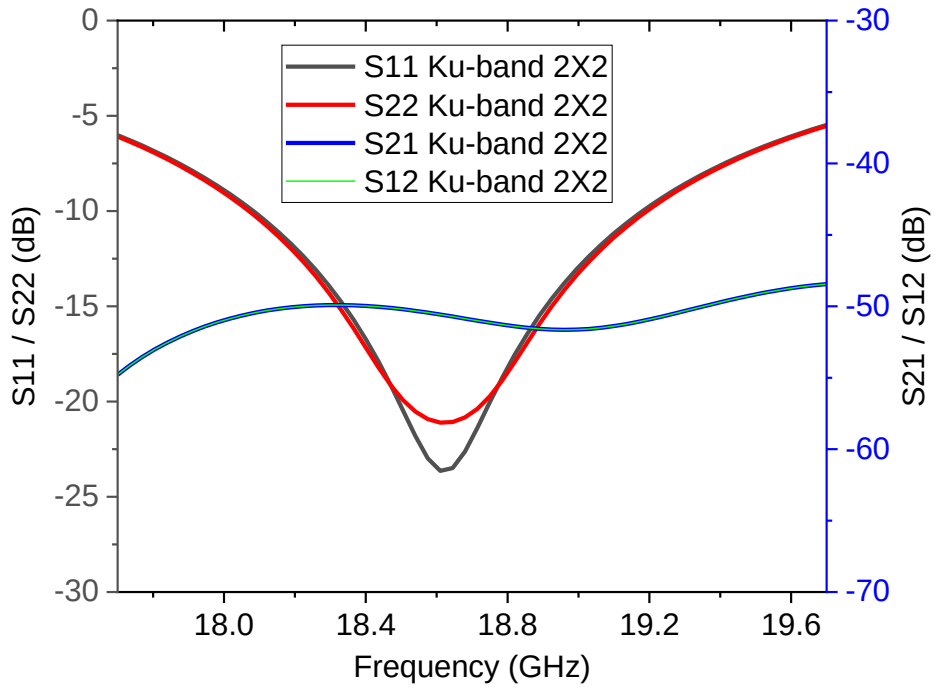

Figure 5. 14 S-parameter result for Ku-band 2 × 2 array antenna

than -45 dB throughout the spectrum. The bandwidth is found around 1.1 GHz ranging from 18.1 GHz to 19.2 GHz. S-parameter result overall shows very good matching and minimum coupling.

Figure 5. 15 (a) and (b) show electric and magnetic field radiation pattern for the Ku-band 2 × 2 array antenna. From the electric field radiation pattern, a maximum gain of 13.7 dBi is found

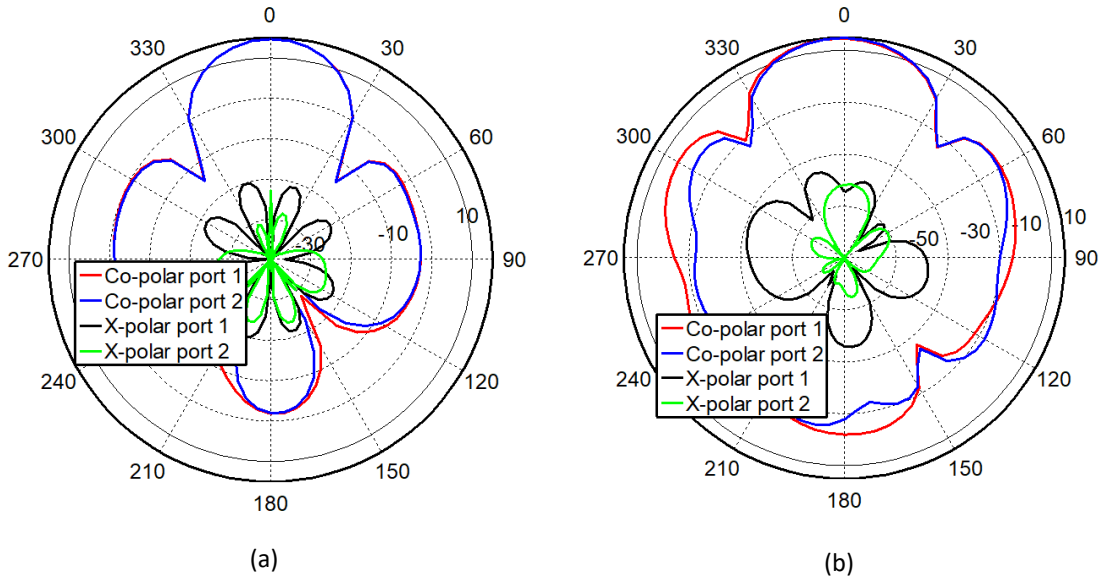

Figure 5. 15 (a) E- and (b) H-plane of 2 × 2 Ku-band array antenna

with 35 dB cross polarization level at 0°. Similarly, for the magnetic field, a gain of 13.7 dBi is found at 0°, with a cross polarization level of around 40 dB. The amount of back-lobe radiation is quite high, and it can be improved using a back-reflector.

5.4.2 4 × 4 Array

The design procedure for the array is an extension of the design performed in the previous section for the 2 × 2 array. First, a power divider for the 4 × 4 feed network is designed by replicating the 2 × 2 structure four times, which is shown in Figure 5. 8 (a). Then another level of power divider is designed to join those four dividers. After that 4 × 4 patches are placed equidistantly, shown in Figure 5. 8 (b) so that they are exactly above the centre of each feed line. The ground plane has 'cross' shaped slots which are shown in Figure 5. 8 (c). The inter-element distance is set to be 0.7λ after optimization to avoid grating-lobes.

5.4.2.1 Simulation result

For the 4 × 4 array, a similar approach is taken. The element antenna being the same, only power divider is extended to suit 4 × 4 structure. Simulation was performed using CST MW Studio 2017 after optimizing the design by tweaking the feed network path and parameter. The result after setting the design environment is presented in this section. Optimization for the feed lines are performed as the length of the feed line plays role in setting the phase difference as the size of the antenna grows, at higher frequency wavelength becomes comparable to the size of the feed lengths in an array configuration.

In Figure 5. 17, S-parameter result is shown in the same figure. S11 and S22 result show very good return loss at the resonant frequency (1.4 GHz). Port-to-port isolation or S21 and S12 are also less than -45 dB throughout the spectrum. The bandwidth is found around 900 MHz ranging from 18.4 GHz to 19.3 GHz. S-parameter result overall shows very good matching and minimum coupling.

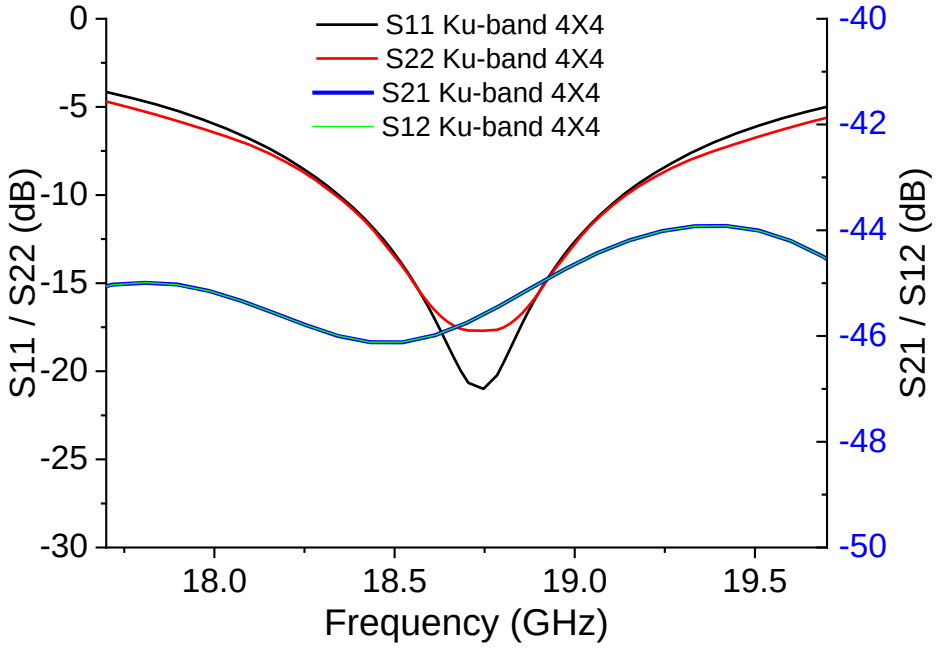

Figure 5. 17 S-parameter result for Ku-band 4 × 4 array antenna

Figure 5. 16 (a) and (b) show electric and magnetic field radiation pattern for the Ku-band 4 × 4 array antenna. From the electric field radiation pattern, a maximum gain of 19.9 dBi is found with 50 dB cross polarization level at 0°. Similarly, for the magnetic field, a gain of 19.7 dBi is found at 0°, with a cross polarization level of around 60 dB. This antenna has a decent amount

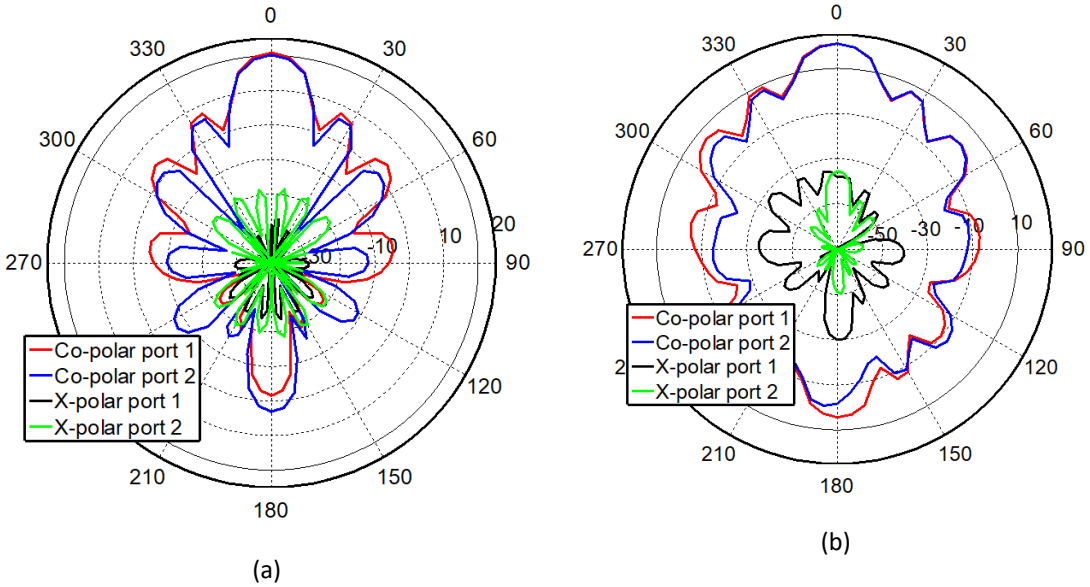

Figure 5. 16 (a) E- and (b) H-plane of 4 × 4 Ku-band array antenna

of back-lobe radiation which can be improved by implementing a back reflector which improves the front-to-back lobe ratio and is discussed in the later part of this chapter.

5.4.3 8 × 8 Array

The design of the 8 × 8 array is also performed using CST MW Studio 2017. Being the largest feed network, first, a power divider for the 8 × 8 feed network is designed, which is shown in Figure 5. 11 (a). Then all the 8 × 8 patches are placed on top of the centre of the feed lines equidistantly, shown in Figure 5. 11 (b). In Figure 5. 11 (c) an expanded view of the feed line is shown to explain and show the complexity of the design better. The ground place structure is shown in Figure 5. 11 (d). The distance between two adjacent elements is set to be 0.7 wavelength to avoid grating-lobes and optimization.

5.4.3.1 Simulation result

Simulation was run using CST MW Studio 2017 after optimizing the design by tweaking the feed network path and parameter. The result after setting the design environment is presented in this section.

In Figure 5. 13, all S-parameter results are shown in the same figure. S11 and S22 results show very good return loss at the resonant frequency (18.7 GHz). Port-to-port isolation or S21 and S12 are also less than -40 dB throughout the spectrum. The bandwidth is found around 500 MHz though S11 and S22 do not follow each other but covering the resonant frequency. S-parameter result overall shows very good matching and minimum coupling.

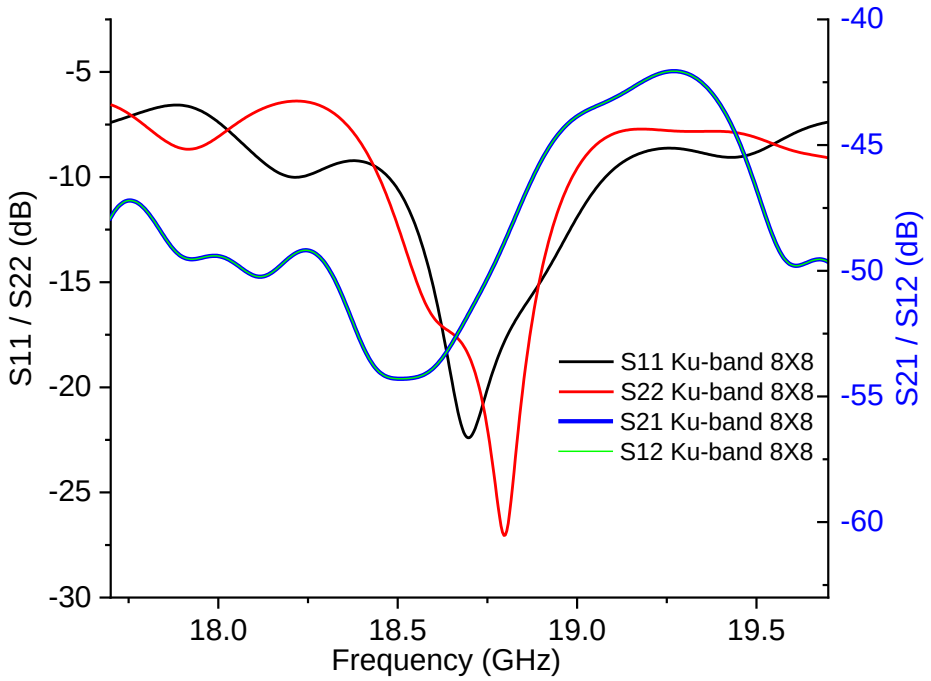

Figure 5. 18 S-parameter result for Ku-band 8 × 8 array antenna

Figure 5. 19 (a) and (b) show electric and magnetic field radiation pattern for the Ku-band 4 × 4 array antenna. From the electric field radiation pattern, a maximum gain of 26.3 dBi is found with 55 dB cross polarization level at 0°. Similarly, for the magnetic field, a gain of 26.2 dBi is found at 0°, with a cross polarization level of around 60 dB. This antenna has a decent amount

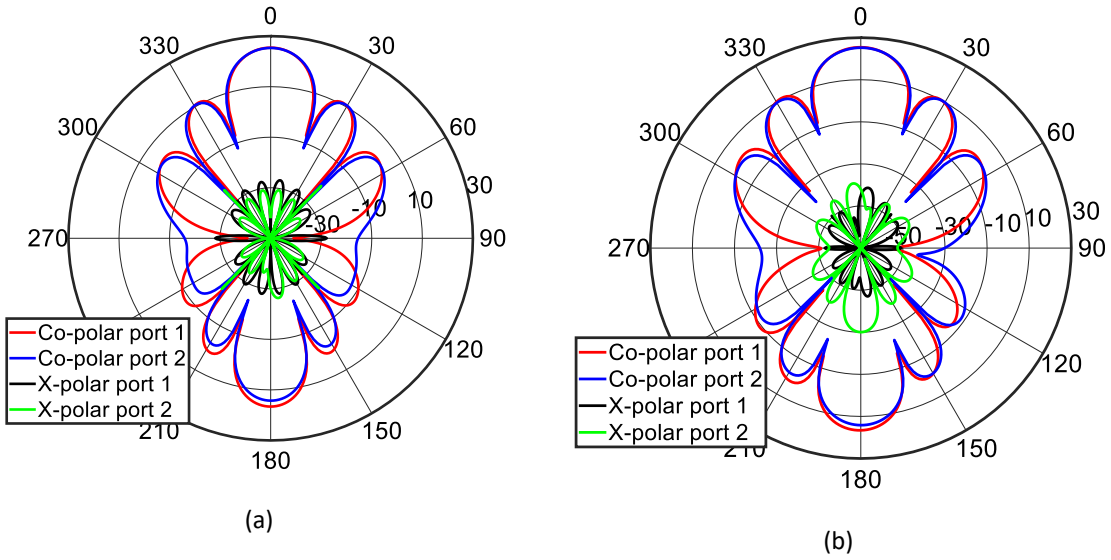

Figure 5. 19 (a) E- and (b) H-plane of 8 × 8 Ku-band array antenna

of back-lobe radiation which can be improved by implementing a back reflector which improves the front-to-back lobe ratio and is discussed in the later part of this chapter.

5.5 Ka-band array

Ku-band antenna requirement is to radiate at 37 GHz with a bandwidth of 1.5 GHz and with port-to-port isolation of over 25 dB. First, 2 × 2 array is designed, then 4 × 4 and finally 8 × 8 designs are simulated and presented.

5.5.1 2 × 2 Array

For the element cell of the Ku-band array, DP ACMSA is selected again as mentioned in the previous chapter. The design of the array is performed using CST MW 2017. Similar to the L-band, first, a power divider for the 2 × 2 feed network is designed, which is shown in Figure 5. 5 (a). Then on top of the centre of the feed network, 2 × 2 patches are placed, shown in Figure 5. 5 (b) so that they are exactly above each feed line. Finally, a cross shaped slotted ground plane was designed in the middle of the 2 feed line layers to complete the design shown in Figure 5. 5 (c). The distance between two adjacent elements is again decided to be 0.7λ which in this case is 5.68 mm. If the distance is over λ then grating-lobes appear. Optimal spacing is always a trade-off as smaller inter-element distance will cause strong coupling and vice versa bigger distance will cause grating-lobe.

5.5.1.1 Simulation result

Simulation was performed using CST MW Studio 2017 after optimizing the design by tweaking the feed network parameter. All the boundary condition was checked, and simulation environment was set to ideal. The result is presented in this section.

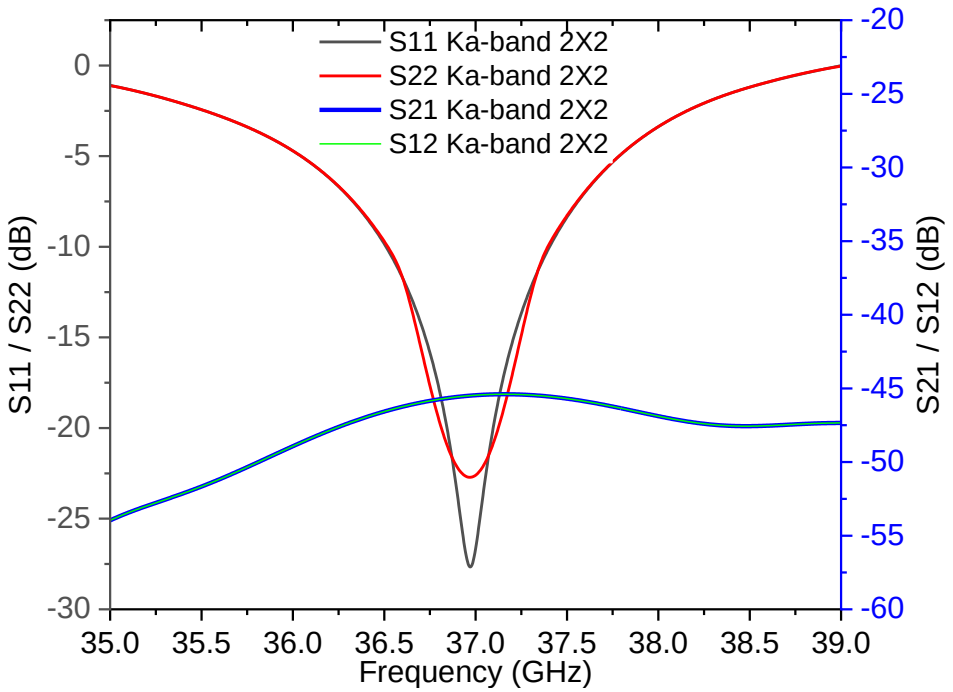

Figure 5. 21 S-parameter result for Ka-band 2 × 2 array antenna

In Figure 5. 21, S-parameter result is shown in the same figure. S11 and S22 result show very good return loss at the resonant frequency (37 GHz). Port-to-port isolation or S21 is also less than -45 dB throughout the spectrum. The bandwidth is found around 1.1 GHz ranging from 36.5 GHz to 37.6 GHz. S-parameter result overall shows very good matching and minimum coupling.

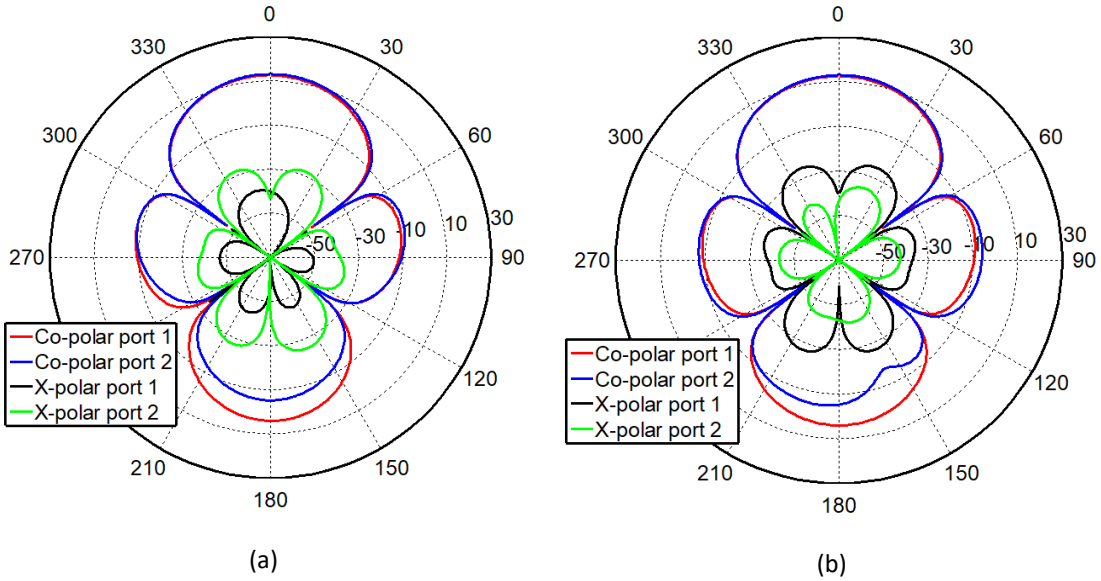

Figure 5. 20 (a) E- and (b) H-plane of 2 × 2 Ka-band array antenna

Figure 5. 20 (a) and (b) show electric and magnetic field radiation pattern for the Ka-band 2 × 2 array antenna. From the electric field radiation pattern, a maximum gain of 13.5 dBi is found with 35 dB cross polarization level at 0°. Similarly, for the magnetic field, a gain of 13.4 dBi is found at 0°, with a cross polarization level of around 50 dB. This antenna has a decent amount of back-lobe radiation which can be improved by implementing a back reflector which improves the front-to-back lobe ratio and is discussed in the later part of this chapter.

5.5.2 4 × 4 Array

The design of the 4 × 4 array is also performed using CST MW Studio 2017. First, a power divider for the 4 × 4 feed network is designed, which is shown in Figure 5. 8 (a). Then similar to the 2 × 2, on top of the centre of the feed network, 4 × 4 patches are placed equidistantly, shown in Figure 5. 8 (b). The patches are exactly above the centre of each feed line. The slot in the ground plane is again 'cross' shaped and was designed in the middle of the 2 feed line layers to complete the design shown in Figure 5. 8 (c). The distance between two adjacent elements is decided to be 0.7λ to avoid grating-lobe and optimization.

5.5.2.1 Simulation result

Simulation was performed using CST MW Studio 2017 after optimizing the design by tweaking the feed network path and parameter. The result after setting the design environment is presented in this section.

In Figure 5. 22, S-parameter result is shown in the same figure. S11 and S22 result show very good return loss at the resonant frequency (37 GHz). Port-to-port isolation or S21 and S12 are

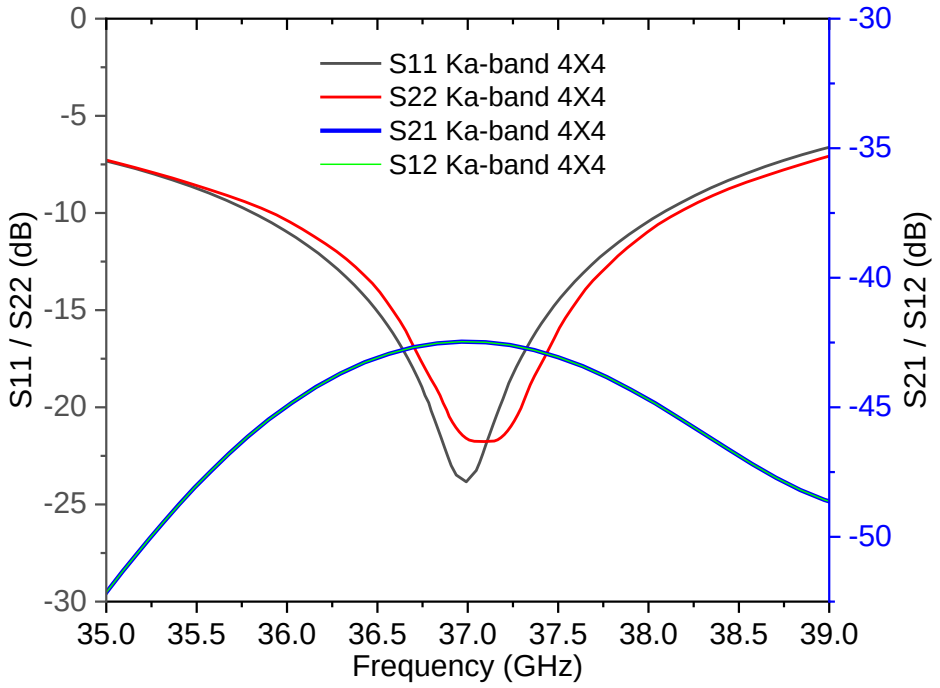

Figure 5. 22 S-parameter result for Ka-band 4 × 4 array antenna

also less than -40 dB throughout the spectrum. The bandwidth is found around 2.4 GHz ranging from 35.8 GHz to 38.2 GHz. S-parameter result overall shows very good matching and minimum coupling.

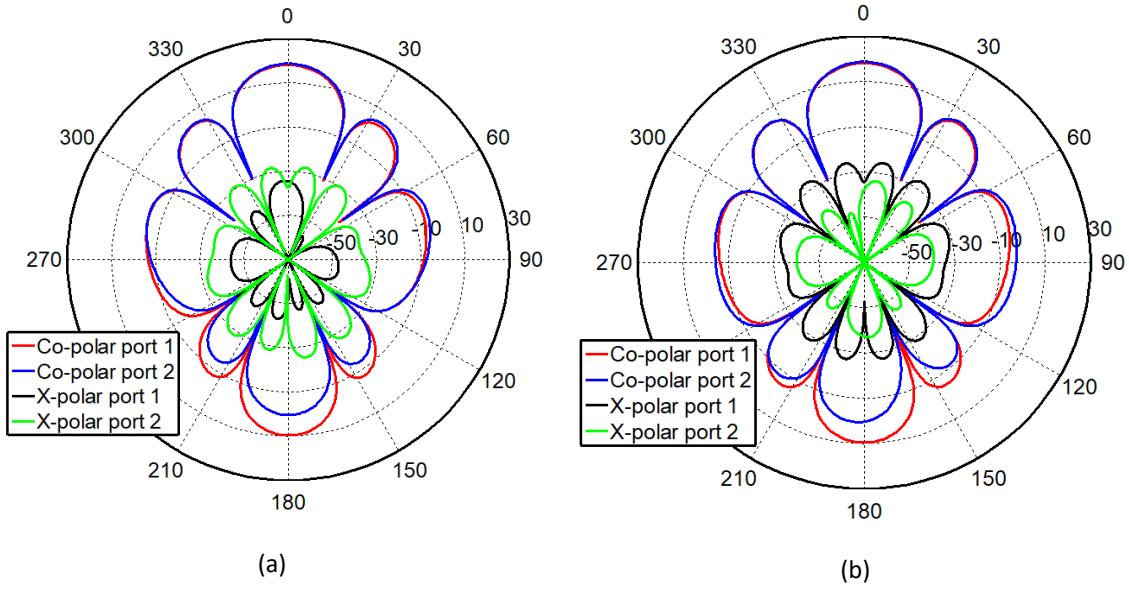

Figure 5. 23 (a) E- and (b) H-plane of 4 × 4 Ka-band array antenna

Figure 5. 23 (a) and (b) show electric and magnetic field radiation pattern for the Ka-band 4 × 4 array antenna. From the electric field radiation pattern, a maximum gain of 19.56 dBi is found with 50 dB cross polarization level at 0°. Similarly, for the magnetic field, a gain of 19.54 dBi is found at 0°, with a cross polarization level of around 60 dB. This antenna has a decent amount of back-lobe radiation which can be improved by implementing a back reflector which improves the front-to-back lobe ratio and is discussed in the later part of this chapter.

5.5.3 8 × 8 Array

The same design technique adopted for designing the 2 × 2 and 4 × 4 array is used again. The challenge of designing 8 × 8 array is its greater number of feed lines in between two adjacent elements. If two microstrip lines are too close to each other, mutual coupling between the lines can affect the radiation parameter and overall antenna efficiency. There is nothing much to do about this without sacrificing the simplicity of the design, but adequate effort is given to ensure maximum spacing between two adjacent microstrip feed lines. The design of the 8 × 8 array is also performed using CST MW Studio 2017. It is similar to the design of the L-band array shown in Figure 5. 11 The distance between two adjacent elements is decided to be 0.7λ to avoid grating-lobe and optimization.

5.5.3.1 Simulation result

Simulation was run using CST MW Studio 2017 after optimizing the design by tweaking the feed network path and parameter. The result after setting the design environment is presented in this section.

In Figure 5. 25, all S-parameter results are shown in the same figure. S11 and S22 results show very good return loss at the resonant frequency (37 GHz). Port-to-port isolation or S21 and S12 are also around -40 dB throughout the spectrum. The bandwidth is found around 2 GHz MHz

though S11 and S22 do not follow each other but covering the resonant frequency. S-parameter result overall shows very good matching and minimum coupling.

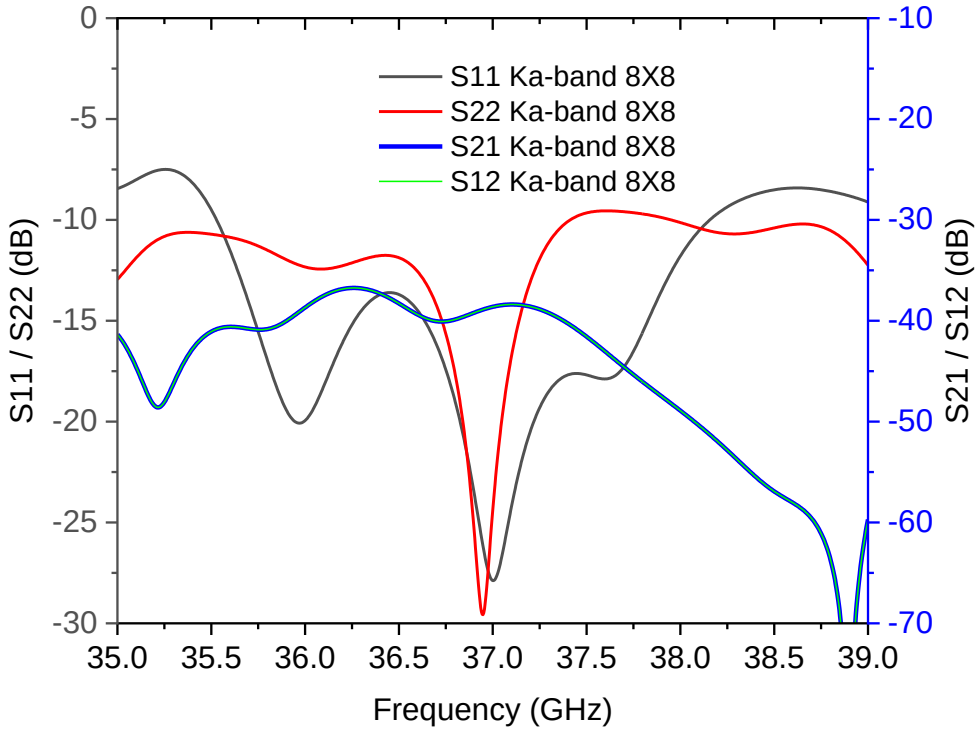

Figure 5. 25 S-parameter result for Ka-band 8 × 8 array antenna

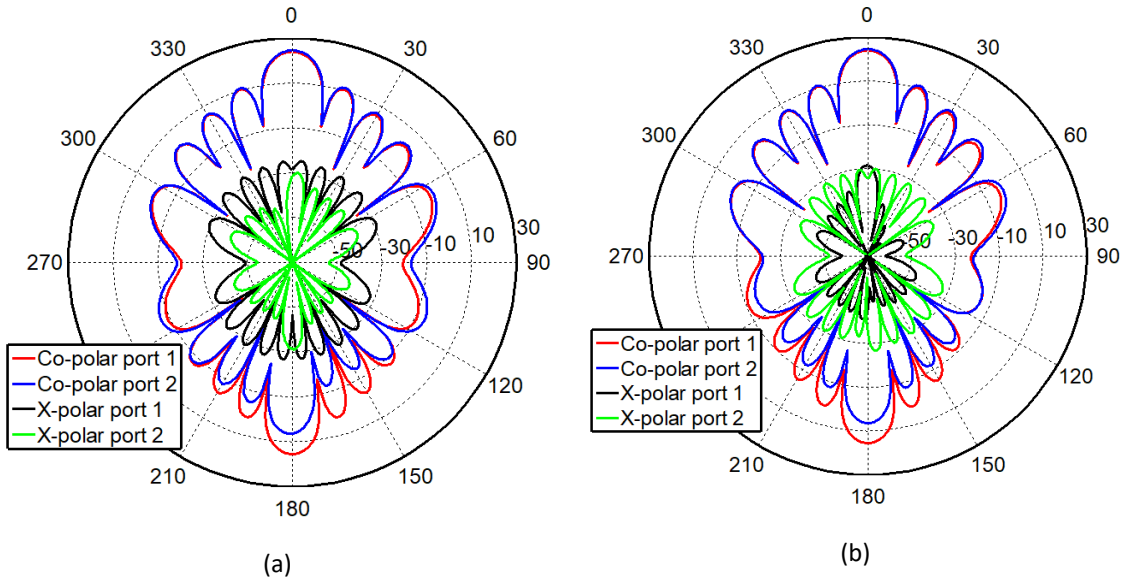

Figure 5. 24 (a) E- and (b) H-plane field of 8 × 8 Ka-band array antenna

Figure 5. 24 (a) and (b) show electric and magnetic field radiation pattern for the Ka-band 8 × 8 array antenna. From the electric field radiation pattern, a maximum gain of 26.5 dBi is found with 55 dB cross polarization level at 0°. Similarly, for the magnetic field, a gain of 26.2 dBi is found at 0°, with a cross polarization level of around 60 dB. Like the Ku-band array, this antenna also has a fair amount of back-lobe radiation which can be improved using a back-reflector which is discussed later.

5.6 Measurement result

After designing the array antennas for three separate bands and simulating in CST MW 2017, the designs are fabricated and measured. Simulation and measurement show similarity with some deviation due to fabrication and measurement imperfection. Not all simulated designs are fabricated and measured and included in this research. L-band array with 2 by 2 elements are included as 8 by 8 or 64 elements take big space and are expensive and already commercially available. Ku- and Ka-bands are fabricated with 8 × 8 elements and measured as they will be used in the further studies and, they prove the functionality of smaller array size such as 2 × 2 and 4 × 4 elements.

5.6.1 2 × 2 L-band antenna

A 2 × 2 L-band array antenna is fabricated and measured. Measurement is performed using Agilent's E8361A PNA series vector network analyser. S-parameter is performed using two channels and radiation pattern measurement is conducted in Monash University's Monash Microwave, Antennas, RFID and Sensors Laboratories (MMARS) anechoic chamber.

The fabricated and assembled L-band 2 × 2 array is shown in Figure 5. 26. The size of the array is bigger than the Ku- and Ka-band due to the lower frequency. Connectors are connected carefully so that they just touch the feed lines of respective polarizations.

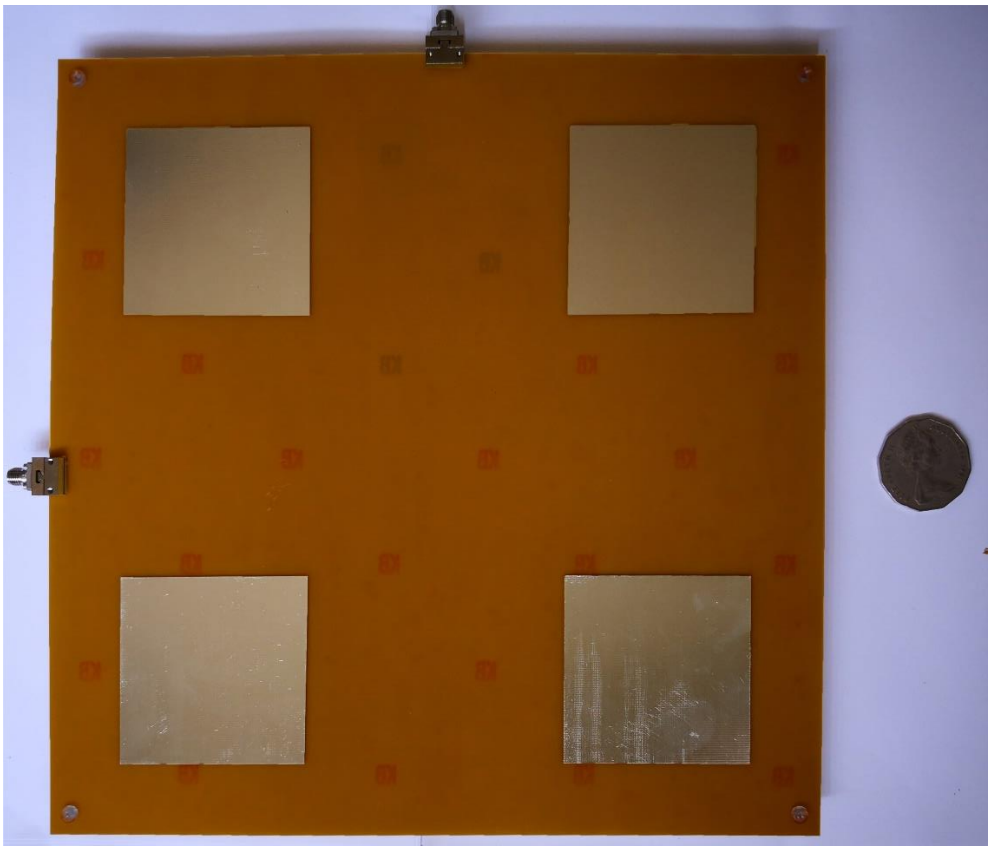

Figure 5. 26 L-band 2 × 2 array antenna with a 50 cent AUD for size comparison.

Figure 5. 27 shows the S-parameter measurement comparison with the simulation results presented in the previous sections. Both simulation and measurement result of S11 and S22 show similarity with a very minor deviation. For the isolation, the measurement shows around

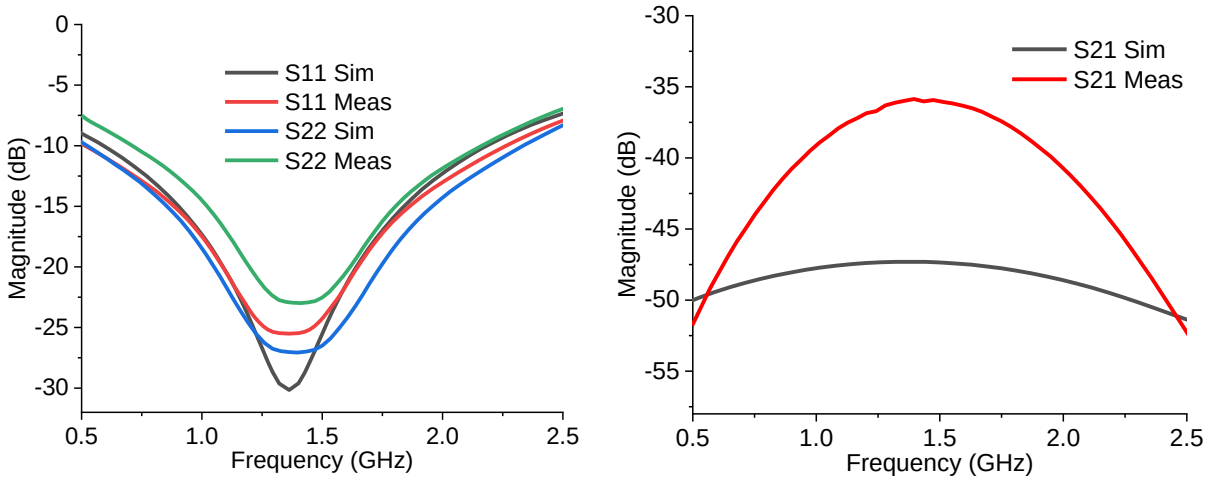

Figure 5. 27 Simulated and measured (a) reflection and (b) port-to-port isolation result for L-band 2 × 2 array antenna

10 dB deviation due to the fabrication and assembly error of the ports as the fabrication resolution only accounts for 0.1 mm accuracy. Overall, port-to-port isolation stays below -35 dB throughout the spectrum.

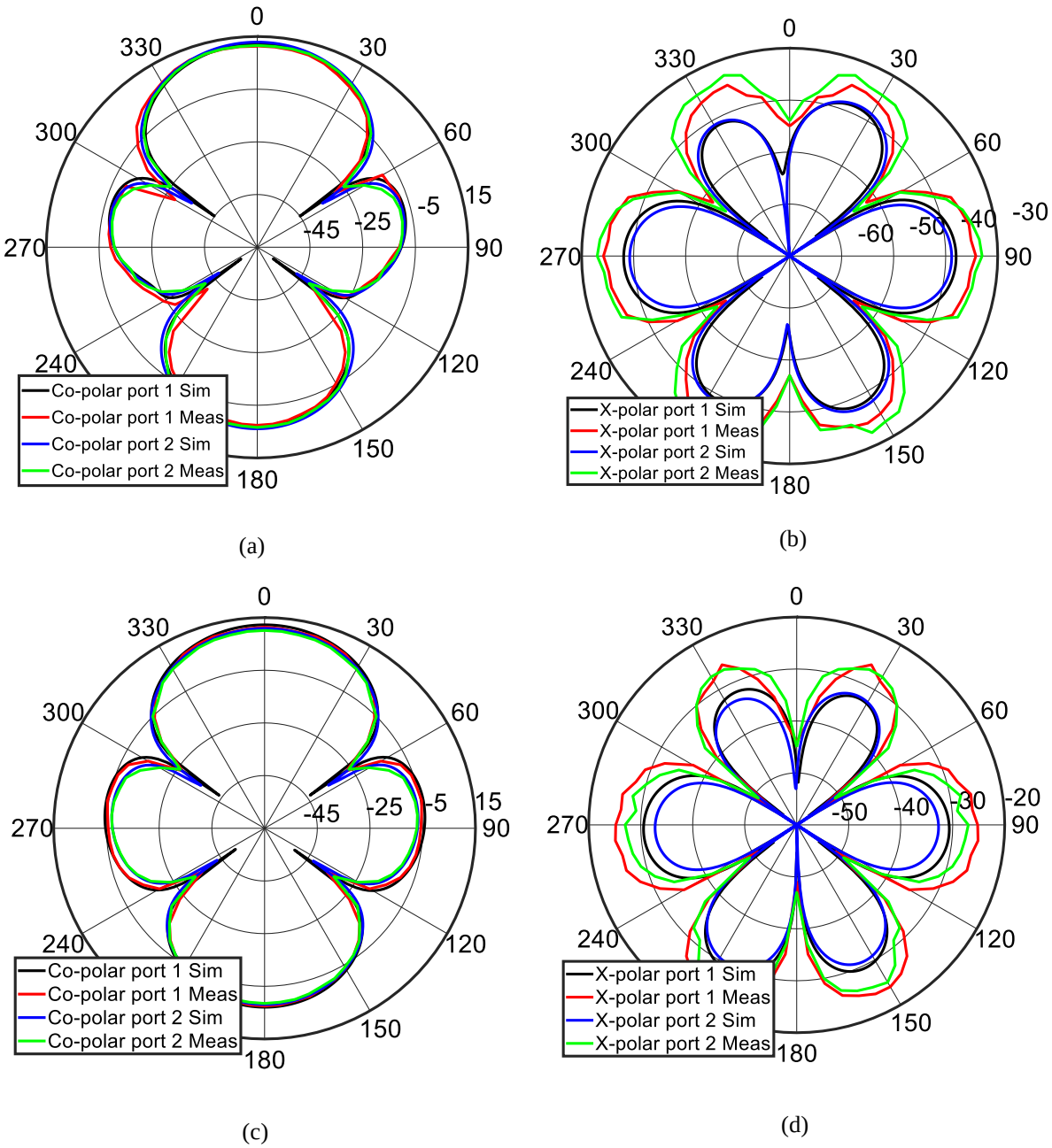

Figure continued to next page

Figure 5. 28 shows the simulation and measurement comparison between electric and magnetic field co and cross polarization result. In all cases, the measurement pattern follows the

simulation pattern very closely with some exception in the cross-polarization measurements as the cross-polarization level being very low difficult to measure.

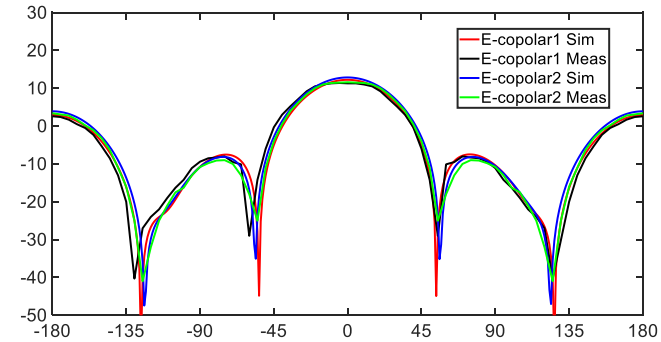

(e)

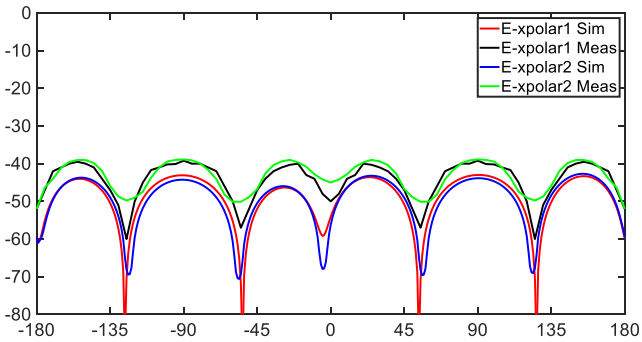

(f)

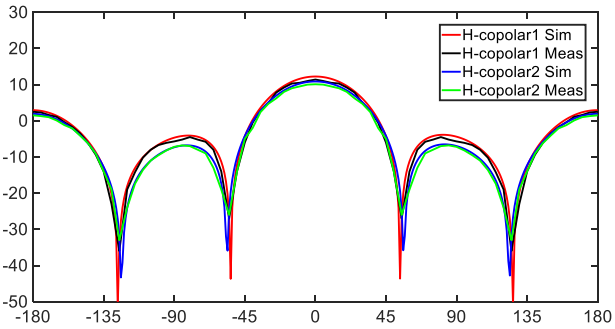

(g)

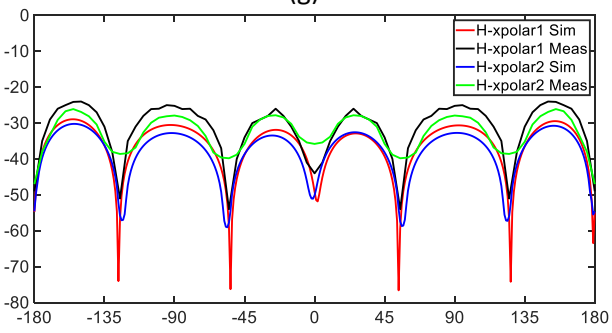

(h)

Figure 5. 28 Simulated and measured (a) E- plane co polar, (b) E- plane cross polar, (c) H- plane co polar and (d) H- plane cross polar radiation pattern for L-band 2 × 2 array antenna; (e), (f), (g) and (h) are line plots of (a), (b), (c) and (d).

5.6.2 8 × 8 Ku-band antenna

An 8 × 8 Ku-band array antenna is fabricated and measured after designing using CST MW Suit 2017. Measurement is performed using Agilent's E8361A PNA series vector network analyser. S-parameter results and radiation pattern is measured and plotted against the simulation result.

S-parameter results are shown in Figure 5. 30. S11 and S22 measured result shows well matched reflection coefficient below -18 dB in both ports. Port-to-port isolation measurement

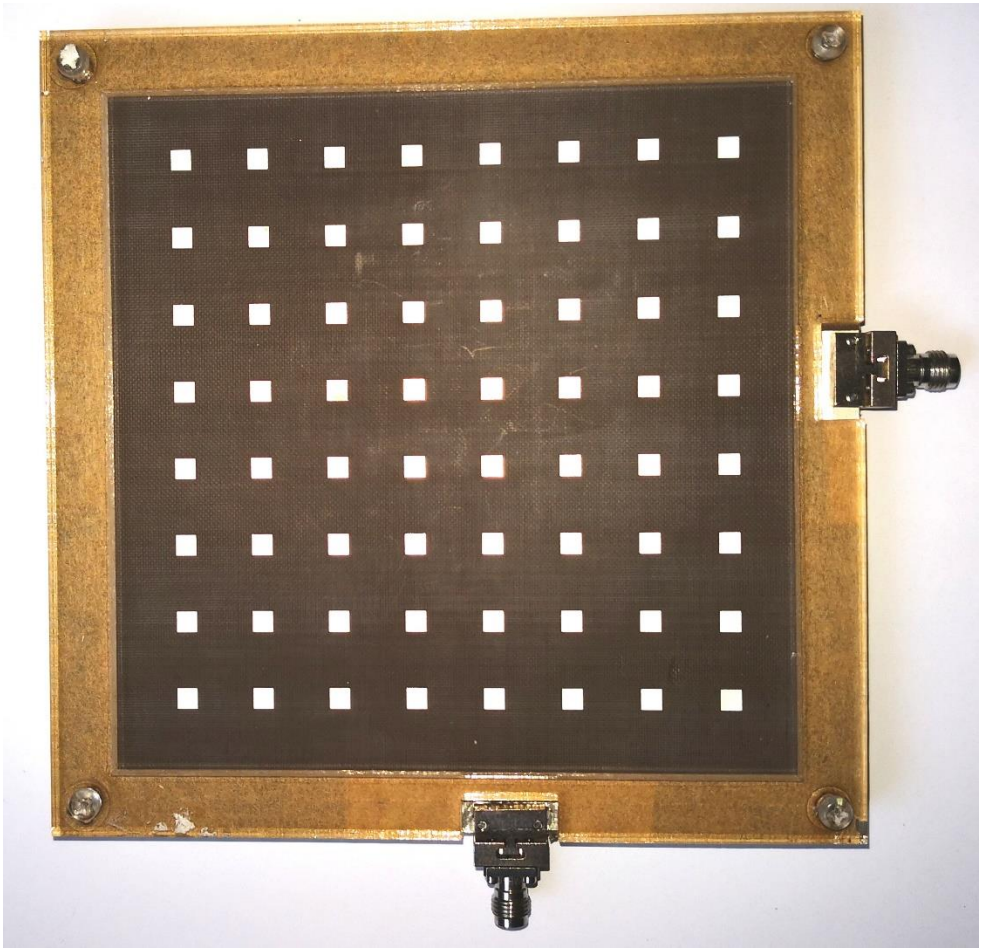

Figure 5. 29 Ku-band 8 × 8 array antenna after fabrication and assemble.

shows similar trend as the simulation result and the isolation is more than 50 dB in the resonant frequency and more than 40 dB throughout the spectrum.

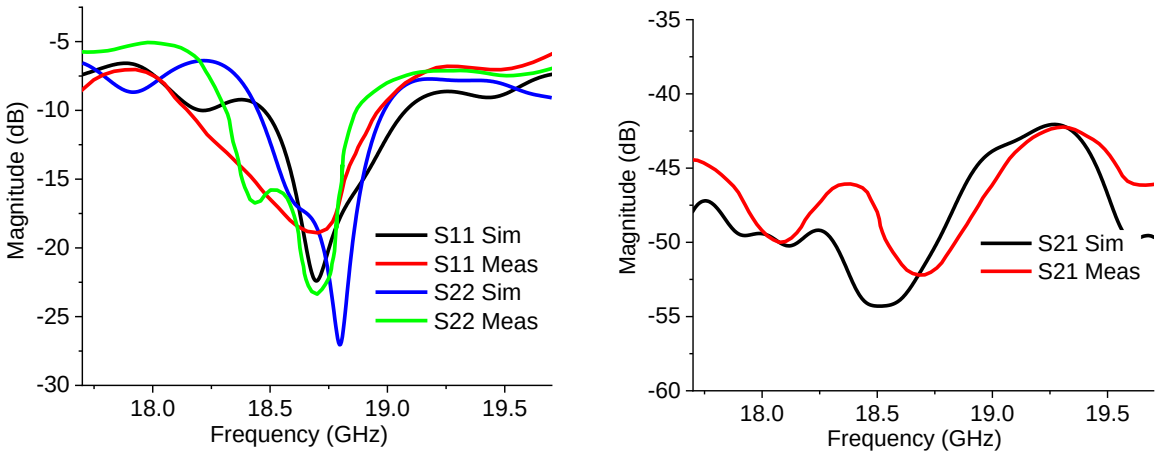

Figure 5. 30 Simulated and measured (a) reflection and (b) port-to-port isolation result for Ku-band 8 × 8 array antenna

Figure 5. 31 shows the radiation pattern simulation versus measurement. Figure 5. 31 (a) shows the electric field co-polar simulation and measurement result for both ports. The main-lobe magnitude of the measured result is around 25 dB for both polarizations, and the pattern follows the simulation pattern closely. Electric field cross-polarization pattern of the simulation and

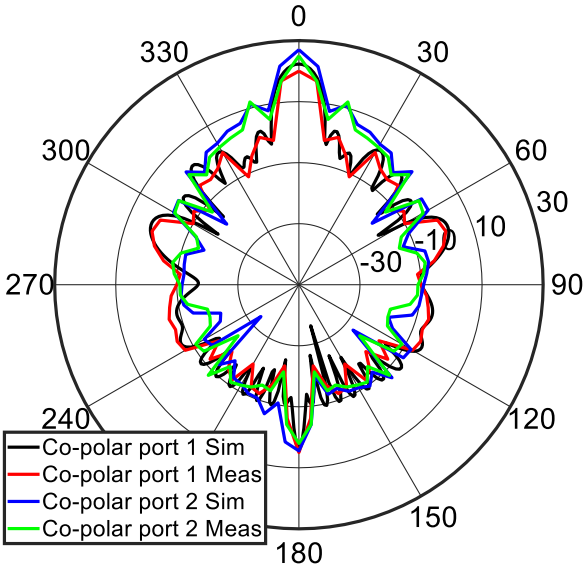

(a)

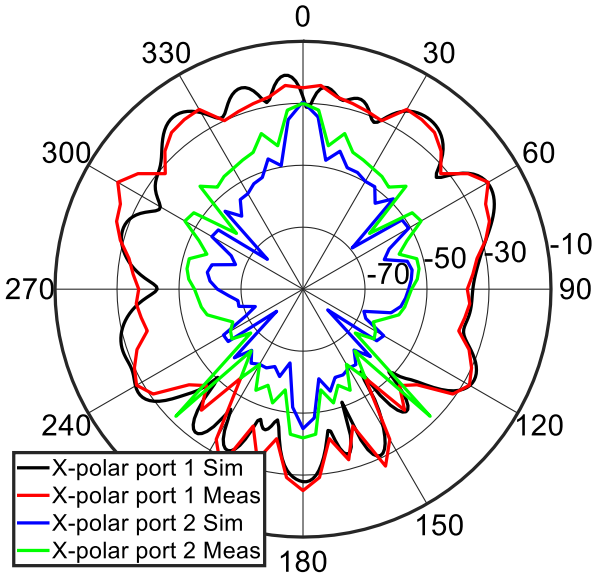

(b)

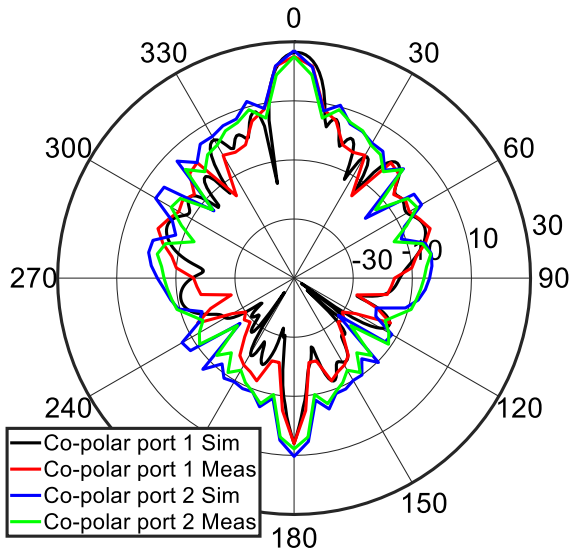

(c)

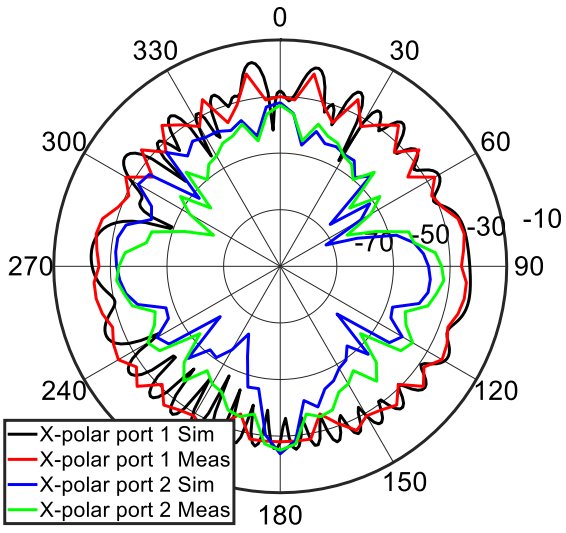

(d)

Figure 5. 31 Simulated and measured (a) E- plane co-polar, (b) E- plane cross-polar, (c) H- plane co-polar and (d) H- plane cross-polar radiation pattern for Ku-band 8 × 8 array antenna

measured result is shown in Figure 5. 31 (b), which shows around -30 dB cross-polarization which makes 55 dB less compared to the main lobe of the electric field at 0°.

Magnetic field co- and cross-polar pattern of the simulation and measured result is shown in Figure 5. 31 (c) and (d). For the co-polar radiation pattern, the magnitude at 0° is again around 25 dB for both polarizations and follow the simulated pattern closely. Similarly, the cross-polarization level at 0° is more than 55 dB less than the co-polarization level.

5.6.3 8 × 8 Ka-band antenna

An 8 × 8 Ka-band antenna is fabricated and measured. Being the highest frequency in this study, meticulous measures were taken for the measurement procedure. Agilent's E8361A PNA series VNA is used to measure the S-parameters and in-house anechoic chamber is used to measure the radiation pattern. The assembled Ka-band array antenna is shown in

Figure 5. 32

Figure 5. 33 shows S-parameter results for the 8 × 8 Ka-band array. S11 and S22 measured result shows well matched reflection coefficient below -20 dB in both ports. Also, measured

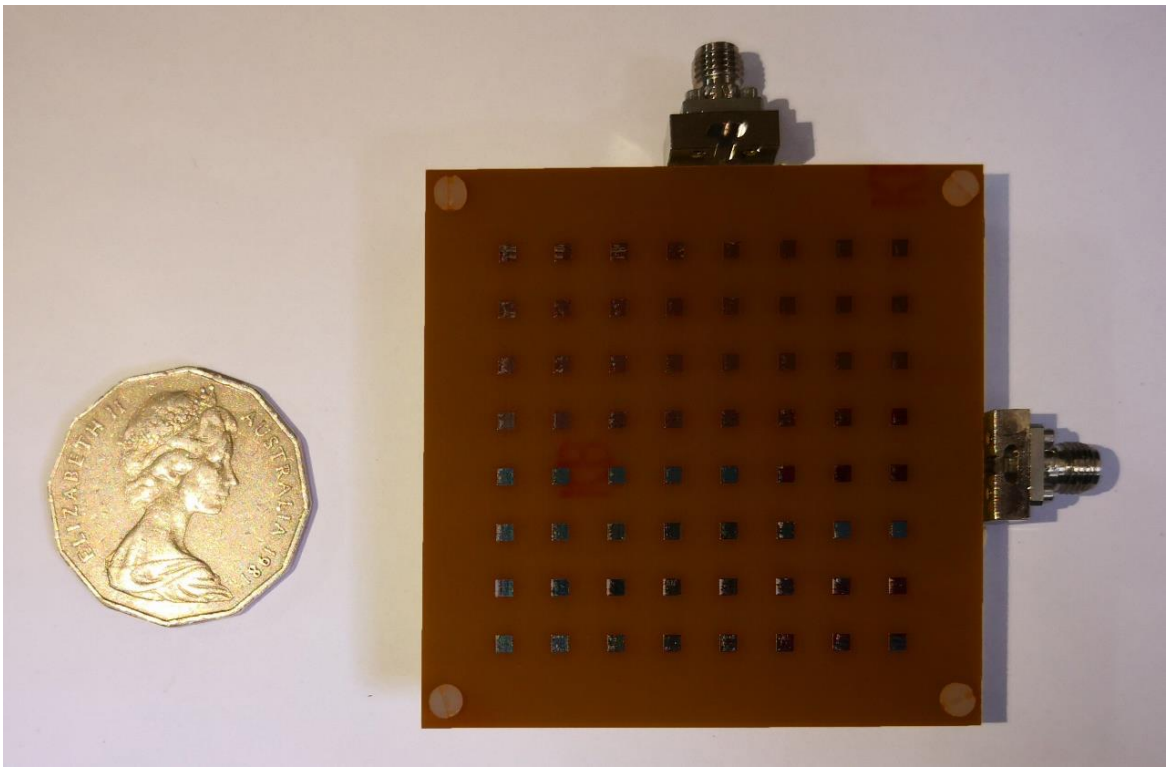

Figure 5. 32 Ka -band 8 × 8 array antenna with a 50 cent AUD for size comparison.

result follows the simulation result trend. Port-to-port isolation measurement shows similar trend as the simulation result and the isolation is more than 35 dB in the resonant frequency and more than 30 dB throughout the spectrum.

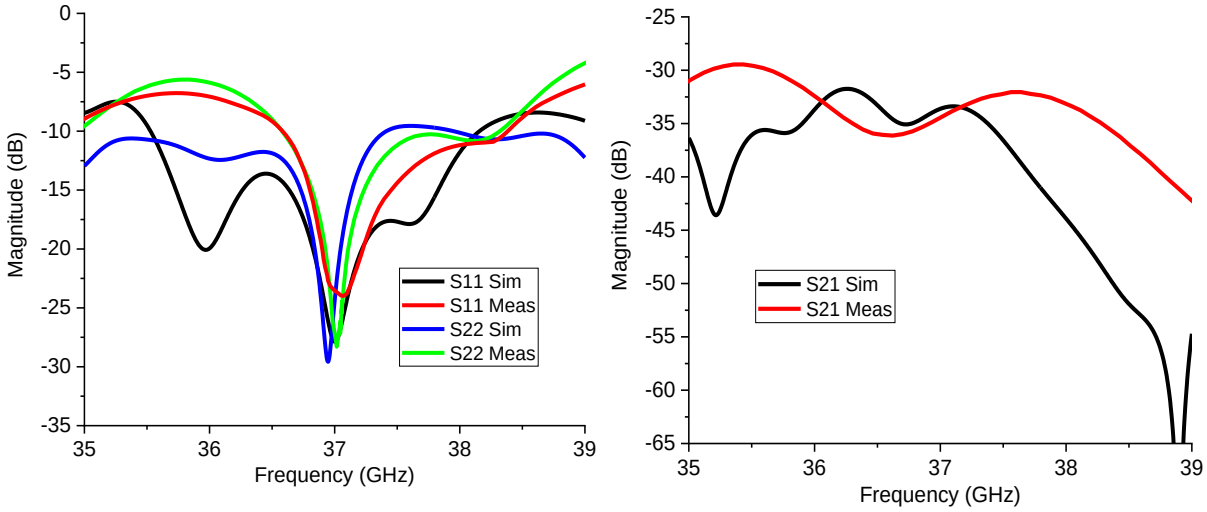

Figure 5. 33 Simulated and measured port-to-port isolation result for Ka-band 8 × 8 array antenna

The reason for the relatively low isolation difference than the Ku-band is, Ka-band being the highest frequency band in this research, has the smallest size hence physical isolation between ports is also very small.

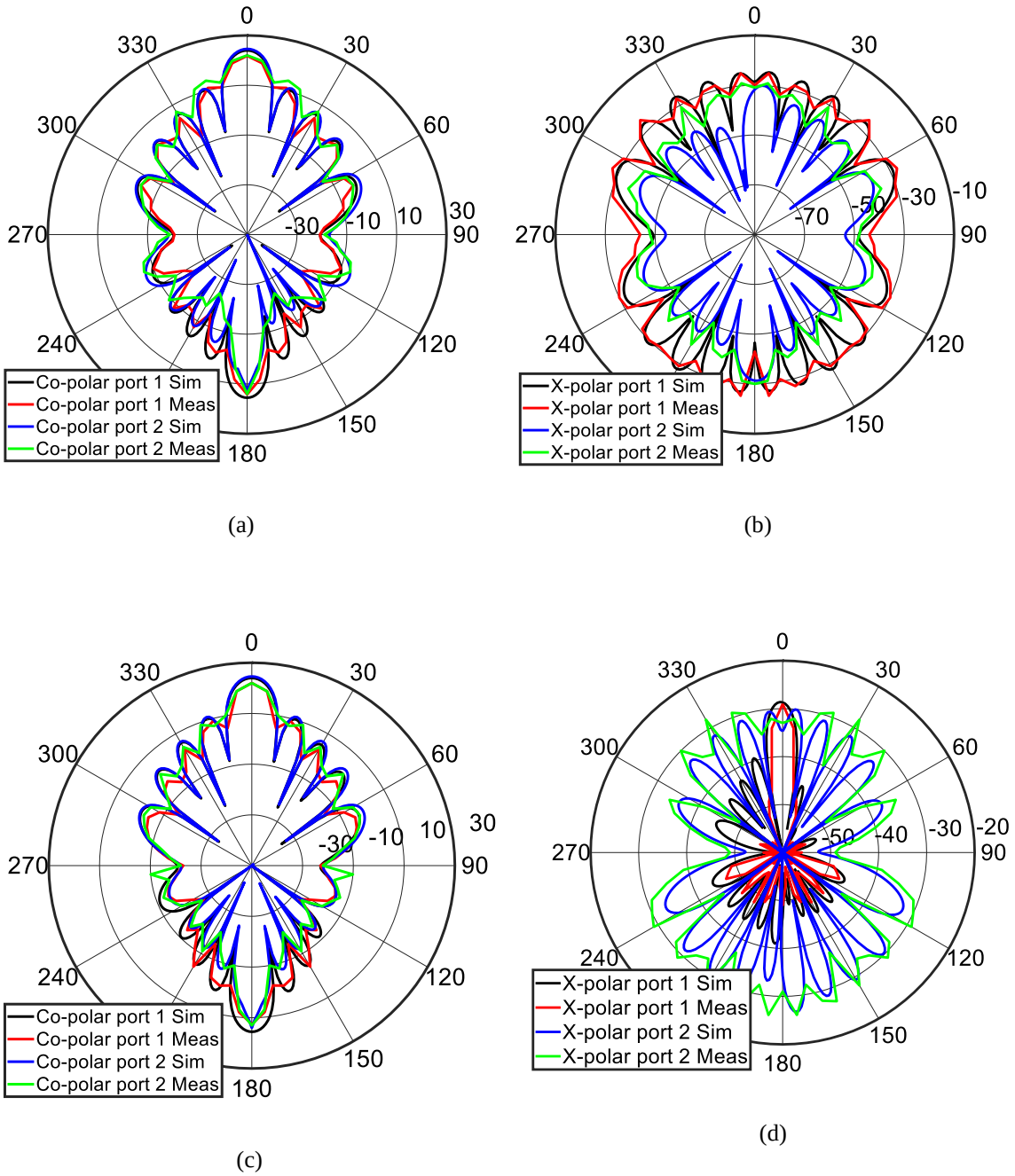

Figure 5. 34 Simulated and measured (a) E- plane co polar, (b) E- plane cross polar, (c) H- plane co polar and (d) H- plane cross polar radiation pattern for Ka-band 8 × 8 array antenna

Figure 5. 34 shows the radiation pattern simulation versus measurement. Figure 5. 34 (a) shows the electric field co-polar simulation and measurement result for both ports. The main-lobe

magnitude of the measured result is around 26 dB for both polarizations and the pattern follows the simulation pattern closely. Electric field cross-polarization pattern of the simulation and measured result is shown in Figure 5. 34 (b), which shows around -30 dB cross-polarization which makes 55 dB less compared to the main lobe of the electric field at 0°. Magnetic field co- and cross-polar pattern of the simulation and measured result is shown in Figure 5. 34 (c) and (d). For the co-polar radiation pattern, the magnitude at 0° is again around 26 dB for both polarizations and follow the simulated pattern closely. Similarly, the cross-polarization level at 0° is more than 55 dB less than the co-polarization level.

5.7 Use of back-reflector to suppress back-lobe radiation

Microstrip antenna arrays, in a linearly or dual polarized configuration, exhibit high front-to-back lobe radiation due to asymmetric E-plane radiation pattern [229-231]. Different complex techniques have been used to improve the efficiency such as using ring-shape director [232], with smaller ground [233], with photonic bandgap back shield [234], using a semitransparent ground plane [235], planar soft surface [236]. These techniques are complex to manufacture and implement and suitable for systems that require very wide bandwidth. In this case, where bandwidth requirement is not very wide, simpler techniques, such as complementary back reflector, where a substrate is etched to complement the patch sizes to improve front-to-back ratio of the radiation [237], can be used. Theoretically just a metal slab placed at $\lambda/4$ distance makes the back-lobe to travel 180° electrical path to enhance the front or main lobe by suppressing the back-lobe radiation [238].

In this study, a substrate is etched completely to reflect the back-lobe towards the main lobe at 180° by carefully positioning at $\lambda/4$ distance from the ground plane. The requirement of the front-to-lobe ratio is 20 dB to ensure radiation not being recognised from the back plane instead of the front plane.

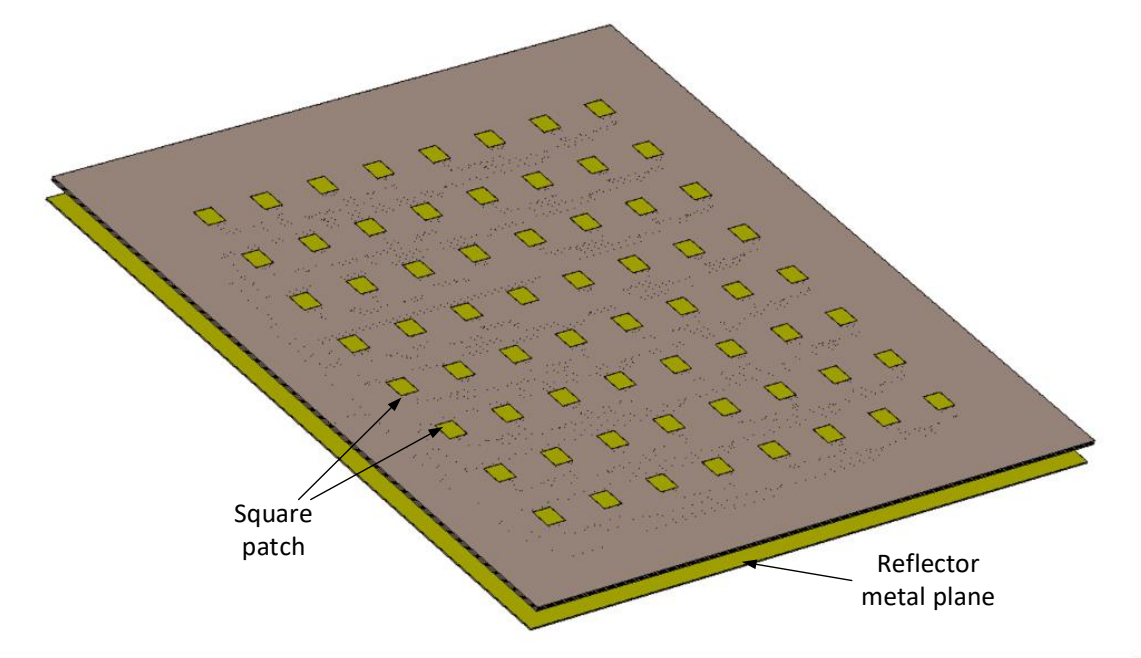

(a)

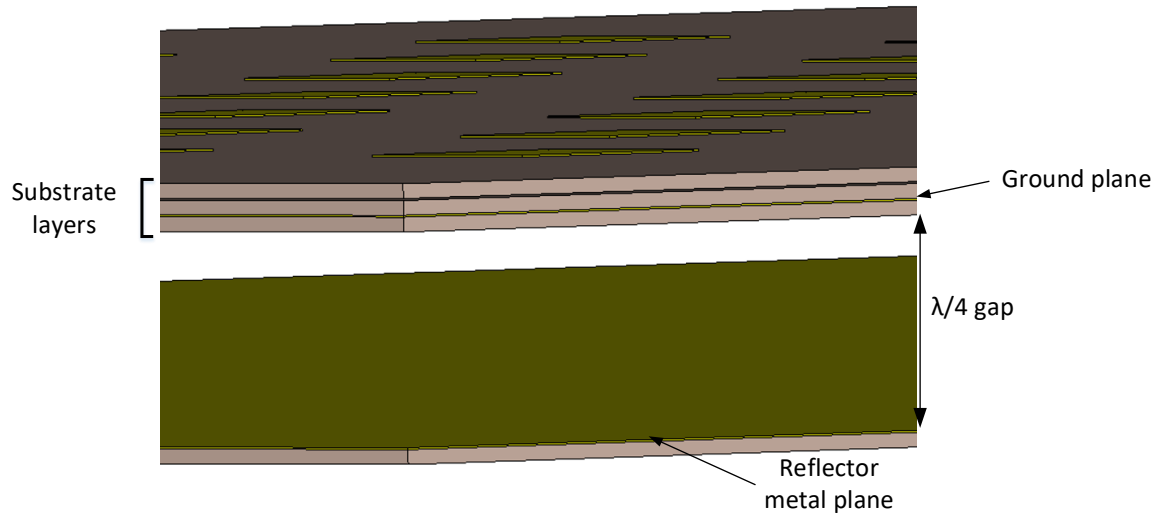

(b)

Figure 5. 35 (a) 3-d view, (b) layer view of Ku-band array with metallic reflector to suppress back-lobe radiation

In Figure 5. 35, the idea of the suppressing the back-lobe is shown. For Ku-band the wavelength is 16.04 mm which is equivalent to 360° in electrical degrees. Back-lobe radiation has 180° difference than the main-lobe. If the metal plate can be place 90° electrical angle apart then the radiation coming from the back-lobe will have to travel 90° and the another 90° back towards the main-lobe. So, another layer of substrate is fully etched and placed 4mm further from the

ground plane. Thus, the back-lobe is suppressed, and it adds to the main-lobe radiation. The simulation result with metallic reflector is shown in

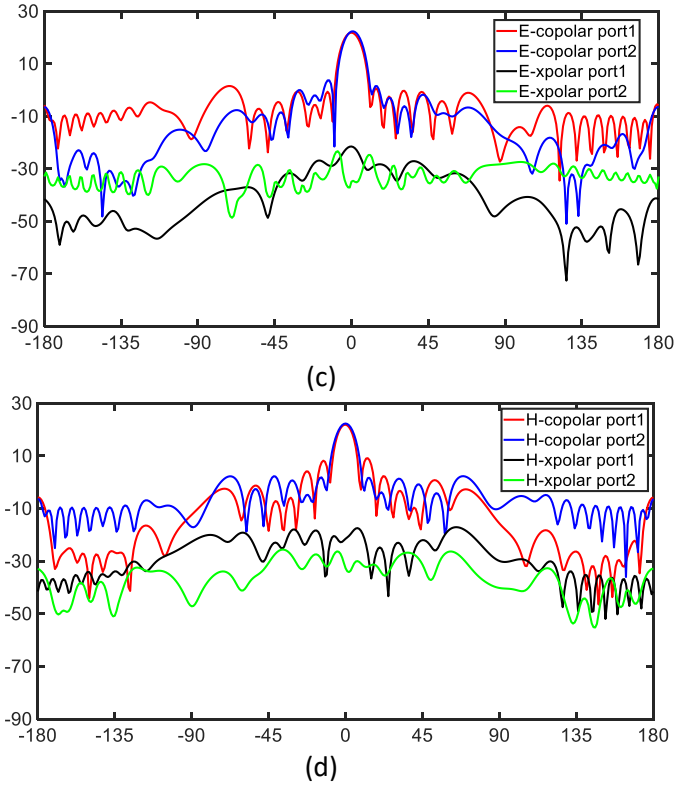

Figure 5. 36, where a front-to-back lobe ratio of around 25 dB is observed, proving the validity of this design.

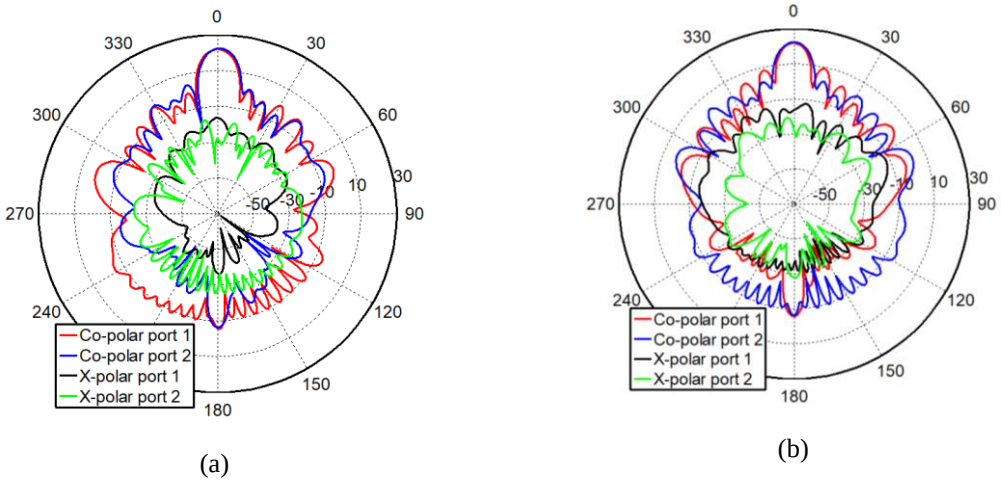

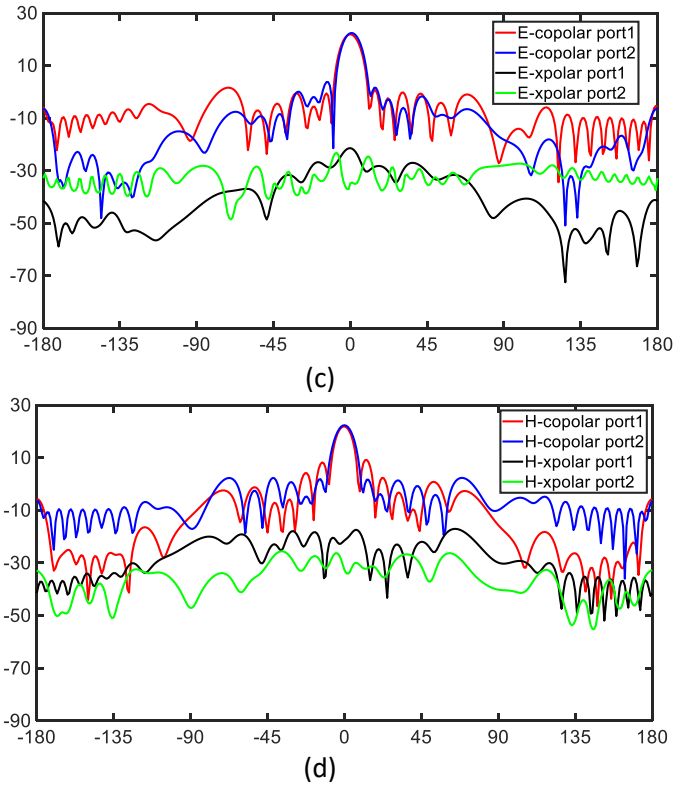

Figure 5. 36 Simulation result of the (a) E- and (b) H-plane radiation pattern of Ku-band array with metallic reflector to suppress back-lobe radiation, (c) and (d) are the line plots for (a) and (b)

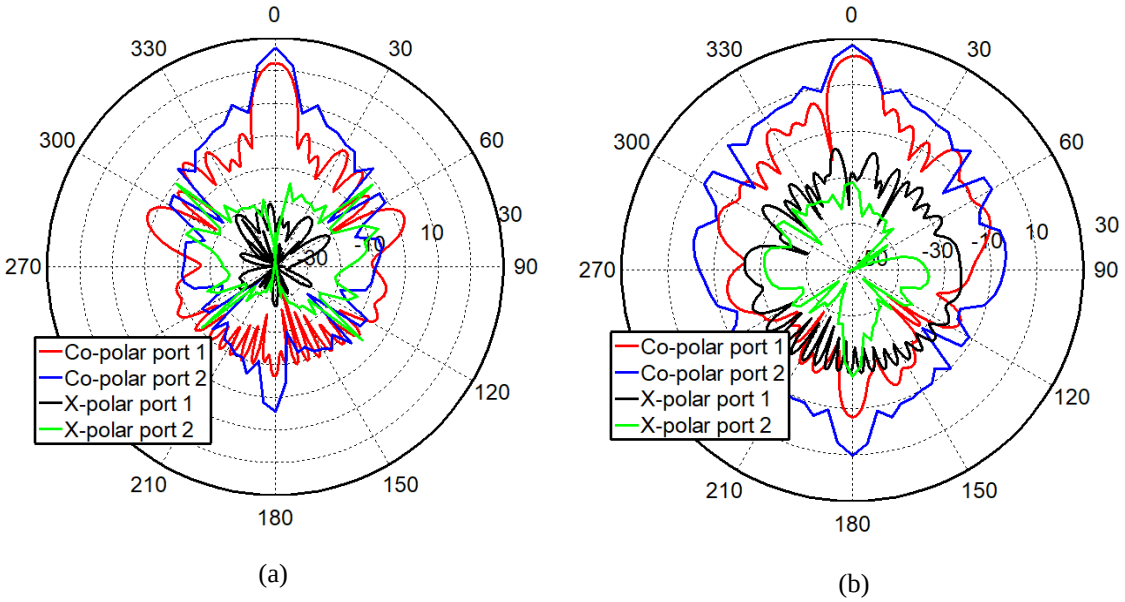

Figure 5. 37 (a) E- and (b) H-plane radiation pattern of Ku-band array with and without metallic reflector to suppress back-lobe radiation

Figure 5. 37, shows the measurement result of electric and magnetic field radiation pattern with and without back reflector. From the figure it can be seen that the back-lobe is suppressed, and main-lobe magnitude is enhanced with inclusion of the back reflector.

5.8 Conclusions

In conclusion, this chapter reviews the literature of the array antenna followed by the theory of the array antenna, simulation and measurement of different array structure of three different bands. The importance of the array antenna is unique as a greater number of array element can increase in the gain of the antenna while still maintain planar shape. Different feeding techniques can be implemented in designing the array antenna, but this chapter outlies the base of the multiband antenna which will be used as a radiometer to work in more than one band. Thus, aperture couple feeding techniques is chosen for the array configuration as the feed layers are in separate layers, aperture couple structure provides advantage for designing multiband stacked design with improved isolation, bandwidth and gain.

The requirements of the array antenna to be used in radiometer are the gain, the isolation, the cross-polarization level and size and shape. The gain of the array antenna must be very high to receive passive signal transmitted from the earth surface. In this chapter, both Ku-band and Ka-band 8 × 8 array antenna displayed a gain over 22 dBi. As the antenna must be a dual-polarized, the isolation between ports needs to be higher. This is an essential design requirement, otherwise signal received form one port can interfere with the signal being received at the other. In this chapter, the array antennas discussed have an isolation over 35 dB in all three frequency bands. For radiometer, to explain the cross-polarization, co-polarized pattern is the identical transmit and receive polarization states such as horizontal – horizontal (HH) and vertical – vertical (VV). Cross polarization level is measured by measuring the transmitting in one

polarization state and receiving in the orthogonal polarization state. Cross polarized radiometer channels are therefore HV and VH. The cross-polar level should be very low for radiometer antenna. In this chapter, the array antenna designed have cross-polarizations of over 30 dB meaning a suitable cross-polar level for the radiometer.

The main challenge of this chapter was to overcome the feeding of Ku- and Ka-band antenna and assemble them accurately before measuring. The accomplishments of this chapter give enthusiasm to study further into the beam shaping algorithm and finally multiband antenna structure which is discussed in the next chapter.

6 Array Analysis

6.1 Overview

After designing the array antenna, it is time to analyse the shape of the beam of the array. In the previous chapter where a different number of the elements array antenna for three different frequencies are discussed, beam shape was not analysed. Feed network provides excitation to individual elements of the array. In the previous chapter, all element antennas in the array configuration received the same amount of excitation making the uniform distribution of power. The problem with uniform excitation is the side-lobe levels are only approximately 13 dB less than the main-lobe, which can be proven theoretically [79]. For the radiometer antenna, the side-lobe level must be below 25 dB than the main-lobe. Beam shaping of an antenna array is a spatial filtering technique that filters out the receiving signals from all other directions except the desired direction. This filtering out procedure is done by attenuating signals from all the other directions. Beam shaping technique has been applied in various areas of signal processing ranging from radar, microphone arrays, sonar, radio astronomy, medical diagnosis and treatment, seismology, to communications [239-245].

An antenna array is a set of antennas placed systematically to send or receive signals that require more power than a single element antenna. The relative distance to each other of the element, gain of the single element, excitation received, and relative phase of the elements determine the total radiation pattern of the array configuration. In an antenna array, depending on the requirement, different elements receive different excitations. If the centre elements receive more excitations than the corner elements, then the side lobe level will be lower than the main-lobe. The distance between elements is another parameter that changes the beam

Chapter Overview

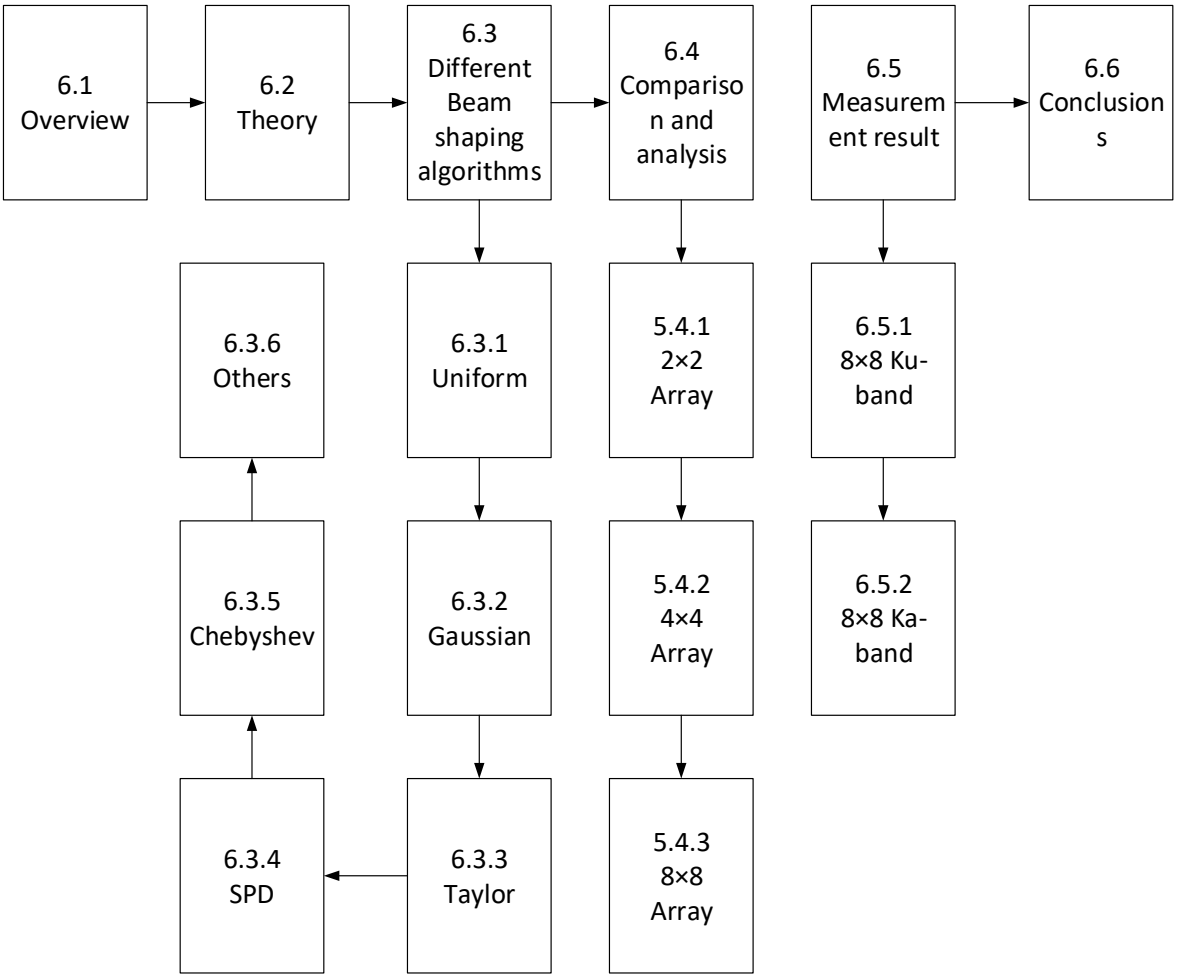

pattern. If the distance between antenna elements are not even, designing becomes complicated. Thus, the only even distance between adjacent elements is considered. If the distance is too close to each other, then the feed network or excitation becomes complex as the feed lines, and even antenna patches can touch each other.

On the other hand, if the distance between two adjacent elements is more than the wavelength, then grating-lobe is seen in the radiation pattern. Grating-lobes can be as predicted by the pattern multiplication theorem. When the array spacing is too larger side-lobes equal to the main-lobe is seen. Grating-lobe is an unwanted situation for the beam pattern. To avoid grating-lobe, the distance between elements should not be too large. To avoid grating-lobe and also avoid designing elements too close to each other, it is required to design elements at a distance

less than the wavelength and more than half the wavelength. Hence an inter-element distance of 0.7λ is chosen. Different beam shaping algorithms such as Gaussian, Chebyshev's, Taylor's, SPD (staircase power distribution) methods are discussed and compared against each other to find the optimized distribution for the array antenna.

6.2 Theory

By definition, beam shaping algorithm is the art or design of the antenna array system, where each antenna receives/transmits different power to form a collective beam pattern. In equation,

For N-element linear array with uniform amplitude and spacing, the array factor for this system [79]-

$$AF = 1 + e^{j(kdcos\theta+\beta)} + e^{j2(kdcos\theta+\beta)} + \cdots e^{j(N-1)(kdcos\theta+\beta)} \quad \ldots\ldots\ldots\ldots 1$$

Or, we can write in summation form in-

$$AF = \sum_{n=1}^{N} e^{j(n-1)(kdcos\theta+\beta)} \quad \ldots\ldots\ldots\ldots 2$$

For this study, the spacing between adjacent elements is chosen to be equal and half of the wavelength. Only the amplitude is varied during the shaping process. The new equation for array factor becomes as –

$$AF = \sum_{n=1}^{N} \delta_n e^{j(n-1)(kdcos\theta+\beta)} \quad \ldots\ldots\ldots\ldots 3$$

For planar array this equation becomes-

$$AF = I_0 \sum_{m=1}^{M} e^{j(m-1)(kd_x \sin\theta \cos\phi + \beta_x)} \sum_{n=1}^{N} e^{j(n-1)(kd_y \sin\theta \sin\phi + \beta_y)} \quad \ldots\ldots\ldots\ldots 4$$

Depending on the distribution, excitation coefficient changes and hence changes the radiation pattern. In this paper, the effect of different distribution on side-lobe level, beamwidth, beam efficiency at a different number of arrays in different beam pointing angle is discussed and compared.

6.3 Different beam shaping algorithms

6.3.1 Uniform Distribution

Uniform distribution is the simplest example of power distribution among all. In this distribution, all the elements are fed with uniform or the same power. So, all the coefficients of the equation become one, and the array factor looks like the following equation.

$$AF = \sum_{n=1}^{N} e^{j(n-1)(kdcos\theta + \beta)} \quad \ldots\ldots\ldots\ldots 5$$

For planar array this equation can be extended and it becomes-

$$AF = I_0 \sum_{m=1}^{M} e^{j(m-1)(kd_x \sin\theta \cos\phi + \beta_x)} \sum_{n=1}^{N} e^{j(n-1)(kd_y \sin\theta \sin\phi + \beta_y)} \quad \ldots\ldots\ldots\ldots 6$$

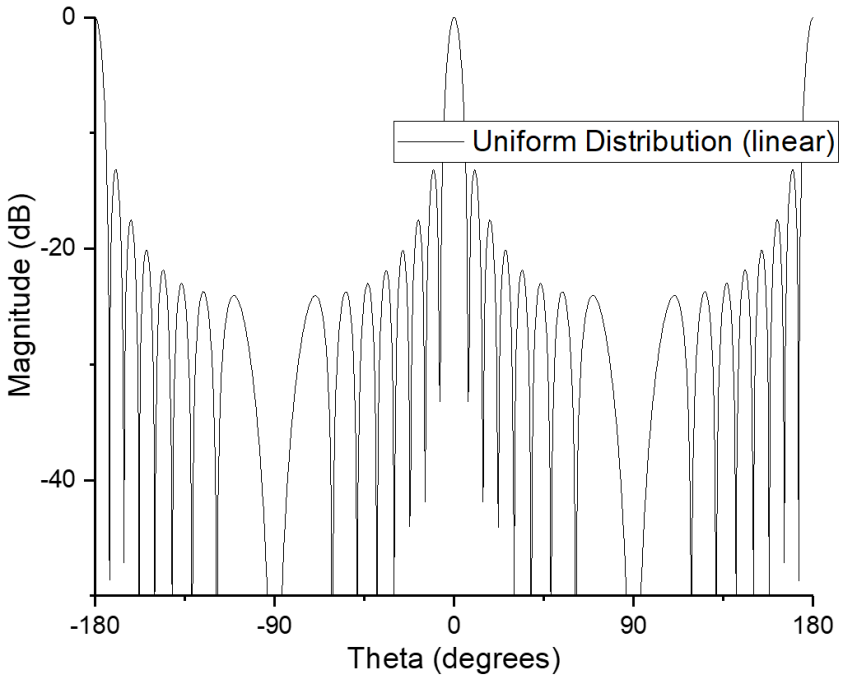

Figure 6. 1 Radiation pattern of the array factor for 25 element linear array with uniform excitation

Theoretically, the uniform distribution results in 13 dB sidelobe level [79]. For 25 elements placed in a linear array, the array factor representation in graph looks like Figure 6. 1. For

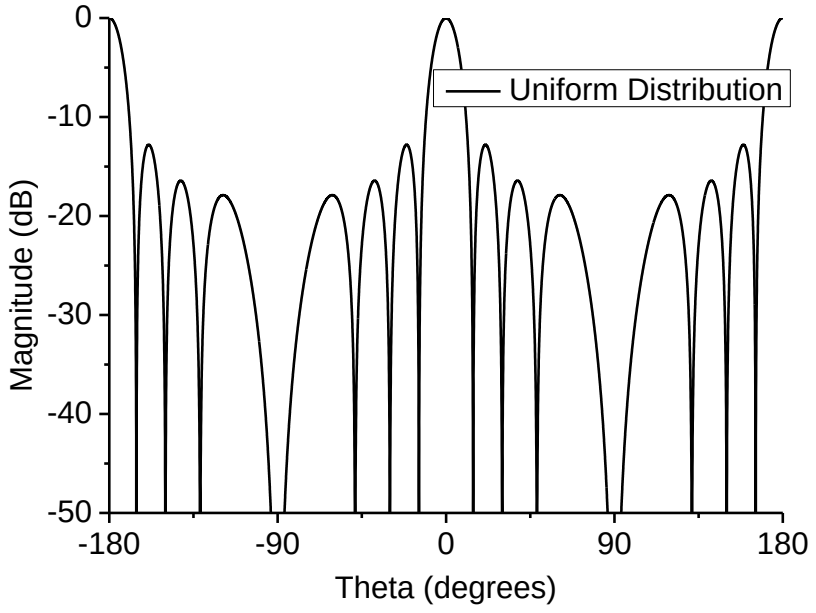

Figure 6. 2 Radiation pattern of the array factor for 8 × 8 element planar array with uniform excitation

planar array configuration, placed 0.7 λ apart from each other in an 8 × 8 array, the array factor is shown in Figure 6. 2.

It is worth mentioning that the greater number of elements, the higher order becomes the equation for the array factor and hence, more ripple in the array factor. Theoretically, the side-lobe level of -13 dB can be observed in the figures to validify the concept.

6.3.2 Gaussian Distribution

The Gaussian or normal distribution is one of the most common distributions in various scientific studies [246]. The mathematical form of this distribution for calculating excitation coefficients can be expressed as-

$$y(x) = a \exp\left(-\frac{(x-\mu)^2}{2\sigma^2}\right) \qquad \text{.....7}$$

Where a = peak value which is unity in this case. μ = mean which determines the position of the graph, in this case, which is centre or zero. σ = standard deviation determines the width of

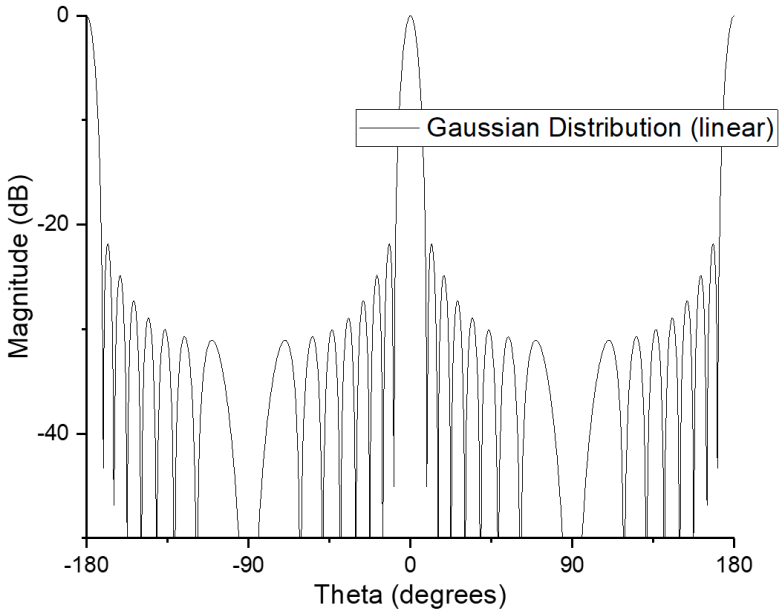

Figure 6. 3 Radiation pattern of the array factor for 25 element linear array with Gaussian excitation

the graph and in this case a crucial parameter to determine the difference between the maximum and minimum power level.

For a planar array, it can be written as –

$$f(x,y) = Aexp\left(-\left(\frac{(x-x_0)^2}{2\sigma_x^2} + \frac{(y-y_0)^2}{2\sigma_y^2}\right)\right) \quad \text{.....8}$$

Where, the 'x' and 'y' subscripts stand for the x- and y-axis directions.

Using practical power ratio between the maximum and the minimum excitations so that the feed line thickness is realizable and practical, and number of antennas, the excitation coefficients are determined. The ratio between the maximum and minimum power is set to be 10 dB. The array factor plot for 25 linear elements array is shown in Figure 6. 3. For a planar array of size 8 × 8, the array factor is shown in Figure 6. 4.

In both figures, it can be seen that the side lobe level is well below -20 dB, which was obtained by providing the maximum power to the middle or centre elements, and the elements at the edges receive minimum excitation.

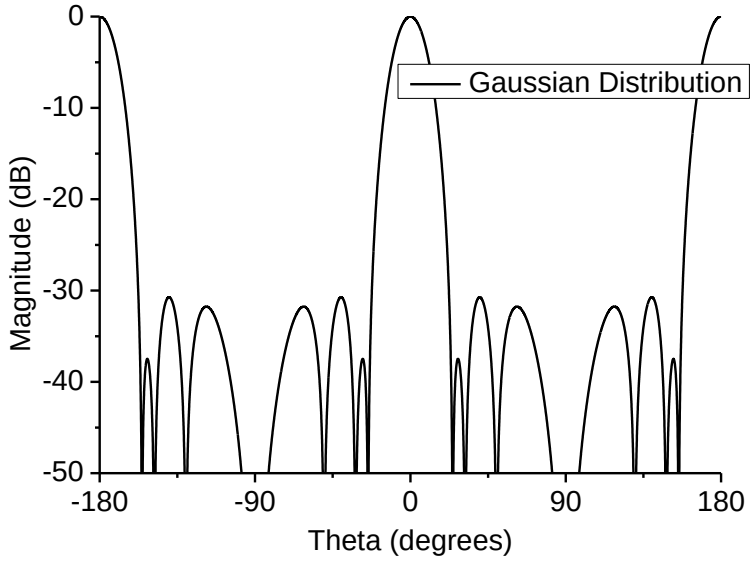

Figure 6. 4 Radiation pattern of the array factor for 8 × 8 element planar array with Gaussian excitation

6.3.3 Taylor Distribution

For engineering the sidelobes, it is necessary to taper the illumination from the centre to the edges. In 1955 Taylor described a system which is known as Taylor illumination [247]. The normalized array factor can be written as [163, 248]-

$$F(u) = \frac{\sin \pi u}{\pi u} \frac{\prod_{n=1}^{\bar{n}-1}\left[1 - \frac{u^2}{\sigma_p^2\left(A^2 + \left(n - \frac{1}{2}\right)^2\right)}\right]}{\prod_{n=1}^{\bar{n}-1}(1 - u^2/n^2)} \qquad \text{.....9}$$

Where, $\sigma_p =$ Taylor parameter as a function of side lobe ratio and the boundary of the region of uniform side lobes. $A =$ peak of the signal $\bar{n} =$ boundary of the region of uniform side lobes and $u = \frac{2a}{\lambda}\sin\theta$ where $2a$ represents the length of the array. In this study, length is chosen in a way that corresponds to the half-wavelength spacing between adjacent elements.

For an odd number of the planar array, the weights for a 2M+1 number of rows and 2N+1 number of columns can be written as –

$$A_{n,m} = \sum_{p=-(\overline{n_{row}}-1)}^{\overline{n_{row}}-1} F_p(\alpha_x, \sigma_x) exp\left(j\frac{\pi}{N}np\right) \sum_{q=-(\overline{n_{column}}-1)}^{\overline{n_{column}}-1} F_q(\alpha_y, \sigma_y) exp\left(j\frac{\pi}{M}n\right.$$

$$= \left[1 + 2\sum_{p=1}^{\overline{n_{row}}-1} F_p(\alpha_x, \sigma_x) cos\left(\frac{\pi}{N}np\right)\right]\left[1 + 2\sum_{q=1}^{\overline{n_{column}}-1} F_q(\alpha_y, \sigma_y) cos\left(\frac{\pi}{M}mq\right)\right] \qquad \text{.....1}$$

$$0$$

And for even number of elements in the array, it becomes –

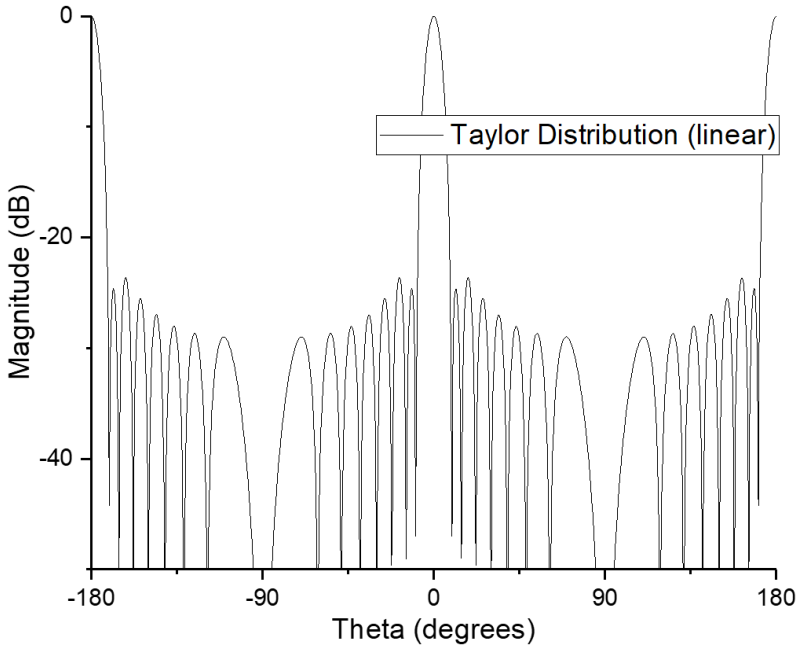

Figure 6. 5 Radiation pattern of the array factor for 25 element linear array with Taylor's excitation

$$A_{n,m} = \left[1 + 2\sum_{p=1}^{\overline{n_{row}}-1} F_p(\alpha_x, \sigma_x) cos\left(\frac{\pi}{N-\frac{1}{2}}(|n| - \frac{1}{2})p\right)\right] . \left[1 + 2\sum_{q=1}^{\overline{n_{column}}-1} F_q(\alpha_y, \sigma_y) cos\left(\frac{\pi}{M-\frac{1}{2}}(|m| - \frac{1}{2})q\right)\right] \quad \text{.....11}$$

The array factor plot for a 25 elements linear array is shown in Figure 6. 5.

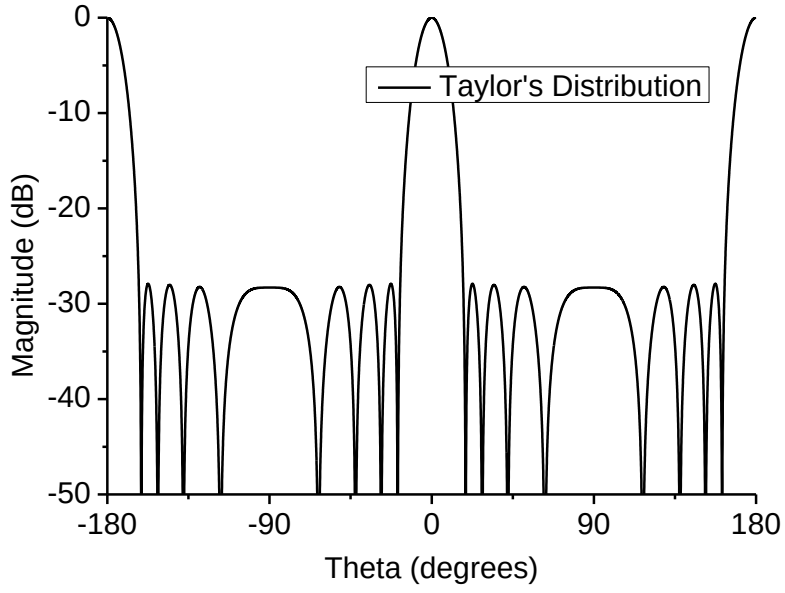

Figure 6. 6 Radiation pattern of the array factor for 8 × 8 element planar array with Taylor's excitation

Taylor's distribution results in a narrow beam array factor. Taylor's parameter or σ_p can be tailored to achieve required side-lobe level. For an 8× 8 planar array, the distribution is shown in Figure 6. 6. Again, the side-lobe level can be seen as a very stable flat constant line on the graph below -25 dB.

6.3.4 Staircase Power Distribution (SPD)

Array Factor (AF) of a one-dimensional array antenna with staircase power distribution (SPD) can be expressed [249, 250] by the following equation

$$AF = \sum_{n=-(N-1)/2}^{(N-1)/2} \delta_1 \exp(jn\psi)$$
$$+ \sum_{n=-\frac{N-1}{2}+N_{s1}}^{\frac{N-1}{2}-N_{s1}} (\delta_2 - \delta_1) \exp(jn\psi)$$
$$+ \sum_{n=-\frac{N-1}{2}+N_{s1}+N_{s2}}^{\frac{N-1}{2}-N_{s1}-N_{s2}} (\delta_3 - \delta_2) \exp(jn\psi) + \dots\dots\dots \qquad \dots\dots\dots\dots 12$$
$$+ \sum_{n=-\frac{N-1}{2}+N_{s1}+N_{s2}+\cdots+N_{sl}}^{\frac{N-1}{2}-N_{s1}-N_{s2}-\cdots-N_{sl}} (\delta_l - \delta_{l-1}) \exp(jn\psi)$$
$$+ \sum_{n=-\frac{N-N_s-1}{2}}^{\frac{N-N_s-1}{2}} (A - \delta_l) \exp(jn\psi)$$

N = Total number of antenna elements, $N_{s1}, N_{s2}, N_{s3}, \dots\dots N_{sl}$ are number of the antenna elements tapered from each side (starting from the edge of the array) for 1st stage, 2nd stage,

3rd stage……. last stage. Here the last stage is defined as the stage before the middle antenna elements.

$N_S = N_{s1} + N_{s2} + N_{s3} + \ldots\ldots + N_{sl}$ = Number of elements tapered from each side, $\psi = \beta d(\sin\theta - \sin\theta_0)$ and $\delta_1, \delta_2, \delta_3, \ldots\ldots \delta_n$ are the amplitudes of the antenna elements of the1st stage, 2nd stage, 3rd stage…….last stage. d = inter- elements (m). $\beta = \frac{2\pi}{\lambda}$ = phase constant. A is the amplitude of middle antenna elements and θ_0 = Direction of beam maximum along the broad side.

For even planar array it can be written as –

$$F_e(u,v) = 4[\sum_{m=-\frac{N-1}{2}}^{\frac{N-1}{2}} \sum_{n=-\frac{N-1}{2}}^{\frac{N-1}{2}} \delta_{mn}^1 \cos(2m-1)\, u.\cos(2n-1)\, v + \sum_{m=\left[-\frac{N-1}{2}\right]+N_{s1}}^{\frac{N-1}{2}-N_{s1}} \sum_{n=m=\left[-\frac{N-1}{2}\right]+N_{s1}}^{\frac{N-1}{2}-N_{s1}} (\delta_{mn}^2 - \delta_{mn}^1)\cos(2m-1)\, u.\cos(2n-1)\, v] \quad \ldots\ldots\ldots\ldots 13$$

Where

$$\mathrm{u} = \frac{\pi d}{\lambda}(\sin\theta\cos\phi - \sin\theta_0\cos\phi_0)$$

$$v = \frac{\pi d}{\lambda}(\sin\theta\sin\phi - \sin\theta_0\sin\phi_0)$$

10 dB ratio between maximum and minimum power level in an evenly distributed power level. The array factor for a 25 elements linear array is plotted in Figure 6. 7. Unlike Taylor's and Chebyshev's distribution, the side-lobes are not constant, but they are still below -20 dB.

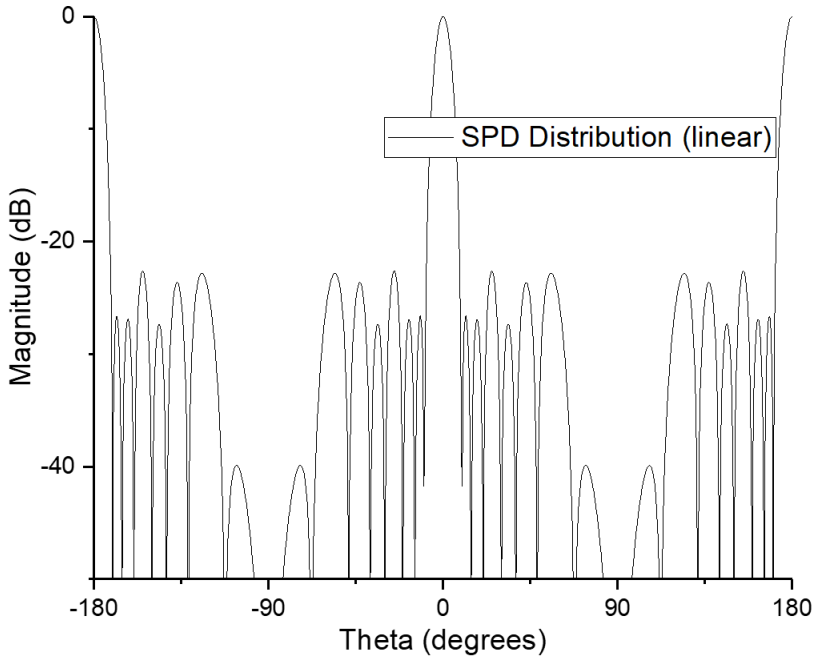

Figure 6. 7 Radiation pattern of the array factor for 25 element linear array with staircase power distribution (SPD)

For the 8 × 8 planar array, the graph for the array factor looks like Figure 6. 8. The side-lobes are less than -30 dB. The advantage of the SPD is to be able to set the number of stages and within the stages the excitation coefficient remains the same.

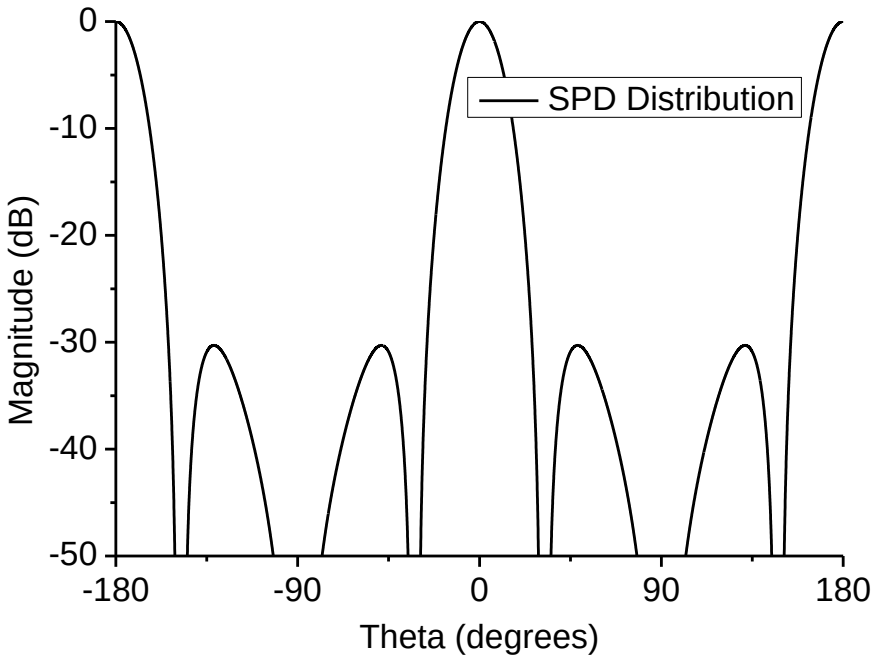

Figure 6. 8 Radiation pattern of the array factor for 8 × 8 element planar array with staircase power distribution (SPD)

6.3.5 Chebyshev's Distribution

Antenna array factors for arrays with uniform weights have unequal sidelobe levels. The optimal sidelobe level (for a given beamwidth) will occur when the sidelobes are all equal in magnitude. This problem was solved by Dolph in 1946. He derives a method for obtaining weights for uniformly spaced linear arrays steered to broadside ($\theta = 90$ degrees). This is a popular weighting method because the sidelobe level can be specified, and the minimum possible null-null beamwidth is obtained. The array factor can be written as [170, 174]-

$$AF = \sum_{n=1}^{N} w_n \cos[2(n-1)u] \qquad \ldots\ldots\ldots\ldots 14$$

For an even array and

$$AF = \sum_{n=1}^{N} w_n \cos(2nu) \qquad \ldots\ldots\ldots\ldots 15$$

For an odd array.

Where $cosu = t/t_0$, t is variable and t_0 is the factor responsible for shaping the sidelobe.

For a planar array, the array factor can be calculated as –

$$E_e(\theta, \phi) = F_e(u, v)$$
$$= 4 \sum_{m=1}^{N} \sum_{n=1}^{N} I_{mn} \cos(2m-1)\, u. \cos(2n-1)v \qquad \ldots\ldots\ldots\ldots 16$$

For an even number of elements in row and column, $L = 2N$. In (16)

$$u = \frac{\pi d}{\lambda}(\sin\theta\cos\phi - \sin\theta_0\cos\phi_0)$$

……..17

$$v = \frac{\pi d}{\lambda}(\sin\theta\sin\phi - \sin\theta_0\sin\phi_0)$$

where d is the spacing between adjacent elements and / is the operating wavelength. For an odd number of elements in each row and column, L= 2N + 1, we have

$$E_o(\theta,\phi) = F_o(u,v)$$

$$= \sum_{m=1}^{N+1}\sum_{n=1}^{N+1}\varepsilon_m\varepsilon_n I_{mn}\cos(2m-1)\,u.\cos(2n-1)v \qquad \text{……..18}$$

The conventional method for designing a planar Chebyshev array is to match $F_e(u,v)$ or $F_o(u,v)$ with a product of two Chebyshev polynomials of the (L- 1) order. For example, if L= 2N, $F_e(u,v)$ in (16) is used:

$$F_e(u,v) = 4T_{L-1}(w_0\cos u)T_{L-1}(w_0\cos v) \qquad \text{……..19}$$

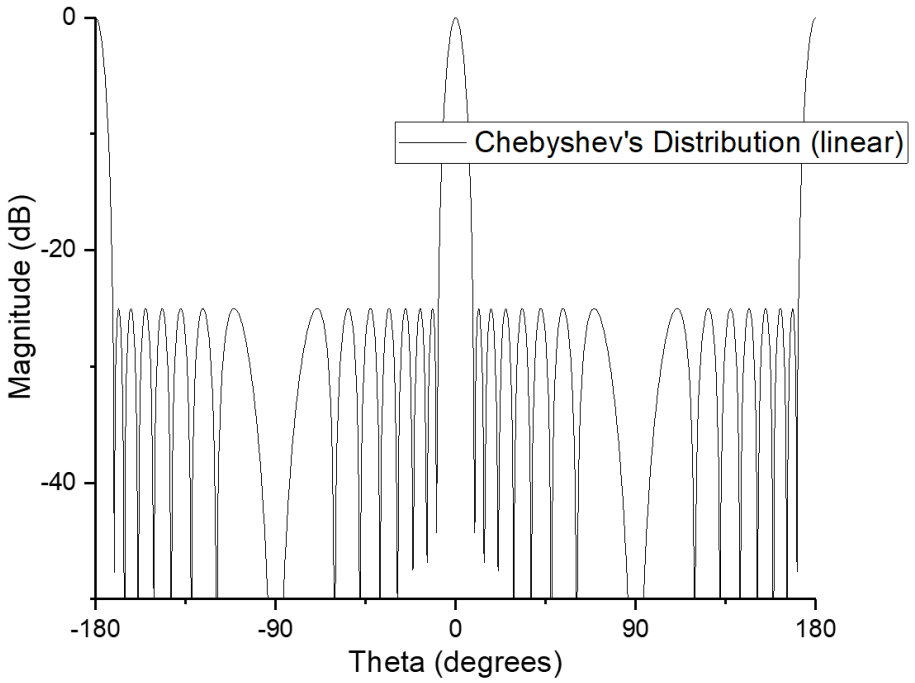

Figure 6. 9 Radiation pattern of the array factor for 25 element linear array with Chebyshev's distribution

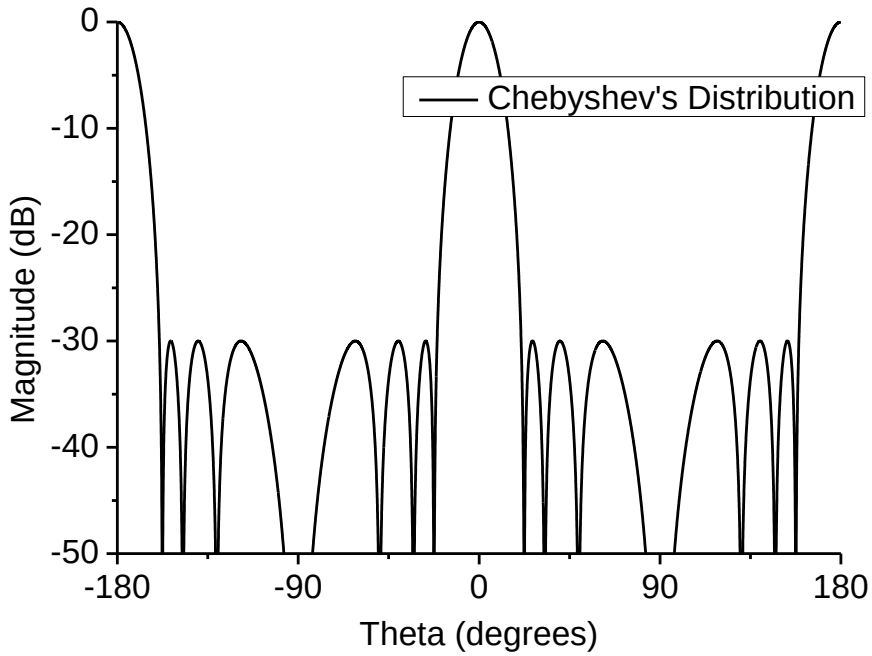

Figure 6. 10 Radiation pattern of the array factor for 8 × 8 element planar array with Chebyshev's distribution

Where w0 is a parameter for controlling sidelobe level. In order to make the radiation pattern a Chebyshev pattern in any cross-section, (19) must be discarded and replaced by a single Chebyshev polynomial. It can be written -

$$F_e(u,v) = 4T_{L-1}(w_0 \cos u \cos v) \qquad \ldots\ldots\ldots\ldots 20$$

Using a further investigation leads to

$$F_e(u,v) = 4\sum_{m=1}^{N}\sum_{n=1}^{N} B_{mn}^{2N} \cos(2m-1)\,u.\cos(2n-1)v \qquad \ldots\ldots\ldots\ldots 21$$

With

$$B_{mn}^{2N} = \sum_{s=(m,n)}^{N} (-1)^{N-s}.\frac{2(2N-1)}{N+s-1}.\binom{N+s-1}{2s-1}.\binom{2s-1}{s-m}.\binom{2s-1}{s-n}.\left(\frac{w_0}{2}\right)^{2s-1} \qquad \ldots\ldots\ldots 22$$

The array factor of Chebyshev's distribution for a 25 elements linear array is shown in Figure 6. 9. The side-lobe level is exactly -25 dB. For a planar array of 8 × 8 size, the side-lobe level is designed to be -30 dB. The array factor is shown in Figure 6. 10.

Chebyshev's distribution ensures the exact same side-lobe level throughout. In the case of radiometer, there is no specific reason that the side-lobes have to be exact at the same level. The requirement is just below a certain level to avoid radiation coming from unwanted angles other than the main lobe.

6.3.6 Other Distributions

Most of the major beam shaping techniques were discussed in this section. There are some other very basic types of distributions. Among them Binomial and Cosine distributions are shown in Figure 6. 11 and Figure 6. 12. The coefficients for each element were found by

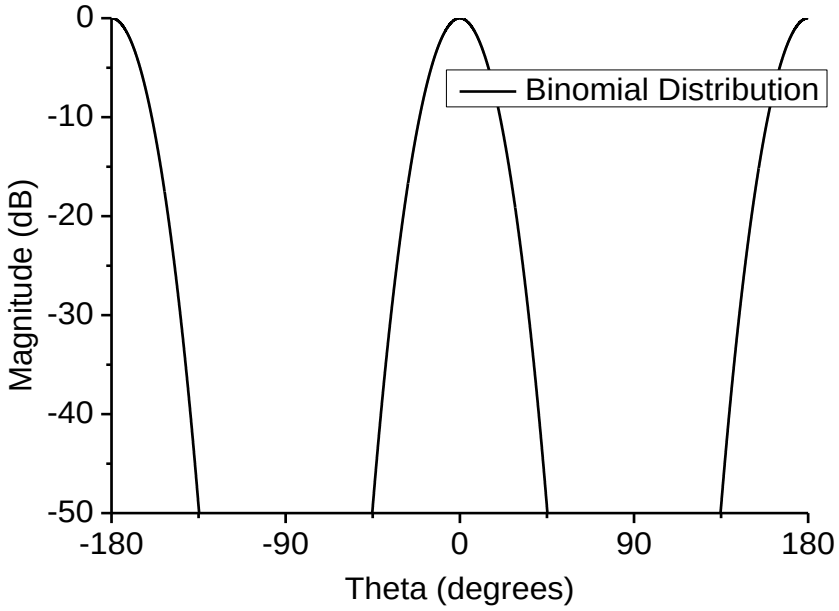

Figure 6. 11 Radiation pattern of the array factor for 8 × 8 element planar array with binomial distribution

Binomial theorem and Cosine equation respectively and then input in the array factor equation to find the array factor and then plotted. The reason for not choosing these distributions are firstly, they show unrealistic widths to fabricate or they lack practicality and secondly, the

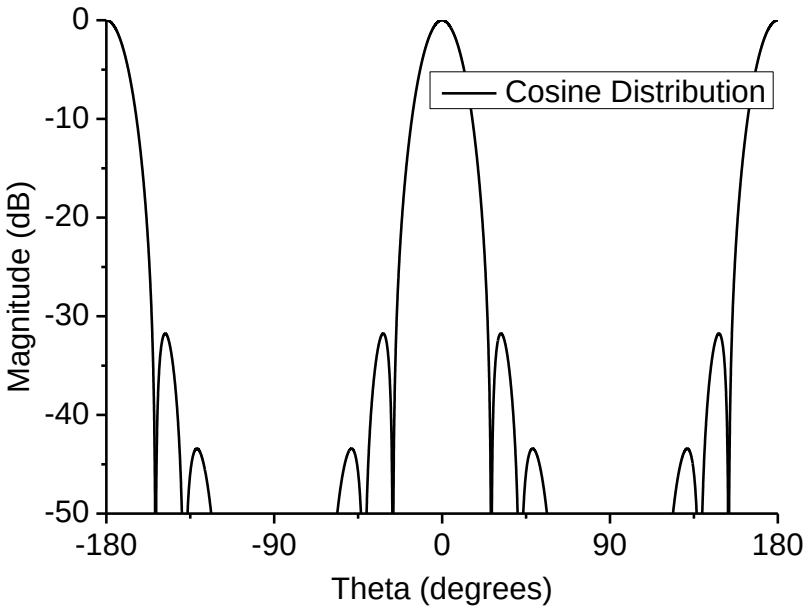

Figure 6. 12 Radiation pattern of the array factor for 8 × 8 element planar array with cosine distribution

requirement of the research is different hence there is no need to design with such low side-lobe level and 3 dB beamwidth.

6.4 Comparison and Discussion

One of the big challenges of the radiometer antenna is to design the feed network for the array in higher frequency. As the frequency gets higher, the size of the feed network becomes smaller, but the number of feeds remains the same. This results in a complex structure when the feed lines also have different widths. Different feeding techniques result in different excitation coefficients and depending on these coefficients, one technique can be easier to implement practically than the other.

In all the techniques except the SPD, the excitation levels are unique. For example, for an 8-element linear array, there will be four different power levels making the design complex for more elements in a planar array. On the other hand, the SPD method restricts the number of

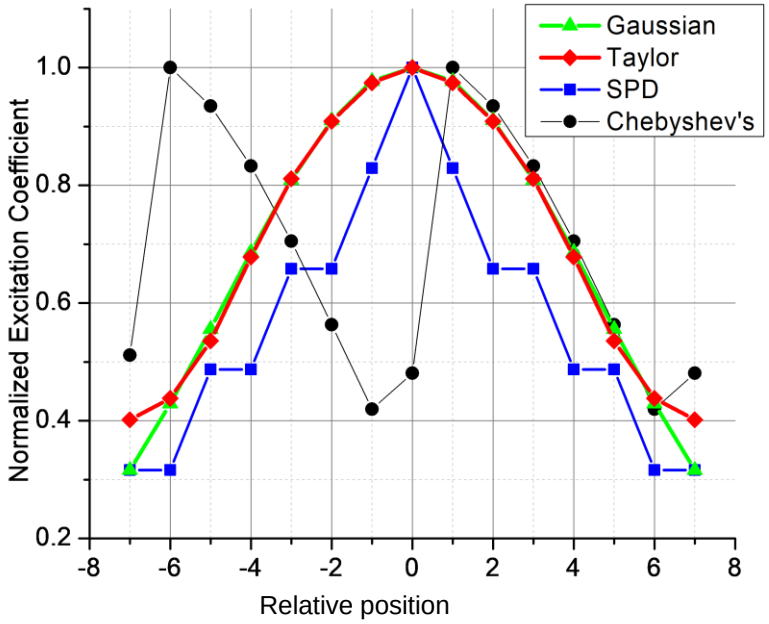

Figure 6. 13 Normalized excitation coefficients for different power distributions

the power or excitation levels hence the fabrication process is easier resulting cheaper cost than the others.

For a 15-element linear array, the normalized excitation coefficients for different power distributions are presented in Figure 6. 13, for 15 element array and around 15 dB power ratio

Table 6. 1 Excitations (%) for different elements for an 8x8 array using the Gaussian distribution

Gaussian Distribution	18.1	28.23	37.47	43.56	43.56	37.47	28.23	18.1
	28.23	43.56	56.52	65.85	65.85	56.52	43.56	28.23
	37.47	56.52	75.07	86.5	86.5	75.07	56.52	37.47
	43.56	65.85	86.5	100	100	86.5	65.85	43.56
	43.56	65.85	86.5	100	100	86.5	65.85	43.56
	37.47	56.52	75.07	86.5	86.5	75.07	56.52	37.47
	28.25	43.56	56.52	65.85	65.85	56.52	43.56	28.25
	18.1	28.23	37.47	43.56	43.56	37.47	28.23	18.1

Table 6. 2 Excitations (%) for different elements for an 8x8 array using the SPD

SPD method								
	16.87	24.5	40.12	40.12	40.12	40.12	24.5	16.87
	24.5	36.57	60.1	60.1	60.1	60.1	36.57	24.5
	40.12	60.1	100	100	100	100	60.1	40.12
	40.12	60.1	100	100	100	100	60.1	40.12
	40.12	60.1	100	100	100	100	60.1	40.12
	40.12	60.1	100	100	100	100	60.1	40.12
	24.5	36.57	60.1	60.1	60.1	60.1	36.57	24.5
	16.87	24.5	40.12	40.12	40.12	40.12	24.5	16.87

between the maximum and minimum power levels. From this figure, the simplicity of the SPD method compared to other methods can be understood. Gaussian and Taylor have quite a similar excitation pattern, and Chebyshev's distribution requires complex excitation power structure.

To explain the simplicity of the SPD method,

Table 6. *1* and Table 6. 2 are shown with the Gaussian and SPD distribution. In both tables, an 8 × 8 array feeding is shown. As this is a planar array, hence the centre elements receive the maximum power and the corner elements receive the minimum. The number of levels is also different. For the Gaussian method, a total number of 9 different excitations are used, whereas in the SPD method only 6 levels are used. For this reason, in this research SPD method is used for designing the arrays.

Beam efficiency gives a general idea of power ratio associated with the main beam and sidelobes. Here, a different number of the array element with different beam pointing angle is compared for different distributions. For Gaussian and Taylor distribution, beam efficiency is over 99% in all the combinations because of low sidelobes. On the other hand, the SPD method

uses fewer power levels compared to others which explains its low beam efficiency. Chebyshev's method ensures equal sidelobe levels which explain its less beam efficiency.

If the sidelobe levels were lowered, then beam efficiency would increase in the case of Chebyshev' distribution. The number of array and beam pointing angle has little effect on the beam efficiency in all the distributions. However, a general pattern can be observed which shows the number of element and beam pointing angle have an inversely proportional effect on the beam efficiency (BE). Comparison of beam efficiency with a different number of arrays with different beam pointing angle is presented in Table 6. 3.

Table 6. 3 Comparison of beam efficiency with different number of arrays with different beam pointing angle

Main Beam Pointing Angle (degree)			5	15	25	35
Number of array element			Beam Efficiency			
Type of Power Distribution	Gaussian	25	99.25	99.32	99.38	98.39
		15	99.49	99.50	99.62	99.65
		9	99.62	99.63	99.76	99.8
	Taylor	25	99.37	99.38	99.40	99.41
		15	99.40	99.42	99.44	99.47
		9	99.45	99.47	99.49	99.58
	Staircase Power Distribution (SPD)	25	98.38	98.02	98.23	98.61
		15	96.14	94.35	94.10	96.60
		9	90.55	89.98	87.15	88.99
	Chebyshev's method	25	94.45	94.73	95.06	95.45
		15	97.2	96.93	97.10	97.58
		9	98.55	98.35	98.47	98.95

Table 6. 4 Comparison of maximum side-lobe level (MSLL) with different number of arrays with different beam pointing angle

Main Beam Pointing Angle (degree)			5	15	25	35
Number of Array Element			MSLL			
Type of Power Distribution	Gaussian	25	-23.2	-23.2	-23.2	-23.2
		15	-26.3	-26.3	-26.3	-26.3
		9	-28.6	-28.6	-28.6	-28.6
	Taylor	25	-21.1	-21.1	-21.1	-21.1
		15	-21.1	-21.1	-21.1	-21.1
		9	-21.1	-21.1	-21.1	-21.1
	SPD	25	-25.2	-25.2	-25.2	-25.2
		15	-20	-20	-20	-20
		9	-13.4	-13.4	-13.4	-13.4
	Chebyshev	25	-25	-25	-25	-25
		15	-25	-25	-25	-25
		9	-25	-25	-25	-25

In many design requirements for long distance communication, remote sensing and so on it is required to have very low sidelobe levels. Gaussian distribution can offer lower sidelobe levels at the expense of higher ratio between highest and lowest power levels. The number of elements in an array has an inversely proportional relationship with MSLL. However, beam pointing angle has no effect on sidelobes. In the Taylor's and Chebyshev's algorithm, designing lower sidelobes is the primary design constraint. Other antenna parameters such as beamwidth and beam efficiency are sacrificed/adjusted to ensure maximum sidelobes. Though both Taylor's and Chebyshev's method design MSLL but Chebyshev's method ensures the same side lobes for all the side lobes. A comparison of maximum side lobe level with a different number of arrays with different beam pointing angle is presented in Table 6. 4.

3 dB beamwidth or half-power beam width has a direct relation with directivity. Some system requires very narrow beam width such as point to point communication whereas some system has a requirement for wide beam width to cover more area. The primary factor for variation in this parameter is the number of elements in an array — generally, the more element, narrower the beam width. Taylor's distribution has the narrowest beam width in comparison to other distributions. Gaussian, SPD and Chebyshev's distribution are very similar to each other and only function of the number of elements in an array. A comparison of 3 dB beamwidth with a different number of arrays with different beam pointing angle is presented in Table 6. 5.

Gaussian and Chebyshev's distribution has similar beam width but different side lobes and diversified power levels of excitation to follow.

Table 6. 5 Comparison of 3 dB beam width with different number of arrays with different beam pointing angles

Main Beam Pointing Angle (degree)			5	15	25	35
Number of array element			3 dB Beamwidth			
Type of Power Distribution	Gaussian	25	4.79	4.93	5.24	5.83
		15	7.88	8.18	8.68	9.62
		9	12.72	13.07	13.97	15.51
	Taylor	25	2.47	2.55	2.71	3.0
		15	4.23	4.37	4.66	5.15
		9	7.43	7.67	8.17	9.05
	Staircase Power Distribution (SPD)	25	4.99	5.14	5.53	6.13
		15	7.98	8.27	8.78	9.73
		9	12.71	13.12	13.97	15.51
	Chebyshev's method	25	4.66	4.81	5.11	5.67
		15	7.92	8.17	8.73	9.67
		9	13.61	14.04	15.01	16.67

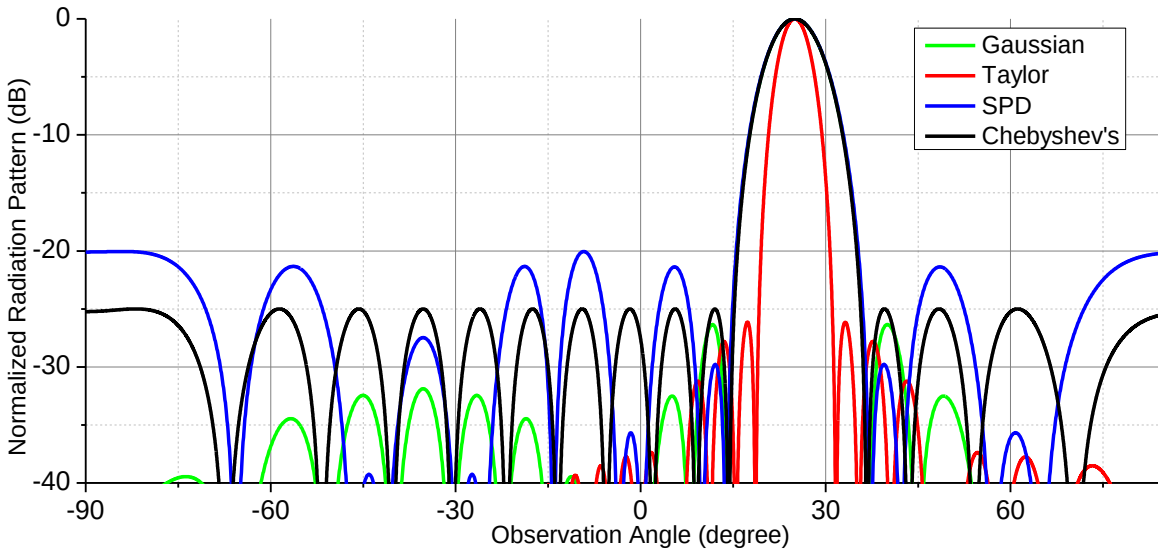

Figure 6. 14 Radiation pattern for a 15-element array at 25° observation angle using different power distributions.

The radiation pattern is shown in Figure 6. 14 is for 15-element linear array at 25° beam pointing angle. This radiation pattern supports and explains all the findings in Table 6.3-5.

Staircase power distribution has the highest side-lobes level which is very difficult to optimize. Overall beam efficiency and beam width are almost the same as Gaussian or Chebyshev's method, but simpler power levels make it a very attractive power distribution for large array elements. Taylor's distribution has higher beam efficiency, easy to manipulate side-lobe levels and narrow 3 dB beamwidth but less control over the ratio of the highest and lowest power level of excitation.

6.5 Measurement result

8 × 8 Ku- and Ka-band array antennas are designed and fabricated. From the last chapter, the antenna array design technique has been adopted. The feed lines in the last chapter was designed for the uniform distribution. In this chapter, different feed widths are designed to achieve required side-lobe level.

6.5.1 8 × 8 Ku-band

6.5.1.1 Structure and design

The SPD method beam shaping is applied on the 8 × 8 Ku-band array which was designed and measured in the last chapter. The feed lines are designed in such a way that the excitation ratios among the elements matches with the Table 6. 2 ratios.

A photograph of the fabricated 8 × 8 Ku-band array antenna is shown in Figure 6. 15. Different layers of this antenna are assembled using a jig and the ports are positioned so that they are just touching the feeds. For better understanding, power divider and feed network are shown in Figure 6. 16 (a) and (b). In these figures, different widths can be seen for different power ratio for different elements of the array antenna. The feed widths are determined by the amount of resistivity required to deliver different amount of power. The power ratio and the width of the feed are proportional to each other as increasing the feed width decreases resistivity hence increasing the power flow. In Figure 6. 16 (c), a layer by layer view is shown. This antenna has

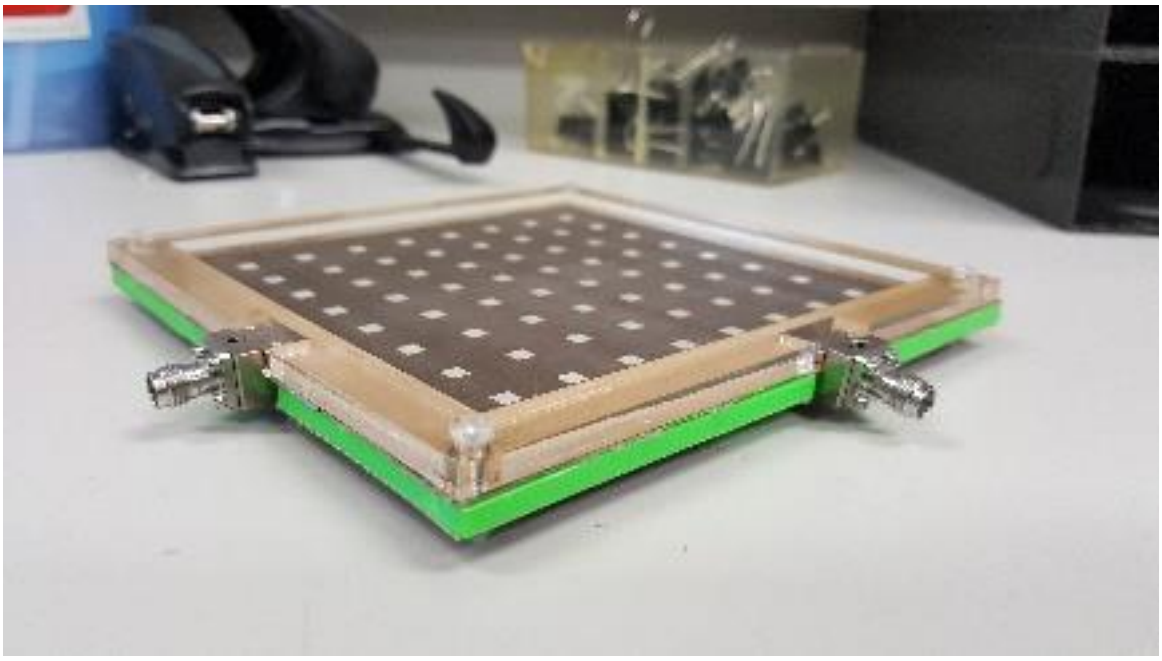

Figure 6. 15 Ku-band 8 × 8 array antenna after fabrication and assemble.

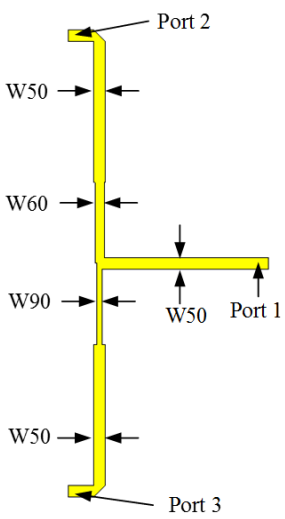
Port 2
W50
W60
W90
W50
Port 1
W50
Port 3

(a)

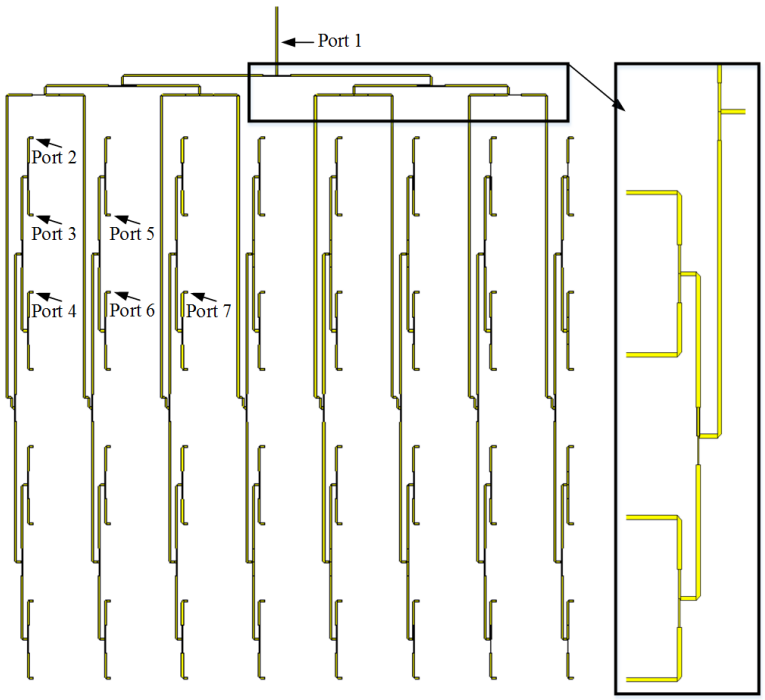
Port 1
Port 2
Port 3
Port 5
Port 4
Port 6
Port 7

(b)

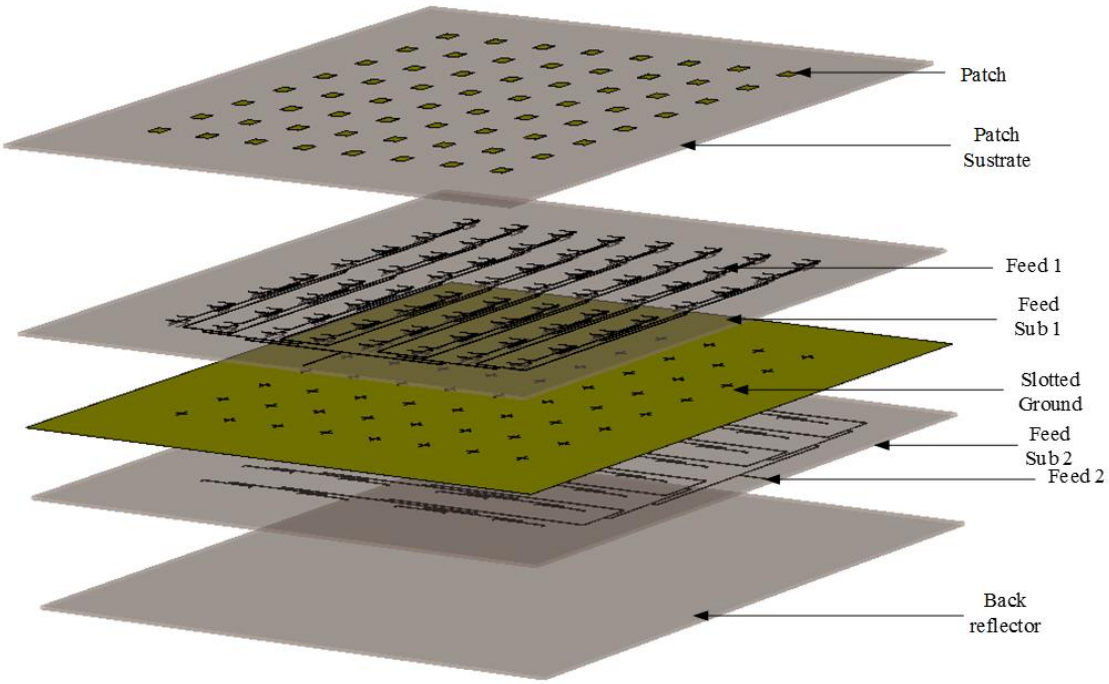
Patch
Patch
Sustrate
Feed 1
Feed
Sub 1
Slotted
Ground
Feed
Sub 2
Feed 2
Back
reflector

(c)

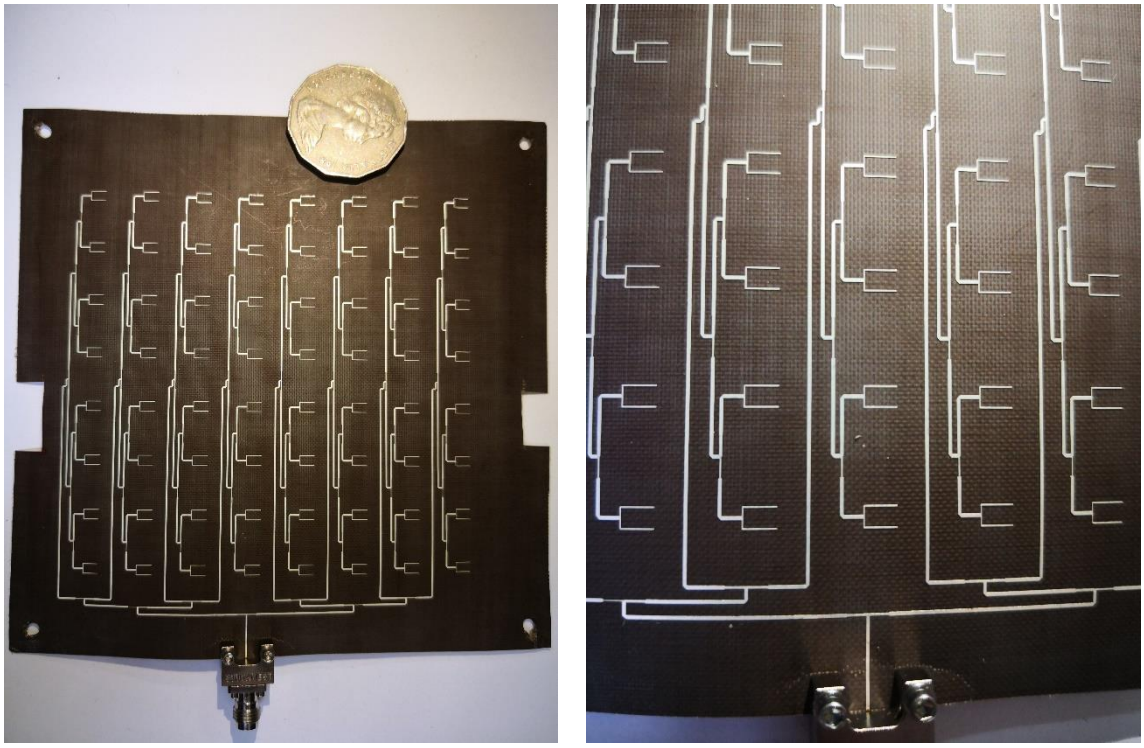

(d)

Figure 6. 16 (a) single power divider, (b) feed network of one polarization, (c) layer view of a Ku-band 8 × 8 array antenna, and (d) fabricated feed lines with a 50 cent AUD to compare the size.

four substrate and five copper layers. From the top, the first one is the patch layer followed by the feed layer, ground plane, another feed layer and finally the back-reflector layer.

6.5.1.2 Results

Simulation was performed using CST MW Studio 2017 after optimizing the design by tweaking the feed network path and parameters. The result after setting the design environment is presented in this section.

In Figure 6. 17 and Figure 6. 18, all S-parameter results are shown. S11 and S22 measured results show very good return loss at the resonant frequency (18.7 GHz) and have the same shape as the simulation result. Port-to-port isolation or S21 and S12 are also less than -40 dB throughout the spectrum. The bandwidth is found around 600 MHz. S-parameter result overall shows very good matching and minimum coupling.

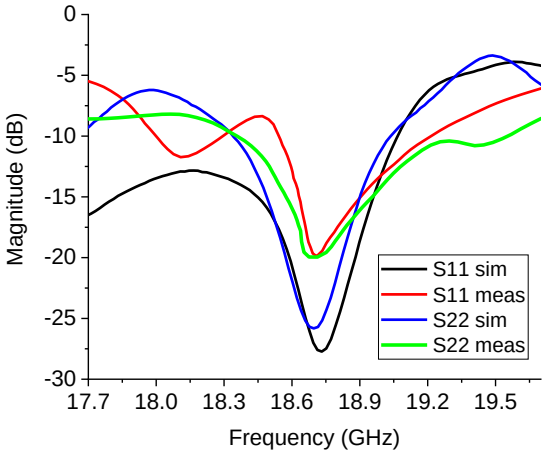

Figure 6. 17 Simulated and measured S-parameter result for Ku-band 8 × 8 array antenna

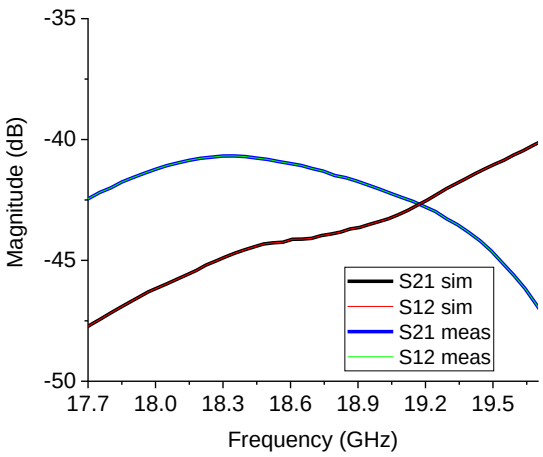

Figure 6. 18 Simulated and measured port-to-port isolation result for Ku-band 8 × 8 array antenna

Figure 6. 18 shows the radiation pattern simulation versus measurement. Figure 6. 18 (a) shows the electric field co-polar simulation and measurement result for both ports. The main-lobe magnitude of the measured result is around 23 dB for both polarizations and the pattern follows the simulation pattern closely. It is important to notice the side-lobe level of the radiation pattern is now less than 25 dB because of the beam shaping and front-to-back-lobe ratio is also increased. The electric field cross-polarization pattern of the simulation and measured result is shown in Figure 6. 18 (b), which shows around -10 dB cross-polarization which makes 45 dB less compared to the main lobe of the electric field at 0°. Magnetic field co- and cross-polar

pattern of the simulation and measured result is shown in Figure 6. 18 (c) and (d). For the co-polar radiation pattern, the magnitude at 0° is again around 23 dB for both polarizations and follow the simulated pattern closely. Similarly, the cross-polarization level at 0° is more than 40 dB less than the co-polarization level. The overall efficiency for the simulation is about 85.5%.

Overall, the simulation and measured result justifies the theory of the beam shaping as the side-lobe level is reduced. Also, implementing a back-reflector suppresses the back-lobe radiation and increases overall efficiency.

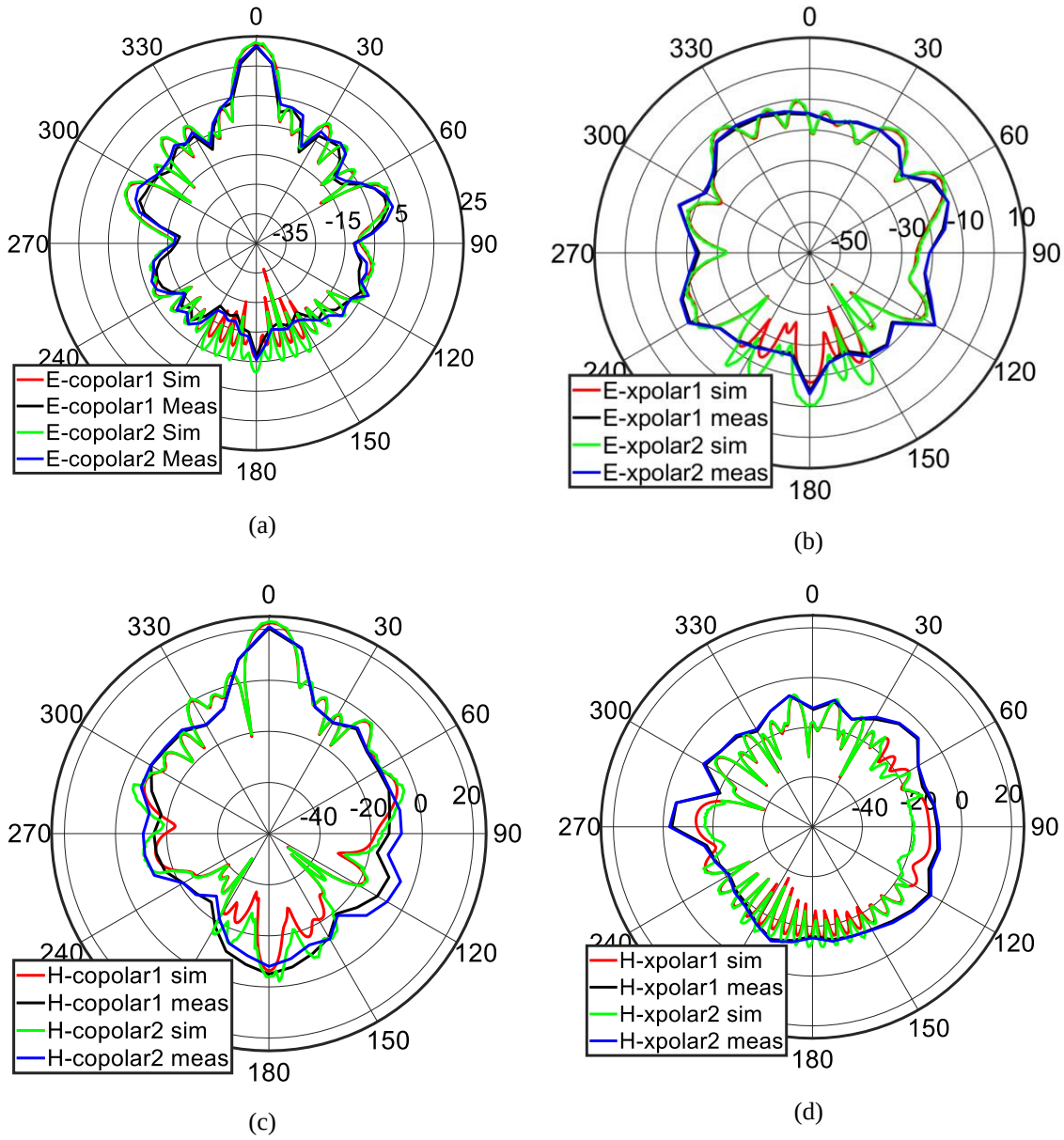

Figure 6. 19 Simulated and measured (a) E- plane co-polar, (b) E- plane cross-polar, (c) H- plane co-polar and (d) H- plane cross-polar radiation pattern for Ku-band 8 × 8 array antenna with beam shaping.

6.5.2 Ka-band 8 × 8 array

6.5.2.1 Structure and design

Similar technique as the Ku-band array antenna is adopted. However, the fabrication becomes complex for this band as the size is smaller than the Ku-band array. For the beam shaping, again the SPD method is implemented. The feed lines are designed in such a way that the

excitation ratios among the elements matches with the Table 6. 2 ratios. The assembled antenna is photographed, and different layers are shown in Figure 6. 20.

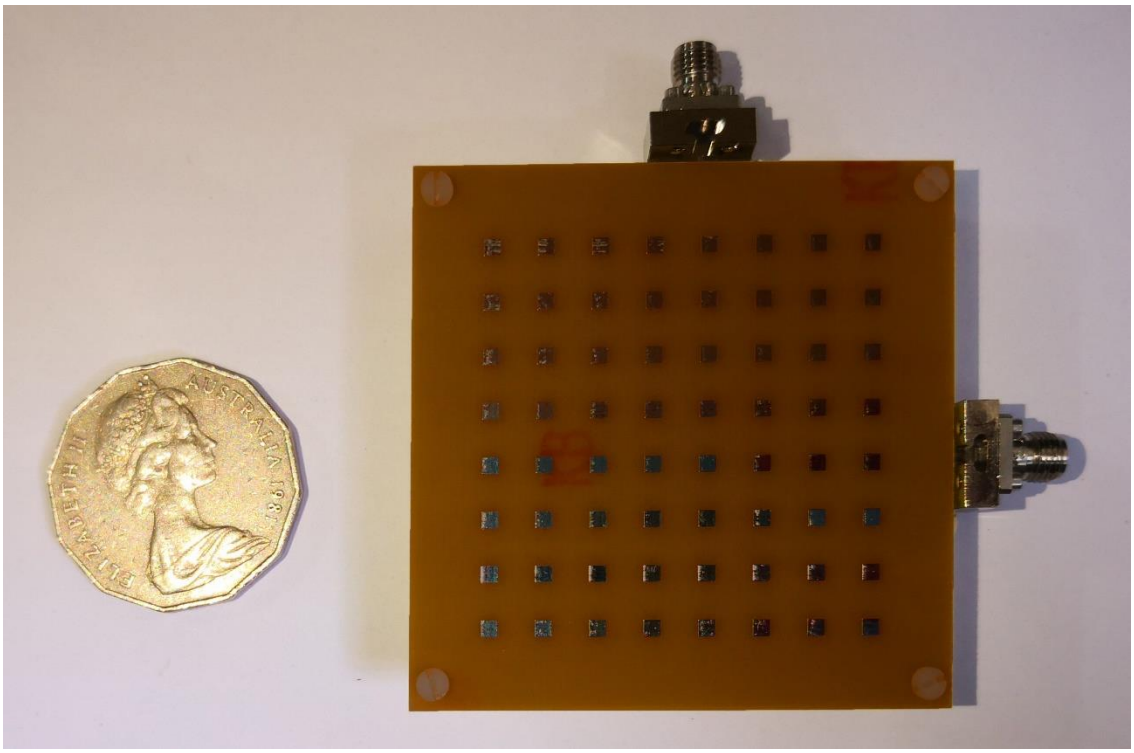

(a)

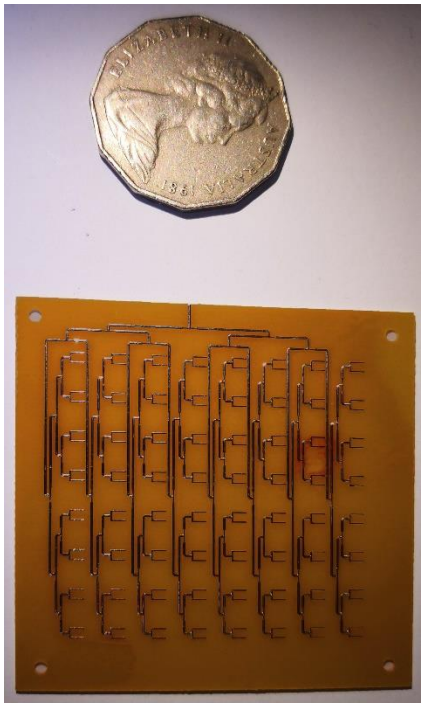

(b)

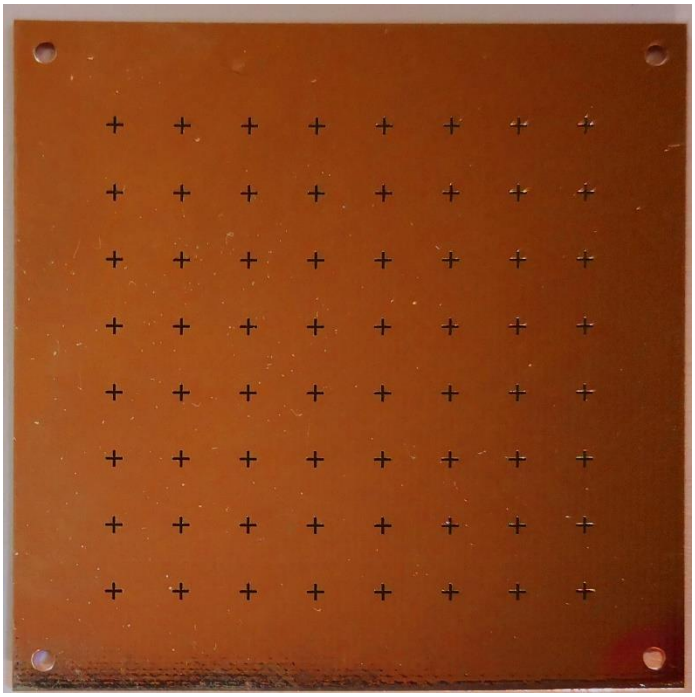

(c)

Figure 6. 20 Ka-band 8 × 8 array antenna (a) after fabrication and assemble, (b) only feed network and (c) ground layer photograph.

6.5.2.2 Results

Simulation was performed using CST MW Studio 2017 after optimizing the design by tweaking the feed network path and parameters. The result after setting the design environment is presented in this section.

In Figure 6. 21, all S-parameter results are shown. S11 and S22 measured results show very good return loss at the resonant frequency (37 GHz) and have very similar shape as the simulation result. Port-to-port isolation or S21 and S12 are also less than -34 dB throughout the spectrum. The bandwidth is found around 2 GHz. S-parameter result overall shows very good matching and minimum coupling.

Figure 6. 21**Error! Reference source not found.** shows the radiation pattern simulation versus m easurement. Figure 6. 22 (a) shows the electric field co-polar simulation and measurement result for both ports. The main-lobe magnitude of the measured result is around 24 dB for both polarizations and the pattern follows the simulation pattern closely. Again, the side-lobe level of the radiation pattern is now less than 25 dB because of the beam shaping and front-to-back-lobe ratio is also increased. The electric field cross-polarization pattern of the simulation and measured result is shown in Figure 6. 22 (b), which shows around -10 dB cross-polarization which makes around 35 dB less compared to the main lobe of the electric field at 0°.

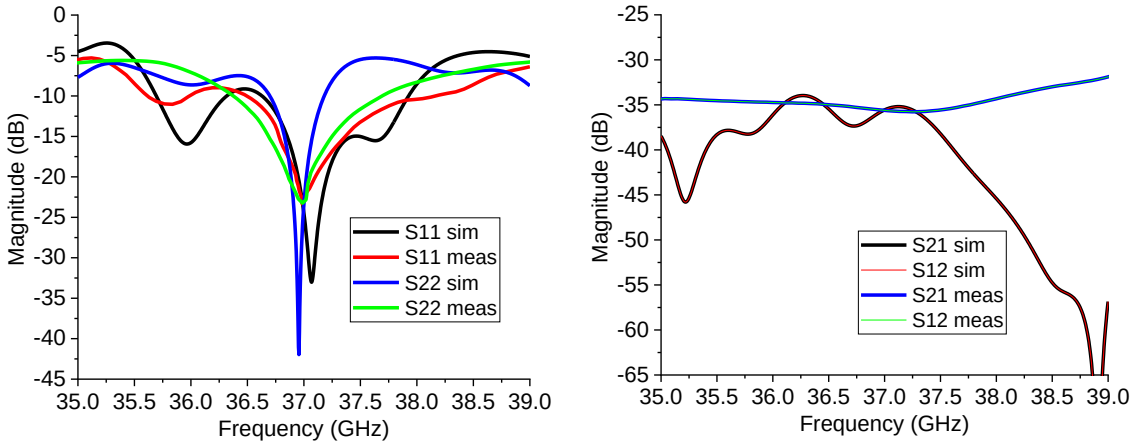

Figure 6. 21 Simulated and measured port-to-port isolation result for Ka-band 8 × 8 array antenna

Magnetic field co- and cross-polar pattern of the simulation and measured result is shown in Figure 6. 22 (c) and (d). For the co-polar radiation pattern, the magnitude at 0° is again around 23.5 dB for both polarizations and follow the simulated pattern closely. Similarly, the cross-polarization level at 0° is around 35 dB less than the co-polarization level.

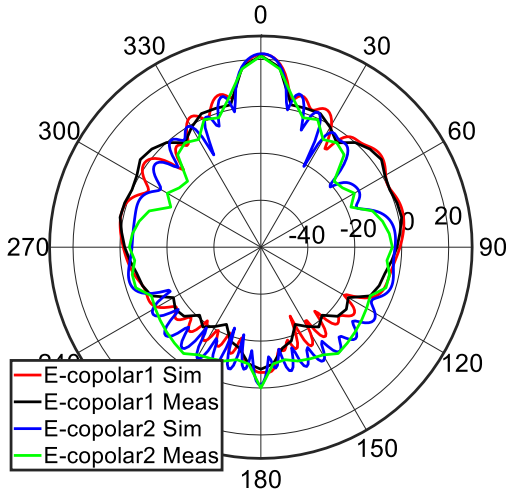

(a)

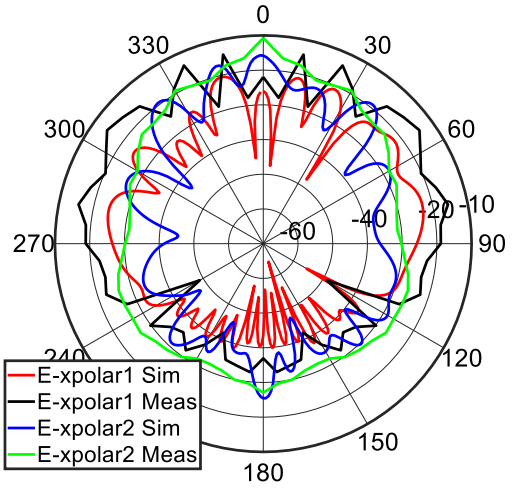

(b)

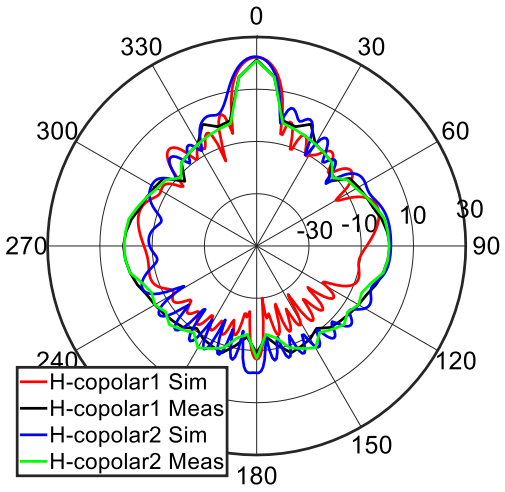

(c)

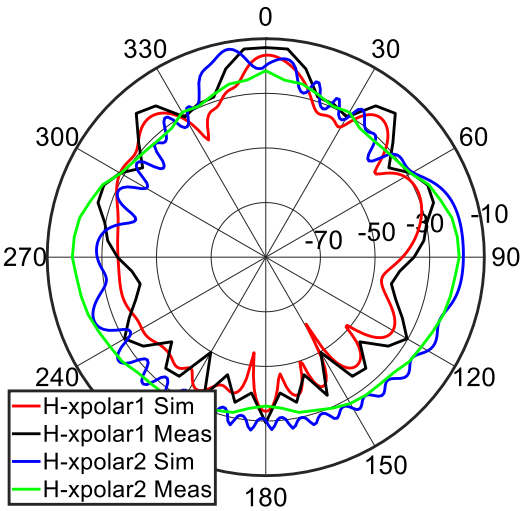

(d)

Figure continued to next page

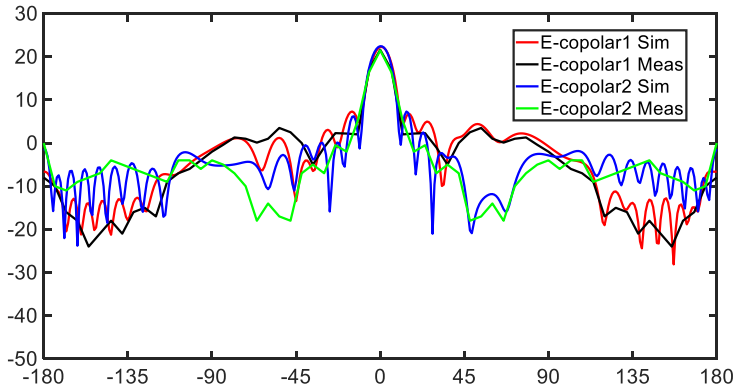

(e)

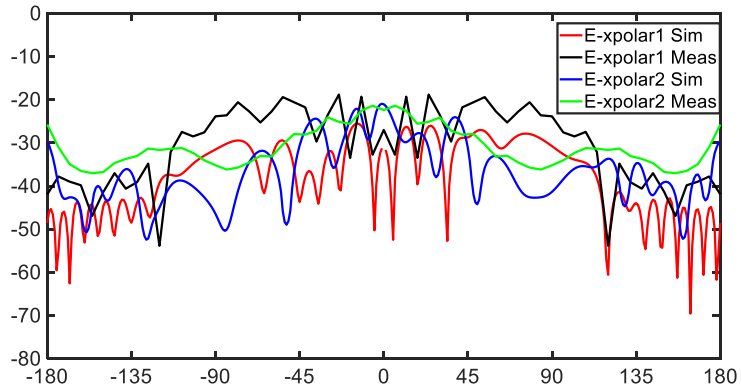

(f)

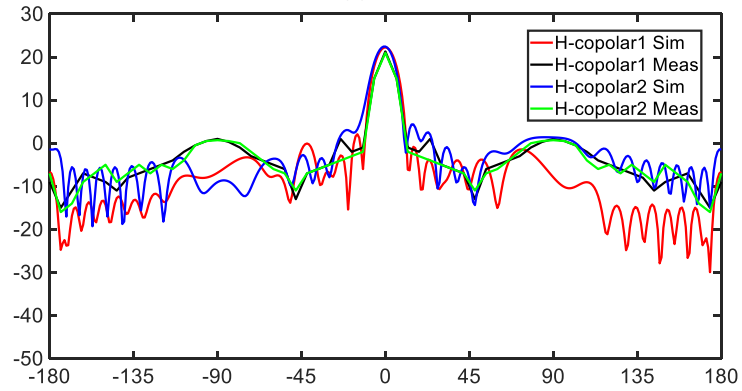

(g)

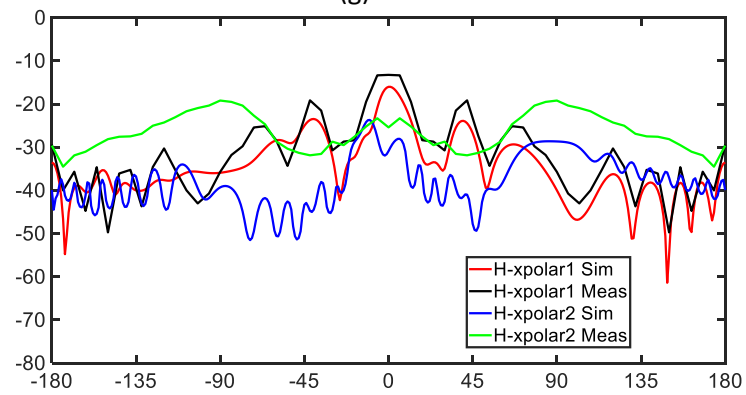

(h)

Figure 6. 22 Simulated and measured (a) E-plane co-polar, (b) E- plane cross-polar, (c) H- plane co-polar and (d) H- plane cross-polar radiation pattern for Ka-band 8 × 8 array antenna with beam shaping, (e), (f), (g) and (h) are line plots (a), (b), (c) and (d).

6.6 Conclusions

Beam shaping is one of the most critical parts of array antenna designing. Depending on the requirements and design constraints a suitable power distribution method can optimize the overall performance of the array. Every power distribution has its advantages and limitations but depending on the requirements one system can be more feasible than others. For a large number of elements in the array with little effect on side lobes, the SPD method can be a potential solution because of fewer power levels. Constant side-lobe level is ensured in Chebyshev's method, but the amplitude of excitation range variation makes it difficult to implement. Gaussian and Taylor's method have similar excitation. Beam efficiency, beamwidth, and side-lobe levels all are connected and important parameters for beam shaping. Depending on the design requirements, the necessity of these parameters can vary, and optimization may require accordingly.

In this chapter different beam shaping algorithms are discussed and then compared to find the best algorithm to suit the radiometer. The SPD method was found to be the most suitable because of its easy to fabricate feature without sacrificing the side-lobe level. From the continuation of the last chapter, in this chapter an 8 × 8 Ku- and an 8 × 8 Ka-band antenna was designed using the SPD beam shaping algorithm. The simulation result shows the reduced side-lobe level proving the concept of the theory. Finally, these antennas are fabricated and assembled for the measurement. The measurement result is found to be consistent with the simulation result hence consistent with the theory of this chapter.

The most important outcome of this chapter is that this chapter gives an independent radiometer antenna system working on a single band. The next step is to extend this research and design a multiband antenna system for the radiometer which is discussed in the next chapter.

7 Multi-band Antenna

7.1 Overview

The current trend in microwave remote sensing radars and radiometers is to measure using multiple frequency bands simultaneously with different polarizations. Having two different frequencies with different physical apertures require more space, add more weight and make system complex. One example of such system is the SIR-C shuttle imaging radar which operated at L- and C- bands, with dual polarizations and not sharing the same aperture [251]. As the satellite systems need reduces size, weight and advanced capabilities, shared aperture design can provide these functionalities. The most common structure of a dual-band dual-polarization (DBDP) antenna array is perforated microstrip patch array with an interleaved structure [252-260]. Two experimented examples of DBDP is discussed in [185, 261] where, L/C and L/X bands were operating in perforated structure. Around 7% bandwidth is achieved in these designs. When the size was increased an extra 5 – 8% bandwidth was obtained [258, 260]. In an overlapped structure where higher band elements are placed above the lower band elements, can increase the thickness of the structure but improve the bandwidth [262, 263]. A similar technique is adopted in this chapter. As the frequency ratio of Ku-band (18.7 GHz) and Ka-band (37 GHz) is almost 1 to 2, the patch dimensions and inter-element distances also have the same ratio. In literature many studies can be found about multi-band antenna but exactly the following technique was not found for extended array which will be discussed in this chapter. Due to the ratio of Ku- and Ka-band, it is possible to place the patches of the Ku- and Ka-bands on the same substrate layer and organize them so that they do not touch each other and still maintain the inter-element distance to avoid grating-lobe. As the number of elements increases, the feed network of each band gets complicated. If the feed networks of different bands and touching each other, they can compromise the antenna performance, hence, different

Chapter Outline

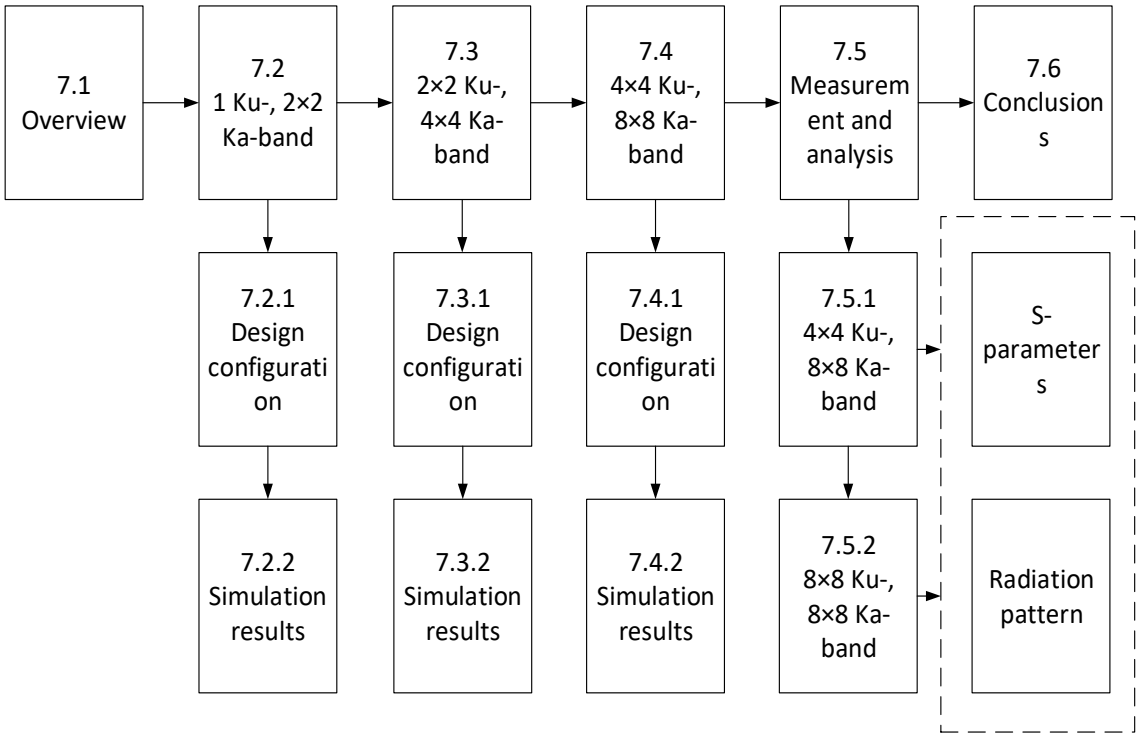

layers for different bands are selected. The ground plane is slotted in the aperture coupled design and as the patches are place so that they are not touching each other, it is possible to design the ground plane in such a way that the slots are also not touching each other and can contribute to individual radiation. A visual representation of such design is shown in Figure 7. 1. In this figure, the layers of a DBDP is shown. The first layer from the top is the patch layer. Patches are placed on the same layer in such a configuration that the lower and higher frequency patches are at equidistant from each other maintaining the 0.7λ according to their frequencies. The next layer in between two substrate layers is the feed network layer of the lower frequency band. The reason for choosing the lower frequency band here is, the lower the frequency the bigger is the size and easier to design. Also, this layer is further from the ground layer than the other feed layer hence the feed lines are wider. If higher frequency is chosen for this layer, with wide feed lines, it would be difficult to design larger arrays.

The next layer is the feed layer for the higher frequency band. The next layer is in the middle and is the ground layer. The ground layer has cross shaped slots placed exactly below the patches. As there are more than one frequency band, hence the slots for the lower frequency bands are surrounded by the higher frequency slots. After the ground layer, the design acts like a mirror, as the next layer is the feed layer for the higher frequency layer followed by the lower frequency feed layer and lastly the back-reflector layer which is optional but important to ensure back-lobe is suppressed. The feed layers provide dual polarizations for both the Ku- and Ka-bands, hence this is a four-port antenna structure and requires four connectors to assemble.

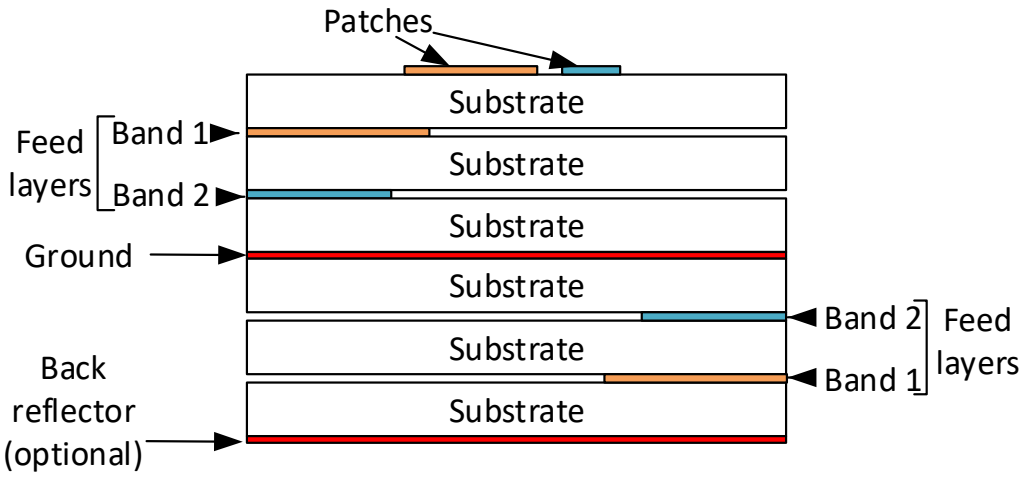

Figure 7. 1 Layer view of multiband antenna for radiometer

The organisation of this chapter is as follows. Starting with one Ku-band surrounded by 2 × 2 Ka-band antennas, the research continues to design 2 × 2 Ku-band with 4 × 4 Ka-band, 4 × 4 Ku-band with 8 × 8 Ka-band and finally 8 × 8 Ku-band with 8 × 8 Ka-band antenna array. Measurement result is provided for 4 × 4 Ku-band with 8 × 8 Ka-band and 8 × 8 Ku-band with 8 × 8 Ka-band antenna array. The simulation and measurement results are compared for both the S-parameter results and radiation patterns. An analysis on the results are performed before the conclusions.

7.2 Ku-, Ka- Multiband with 1 Ku- and 2 × 2 Ka- band configuration

7.2.1 Design Configuration

The different dimensions of the Ku- and Ka-bands allow the patches to be in the same layer. A layer by layer view of 1 Ku- and 2 × 2 Ka-band multiband antenna is shown in Figure 7. 2. The patch sizes are a function of the frequency of operation. Since Ku-band operates at 18.7 GHz and Ka-band operates at 37 GHz, the ratio between patch sizes of these antennas are 2 to 1. Hence, both patches can be designed on the same layer without touching each other. However,

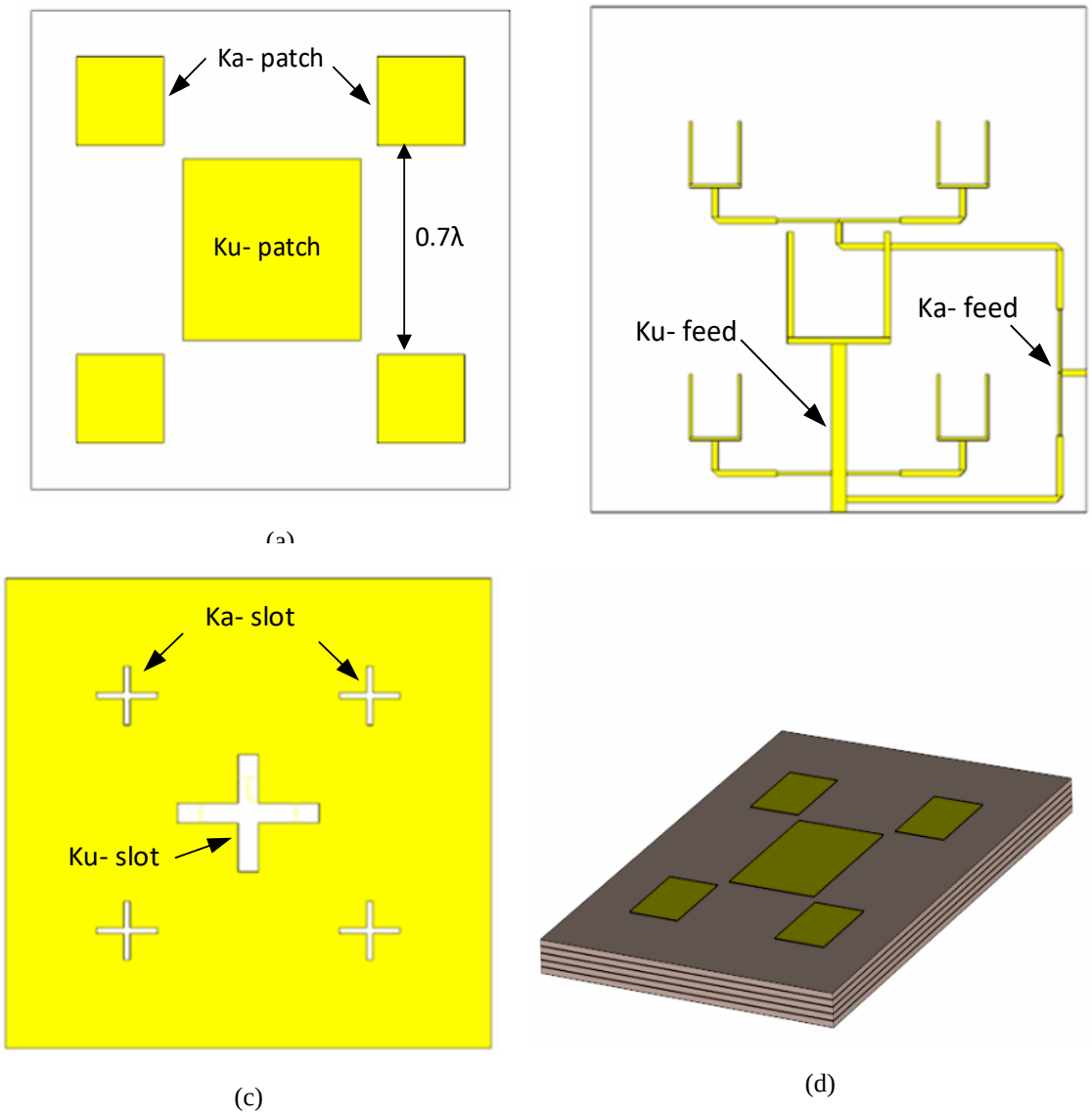

Figure 7. 2 (a) Patch layer, (b) two feed layers from top, (c) ground plane and (d) 3-d view of 1 Ku- and 2 × 2 Ka- band

the feed layers are in different layers and hence their corresponding 50Ω widths are different. The Ku-band being further from the ground plane, has greater width than the Ka-band and can be seen from figure (b). The inter-element distance between two adjacent Ka-band is set to be 0.7λ to avoid grating-lobe.

7.2.2 Simulation Result

7.2.2.1 S- parameter Results and Analysis

Simulation was performed using CST MW Studio 2017 after optimizing the design by tweaking the feed network parameter. All the boundary condition was checked, and simulation environment was set to ideal. The result is presented in this section. The challenge of this design was the distance between the ground plane and feed layer because now there are two substrates and a Ka-band feed. The line width for the 50 Ω feed is changed accordingly.

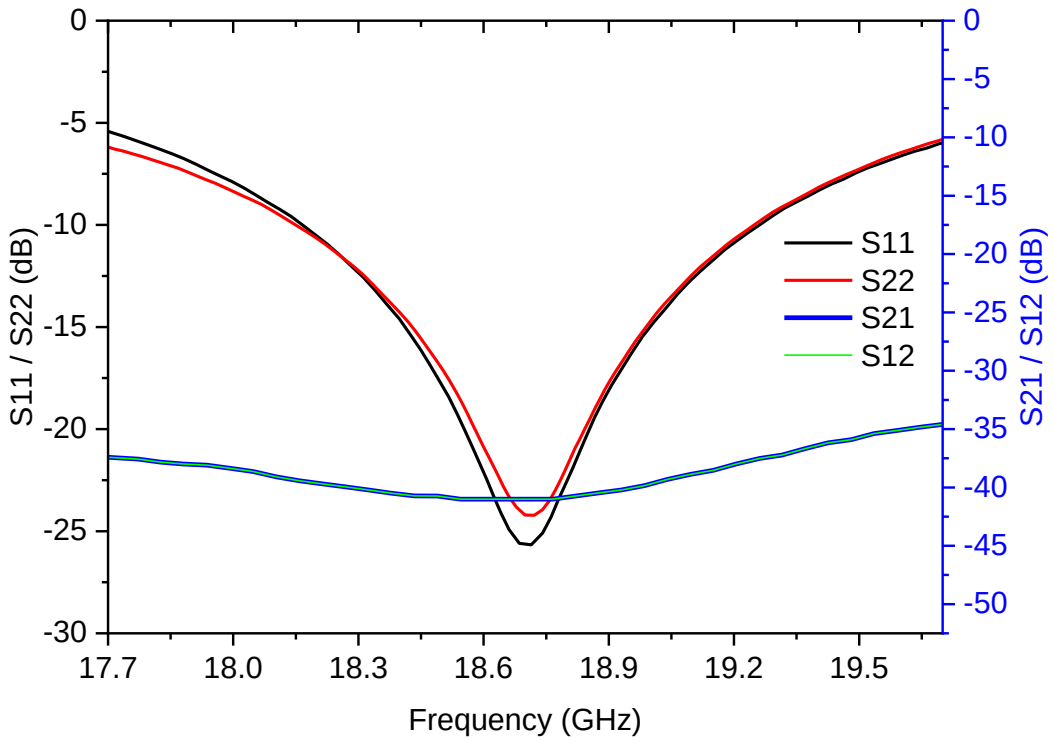

Figure 7. 3 S-parameter result for Ku-band element in the one Ku- and 2 × 2 Ka- multiband antenna

In Figure 7. 3, S-parameter result is shown in the same figure. S11 and S22 result show very good return loss at the resonant frequency (18.7 GHz). Port-to-port isolation or S21 is also less than -35 dB throughout the spectrum. The bandwidth is found around 1.1 GHz ranging from 18.1 GHz to 19.2 GHz. S-parameter result overall shows very good matching and minimum coupling.

S-parameter result is shown in Figure 7. 4. S11 and S22 result show very good return loss at the resonant frequency (37 GHz). Port-to-port isolation or S21 is also less than -45 dB at 37 GHz of the spectrum. The bandwidth is found to be around 3 GHz. S-parameter result overall shows very good matching and minimum coupling.

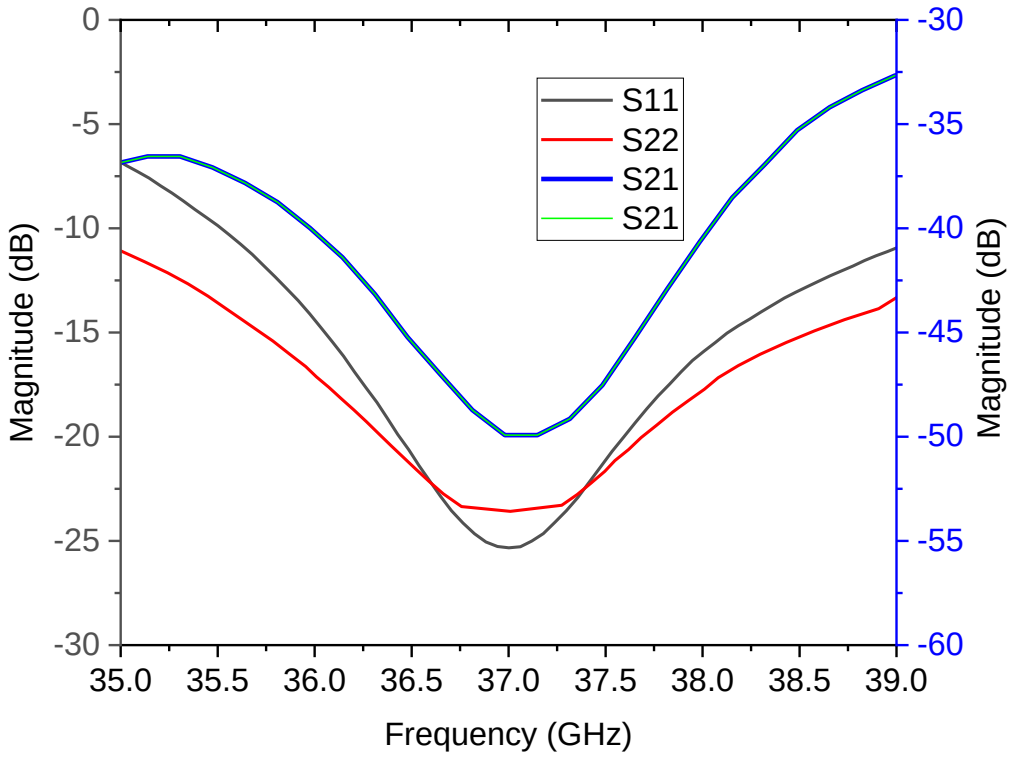

Figure 7. 4 S-parameter result for Ka-band element in the one Ku- and 2 × 2 Ka- multiband antenna

7.2.2.2 Gain Results and Analysis

Figure 7. 5 (a) and (b) show electric and magnetic field radiation pattern for the Ku-band of the one Ku- and 2 × 2 Ka-band array antenna. From the electric field radiation pattern, a maximum gain of 8.7 dBi is found with 65 dB cross polarization level at 0°. Similarly, for the magnetic field, a gain of 8.6 dBi is found at 0°, with a cross polarization level of around 55 dB.

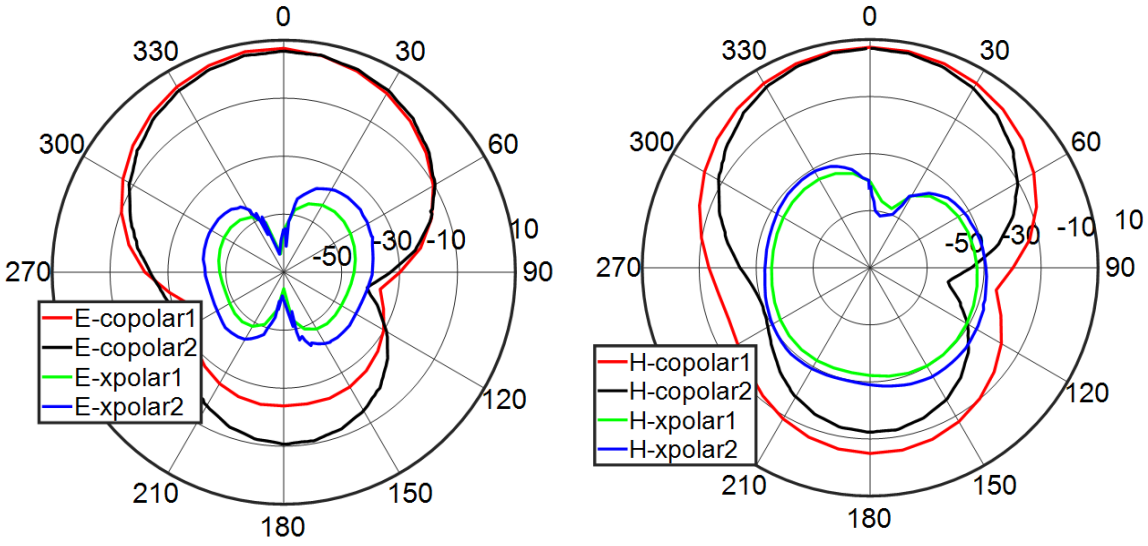

(a) (b)

Figure 7. 5 (a) E- and (b) H-plane field pattern for Ku-band element in the one Ku- and 4 × 4 Ka- multiband antenna.

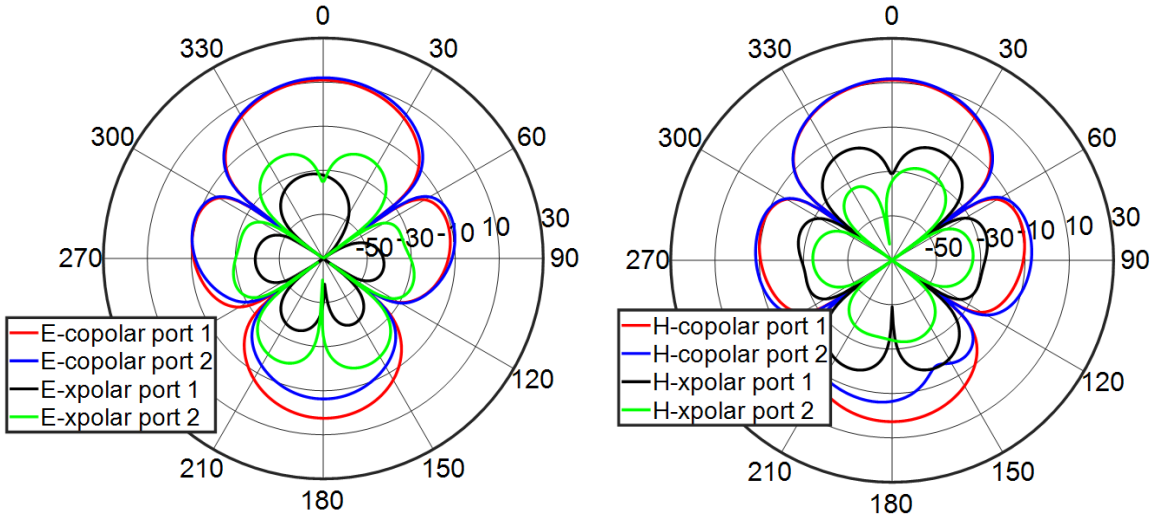

(a) (b)

Figure 7. 6 (a) E- and (b) H-plane field pattern for Ka-band element in the one Ku- and 4 × 4 Ka- multiband antenna.

Figure 7. 6 (a) and (b) show electric and magnetic field radiation pattern for the Ka-band of the one Ku- and 2 × 2 Ka-band array antenna. From the electric field radiation pattern, a maximum gain of 11.5 dBi is found with 38 dB cross polarization level at 0°. Similarly, for the magnetic field, a gain of 11.4 dBi is found at 0°, with a cross polarization level of around 40 dB.

7.3 Ku-, Ka- Multiband with 2 × 2 Ku- and 4 × 4 Ka- band configuration

7.3.1 Design Configuration

DP ACMSA is selected in all feeding techniques as mentioned in the previous chapter. The design of the array is performed using CST MW 2017. First, a power divider for the Ku-band 2 × 2 feed network is designed. Then on top of the centre of the feed network, 2 × 2 patches are placed so that they are exactly above each feed line. Finally, a cross shaped slotted ground plane was designed in the middle of the 2 feed line layers to complete the. The distance between two adjacent elements is again decided to be 0.7λ which in this case is 11.23 mm. If the distance is over λ then grating-lobes appear. Optimal spacing is always a trade-off as smaller inter-element distance will cause strong coupling and vice versa bigger distance will cause grating-lobe. Similarly, 4 × 4 Ka-band antenna is designed. The inter-element distance between two adjacent Ka-band is also chosen to be 0.7λ. Again, as Ku-band operates at 18.7 GHz and Ka-band operates at 37 GHz, the ratio between patch sizes of these antennas are 2 to 1. Hence, both patches can be designed on the same layer without touching each other. The antenna layers are shown in Figure 7. 7. However, the feed layers are in different layers and hence their corresponding 50Ω widths are different. The Ku-band being further from the ground plane, has greater width than the Ka-band and can be seen from figure (b).

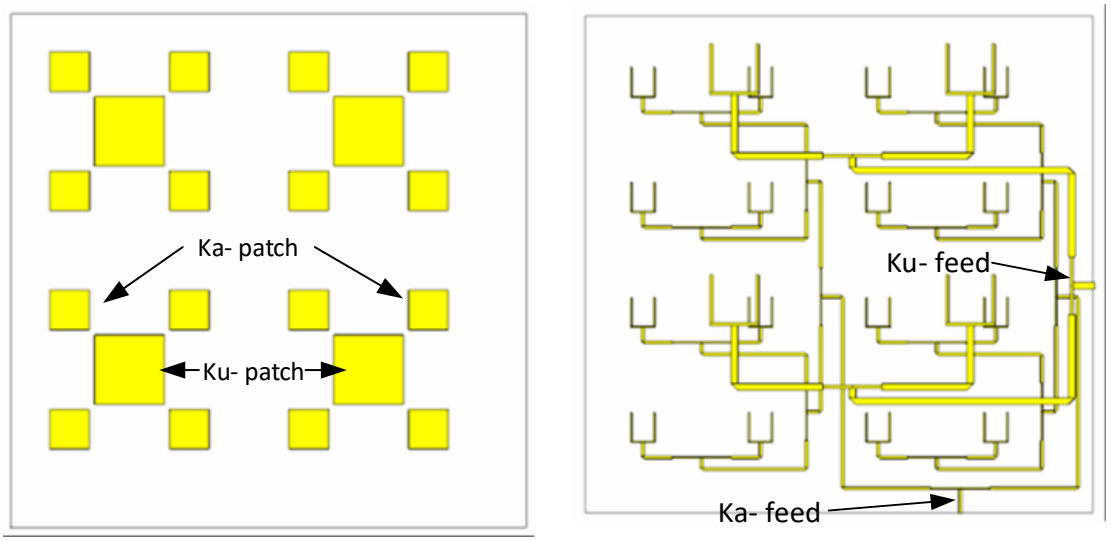

(a) (b)

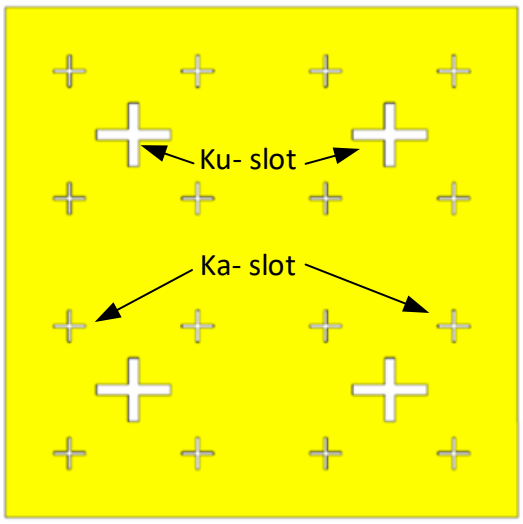

(c)

Figure 7. 7 (a) Patch layer, (b) two feed layers from top, (c) ground plane of the 2 × 2 Ku- and 4 × 4 Ka- band - multiband antenna

7.3.2 Simulation Result

7.3.2.1 S- parameter Results and Analysis

Simulation was performed using CST MW Studio 2017 after optimizing the design by tweaking the feed network parameter. All the boundary condition was checked, and simulation

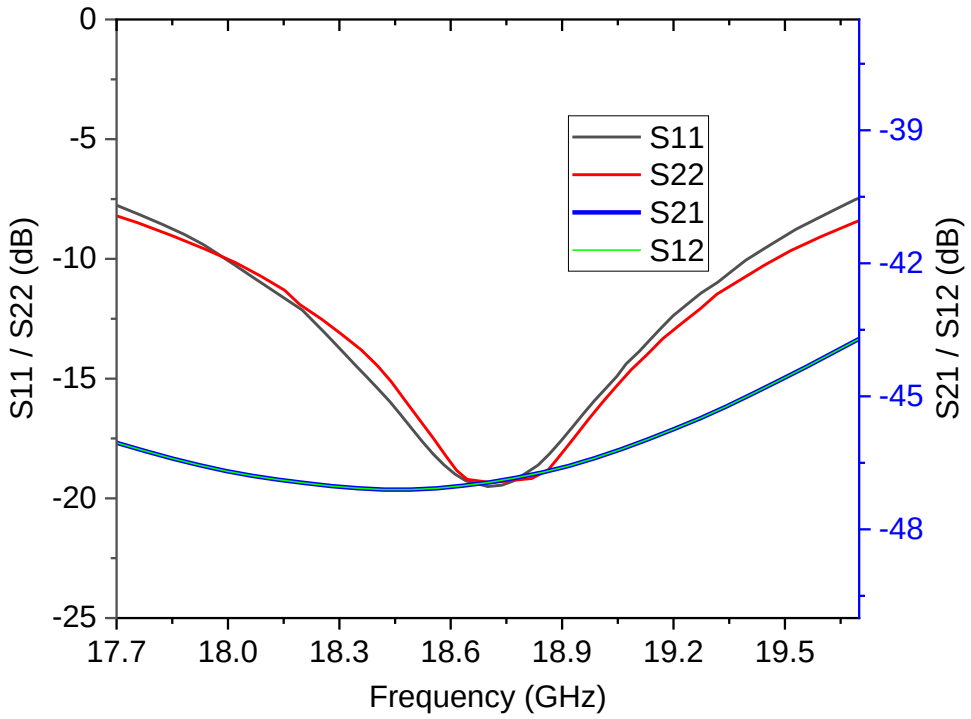

Figure 7. 8 S-parameter result for Ku-band element in the 2 × 2 Ku- and 4 × 4 Ka- band - multiband antenna

environment was set to ideal. The result of the Ku-band array is presented in this section. In Figure 7. 8, S-parameter results are shown in the same figure. S11 and S22 result show very good return loss at the resonant frequency (18.7 GHz). Port-to-port isolation or S21 is also less

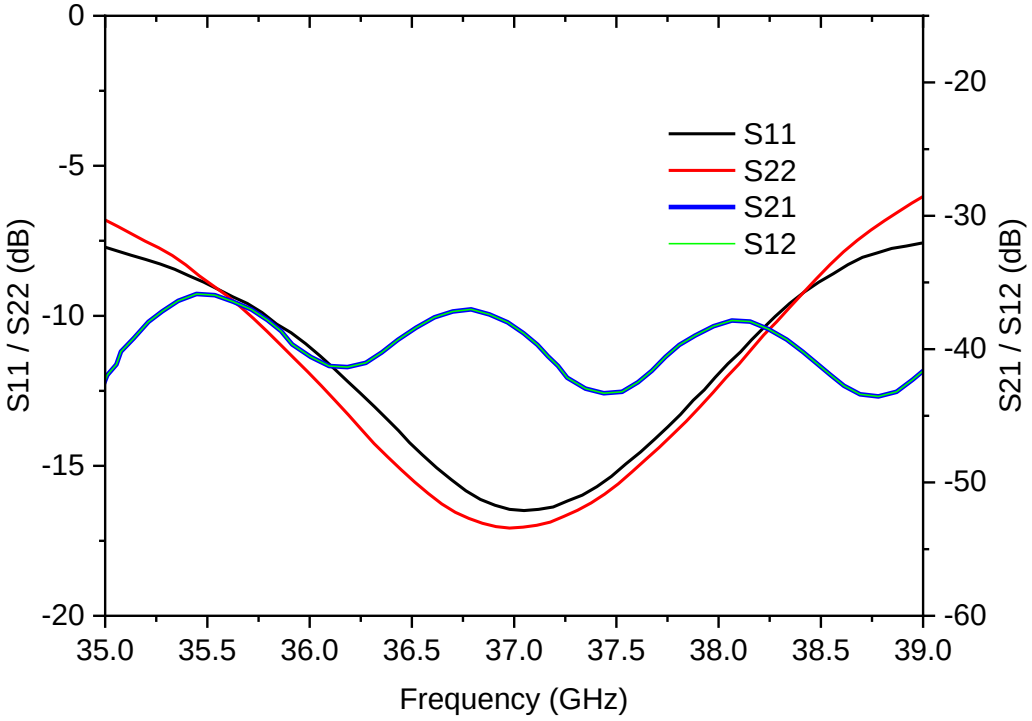

Figure 7. 9 S-parameter result for Ka-band element in the 2 × 2 Ku- and 4 × 4 Ka- band - multiband antenna

than -42 dB throughout the spectrum. The bandwidth is found around 1.1 GHz ranging from 18.0 GHz to 19.1 GHz. S-parameter result overall shows very good matching and minimum coupling.

In Figure 7. 9, S-parameter results of the Ka-band array are shown in the same figure. S11 and S22 result show very good return loss at the resonant frequency (37 GHz). Port-to-port isolation or S21 and S12 are also less than -40 dB throughout the spectrum. The bandwidth is found around 3 GHz ranging from 35.5 GHz to 38.5 GHz. S-parameter result overall shows very good matching and minimum coupling.

7.3.2.2 Gain Results and Analysis

Figure 7. 10 (a) and (b) show electric and magnetic field radiation pattern for the Ku-band 2 × 2 array antenna. From the electric field radiation pattern, a maximum gain of 12.7 dBi is found with 36 dB cross polarization level at 0°. Similarly, for the magnetic field, a gain of 12.8 dBi is found at 0°, with a cross polarization level of around 40 dB. This antenna has a decent amount of back-lobe radiation which can be improved by implementing a back reflector.

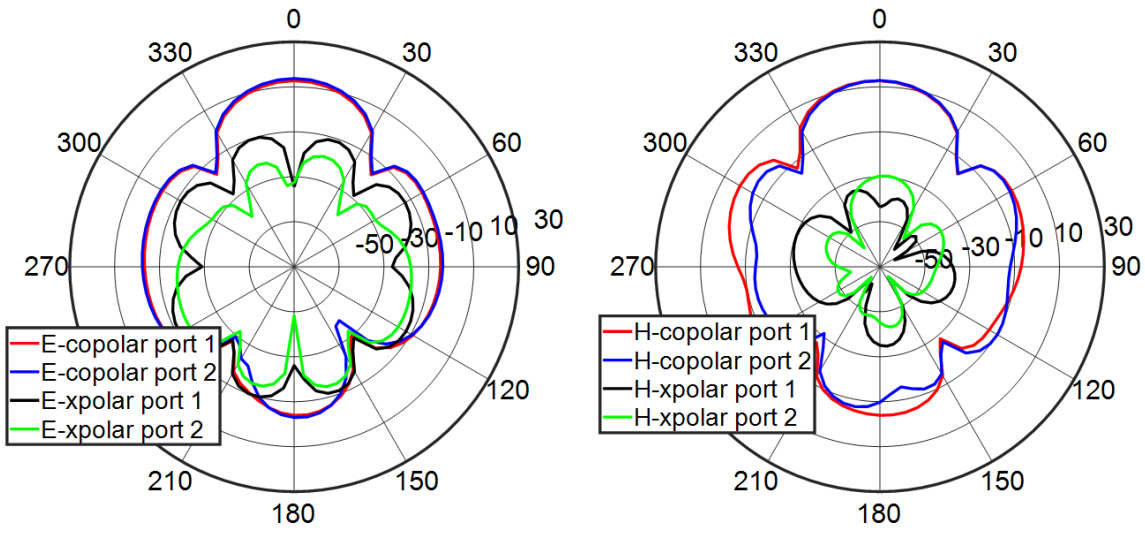

(a) (b)

Figure 7. 10 (a) E- and (b) H-plane field pattern for Ku-band element in the 2 × 2 Ku- and 4 × 4 Ka- band - multiband antenna.

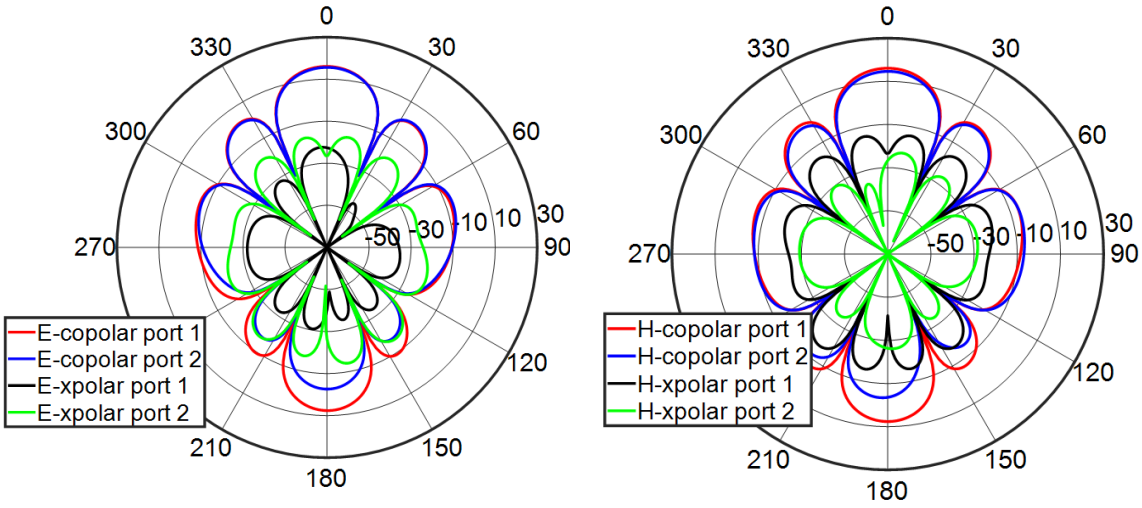

Figure 7. 11 (a) E- and (b) H-plane field pattern for Ka-band element in the 2 × 2 Ku- and 4 × 4 Ka- band - multiband antenna.

Figure 7. 11 (a) and (b) show electric and magnetic field radiation pattern for the Ka-band 4 × 4 array antenna. From the electric field radiation pattern, a maximum gain of 18.7 dBi is found with 50 dB cross polarization level at 0°. Similarly, for the magnetic field, a gain of 18.55 dBi is found at 0°, with a cross polarization level of around 60 dB. This antenna has a decent amount of back-lobe radiation which can be improved by implementing a back reflector.

7.4 Ku-, Ka- Multiband with 4 × 4 Ku- and 8 × 8 Ka- band - multiband antenna band configuration

7.4.1 Design Configuration

For designing 4 × 4 Ku and 8 × 8 Ka-band multiband antenna, again CST MW Studio 2017 is used. It is important to note that, the patches are independent as they are not touching each other. This kind of configuration is possible as the frequency ratio of these two bands are almost 2 to 1. Designing from the top, first the patches are placed 0.7λ distant from each other. Then, one by one feed layer for Ku-band, Ka-band, ground layer and then again Ka-band feed layer and Ka-band feed layer is designed. Ku-band operates at 18.7 GHz and Ka-band operates at 37

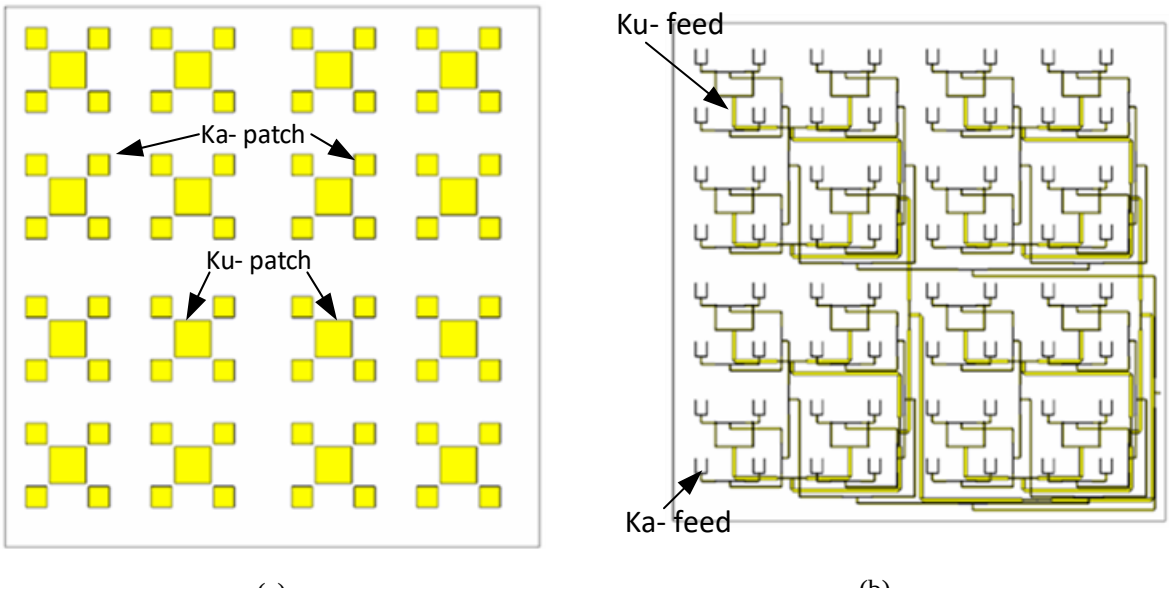

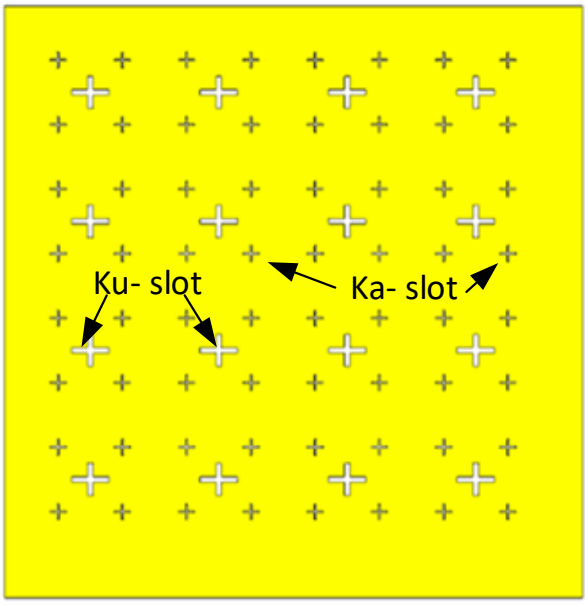

(c)

Figure 7. 12 (a) Patch layer, (b) two feed layers from top, (c) ground plane of the 4 × 4 Ku- and 8 × 8 Ka- band - multiband antenna

GHz, the ratio between patch sizes of these antennas are 2 to 1. Hence, both patches can be designed on the same layer without touching each other. The antenna layers are shown in Figure 7. 12. However, the feed layers are in different layers and hence their corresponding 50Ω widths are different. The Ku-band being further from the ground plane, has greater width than the Ka-band and can be seen from figure (b).

7.4.2 Simulation Result

7.4.2.1 S- parameter Results and Analysis

After a rigorous design and optimization, simulation was performed using CST MW Studio 2017 after setting up the boundary conditions and environment accordingly. The S-parameter

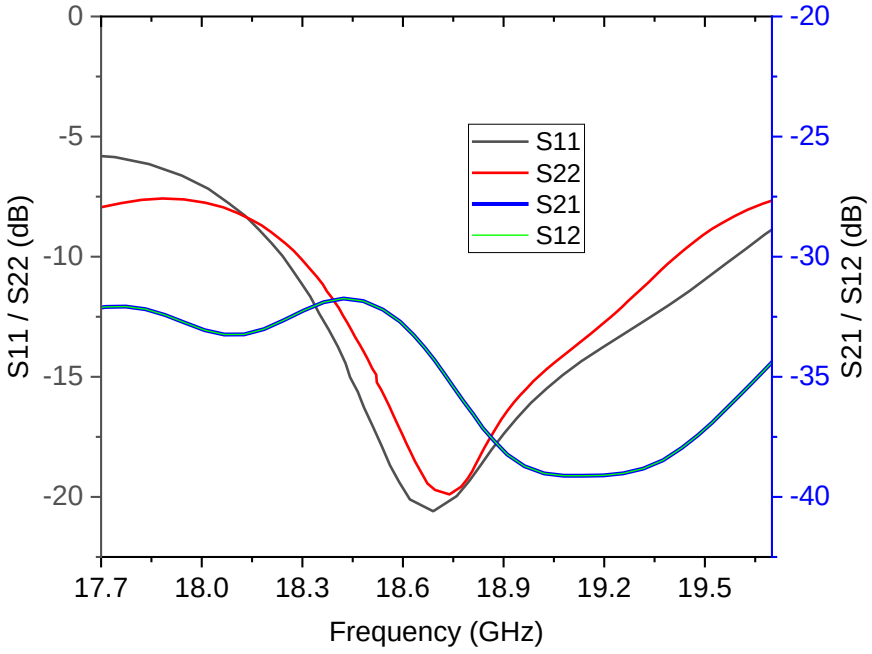

Figure 7. 13 S-parameter result for Ku-band element in the 4 × 4 Ku- and 8 × 8 Ka- band - multiband antenna

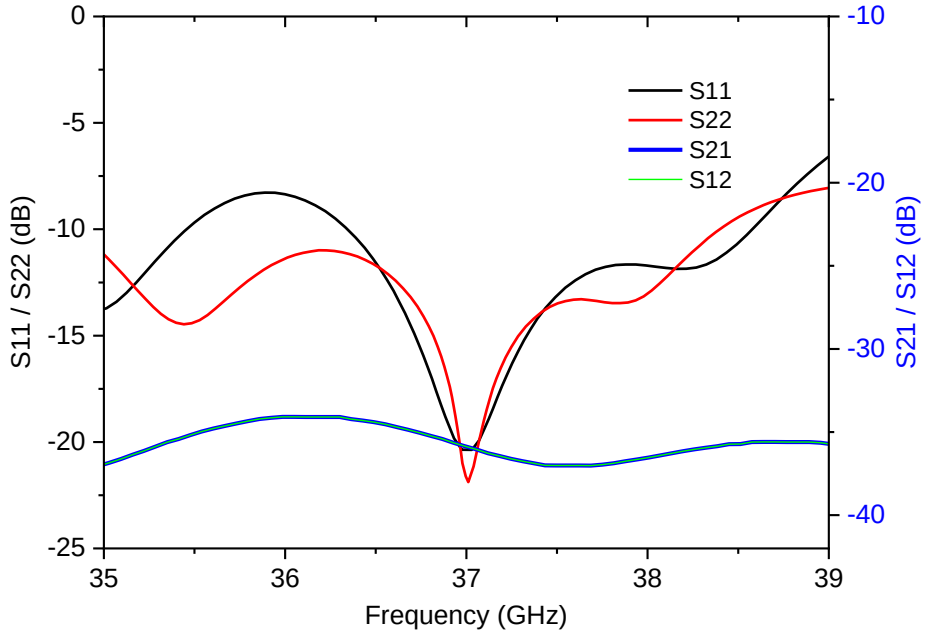

Figure 7. 14 S-parameter result for Ka-band element in the 4 × 4 Ku- and 8 × 8 Ka- band - multiband antenna

results for the Ku- and Ka- bands are shown respectively in Figure 7. 13 and Figure 7. 14. For the Ku-band, the resonant frequency where the best match achieved is at 18.7 GHz proving the design to an efficient one. The bandwidth around 18.7 GHz frequency is also higher than the 500 MHz requirement. S21 or S12 or isolation between ports is also higher than 30 dB which is better than the requirement (25 dB).

For the Ka-band S-parameter results, both S11 and S22 resonate at 37 GHz with bandwidth wider than the requirement. Also, the isolation between ports is greater than 35 dB which makes this design suitable for fabrication and further investigation.

7.4.2.2 Gain Results and Analysis

Figure 7. 15 (a) and (b) show electric and magnetic field radiation pattern for the Ku-band 4 × 4 array antenna. From the electric field radiation pattern, a maximum gain of 19.0 dBi is found with 45 dB cross polarization level at 0°. Similarly, for the magnetic field, a gain of 18.9 dBi is found at 0°, with a cross polarization level of around 50 dB. This antenna has a decent amount of back-lobe radiation which can be improved by implementing a back reflector which improves the front-to-back lobe.

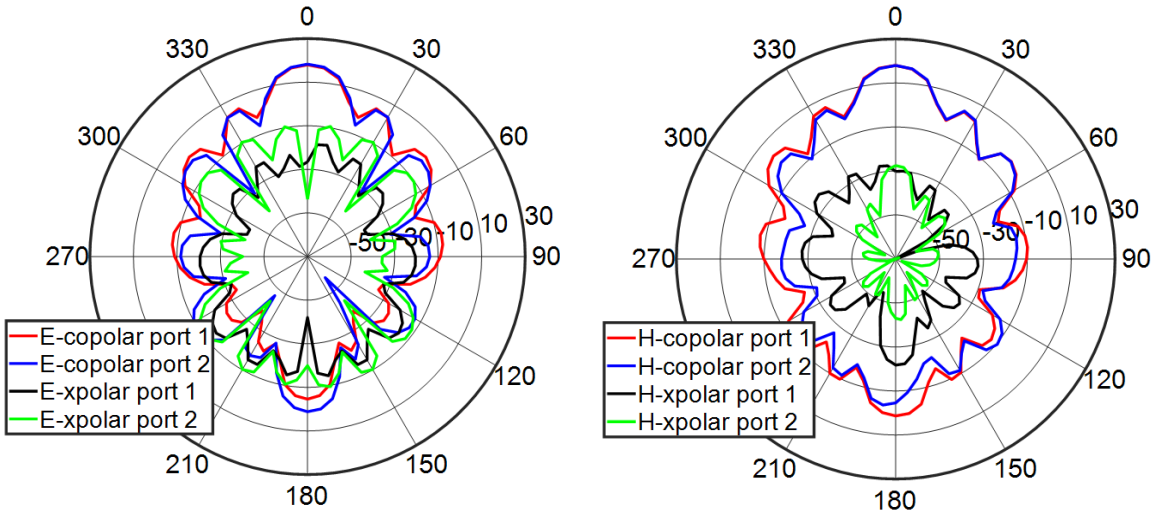

Figure 7. 15 (a) E- and (b) H-plane field pattern for Ku-band element in the 4 × 4 Ku- and 8 × 8 Ka- band - multiband antenna.

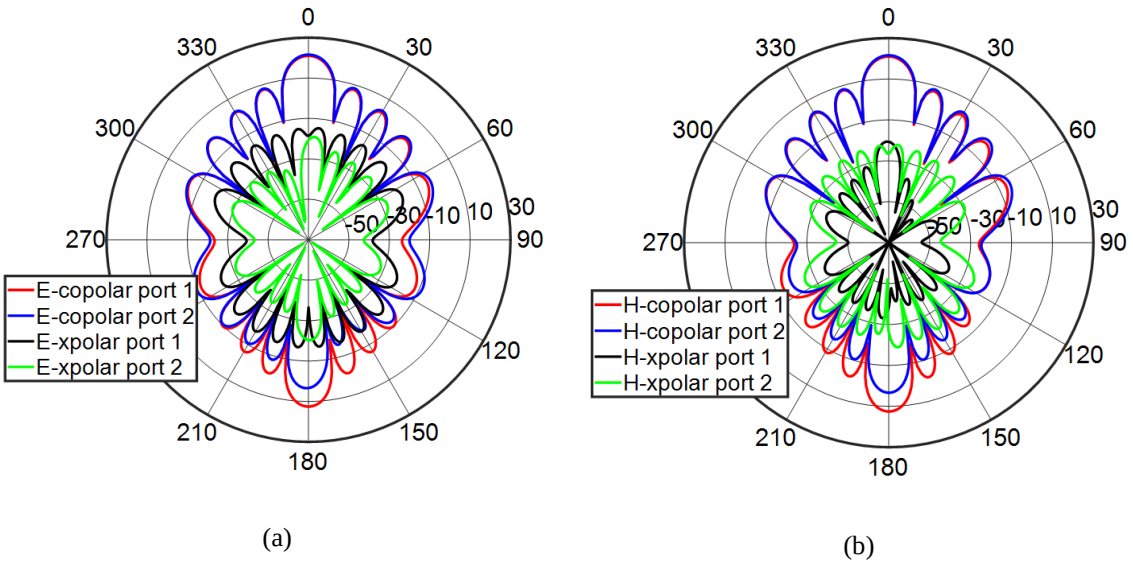

(a) (b)

Figure 7. 16 (a) E- and (b) H-plane field pattern for Ka-band element in the 4 × 4 Ku- and 8 × 8 Ka- band - multiband antenna.

Figure 7. 16 (a) and (b) show electric and magnetic field radiation pattern for the Ka-band 8 × 8 array antenna. From the electric field radiation pattern, a maximum gain of 25.5 dBi is found with 50 dB cross polarization level at 0°. Similarly, for the magnetic field, a gain of 25.2 dBi is found at 0°, with a cross polarization level of around 55 dB. This antenna has a decent amount of back-lobe radiation which can be improved by implementing a back reflector which improves the front-to-back lobe ratio.

7.5 Measurement Results and Analysis

Fabrication and measurement results are achieved for 4 × 4 Ku- and 8 × 8 Ka-band and 4 × 4 Ku- and 8 × 8 Ka-band multiband antenna. S-parameter and radiation pattern are obtained using Agilent's E8361A PNA series vector network analyser in the anechoic chamber. Meticulous measures were taken to ensure other radiations are absent while measuring the S-parameter and radiation pattern result.

7.5.1 4 × 4 Ku- and 8 × 8 Ka-band

Fabrication is done with meticulous precision and measurement is performed carefully. Photograph of the antenna is shown in Figure 7. 17 (a) and (b). The Ku-band patches are surrounded by the Ka-band patches. The connectors are touching the feed lines in the middle layers. Results obtained from Chapter 6 regarding amplitude weighing for SPD method is used for this simulation and fabrication.

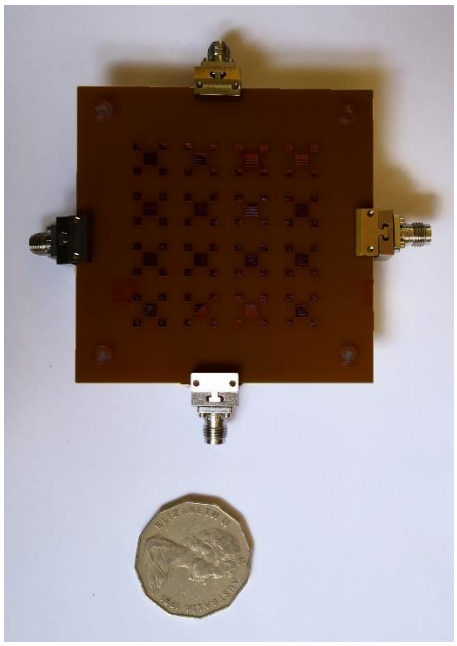

(a)

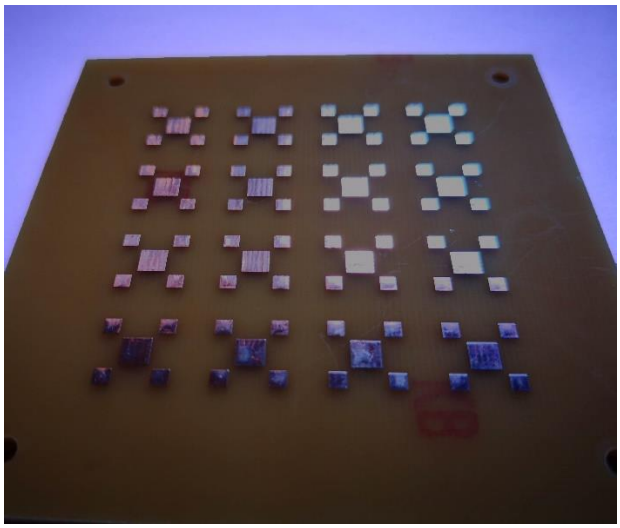

(b)

Figure 7. 17 Assembled 4 × 4 Ku- and 8 × 8 Ka-band antenna (a) size comparison, (b) zoomed in patch layers

7.5.1.1 S-parameter result

As per design guideline, S11 and S22 should be below -10 dB at the design bandwidth. S-parameter results show similarly a good match between the simulation and the measurement for the 4 × 4 Ku-band of the 4 × 4 Ku- and 8 × 8 Ka- band - multiband antenna. In Figure 7. 18 (a) both S11 and S22 measurement result is shown and the result seem to resonate at 18.7 GHz with a bandwidth of approximately 1 GHz. At 18.7 GHz, the S11 and S22 levels are -19 dB and -17 dB. For isolation between the ports, S21 or S12 should be below -25 dB according to

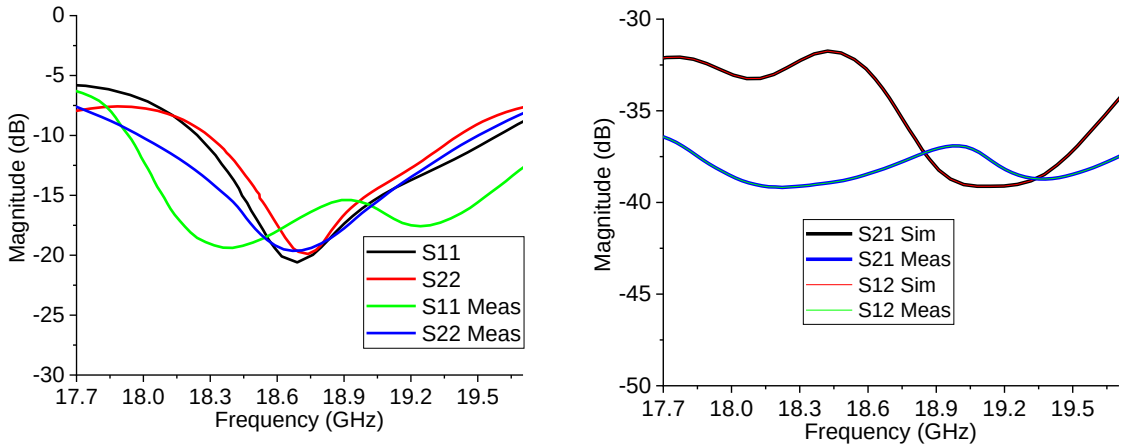

(a) (b)

Figure 7. 18 S-parameter results of (a) Reflection coefficient S11 and S22 and (b) isolation between ports S21 and S12 simulation and measurement for Ku-band element in the 4 × 4 Ku- and 8 × 8 Ka- band - multiband antenna.

the design goal. In Figure 7. 18 (b), S11 and S22 are compared with the simulation result and is found to be less than -30 dB throughout the spectrum and hence meet the design requirement of 25 dB isolation easily.

For the Ka-band configuration, it is an 8 × 8 array. The reflection coefficient or S11 / S22 and isolation or S21 / S12 measurement results are shown along with the simulation result in Figure 7. 19. The measurement results of the reflection coefficient or S11 / S22 follow the simulation result very well proving the design and fabrication efficiency. Both the S11 and S22 resonate

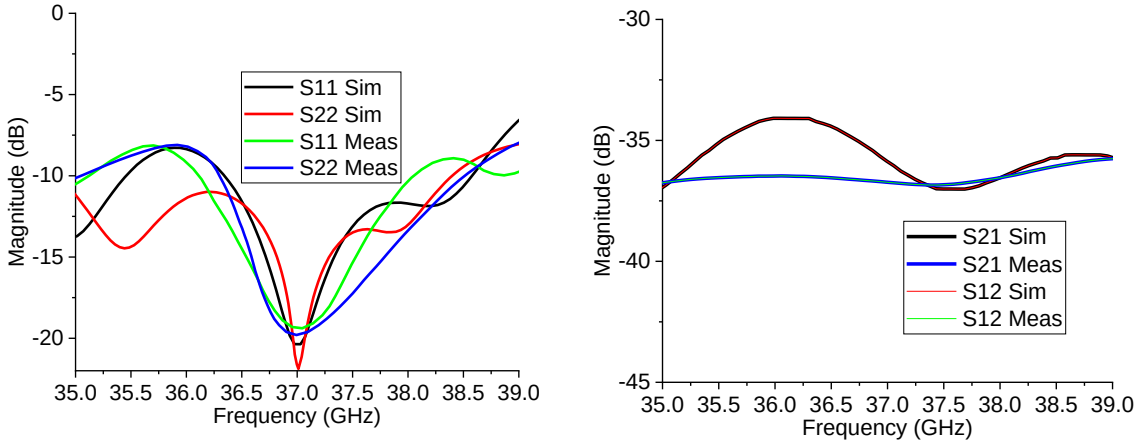

(a) (b)

Figure 7. 19 S-parameter results of (a) Reflection coefficient S11 and S22 and (b) isolation between ports S21 and S12 simulation and measurement for Ka-band element in the 4 × 4 Ku- and 8 × 8 Ka- band - multiband antenna.

at 37 GHz with a magnitude of -19 dB and -19.4 dB. The bandwidth is more than 1.5 GHz around the resonant frequency. The isolation or S21/ S12 also follow the simulation result as the isolation is more than 35 dB throughout the spectrum.

7.5.1.2 Radiation pattern

Two identical antennas are used to measure the radiation pattern by calculating the amount of radiation transmitted and received. The measurement result is then plotted in the same plot as the simulation result. In Figure 7. 20 (a) and (b), the electric field radiation pattern of the Ku-band of the 4 × 4 Ku- and 8 × 8 Ka- band multiband antenna is shown.

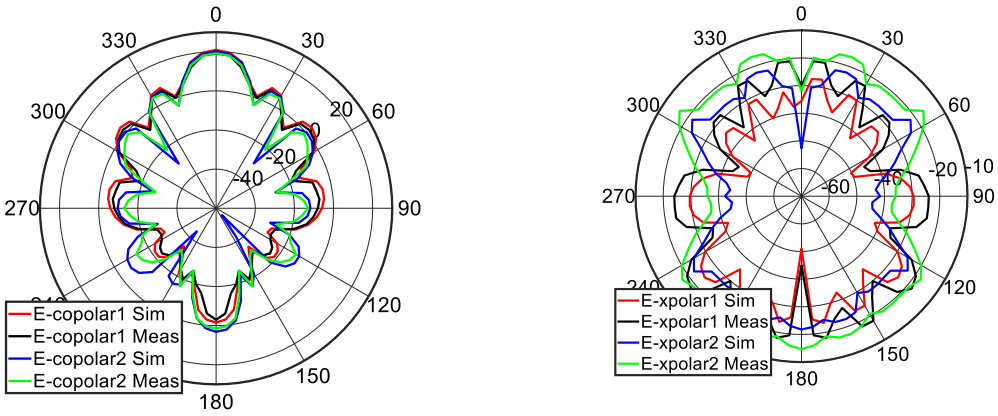

(a) (b)

Figure 7. 20 Simulation and measurement result of E-plane radiation pattern for (a) co-polar and (b) cross-polar of the Ku-band element in the 4 × 4 Ku- and 8 × 8 Ka- band - multiband antenna.

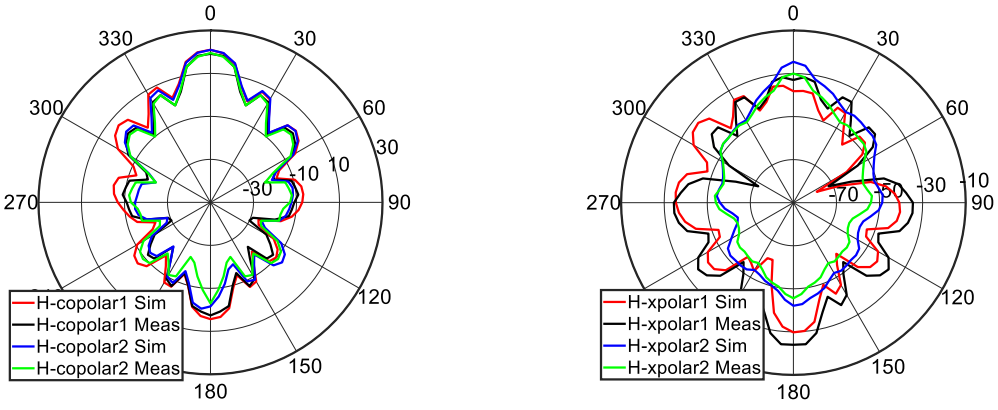

(a) (b)

Figure 7. 21 Simulation and measurement result of H-plane radiation pattern for (a) co-polar and (b) cross-polar of the Ku-band element in the 4 × 4 Ku- and 8 × 8 Ka- band - multiband antenna.

Both the co-polar and cross-polar pattern follow each other in the same fashion. The magnitude of the co-polar pattern at 0° is maximum for co-polar radiation. The cross-polar level is very low at 0° making the design very suitable for radiometer operation. The magnitude for co-polar electric field is 19.7 dBi and for cross-polar, it is -30 dB.

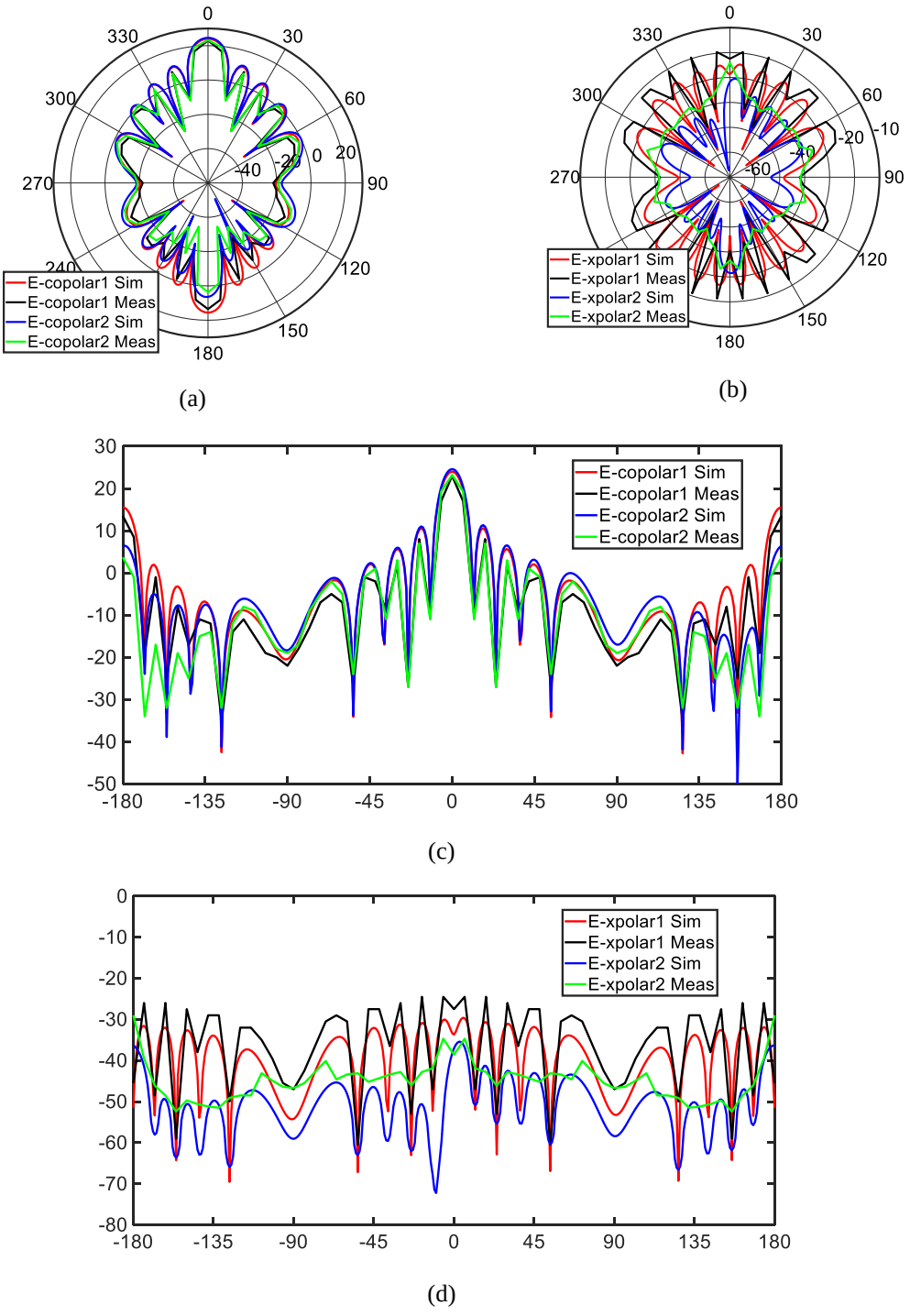

Figure 7. 22 Simulation and measurement result of E-plane radiation pattern for (a) co-polar and (b) cross-polar of the Ka-band element in the 4 × 4 Ku- and 8 × 8 Ka- band - multiband antenna, (c) and (d) line plot of (a) and (b)

For the magnetic field radiation pattern, the measurement result of the Ku-band is shown in Figure 7. 21. Both co-polar and cross-polar measurement results follow the simulation radiation pattern. The main beam is again at 0° for the co-polar and the magnitude is 19.7 dBi. For the cross-polar pattern, at 0° the cross-polar level is at around -28 dB.

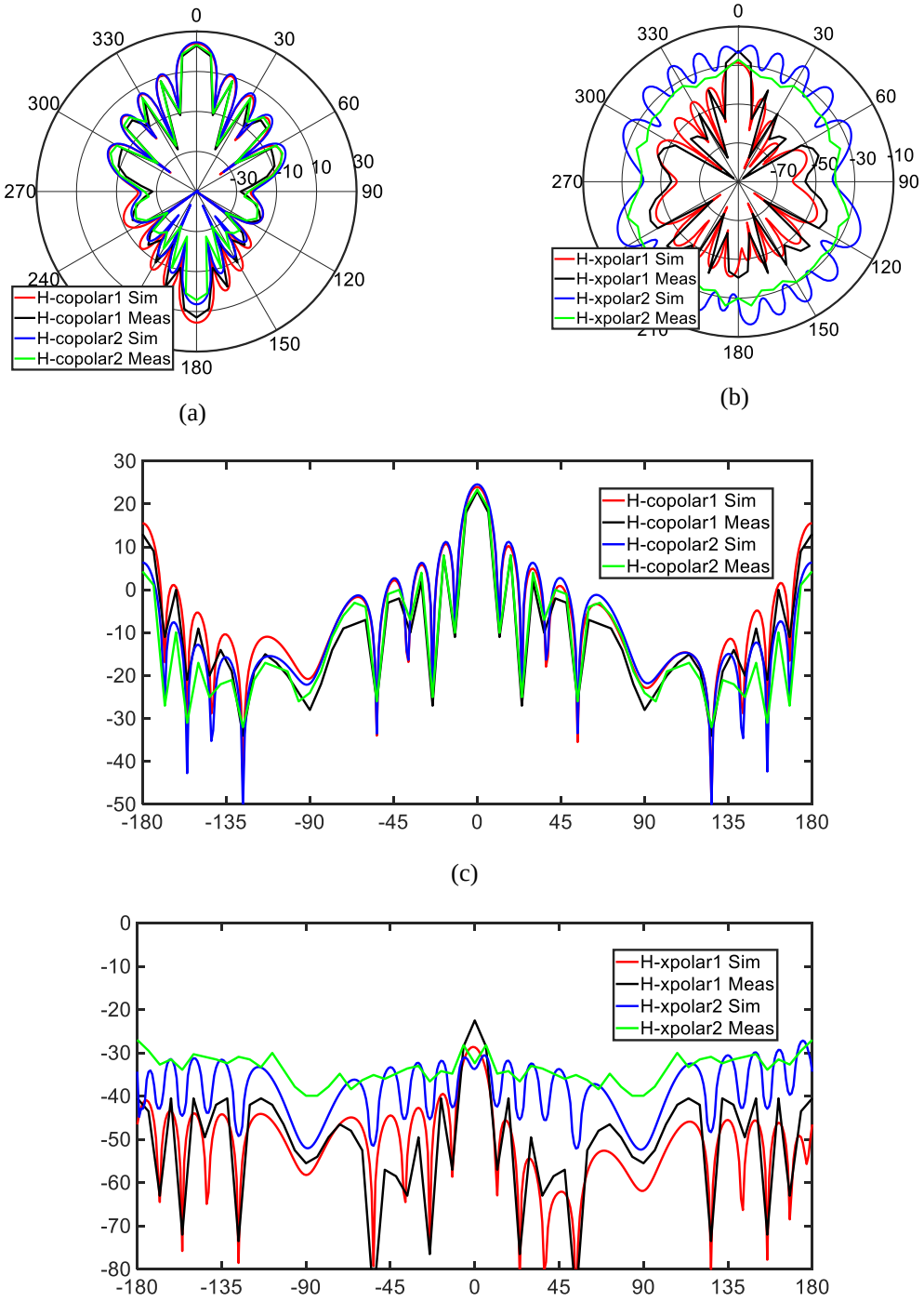

Figure 7. 23 Simulation and measurement result of H-plane radiation pattern for (a) co-polar and (b) cross-polar of the Ka-band element in the 4 × 4 Ku- and 8 × 8 Ka- band - multiband antenna, (c) and (d) line plot of (a) and (b).

For the 8 × 8 Ka- band array, the radiation pattern result for the electric field is shown in Figure 7. 22. In Figure 7. 22 (a) the co-polar pattern is plotted for both the simulation and measurement. The measurement result and the simulation result have the same shape and follow each other closely. For the co-polar pattern, the main lobe is at 0° and the magnitude is 23.2 dBi. For the cross-polar pattern, the minimum cross polarization is also at 0° and the magnitude is -27 dB.

For the magnetic field pattern, Figure 7. 23 (a) and (b) show the co-polar and cross-polar radiation patterns. For both ports, again the simulation result follows the measurement result. The main lobe of the co-polar pattern is at 0° and the magnitude is 23.2 dBi. For the cross-polarization pattern, the cross polarization at 0° is -28 dB.

7.5.2 8 × 8 Ku- and 8 × 8 Ka-band

After fabrication and assembly, the Assembled 8 × 8 Ku- and 8 × 8 Ka-band antenna is measured. Photograph of the assembled antenna is shown in Figure 7. 24. There are four connectors to connect to the four ports. Two ports are for the Ku-band and the rest two ports are for the Ka-band dual polarizations.

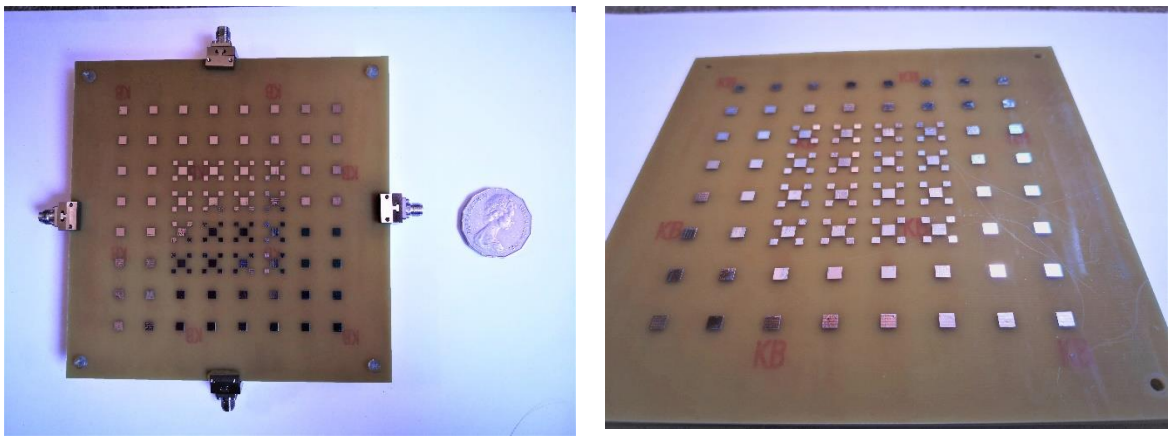

(a) (b)

Figure 7. 24 Assembled 8 × 8 Ku- and 8 × 8 Ka- multi-band antenna (a) size comparison, (b) zoomed in patch layers

7.5.2.1 S-parameter result

S-parameter results show a similar trend between the simulation and the measurement. As a must requirement, S11 and S22 should be below -10 dB. In Figure 7. 25 (a) both S11 and S22 measurement result is shown for the 8 × 8 Ku-band and the result seem to resonate at 18.7 GHz with a bandwidth of approximately 1 GHz. At 18.7 GHz, the S11 and S22 levels are -20 dB and -21.3 dB. For isolation between the ports, according to the design goal, S21 or S12 should be below -25 dB. In Figure 7. 25 (b), S21 and S12 are compared with the simulation result and is found to be less than -40 dB throughout the spectrum and hence meet the design requirement of 25 dB isolation easily.

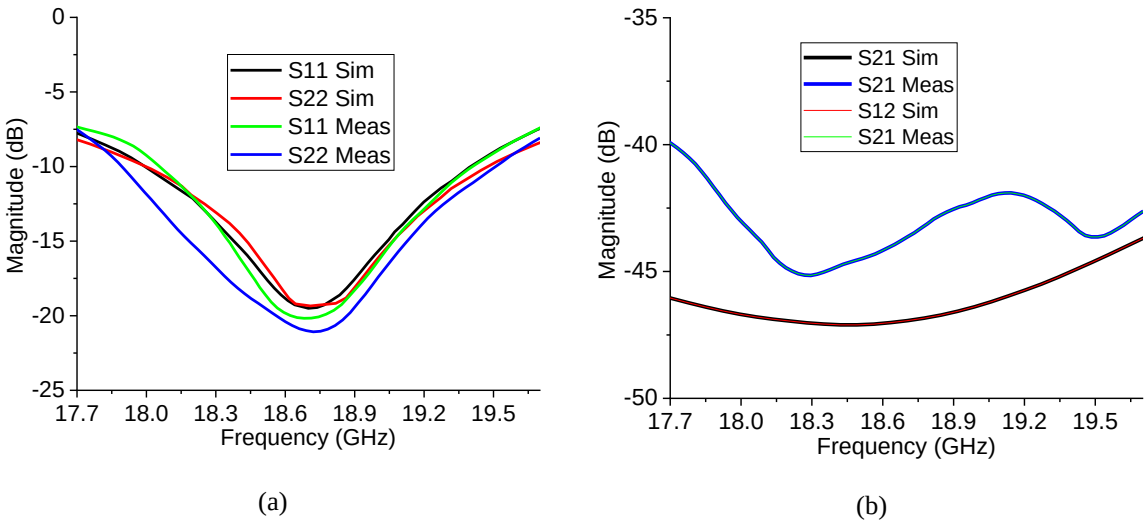

(a) (b)

Figure 7. 25 S-parameter results of (a) Reflection coefficient S11 and S22 and (b) isolation between ports S21 and S12 simulation and measurement for Ku-band element in the 8 × 8 Ku- and 8 × 8 Ka-band multiband antenna.

For the Ka-band configuration, it is also an 8 × 8 array. The reflection coefficient or S11 / S22 and isolation or S21 / S12 measurement results are shown along with the simulation result in Figure 7. 26. The measurement results of the reflection coefficient or S11 / S22 follow the simulation result very well proving the design and fabrication validity. Both the S11 and S22 resonate at 37 GHz with a magnitude of -17.1 dB and -15.8 dB. The bandwidth is more than 2

GHz around the resonant frequency. The isolation or S21/ S12 also follow the simulation result as the isolation is more than 35 dB throughout the spectrum.

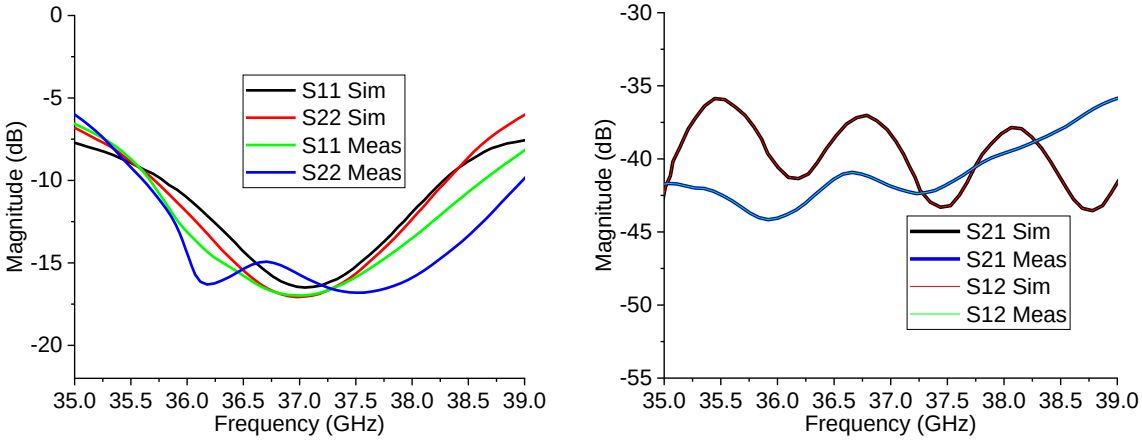

(a) (b)

Figure 7. 26 S-parameter results of (a) Reflection coefficient S11 and S22 and (b) isolation between ports S21 and S12 simulation and measurement for Ka-band element in the 8 × 8 Ku- and 8 × 8 Ka-band multiband antenna.

7.5.2.2 Radiation pattern

Using state-of-the-art anechoic chamber, Agilent's VNA and two identical antennas, the fabricated antenna is measured and using Matlab and Origin, plotted against the simulated data generated in CST. In Figure 7. 27 (a) and (b), the electric field radiation pattern of the Ku-band of the 8 × 8 Ku- and 8 × 8 Ka- band multiband antenna is shown. The co-polar and cross-polar results show very similarity with the simulated results. The magnitude of the co-polar pattern at 0° is maximum for the co-polar and minimum for the cross-polar pattern. This feature makes the design very suitable for the radiometer operation. The magnitude for co-polar electric field is 22.22 dBi and for cross-polar, it is -21.1 dB.

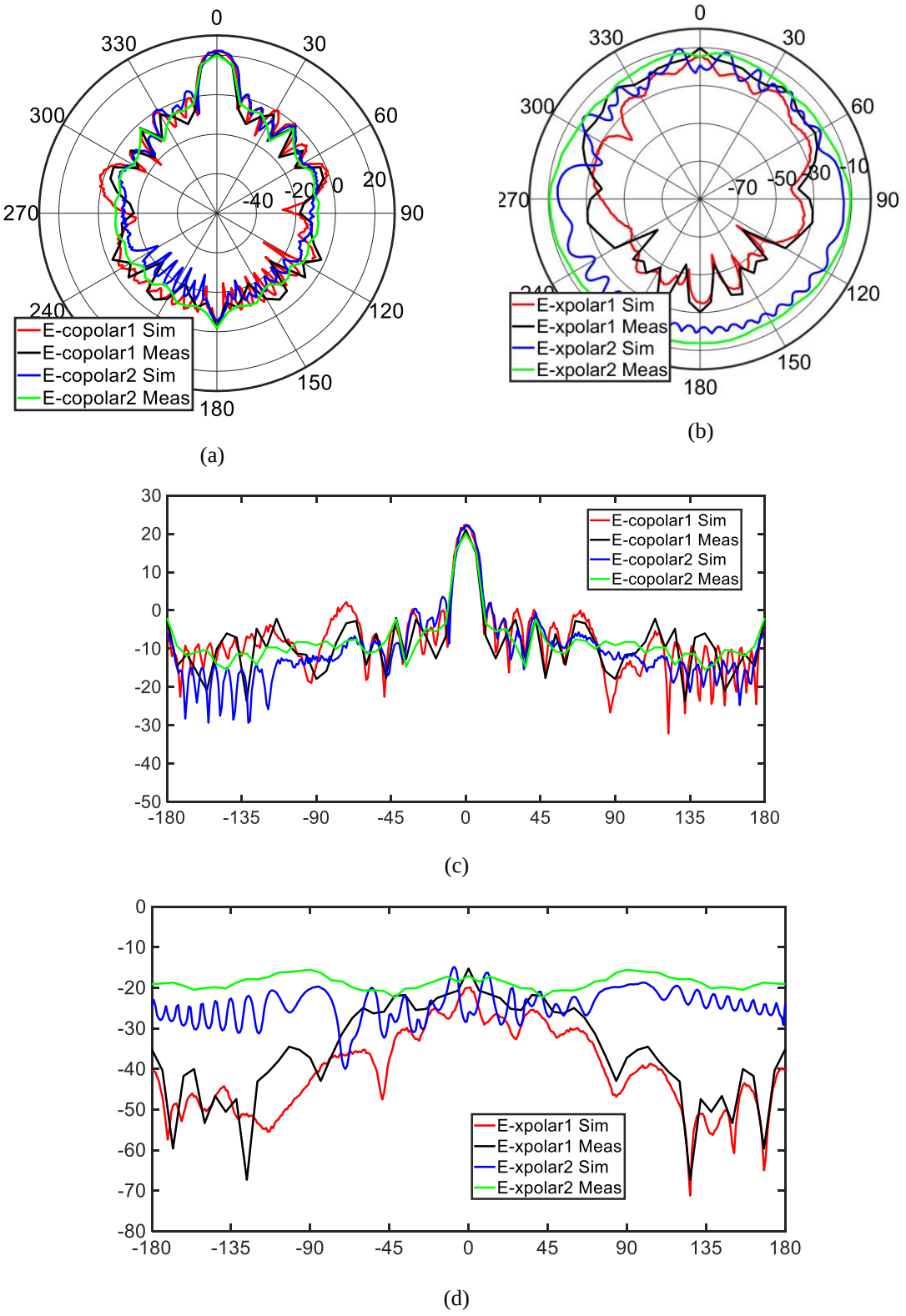

Figure 7. 27 Simulation and measurement result of E-plane radiation pattern for (a) co-polar and (b) cross-polar of the Ku-band element in the 8 × 8 Ku- and 8 × 8 Ka- band - multiband antenna, (c) and (d) line plot of (a) and (b)

For the magnetic field, the measurement result of the Ku-band is shown in Figure 7. 28. Both co-polar and cross-polar measurement results follow the simulation pattern. The main beam is

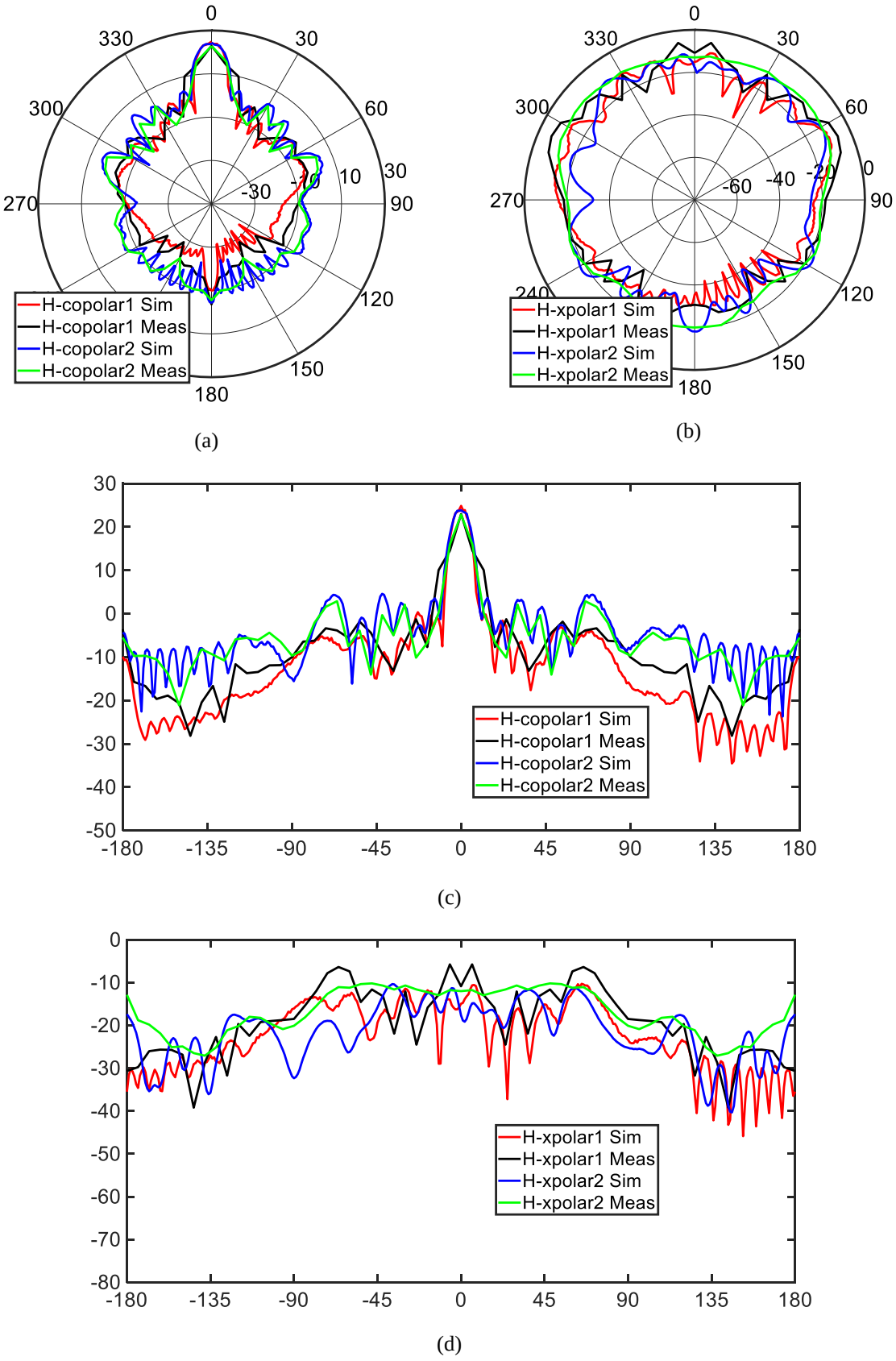

Figure 7. 28 Simulation and measurement result of H-plane radiation pattern for (a) co-polar and (b) cross-polar of the Ku-band element in the 8 × 8 Ku- and 8 × 8 Ka- band - multiband antenna, (c) and (d) line plot of (a) and (b)

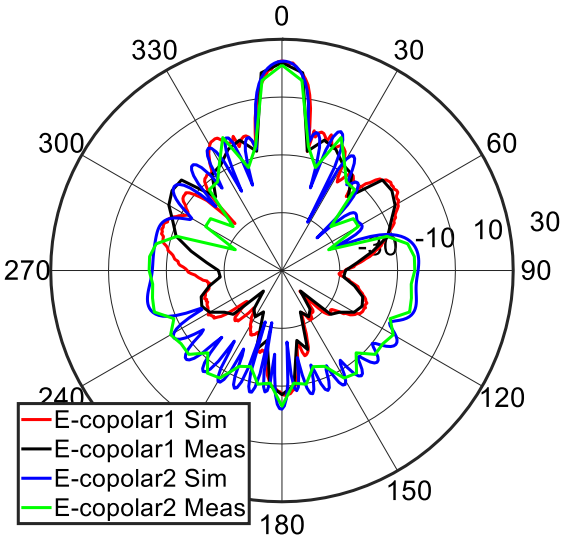

(a)

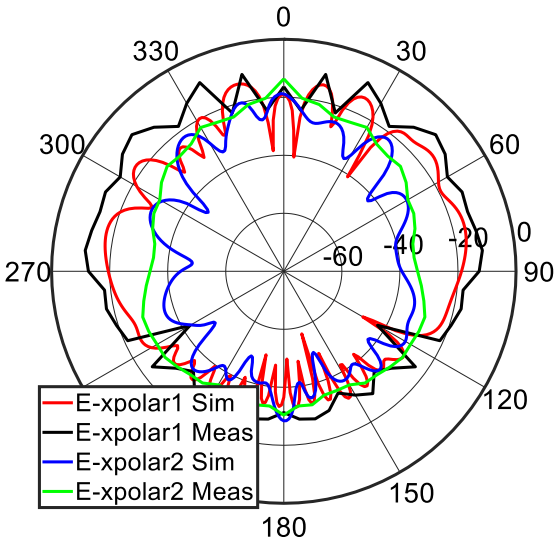

(b)

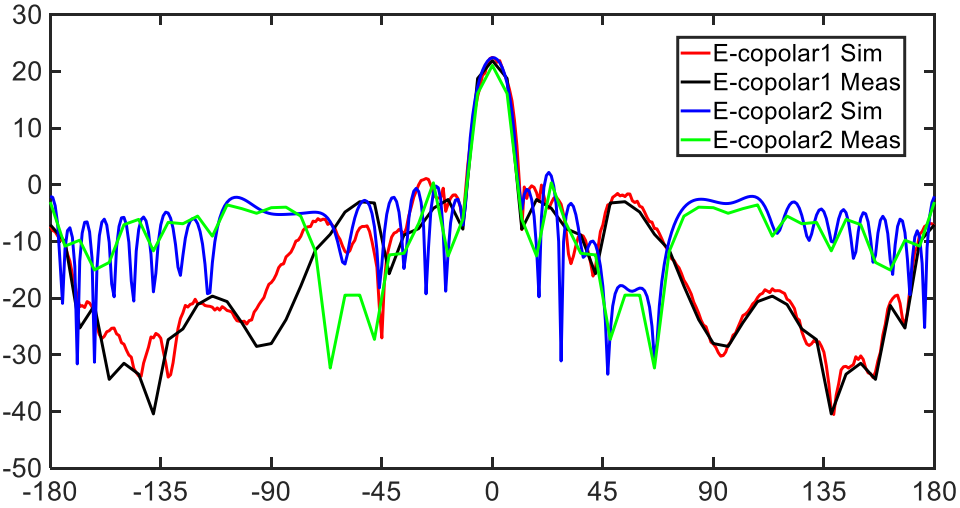

(c)

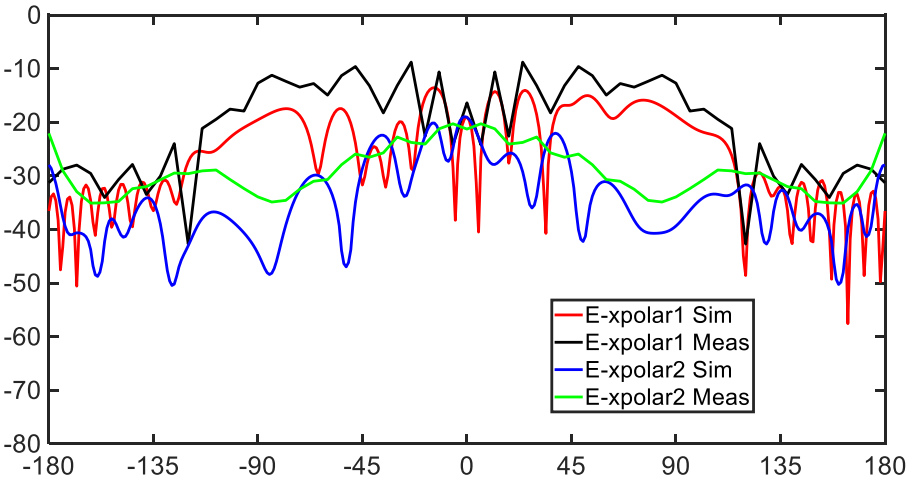

(d)

Figure 7. 29 Simulation and measurement result of E-plane radiation pattern for (a) co-polar and (b) cross-polar of the Ka-band element in the 8 × 8 Ku- and 8 × 8 Ka- band - multiband antenna, (c) and (d) line plot of (a) and (b)

minimum is at 0° at around -20 dB. For the 8 × 8 Ka- band array, the radiation pattern result

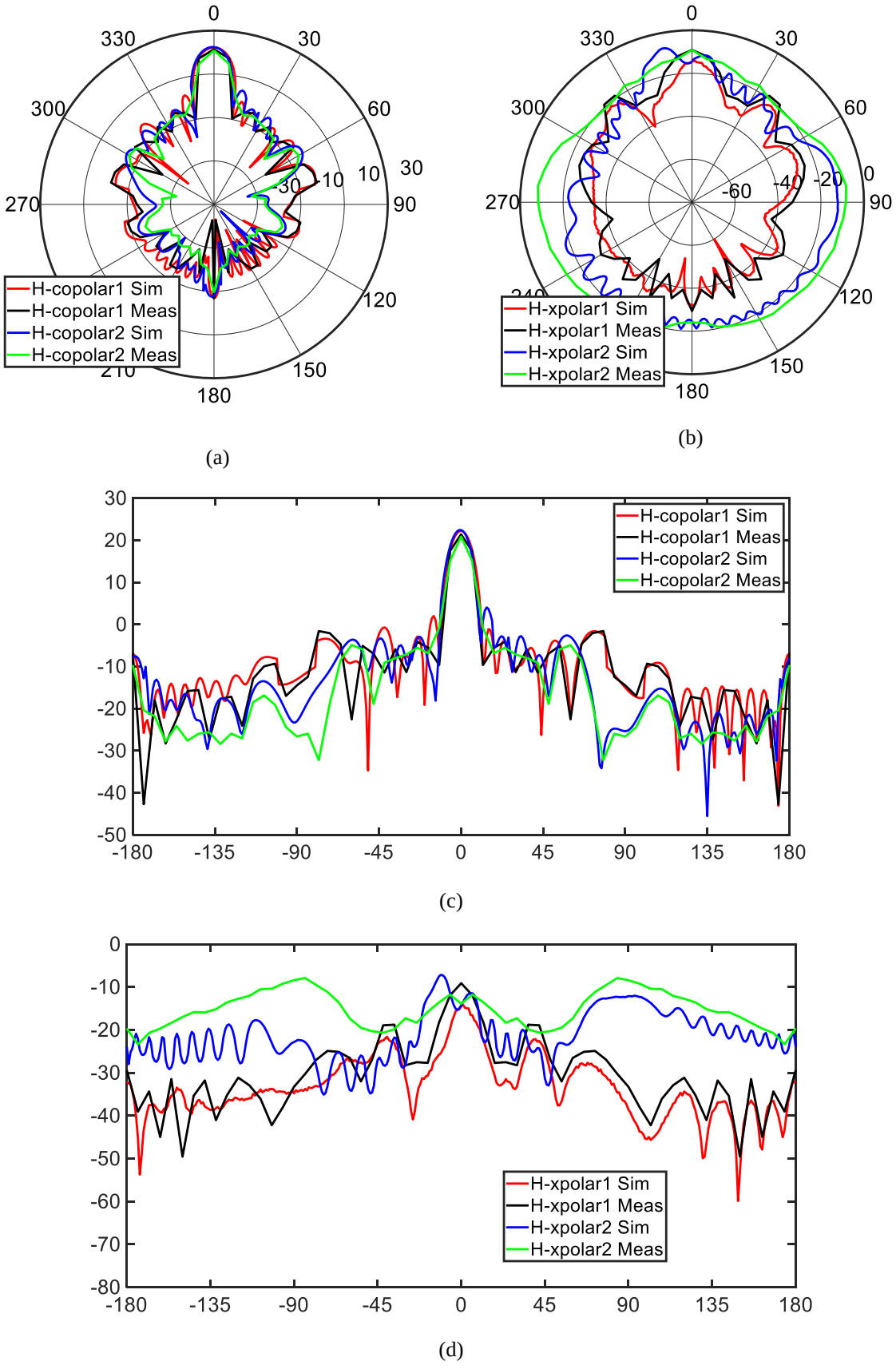

Figure 7. 30 Simulation and measurement result of H-plane radiation pattern for (a) co-polar and (b) cross-polar of the Ka-band element in the 8 × 8 Ku- and 8 × 8 Ka- band - multiband antenna, (c) and (d) line plot of (a) and (b)

for the electric field is shown in Figure 7. 29. In Figure 7. 29 (a) the co-polar pattern is plotted for both the simulation and measurement. The measurement result follows the simulation result closely. For the co-polar pattern, the main lobe is at 0° and the magnitude is 23.1 dBi. For the cross-polar pattern, the minimum cross polarization is also at 0° and the magnitude is -20 dB.

For the magnetic field pattern, Figure 7. 30 (a) and (b) show the co-polar and cross-polar radiation patterns. For both ports, the measurement result is similar to the simulation result. The main lobe of the co-polar pattern is at 0° and the magnitude is 23.2 dBi. For the cross-polarization pattern, the cross polarization at 0° is -18 dB providing over 40 dB cross-polarization level at 0°.

7.6 Conclusions

In conclusion, this chapter discusses multi-band structure of Ku- and Ka-band array. Starting with an overview, this chapter discusses the structure, simulation and measurement of different number of array element and compare them by plotting.

The main finding of this chapter is the 8 × 8 Ku- and 8 × 8 Ka- band - multiband antenna, that can be used in the receiver module of the radiometer system that can collect data. The compact size and light weight of this antenna has made this ready to be used in a drone to fly over a field and collect moisture data to be processed.

Starting with one single Ku-band surrounded by four Ka-band, then using the same design technique to extend the combination to 2 × 2 Ku- and 4 × 4 Ka- band, then to 4 × 4 Ku- and 8 × 8 Ka- band and finally 8 × 8 Ku- and 8 × 8 Ka- band - multiband antenna. The frequency ratio of Ku-band at 18,7 GHz and Ka-band at 37 GHz makes the design possible. The ratio of the dimensions of the patch and inter-element distance become around 2 to 1, making the patches placed on the same layer without touching each other and still maintain symmetry.

The most challenging part of this design is to design the feed network. In the aperture coupled design, the feed line induces the radiation in the patch layer and the slotted ground plane. It is important to place the feed line exactly aligned with the ground slot and the patch. The complex part of this design is to design the feed network so that they do not overlap each other at the ground slot and patch. Also, whenever two microstrip lines are close to each other, spurious radiation results distortion in the radiation pattern and as well as overall impedance matching. On the other hand, if the antennas are too far from each other grating-lobe takes place and deteriorates the main lobe with equal side lobes. Grating-lobe is a bigger problem than the little spurious radiation, so this sacrifice is made. Hence the radiation patterns are not exactly symmetric, but they still have a clear distinct main lobe. Also, in the layered design each feed network is placed in different layer meaning the Ku-band are put further from the ground plane than the Ka-band. Further distance from the ground plane results in wider feed line, so optimization is necessary to design the Ku-band antenna.

The SPD beam shaping algorithm is again applied on the array to shape the beam and suppress side lobes. A back reflector is also used to suppress the back-lobe radiation. The S-parameters and the radiation pattern for both bands are both simulated and measured after fabrication. The simulation and the measurement results are consistent and a proof of efficient designing.

Inclusion of 16 × 16 Ka-band is thought for future work. L-band array in the multiband structure is also planned for future work.

In the end, these findings of this chapter can provide a cheap and efficient way to approximating the soil moisture data for Ku- and Ka-bands to improve resolution of the footprint of the radiometer.

8 Soil Moisture Measurement

8.1 Overview

After designing, fabrication and measurement of L-, Ku- and Ka-band antenna arrays and multi-band array, this chapter discusses the sensitivity measurement of these antennas for different moisture content of soil. Soil has different dielectric constants for different moisture contents and hence different emissions. The emission changes due to the change in the soil moisture or in another word due to the change in the dielectric constant of the soil. The goal of this chapter is not to measure the soil moisture content as many approximations are there to make and depending on soil type the retrieval algorithm can be different and most importantly the receiver part is not yet ready to test. Instead of the receiver part that is mobile and portable for the aircraft or drone, spectrum analyser is used to detect the radiation emitting from the soil by the antenna.

The two most important things that play vital role in the soil moisture retrieval are the emissivity of the soil and the relationship between the dielectric property of soil and its reflection coefficient. The emissivity can be expressed as the ratio of the heat energy radiated from a material to that radiated from a perfect blackbody, at the same wavelength, temperature and the same viewing conditions. For a perfect reflector the emissivity is 0 and for a perfect blackbody or emitter it is 1. The emissivity of a surface depends on both the material and the nature of the surface. The emissivity also depends on the temperature of the surface as well as the wavelength and the angle. The implications of the influence of the soil moisture on the emissivity is a widely discussed research[264]. Modelling of the soil structure and algorithm

Chapter Outline

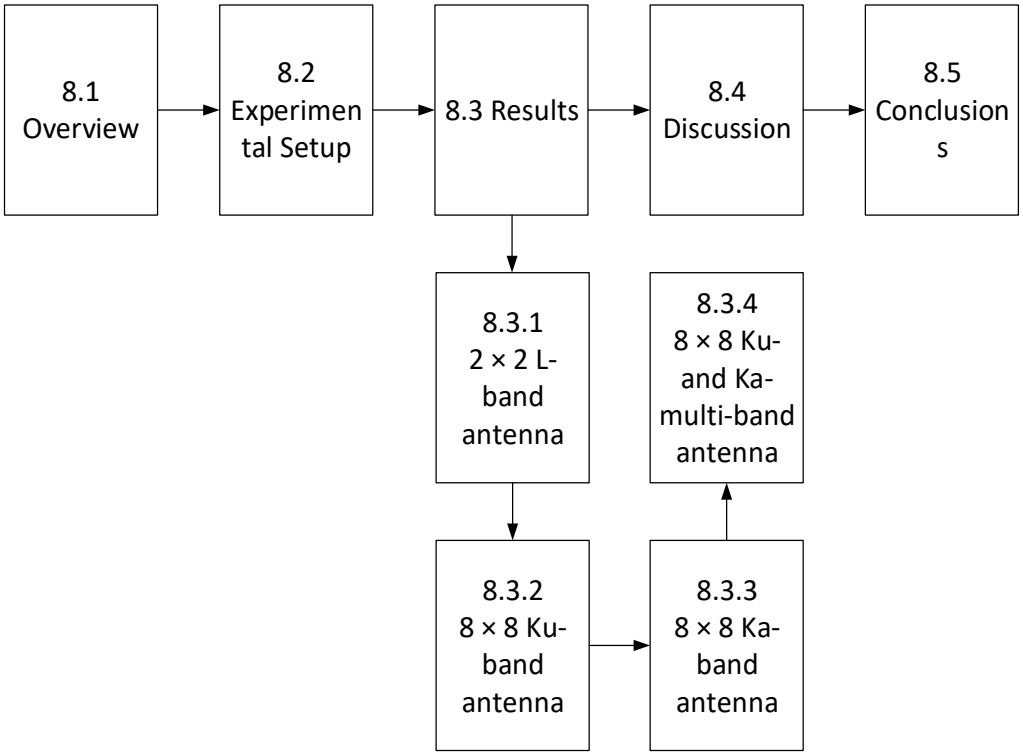

for the grey body approximation are not the scope of this research but will play role in the outcome of the soil moisture content.

The dielectric properties of soil are affected due to the moisture content of the soil [265]. This relationship can be used to estimate and measure soil moisture [265-271]. Soil, consisting of many components, show different water holding attribute, salinity and metallic contents that affect the dielectric property. Considering soil classified as silty sand containing 77% sand, 14% clay and 9% slit, it was found in [266] that soil with dielectric constant at around 4, having only 8% water exhibits dielectric constant of around 4. For 29% moisture, the dielectric constant value rises up to 14 and the trend implies that the more water is present the more will be the dielectric constant. The dielectric constant of a material has direct relationship with the amount of emission. The higher the dielectric constant of any material, the more power is emitted and hence can be received.

Soil structure and moisture retrieval algorithm being out of scope, simplified relationship between moisture and emissivity is considered in this chapter. The assumptions that are made include soil dielectric constant increases with the increase in its water content and soil with higher dielectric constant emits more radiation than low dielectric constant soil. Temperature, ambience and radiation from outside were constant during the whole experiment.

In this chapter, an experimental set up is established that is used as a proof of concept of the performance of the antenna system that was developed in the previous chapters. The outcome of this chapter is to detect variation in moisture content in soil in a controlled environment.

8.2 Experimental Setup

The experimental setup is developed in the MMARS (Monash Microwave, Antennas, RFID and Sensors) lab by Mr. Jiewei Feng, who is working on the receiving part of the antenna system. A conceptual schematic view is shown in Figure 8. 1. The spectrum analyser is a Rohde and Schwarz FSV Signal Analyzer 9kHz to 40 GHz. The low noise amplifiers have different

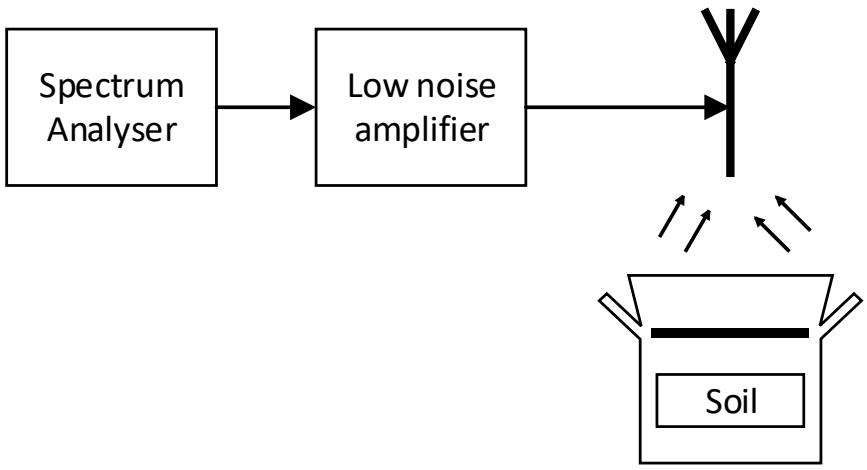

Figure 8. 1 Conceptual measurement set up schematic developed by Mr. Jiewei Feng from Monash University

gains for different frequencies ranging between 20 dB to 40 dB for higher frequencies. The experimental setup photos are presented in Figure 8. 2 and Figure 8. 3.

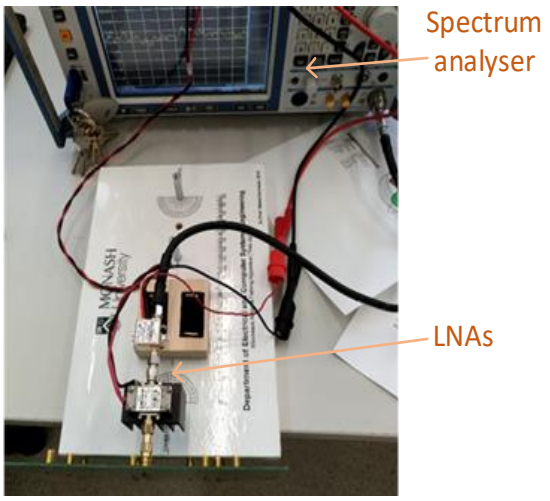

Figure 8. 2 Experimental setup with the spectrum analyser.

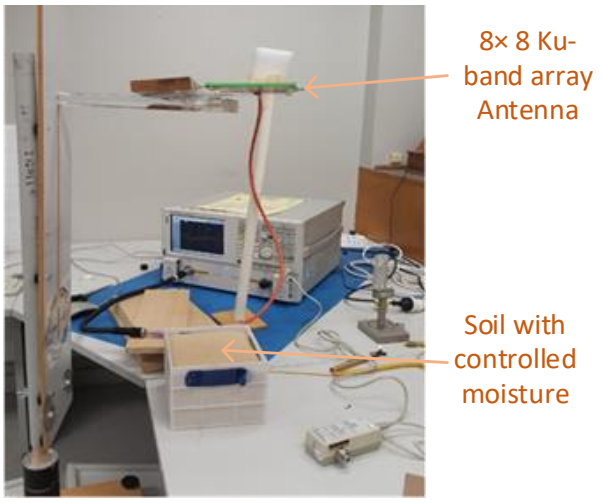

Figure 8. 3 Antenna positioning above the test soil for soil moisture measurement

8.3 Results

The measurement was performed using 2 × 2 L-band, 8 × 8 Ku-band, 8 × 8 Ka-band, and 8 × 8 Ku- and 8 × 8 Ka-band multiband antennas. In each case, the measurement was performed in a controlled environment in the same temperature, air pressure and ambient lighting. Other microwave radiations were limited, and absorber foams were used to shield the setup in the utmost practical way. During the measurement, the clay soil was first dried using an electric oven, then water was measured and added to the dry soil to achieve wet soil with required moisture content. Then the measurement was performed, and the process was repeated. The spectrum analyser provides the received power level from the soil moisture as the antenna main-lobe was placed towards the soil. The distance between the antenna and the soil was set to be greater than the far field distance of the antenna. Depending on the moisture content, the

received power of the spectrum analyser was different, and the result are documented in this section.

8.3.1 2 × 2 L-band antenna

For the 2 × 2 L-band antenna, the result is shown here. The result shows the variation in the received signal strength with change in the moisture content. The far field distance for this structure is 270 mm, so the distance between the antenna and the soil was set to be around 300 mm in this case. The result is shown in Figure 8. 4.

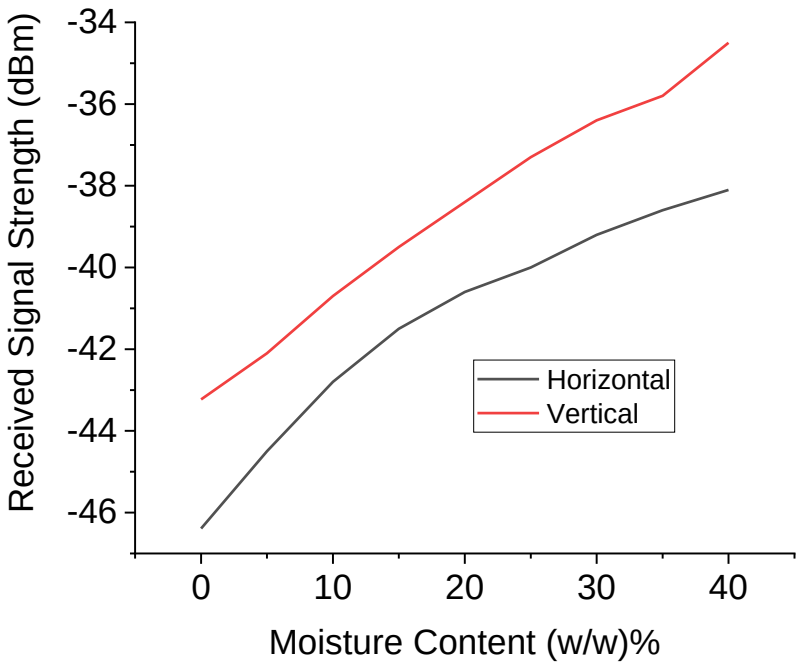

Figure 8. 4. The x-axis of this graph is the percentage of moisture present in the soil. The moisture content is calculated using the following formula [272].

$$Percentage\ moisture = \frac{(weight\ of\ wet\ soil - wet\ of\ dry\ soil)}{wet\ of\ dry\ soil} \times 100 \quad \text{.....(1)}$$

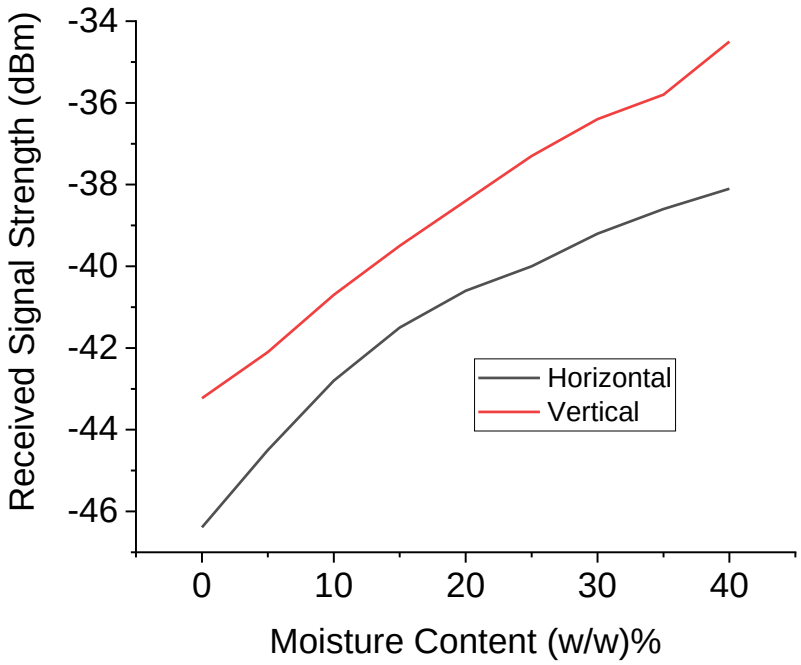

Figure 8. 4 Received signal strength variation with change in the moisture content for 2 × 2 L-band antenna.

The result shows the relationship between the moisture content and received power from the spectrum analyser. The more moisture is present, the more becomes the dielectric constant and hence more emissivity though the relationship is not simple but in this case this relationship is assumed as the soil and ambience are considered to be unchanged. Hence, the received power is increased with increase in the moisture content. Both the horizontal and vertical polarization of the antennas follow the same trend and their rate of change is also very similar. However, they have an offset which is due to the structure and different polarizations of the antenna system. The similar equation, assumptions and technique is used for measuring the Ku- and Ka-band antenna in next sections.

8.3.2 8 × 8 Ku-band antenna

For the Ku-band antenna, the received power level is relatively lower than that received from the L-band. The sensitivity of the moisture variation is also less than the L-band as expected.

The Figure 8. 5 shows the received power from the spectrum analyser with variation in the moisture content.

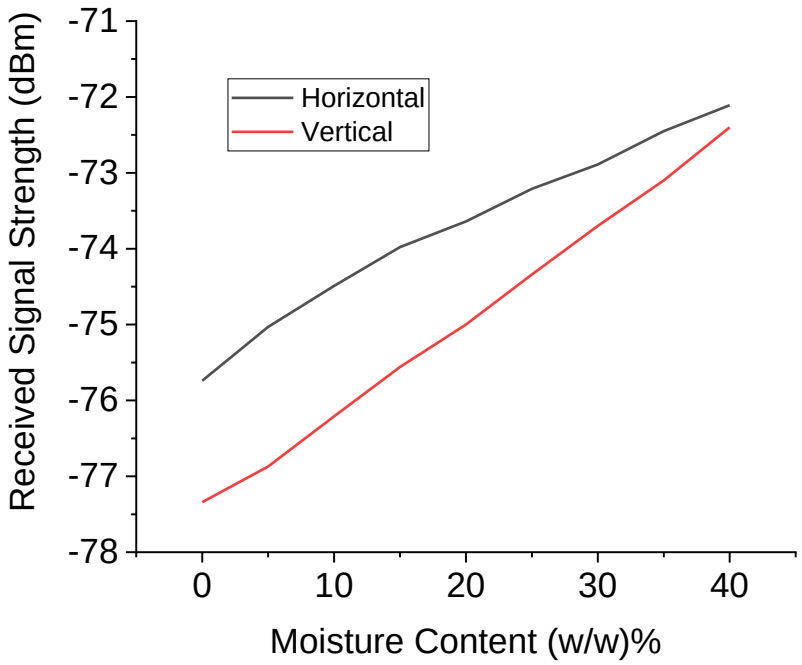

Figure 8. 5 Received signal strength variation with change in the moisture content for 8 × 8 Ku-band antenna.

The result is obtained using a low noise amplifier (LNA) otherwise the difference is not tangible due to the noise. For the horizontal and vertical ports, an offset is observed which is also expected due to the nature of the design. The level of the power received is around -75 dBm, which is enough to process in the receiving module but can be improved further with a better LNA. Again, similar trend is observed for the horizontal and vertical polarizations and the offset between these two polarizations is around 2 dBm.

8.3.3 8 × 8 Ka-band antenna

Ka-band is the highest frequency band among the other bands discussed in this thesis. Being the highest frequency band, this shows the lowest sensitivity due to the moisture content variation. The received power is very low and around -80 dBm range. A quality LNA was used

to amplify the received power without affecting the noise. As the moisture content increases, the received power increases quite steadily.

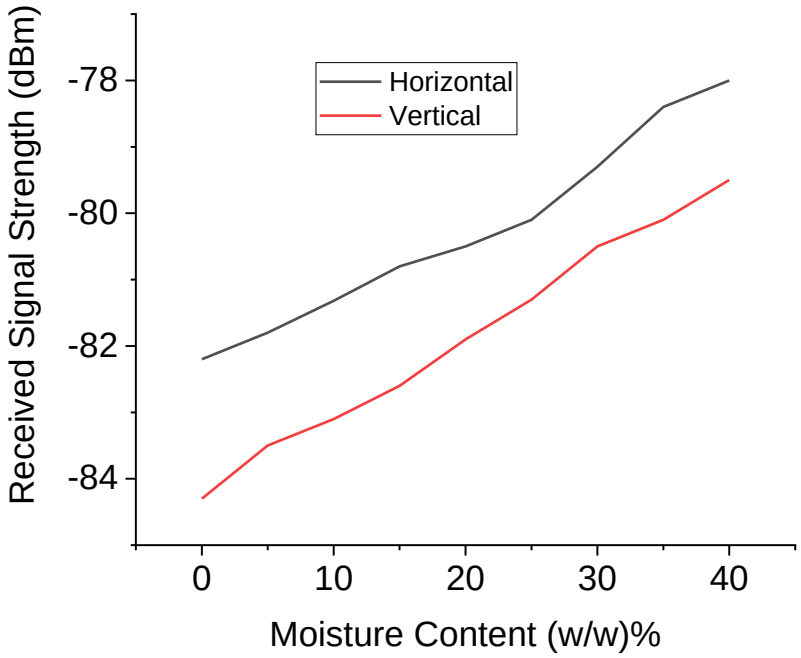

Figure 8. 6 Received signal strength variation with change in the moisture content for 8 × 8 Ka-band antenna.

Both the horizontal and vertical port results are measured and shown in Figure 8. 6. Around 2 dBm offset is seen to be present between these two orthogonal polarizations. The relationship between these two ports are of less significant for the moisture retrieval calculation.

8.3.4 8 × 8 Ka-band, and 8 × 8 Ku- and 8 × 8 Ka-band multiband antenna

The multiband antenna works in both Ku- and Ka-bands and it has four ports for the horizontal and vertical polarizations of each band. Technically it is two different antennas that has the same physical aperture. The result of the measurement is similar to what was found in the individual 8 × 8 Ku- and 8 × 8 Ka-band antenna but with a small deviation due to the different structure. The results are shown in Figure 8. 7.

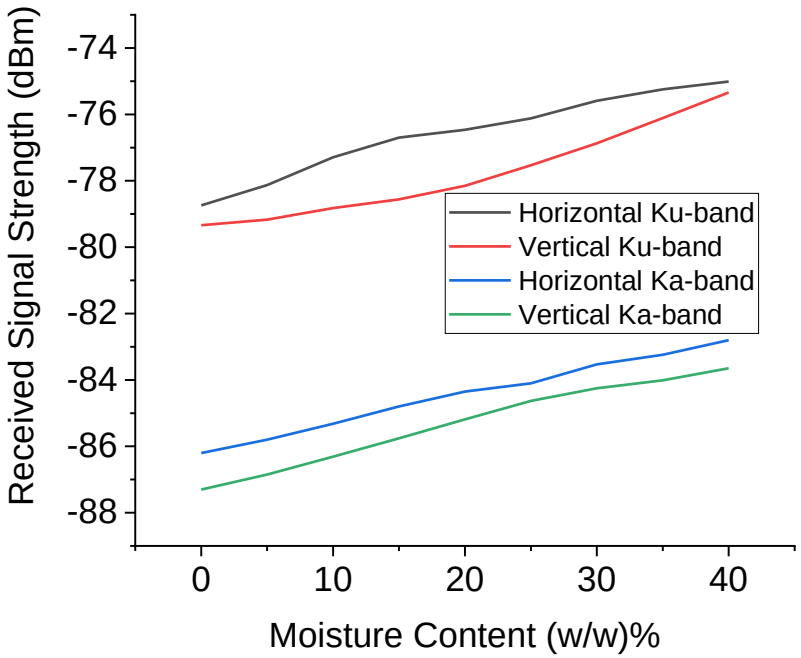

Figure 8. 7 Received signal strength variation with change in the moisture content for 8 × 8 Ku- and 8 × 8 Ka-band multiband antenna.

8.4 Discussion

From the measurements that are performed, it can be observed that the variation in the moisture content results from the variation in the moisture content of soil. The experimental set up ensures that there is only one variable which in this case is the moisture content of the soil and hence the resultant variation in the received power must be due to that variation. This is assumed to be the proof of concept for the measurement. These data if stored locally can be used to compared against historical data to compare the moisture content from history. In real world, this method will need to be modified as there are other variables such as temperature, type of soil, humidity and so on. The challenge of this measurement was to ensure the same temperature, humidity and microwave noise in the environment during the data collection. The measurement was time consuming and maximum effort was put in order to maintain the confidence of the data. The exclusions of this measurement are the effect of penetration depth due to different frequency bands, the humidity of the environment present during the

measurement as it was controlled by the airflow control system. Overall, this measurement results prove the sensitivity of the antenna with moisture variation in soil and the future plans are to use this system with a combination of algorithms based on the climate and soil type to achieve better results. At this stage this solution will only provide data with respect to a historical dataset but in order to convert this data into brightness temperature the back end of the antenna or the receiver module has to be designed. Conclusions

This chapter discusses about the soil moisture measurement technique for the validation of the antenna system designed in this thesis. Soil moisture is one of the most important parameters in agriculture, weather prediction, disaster modelling and in the context of Australia, it is even more important as water is scarce. The proposed antenna system was designed, fabricated and measured in terms of antenna properties such as gain, directivity, return loss, isolation and radiation pattern but in order to prove the validity of the antennas, it is important to test them to measure their sensitivity for different soil moisture content. This chapter studies the sensitivity of the antennas designed in the previous chapters for different soil moistures and documents the result. The most important finding of this chapter is, it provides the proof of concept of the natural emission variation of the soil with variation in its moisture content. The shortcomings of this chapter are, the soil depth was not discussed as different frequencies (L-, Ku- and Ka-bands) have different penetration depth and in real scenario, the soils have different structure, water capacity and hence emissivity.

9 Conclusions and Future Works

The work presented in this thesis has been concerned with antenna elements design, array synthesis, beam shaping network design, multiband antenna formation and their potential impact on radiometer antenna system for soil moisture measurement. The motivation of the work can be summarised as follows. Microwave sensors can be categorized as active and passive, where passive being the most promising approach to measure the near surface soil moisture. The all-weather sensing ability, a fairly direct relationship between soil moisture and the permittivity of soil, and less sensitivity to vegetation, and roughness of the surface have made passive sensing an attractive method for last few decades. Therefore, Soil Moisture and Ocean Salinity (SMOS) mission launched by the European Space Agency (ESA), in November 2009, and the Soil Moisture Active and Passive (SMAP) mission launched by the National Aeronautics and Space Administration (NASA), in 2015, both employ an L-band (1.41 GHz) radiometer to measure microwave emission from the land surface globally every 2 - 3 days. These satellites have a target accuracy of 0.04 m^3/m^3 through a radiometric transfer model and they retrieve the top ~5 cm soil moisture. This technique has serious implications such as its low spatial resolution, which is on the order of 40 km. The concern is to use this data for the agriculture sector as well as water management and weather forecasting. To use the soil moisture data for the agriculture sector, the resolution needs to be higher and the footprint of the antenna beam needs to be smaller. Active microwave sensing or radar can produce higher resolution, but it is impacted by the soil roughness and complex design as well as expensive architecture. Higher frequency radiometers can improve the resolution, but they lack the sensitivity and depth in the soil. To avail the advantage of both passive and higher resolution

sensing, multi-band radiometer working on L-band as well as Ku- and Ka-band can be employed. The antenna system is fully passive mitigating the effect of soil roughness, and Ku- and Ka-bands have higher resolution to improve the accuracy of the measurement. The work associated with the design and the development of these antenna systems has formed a significant part of a large Australian Research Council grant project, which has been awarded to the candidate's supervisor Associate Professor Nemai Chandra Karmakar.

9.1 Fulfilling the goal of the thesis

As the main goal of this thesis project, a planar multiband antenna array working in Ku- and Ka-band ready to work as a standalone system to augment with L-band array has been designed, fabricated and measured. Also, L-band 8 × 8 along with Ku- and Ka-band 8 × 8 array have been designed. Due to the size of the L-band, 2 × 2 array has been tested and measured. Ku- and Ka-band 8 × 8 array antenna have been designed, fabricated, measured and analysed to be used as an independent radiometer system.

Starting with linear polarized antenna, three separate designs of L-, Ku- and Ka-band element antenna have been discussed in Chapter 3. The challenge of this chapter was to find the suitable feeding technique that can be implemented in array structure for future research. Commercially used designing and simulation software CST has been used to design, optimize and simulate. In each design, the choice of substrate and thickness was kept the same for keeping the design as simple and symmetric as possible. Different substrates and feeding techniques have been explored before choosing the TLX-8 substrate from Taconic with a substrate thickness of 0.127 mm. The reason behind choosing such a thin substrate is to minimize the width of the feed lines for the L-, Ku- and Ka-bands. The width of the feed lines depends on the substrate permittivity, frequency of operation and the distance from the ground plane. The feeding technique was chosen to be aperture-coupled feeding, as this technique allows to have separate feeding layers for different bands and polarizations. After performing optimization in simulation, a good

matching was found along with decent gain and radiation pattern. Finally, a single element Ku-band with linear polarization was fabricated and measured in Monash University's state-of-the-art anechoic chamber for reflection performance and radiation pattern. The measurement result was found to be aligned with the simulation result. As designing and optimization can be very time consuming, a step-by-step flow chart has been developed after reporting the effect of changing various design parameters of the LP antennas.

In Chapter 4, dual-polarized design of the three L-, Ku- and Ka-bands are discussed. After designing the antennas for the linear polarization, the natural next step was to extend the design to adapt dual-polarized design. Introducing one extra polarization provides one extra set of data from another polarization which is orthogonal to the linear polarization discussed in Chapter 3. The target was to design single element antenna working on L-, Ku- and Ka-bands, that have very good reflection coefficient or low reflection loss, very high isolation between the orthogonal ports or polarizations and decent gain. Again, TLX-8 with 0.127 mm thickness substrate was chosen for the design. The simulation was performed using CST Microwave Studio 2017. The feeding technique was chosen to be aperture-coupled with cross-shaped slots. The feed lines used were 'Y' shaped with a power divider. Two 100 Ω lines coming out of a 50 Ω feed line ensures a very high isolation with good reflection coefficient. A decent gain was found for all three bands. After designing and optimizing, the next step was to fabricate and measure the performance. The measurement results followed the simulation result closely. Some fabrication and measurement error were present due to the connector assembly, and transportation but the overall performance was encouraging to design for the array antenna for further research. Similar to the previous chapter, again a step-by-step flow chart has been developed to help designing the DP aperture-coupled antenna working between these frequency bands.

After designing the single element antenna in both linear and dual polarizations for the L-, Ku- and Ka-bands, the next step was to design them in an array configuration for better gain and concentrated beam shape. The requirement of the project asked for 8 × 8 array antenna system for all three bands. For the L-band system, the 8 × 8 array would take up huge space and the Ku- and Ka-band arrays can be placed between two adjacent elements of the L-band. Also, in the multilayered structure, the L-band feed layers will be on the most distant feed layer from the ground layer thus, L-band array design has been done up to 8 × 8 for simulation only. A 2 × 2 L-band antenna was fabricated and measured as the other bands will be placed in between these four L-band elements. For the Ku- and Ka-band array, the design was started from the scratch. Using the dual-polarized element antenna developed in Chapter 4, first a 2 × 2 array was developed. Upon optimization and further research, the array was extended from the 2 × 2 to 4 × 4 and then 8 × 8 elements. On each step, the feed networks have been optimized to provide the best matching and high isolation as well as decent gain and cross-polarization level. There were many challenges to overcome including the Ka-band 8 × 8 design where due to the small size of the Ka-band, the feed lines are very close to each other. On one hand, placing antennas half-wavelength apart would put the feed lines too close to each other resulting coupling and distortion, on the other hand, placing antennas too far from each other would result in grating-lobe. Optimization is required to find the balance between these two effects and 0.7 wavelength was set to be the inter-element distance between two adjacent elements. Another problem that was present before adding a back-reflector was the back-lobe radiation. The main-lobe should ideally radiate all the energy but theoretically it is not possible. Portion of the radiation are radiated from the side-lobes and due to the aperture-coupled feeding, a significant portion of radiation also radiates from the back-lobe. The back-reflector is a metallic structure carefully placed to reflect the back radiation and redirect towards the main-lobe. The way to implement this is to place the reflector at a distance of ¼ wavelength which results in

90° phase difference. The back-radiation travel ¼ wavelength and reflects back another ¼ wavelength making ½ wavelength or 180° phase difference. The incident wave of back-radiation already has 180° phase difference to the main-lobe and introducing a back-reflector contributes another 180° making a 360° or 0° phase difference to the main-lobe. In this way, the back-reflector actually improves the main-lobe radiation.

In Chapter 5, the array antenna designing was performed for 8 × 8 L-, Ku- and Ka-bands but the feed network was uniform. Uniform feeding network resulted in -13 dB sidelobe level, which can also be proven from the theory. The problem with sidelobe is, if the sidelobes are too high, the power within the main-lobe and sidelobes become comparable. If the power radiated from the main-lobe and sidelobes are similar, it will pick up signals from all directions and it will be difficult to differentiate data received from the main-lobe and from the sidelobes. Thus, it is important to suppress the maximum sidelobe level (MSLL) to at least 25 dB below the main lobe and is the main concern in Chapter 6. The easiest way to manipulate sidelobe level is to excite the centre elements of the array more power than the elements on the corners. Gaussian, Taylor's, Chebyshev's are few common beam shaping techniques that provides lower sidelobe level. The problem with these distribution systems is practicality and cost efficiency. In order to ensure more than 25 dB suppressed sidelobes, the excitation of the corner element should be around 10 dB less than that of the centre elements, the next element from the corner should have excitation difference of around 8 dB and so on. For 8 × 8 array elements, these beam shaping techniques suggest more than 7 different power levels or 7 different line width. Due to the expensive fabrication process, the precision and sensitivity of the copper line plays significant role while pricing. If it was possible to design the feed network using fewer power levels, then it would be possible to fabricate with less precision and inexpensively. Staircase power distribution (SPD) method offers fewer power levels with similar performance when it comes to suppress the sidelobe levels. The array antenna designed in Chapter 5 for Ku-

and Ka-band are the subject of this chapter where different beam shaping algorithm was applied. Finally, for fabrication process, SPD method was chosen. The measure results displayed sidelobe levels below 25 dB with only 5 power levels. A brief analysis on different beam shaping technique was discussed. Few qualitative entities such as beam efficiency, maximum sidelobe level and 3 dB beamwidth for different algorithms were compared, plotted and analysed against each other before the conclusions.

In Chapter 7, multi-band antenna is discussed. As mentioned earlier, an 8 × 8 L-band antenna takes huge space compared to 8 × 8 Ku- and Ka-band, thus only 8 × 8 Ku- and 8 × 8 Ka-band antennas are designed in the same shared aperture to work as an independent radiometer system to be used with an L-band radiometer system. Designing multiband antenna was the most complex design in this thesis, as it involved all the techniques discussed in the previous chapters plus multi-layered bands. The design procedure started from one Ku-band surrounded by 2 × 2 Ka-band elements. As the frequency of Ku- and Ka-bands have a ratio of 1: 2, the size of the patches for Ku- and Ka-bands have a ratio of 2:1 and it becomes possible to place one Ku-band patch in the centre surrounded by four Ka-band patches without touching each other. As, the design grows from one Ku-band by 2 × 2 Ka-band to 2 × 2 Ku-band by 4 × 4 Ka-band, the feeding design becomes more complex. The complex part comes from the fact that, the slots in the ground plane of one band are not to be over/under passed by the feed lines of another band. To achieve this, the feed lines are designed very carefully. In some cases, it was impossible to avoid this situation, but optimization was achieved to minimize the effect of coupling. After this design, 4 × 4 Ku-and 8 × 8 Ka-band design was performed and optimized. This design was also fabricated and measured to compare with the simulation result. It is important to note that, for the multiband structure, as there are extra layers of feed lines, the line widths are different for different bands. The Ku-band feed layers were placed further from the ground plane to make use of the more space between the elements than that of the Ka-band.

Finally, an 8 × 8 Ku-band surrounded by 8 × 8 Ka-band multiband antenna was developed. Upon further investigation on the beam shaping and back-lobe suppression technique, this antenna was also fabricated, measured and analysed to compare with the simulation results. For future work, inter-band isolation is proposed as isolation between Ku- and Ka-band antenna is very important.

Chapter 8 presents the measurement results of the 2 × 2 L-band, 8 × 8 Ku-band, 8 × 8 Ka-band and 8 × 8 Ku- and Ka-band multiband antenna. The antennas are placed towards a sample soil and the received emission is measured using spectrum analyser in Monash University's MMARS lab.

9.2 Contributions

The novel outcomes of this thesis have been communicated through five peer reviewed conference publications and 2 under review journals. These contributions are listed below-

1. Chapter 1 and 2: Introduction and Literature Review

The overview of the soil moisture measurement using smart antennas are published in one conference proceeding-

- M. Hassan and N. C. Karmakar, "Soil moisture measurement using smart antennas," in Electrical and Computer Engineering (ICECE), 2014 International Conference on, 2014, pp. 192-195.

The prospect of using surface integrated wave (SIW) antenna for soil moisture radiometer is discussed and published in the following conference-

- Shahriar Hasan Shehab, M. Hassan and N. C. Karmakar, "SIW slot antenna at Ka-band for soil moisture radiometer system" 2017 The 11th International Conference on Sensing Technology, Sydney, NSW, 2017

2. Chapter 3: Linearly Polarized Antenna

Before choosing the dual-polarized feeding technique as the most suitable for this project, few studies including slot antennas working at Ka-band with linear polarization was explored. Starting with a single element, a 4 × 4 element array was developed. The findings of this research are published in the following conference proceeding-

- M. Hassan, S. Dey and N. C. Karmakar, "Ka-band complementary reflector backed slot antenna array for soil moisture radiometer," *2015 International Symposium on Antennas and Propagation (ISAP)*, Hobart, TAS, 2015, pp. 1-4.

3. Chapter 4: Dual Polarized Antenna

A DP antenna working at Ku-band with high isolation is published in a conference proceeding. Different aperture-coupled configurations comparing the performance and explanation is discussed in this work.

- M. Hassan and N. C. Karmakar, "Design Considerations of DP ACPA with Higher Isolation at Ku-band for Soil Moisture Radiometer" *2017 IEEE Asia Pacific Microwave Conference (APMC)*, Kuala Lumpur, Malaysia, 2017

4. Chapter 5: Array Antenna Design

Array synthesis with beam shaping for Ku- and Ka-band 8 × 8 elements are discussed and two journals are under review in IEEE Transactions on Antenna and Propagation and Progress In Electromagnetics Research (PIER).

5. Chapter 6: Array Analysis

Different beam shaping algorithm for the radiometer antenna is discussed and published in the following conference proceeding –

- M. Hassan and N. C. Karmakar, "Comparative study of different power distribution methods for array antenna beamforming for soil moisture radiometer" *2017 The 11th International Conference on Sensing Technology*, Sydney, NSW, 2017

6. Chapter 7: Multiband Antenna

Multiband antenna array for soil moisture radiometer is discussed and a journal is submitted to IEEE Access and is under review.

9.3 Future directions

The following issues are needed to be addressed in future for further enhancement of the radiometer antenna proposed in this research:

Triple band multi-layered design with L-, Ku- and Ka-bands in the same physical aperture can be designed using the same principal discussed in Chapter 7. L-band has larger size, and the system will not be suitable to fit in smaller drone but still can be fitted in an aircraft.

Phased array system: L-band phased array system can be obtained commercially and are being used in different expeditions but designing phased array systems for the Ku- and Ka-band are challenging due to their smaller size. Different technology such as, GaAs 1.5 µm can be implemented for designing the phase shifters. This technology is being investigated at the candidate's research group at present.

Back-end receiver: The antenna system developed in this thesis will act as a front end for the radiometer system, but to process the data and calculate the brightness temperature, a receiver module must be developed. This back-end receiver system development is also a part of the research project granted by the ARC. The candidate and his colleagues are working on the development at present.

Soil moisture retrieval algorithm: Due to the variation in the soil surface, the data received by the radiometer must be translated keeping the terrain and effect of vegetation in mind. In the Department of Civil Engineering, here at Monash University, different techniques are being investigated.

Assemble and test: The antenna, phase shifters and the back-end circuitry must be assembled before testing and using to measure soil moisture. Given the complexity of the design, this will be a challenging task.

References

[1] T. L. Delworth and S. Manabe, "The influence of potential evaporation on the variabilities of simulated soil wetness and climate," *Journal of Climate,* vol. 1, no. 5, pp. 523-547, 1988.

[2] W. Wagner, K. Scipal, C. Pathe, D. Gerten, W. Lucht, and B. Rudolf, "Evaluation of the agreement between the first global remotely sensed soil moisture data with model and precipitation data," *Journal of Geophysical Research: Atmospheres (1984–2012),* vol. 108, no. D19, 2003.

[3] D. Entekhabi, I. Rodriguez-Iturbe, and F. Castelli, "Mutual interaction of soil moisture state and atmospheric processes," *Journal of Hydrology,* vol. 184, no. 1, pp. 3-17, 1996.

[4] C. Prigent, F. Aires, W. B. Rossow, and A. Robock, "Sensitivity of satellite microwave and infrared observations to soil moisture at a global scale: Relationship of satellite observations to in situ soil moisture measurements," *Journal of Geophysical Research: Atmospheres (1984–2012),* vol. 110, no. D7, 2005.

[5] A. C. Beljaars, P. Viterbo, M. J. Miller, and A. K. Betts, "The anomalous rainfall over the United States during July 1993: Sensitivity to land surface parameterization and soil moisture anomalies," *Monthly Weather Review,* vol. 124, no. 3, pp. 362-383, 1996.

[6] J. R. Wang and B. J. Choudhury, "Remote sensing of soil moisture content, over bare field at 1.4 GHz frequency," *Journal of Geophysical Research: Oceans,* vol. 86, no. C6, pp. 5277-5282, 1981.

[7] E. G. Njoku and J.-A. Kong, "Theory for passive microwave remote sensing of near-surface soil moisture," *Journal of Geophysical Research,* vol. 82, no. 20, pp. 3108-3118, 1977.

[8] T. J. Jackson and T. J. Schmugge, "Passive microwave remote sensing system for soil moisture: some supporting research," *Geoscience and Remote Sensing, IEEE Transactions on,* vol. 27, pp. 225--235, 1989.

[9] Z. Xiwu, P. R. Houser, J. P. Walker, and W. T. Crow, "A method for retrieving high-resolution surface soil moisture from hydros L-band radiometer and Radar observations," *Geoscience and Remote Sensing, IEEE Transactions on,* vol. 44, no. 6, pp. 1534-1544, 2006.

[10] O. P. N. Calla *et al.*, "Measurement of soil moisture using microwave radiometer," in *Recent Advances in Microwave Theory and Applications, 2008. MICROWAVE 2008. International Conference on*, 2008, pp. 621-624.

[11] S. Murai, *Remote Sensing Note Chapter 3*. Japan Association on Remote Sensing, 1993.

[12] M. D. S. Bhuiyan, N. C. Karmakar, and J. G. Webster, "Defected Ground Structures for Microwave Applications," in *Wiley Encyclopedia of Electrical and Electronics Engineering*: John Wiley & Sons, Inc., 1999.

[13] D. Entekhabi *et al.*, "An agenda for land surface hydrology research and a call for the second international hydrological decade," *Bulletin of the American Meteorological Society,* vol. 80, no. 10, pp. 2043-2058, 1999.

[14] W. F. Krajewski *et al.*, "A remote sensing observatory for hydrologic sciences: A genesis for scaling to continental hydrology," *Water Resources Research,* vol. 42, no. 7, 2006.

[15] W. Wagner, V. Naeimi, K. Scipal, R. de Jeu, and J. Martínez-Fernández, "Soil moisture from operational meteorological satellites," *Hydrogeology Journal,* vol. 15, no. 1, pp. 121-131, 2007.

[16] J. D. Bolten, W. T. Crow, X. Zhan, T. J. Jackson, and C. A. Reynolds, "Evaluating the utility of remotely sensed soil moisture retrievals for operational agricultural drought monitoring," *IEEE Journal of Selected Topics in Applied Earth Observations and Remote Sensing,* vol. 3, no. 1, pp. 57-66, 2010.

[17] A. d. De Wit and C. Van Diepen, "Crop model data assimilation with the Ensemble Kalman filter for improving regional crop yield forecasts," *Agricultural and Forest Meteorology,* vol. 146, no. 1-2, pp. 38-56, 2007.
[18] R. D. Koster *et al.*, "Regions of strong coupling between soil moisture and precipitation," *Science,* vol. 305, no. 5687, pp. 1138-1140, 2004.
[19] R. D. Koster, Z. Guo, R. Yang, P. A. Dirmeyer, K. Mitchell, and M. J. Puma, "On the nature of soil moisture in land surface models," *Journal of Climate,* vol. 22, no. 16, pp. 4322-4335, 2009.
[20] C. P. Weaver and R. Avissar, "Atmospheric disturbances caused by human modification of the landscape," *Bulletin of the American Meteorological Society,* vol. 82, no. 2, pp. 269-282, 2001.
[21] R. D. Koster, S. P. Mahanama, B. Livneh, D. P. Lettenmaier, and R. H. Reichle, "Skill in streamflow forecasts derived from large-scale estimates of soil moisture and snow," *Nature Geoscience,* vol. 3, no. 9, p. 613, 2010.
[22] T. Schmugge, T. Jackson, and H. McKim, "Survey of methods for soil moisture determination," *Water Resources Research,* vol. 16, no. 6, pp. 961-979, 1980.
[23] E. T. Engman, "Applications of microwave remote sensing of soil moisture for water resources and agriculture," *Remote Sensing of Environment,* vol. 35, no. 2-3, pp. 213-226, 1991.
[24] S. Idso, R. Jackson, R. Reginato, B. Kimball, and F. Nakayama, "The dependence of bare soil albedo on soil water content," *Journal of Applied Meteorology,* vol. 14, no. 1, pp. 109-113, 1975.
[25] J. C. Price, "Thermal inertia mapping: A new view of the earth," *Journal of Geophysical Research,* vol. 82, no. 18, pp. 2582-2590, 1977.
[26] J. O. Adegoke and A. M. Carleton, "Relations between soil moisture and satellite vegetation indices in the US Corn Belt," *Journal of Hydrometeorology,* vol. 3, no. 4, pp. 395-405, 2002.
[27] X. Wang, H. Xie, H. Guan, and X. Zhou, "Different responses of MODIS-derived NDVI to root-zone soil moisture in semi-arid and humid regions," *Journal of hydrology,* vol. 340, no. 1-2, pp. 12-24, 2007.
[28] P. C. Dubois, J. Van Zyl, and T. Engman, "Measuring soil moisture with imaging radars," *IEEE Transactions on Geoscience and Remote Sensing,* vol. 33, no. 4, pp. 915-926, 1995.
[29] J. Shi, J. Wang, A. Y. Hsu, P. E. O'Neill, and E. T. Engman, "Estimation of bare surface soil moisture and surface roughness parameter using L-band SAR image data," *IEEE Transactions on Geoscience and Remote Sensing,* vol. 35, no. 5, pp. 1254-1266, 1997.
[30] A. M. Shutko and E. Reutov, "Mixture formulas applied in estimation of dielectric and radiative characteristics of soils and grounds at microwave frequencies," *IEEE Transactions on Geoscience and Remote Sensing,* no. 1, pp. 29-32, 1982.
[31] T. Schmugge, P. E. O'Neill, and J. R. Wang, "Passive microwave soil moisture research," *IEEE Transactions on Geoscience and Remote Sensing,* no. 1, pp. 12-22, 1986.
[32] T. J. Jackson and T. J. Schmugge, "Passive microwave remote sensing system for soil moisture: Some supporting research," *IEEE Transactions on Geoscience and Remote Sensing,* vol. 27, no. 2, pp. 225-235, 1989.
[33] E. G. Njoku *et al.*, "Observations of soil moisture using a passive and active low-frequency microwave airborne sensor during SGP99," *IEEE Transactions on Geoscience and Remote Sensing,* vol. 40, no. 12, pp. 2659-2673, 2002.
[34] T. J. Jackson *et al.*, "Soil moisture retrieval using the C-band polarimetric scanning radiometer during the Southern Great Plains 1999 Experiment," *IEEE Transactions on Geoscience and Remote Sensing,* vol. 40, no. 10, pp. 2151-2161, 2002.
[35] J.-P. Wigneron, A. Chanzy, J.-C. Calvet, and N. Bruguier, "A simple algorithm to retrieve soil moisture and vegetation biomass using passive microwave measurements over crop fields," *Remote Sensing of Environment,* vol. 51, no. 3, pp. 331-341, 1995.

[36] E. G. Njoku, T. J. Jackson, V. Lakshmi, T. K. Chan, and S. V. Nghiem, "Soil moisture retrieval from AMSR-E," *IEEE transactions on Geoscience and remote sensing,* vol. 41, no. 2, pp. 215-229, 2003.
[37] E. G. Njoku and L. Li, "Retrieval of land surface parameters using passive microwave measurements at 6-18 GHz," *IEEE Transactions on Geoscience and Remote Sensing,* vol. 37, no. 1, pp. 79-93, 1999.
[38] D. Aubert, C. Loumagne, and L. Oudin, "Sequential assimilation of soil moisture and streamflow data in a conceptual rainfall–runoff model," *Journal of Hydrology,* vol. 280, no. 1-4, pp. 145-161, 2003.
[39] J. Schnürer, M. Clarholm, S. Boström, and T. Rosswall, "Effects of moisture on soil microorganisms and nematodes: a field experiment," *Microbial ecology,* vol. 12, no. 2, pp. 217-230, 1986.
[40] T. Jackson, M. Hawley, and P. O'neill, "PREPLANTING SOIL MOISTURE USING PASSIVE MICROWAVE SENSORS 1," *JAWRA Journal of the American Water Resources Association,* vol. 23, no. 1, pp. 11-19, 1987.
[41] S. Saha, "Assessment of regional soil moisture conditions by coupling satellite sensor data with a soil-plant system heat and moisture balance model," *Remote Sensing,* vol. 16, no. 5, pp. 973-980, 1995.
[42] W. G. Bastiaanssen, D. J. Molden, and I. W. Makin, "Remote sensing for irrigated agriculture: examples from research and possible applications," *Agricultural water management,* vol. 46, no. 2, pp. 137-155, 2000.
[43] D. M. Chung, B. D. Trong, and V. T. L. Anh, "Passive microwave remote sensing for estimation of rice water content in Vietnam," in *Geoscience and Remote Sensing Symposium, 2003. IGARSS'03. Proceedings. 2003 IEEE International*, 2003, vol. 2, pp. 905-907: IEEE.
[44] A. K. Betts, J. H. Ball, A. Beljaars, M. Miller, and P. Viterbo, "Coupling between land-surface boundary-layer parameterizations and rainfall on local and regional scales: Lessons from the wet summer of 1993," in *Fifth Symp. on Global Change Studies*, 1994, pp. 174-181.
[45] E. T. Engman, "Soil moisture needs in earth sciences," 1992.
[46] R. D. Koster, M. J. Suarez, R. W. Higgins, and H. M. Van den Dool, "Observational evidence that soil moisture variations affect precipitation," *Geophysical Research Letters,* vol. 30, no. 5, 2003.
[47] M. Drusch, E. F. Wood, and C. Simmer, "Up-scaling effects in passive microwave remote sensing: ESTAR 1.4 GHz measurements during SGP'97," *Geophysical research letters,* vol. 26, no. 7, pp. 879-882, 1999.
[48] M. Jung *et al.*, "Recent decline in the global land evapotranspiration trend due to limited moisture supply," *Nature,* vol. 467, no. 7318, p. 951, 2010.
[49] P. Falloon, C. D. Jones, M. Ades, and K. Paul, "Direct soil moisture controls of future global soil carbon changes: An important source of uncertainty," *Global Biogeochemical Cycles,* vol. 25, no. 3, 2011.
[50] S. I. Seneviratne *et al.*, "Investigating soil moisture–climate interactions in a changing climate: A review," *Earth-Science Reviews,* vol. 99, no. 3-4, pp. 125-161, 2010.
[51] W. Cai, T. Cowan, P. Briggs, and M. Raupach, "Rising temperature depletes soil moisture and exacerbates severe drought conditions across southeast Australia," *Geophysical Research Letters,* vol. 36, no. 21, 2009.
[52] V. Castillo, A. Gomez-Plaza, and M. Martınez-Mena, "The role of antecedent soil water content in the runoff response of semiarid catchments: a simulation approach," *Journal of Hydrology,* vol. 284, no. 1-4, pp. 114-130, 2003.
[53] J. Spinhirne, S. Palm, D. L. Hlavka, W. D. Hart, and A. Mahesh, *Global and Polar Cloud Cover from the Geoscience Laser Altimeter System, Observations and Implications*. 2004, p. 04.
[54] K. White, A. P. Cracknell, and L. W. B. Hayes, *Introduction to Remote Sensing*. 1993, p. 89.

[55] F. T. Ulaby, R. K. Moore, and A. K. Fung, "Microwave Remote Sensing-Active and Passive-Volume I-Microwave Remote Sensing Fundamentals and Radiometry (v. 1)," 1981.
[56] F. J. Wentz, "Measurement of oceanic wind vector using satellite microwave radiometers," *IEEE Transactions on Geoscience and Remote Sensing,* vol. 30, no. 5, pp. 960-972, 1992.
[57] S. T. Brown, C. S. Ruf, and D. R. Lyzenga, "An emissivity-based wind vector retrieval algorithm for the WindSat polarimetric radiometer," *IEEE transactions on geoscience and remote sensing,* vol. 44, no. 3, pp. 611-621, 2006.
[58] F. T. Ulaby, R. K. Moore, and A. K. Fung, "Microwave remote sensing active and passive-volume III: from theory to applications," 1986.
[59] E. G. Njoku and D. Entekhabi, "Passive microwave remote sensing of soil moisture," *Journal of hydrology,* vol. 184, no. 1-2, pp. 101-129, 1996.
[60] T. Jackson and D. E. Le Vine, "Mapping surface soil moisture using an aircraft-based passive microwave instrument: Algorithm and example," *Journal of Hydrology,* vol. 184, no. 1-2, pp. 85-99, 1996.
[61] P. Pampaloni, L. Chiarantini, P. Coppo, S. Gagliani, and G. Luzi, "Multifrequency passive microwave remote sensing of soil moisture and roughness AU - PALOSCIA, S," *International Journal of Remote Sensing,* vol. 14, no. 3, pp. 467-483, 1993/02/01 1993.
[62] E. J. Kim, J. C. Shiue, T. Doiron, C. Principe, and A. Rodriguezs, "A preview of AMSR: Airborne C-band Microwave Radiometer (ACMR) observations from SGP99," in *IGARSS 2000. IEEE 2000 International Geoscience and Remote Sensing Symposium. Taking the Pulse of the Planet: The Role of Remote Sensing in Managing the Environment. Proceedings (Cat. No.00CH37120)*, 2000, vol. 3, pp. 1060-1062 vol.3.
[63] N. Ye *et al.*, "Towards Multi-Frequency Soil Moisture Retrieval Using P- and L-Band Passive Microwave Sensing Technology," in *IGARSS 2018 - 2018 IEEE International Geoscience and Remote Sensing Symposium*, 2018, pp. 3707-3710.
[64] S. Mori *et al.*, "KydroSAT: a Ku/Ka band synthetic aperture radar space mission concept for high-resolution mapping of hydrometeorological parameters," in *Active and Passive Microwave Remote Sensing for Environmental Monitoring*, 2017, vol. 10426, p. 1042603: International Society for Optics and Photonics.
[65] Y. H. Kerr *et al.*, "The SMOS mission: New tool for monitoring key elements ofthe global water cycle," *Proceedings of the IEEE,* vol. 98, no. 5, pp. 666-687, 2010.
[66] D. Entekhabi *et al.*, "The soil moisture active passive (SMAP) mission," *Proceedings of the IEEE,* vol. 98, no. 5, pp. 704-716, 2010.
[67] S. Chan *et al.*, "Development and assessment of the SMAP enhanced passive soil moisture product," *Remote sensing of environment,* vol. 204, pp. 931-941, 2018.
[68] D. Entekhabi *et al.*, "SMAP handbook–soil moisture active passive: Mapping soil moisture and freeze/thaw from space," 2014.
[69] T. Jackson *et al.*, "Soil moisture verification study of the ESTAR microwave radiometer-Walnut Gulch, AZ 1991," 1992.
[70] A. R. Thompson, J. M. Moran, and G. W. Swenson, *Interferometry and synthesis in radio astronomy*. Springer, 1986.
[71] P. J. Napier, A. R. Thompson, and R. D. Ekers, "The very large array: Design and performance of a modern synthesis radio telescope," *Proceedings of the IEEE,* vol. 71, no. 11, pp. 1295-1320, 1983.
[72] C. Swift, "ESTAR: The Electronically Scanned Thinned Array Radiometer for remote sensing measurement of soil moisture and ocean salinity," 1993.
[73] H.-J. C. Blume, B. M. Kendall, and J. C. Fedors, "Measurement of ocean temperature and salinity via microwave radiometry," *Boundary-Layer Meteorology,* vol. 13, no. 1-4, pp. 295-308, 1978.

[74] C. T. Swift and R. E. Mcintosh, "Considerations for microwave remote sensing of ocean-surface salinity," *IEEE Transactions on Geoscience and Remote Sensing,* no. 4, pp. 480-491, 1983.
[75] R. Bindlish, T. Jackson, M. Cosh, T. Zhao, and P. O'neill, "Global soil moisture from the Aquarius/SAC-D satellite: Description and initial assessment," *IEEE Geoscience and Remote Sensing Letters,* vol. 12, no. 5, pp. 923-927, 2015.
[76] Y. Luo *et al.*, "Potential soil moisture products from the aquarius radiometer and scatterometer using an observing system simulation experiment," *Geoscientific Instrumentation, Methods and Data Systems,* vol. 2, no. 1, pp. 113-120, 2013.
[77] W. J. Wilson, A. B. Tanner, F. A. Pellerano, and K. A. Horgan, "Ultra stable microwave radiometers for future sea surface salinity missions," Pasadena, CA: Jet Propulsion Laboratory, National Aeronautics and Space …2005.
[78] D. Le Vine, G. Lagerloef, S. Yueh, F. Pellerano, E. Dinnat, and F. Wentz, "Aquarius mission technical overview," in *Geoscience and Remote Sensing Symposium, 2006. IGARSS 2006. IEEE International Conference on*, 2006, pp. 1678-1680: IEEE.
[79] C. A. Balanis, *Antenna Theory: Analysis and Design*. Wiley, 2005.
[80] E. Ávila-Navarro and C. Reig, "Directive Microstrip Antennas for Specific Below -2.45 GHz Applications," *International Journal of Antennas and Propagation,* vol. 2012, 2012.
[81] Y. Dong and T. Itoh, "Planar Ultra-Wideband Antennas in Ku- and K-Band for Pattern or Polarization Diversity Applications," *IEEE Transactions on Antennas and Propagation,* vol. 60, no. 6, pp. 2886-2895, 2012.
[82] M. M. Islam, M. T. Islam, and M. R. I. Faruque, "Dual-Band Operation of a Microstrip Patch Antenna on a Duroid 5870 Substrate for Ku- and K-Bands," *The Scientific World Journal,* vol. 2013, 2013.
[83] M. V. Lukic and D. S. Filipovic, "Surface-Micromachined Dual <emphasis>Ka</emphasis>-Band Cavity Backed Patch Antenna," *IEEE Transactions on Antennas and Propagation,* vol. 55, no. 7, pp. 2107-2110, 2007.
[84] L. Jianxin, C. C. Chiau, C. Xiaodong, and C. G. Parini, "Study of a printed circular disc monopole antenna for UWB systems," *IEEE Transactions on Antennas and Propagation,* vol. 53, no. 11, pp. 3500-3504, 2005.
[85] L. Xian-Ling, Z. Shun-Shi, and Y. Feng-Wei, "Compact UWB tapered-CPW-fed planar monopole antenna," in *2005 Asia-Pacific Microwave Conference Proceedings*, 2005, vol. 4, p. 3 pp.
[86] X. Liang, S. Zhong, and W. Wang, "Elliptical planar monopole antenna with extremely wide bandwidth," *Electronics Letters,* vol. 42, no. 8, pp. 441-442, 2006.
[87] W. Wei, Z. Shun-Shi, and L. Xian-Ling, "A broadband CPW-fed arrowlike printed antenna," in *IEEE Antennas and Propagation Society Symposium, 2004.*, 2004, vol. 1, pp. 751-754 Vol.1.
[88] Y. Ho, D. Su, and J. Ma, "Analysis and design of Ultra Wide Band Planar monopole antenna," in *2008 8th International Symposium on Antennas, Propagation and EM Theory*, 2008, pp. 244-247.
[89] A. Panahi, X. L. Bao, K. Yang, O. O'Conchubhair, and M. J. Ammann, "A Simple Polarization Reconfigurable Printed Monopole Antenna," *IEEE Transactions on Antennas and Propagation,* vol. 63, no. 11, pp. 5129-5134, 2015.
[90] M. Moosazadeh and S. Kharkovsky, "Compact and Small Planar Monopole Antenna With Symmetrical L- and U-Shaped Slots for WLAN/WiMAX Applications," *IEEE Antennas and Wireless Propagation Letters,* vol. 13, pp. 388-391, 2014.
[91] Q. Jinghui, L. Shu, Z. Lingling, and L. Guolin, "Study of planar ultrawide-band antennas," in *2008 4th International Conference on Ultrawideband and Ultrashort Impulse Signals*, 2008, pp. 60-62.
[92] C. Zhi Ning and Q. Xianming, "Research and development of planar UWB antennas," in *2005 Asia-Pacific Microwave Conference Proceedings*, 2005, vol. 1, p. 4 pp.

[93] J. Liang, L. Guo, C. C. Chiau, X. Chen, and C. G. Parini, "Study of CPW-fed circular disc monopole antenna for ultra wideband applications," *IEE Proceedings - Microwaves, Antennas and Propagation,* vol. 152, no. 6, pp. 520-526, 2005.
[94] G. Adamiuk, M. Janson, W. Wiesbeck, and T. Zwick, "Dual-polarized UWB antenna array," in *2009 IEEE International Conference on Ultra-Wideband*, 2009, pp. 164-169.
[95] Q. He, B. Wang, and J. He, "Wideband and Dual-Band Design of a Printed Dipole Antenna," *IEEE Antennas and Wireless Propagation Letters,* vol. 7, pp. 1-4, 2008.
[96] Z. Zhijun, M. F. Iskander, J. C. Langer, and J. Mathews, "Wideband dipole antenna for WLAN," in *IEEE Antennas and Propagation Society Symposium, 2004.*, 2004, vol. 2, pp. 1963-1966 Vol.2.
[97] C. Tsai, W. Chen, C. Lin, J. Guo, and C. Lu, "An Asymmetry Printed WLAN/WiMax Dipole Antenna," in *2011 Fifth International Conference on Genetic and Evolutionary Computing*, 2011, pp. 135-138.
[98] Y. Qian, W. R. Deal, N. Kaneda, and T. Itoh, "Microstrip-fed quasi-Yagi antenna with broadband characteristics," *Electronics Letters,* vol. 34, no. 23, pp. 2194-2196, 1998.
[99] H. Cheunsoo, Q. Yongxi, and T. Itoh, "A modified quasi-Yagi planar antenna with wideband characteristics in C-band," in *IEEE Antennas and Propagation Society International Symposium. 2001 Digest. Held in conjunction with: USNC/URSI National Radio Science Meeting (Cat. No.01CH37229)*, 2001, vol. 3, pp. 154-157 vol.3.
[100] G. Quintero and A. K. Skrivervik, "Analysis of planar UWB elliptical dipoles fed by a coplanar stripline," in *2008 IEEE International Conference on Ultra-Wideband*, 2008, vol. 1, pp. 113-116.
[101] W. K. Toh, X. Qing, and Z. N. Chen, "A Planar UWB Patch-Dipole Antenna," *IEEE Transactions on Antennas and Propagation,* vol. 59, no. 9, pp. 3441-3444, 2011.
[102] H. G. Schantz, "A brief history of UWB antennas," in *IEEE Conference on Ultra Wideband Systems and Technologies, 2003*, 2003, pp. 209-213.
[103] W. Xuan Hui and C. Zhi Ning, "Comparison of planar dipoles in UWB applications," *IEEE Transactions on Antennas and Propagation,* vol. 53, no. 6, pp. 1973-1983, 2005.
[104] A. Hees and J. Detlefsen, "Ultra broadband dual polarized dipole array with metallic reflector," in *2009 IEEE International Conference on Ultra-Wideband*, 2009, pp. 744-747.
[105] B. G. Duffley, G. A. Morin, M. Mikavica, and Y. M. M. Antar, "A wide-band printed double-sided dipole array," *IEEE Transactions on Antennas and Propagation,* vol. 52, no. 2, pp. 628-631, 2004.
[106] P. Lindberg, E. Ojefors, Z. Barna, A. Thornell-Pers, and A. Rydberg, "Dual wideband printed dipole antenna with integrated balun," *IET Microwaves, Antennas & Propagation,* vol. 1, no. 3, pp. 707-711, 2007.
[107] L. Yang, G. Orecchini, G. Shaker, H. Lee, and M. M. Tentzeris, "Battery-free RFID-enabled wireless sensors," in *2010 IEEE MTT-S International Microwave Symposium*, 2010, pp. 1528-1531.
[108] B. Q. Wu and K. Luk, "A Broadband Dual-Polarized Magneto-Electric Dipole Antenna With Simple Feeds," *IEEE Antennas and Wireless Propagation Letters,* vol. 8, pp. 60-63, 2009.
[109] Q. Xue, S. W. Liao, and J. H. Xu, "A Differentially-Driven Dual-Polarized Magneto-Electric Dipole Antenna," *IEEE Transactions on Antennas and Propagation,* vol. 61, no. 1, pp. 425-430, 2013.
[110] M. Li and K. Luk, "A Differential-Fed Magneto-Electric Dipole Antenna for UWB Applications," *IEEE Transactions on Antennas and Propagation,* vol. 61, no. 1, pp. 92-99, 2013.
[111] L. Siu, H. Wong, and K. Luk, "A Dual-Polarized Magneto-Electric Dipole With Dielectric Loading," *IEEE Transactions on Antennas and Propagation,* vol. 57, no. 3, pp. 616-623, 2009.
[112] Y. Gou, S. Yang, J. Li, and Z. Nie, "A Compact Dual-Polarized Printed Dipole Antenna With High Isolation for Wideband Base Station Applications," *IEEE Transactions on Antennas and Propagation,* vol. 62, no. 8, pp. 4392-4395, 2014.

[113] Y. Liu, H. Yi, F. Wang, and S. Gong, "A Novel Miniaturized Broadband Dual-Polarized Dipole Antenna for Base Station," *IEEE Antennas and Wireless Propagation Letters,* vol. 12, pp. 1335-1338, 2013.
[114] G. Adamiuk, S. Beer, W. Wiesbeck, and T. Zwick, "Dual-Orthogonal Polarized Antenna for UWB-IR Technology," *IEEE Antennas and Wireless Propagation Letters,* vol. 8, pp. 981-984, 2009.
[115] G. Adamiuk, C. Rusch, X. Li, M. Janson, and T. Zwick, "Dual-polarized UWB antenna for high-resolution-imaging-systems," in *2011 International Workshop on Antenna Technology (iWAT)*, 2011, pp. 239-242.
[116] J. Volakis, *Antenna engineering handbook*, Fourth Ed. ed. New York: McGraw-Hill Professional, 2007.
[117] C. Harrison and C. Williams, "Transients in wide-angle conical antennas," *IEEE Transactions on Antennas and Propagation,* vol. 13, no. 2, pp. 236-246, 1965.
[118] S. N. Samaddar and E. L. Mokole, "Biconical antennas with unequal cone angles," *IEEE Transactions on Antennas and Propagation,* vol. 46, no. 2, pp. 181-193, 1998.
[119] S. Zhongxiang and F. Chao, "A new dual-polarized broadband horn antenna," *IEEE Antennas and Wireless Propagation Letters,* vol. 4, pp. 270-273, 2005.
[120] R. Dehdasht-Heydari, H. R. Hassani, and A. R. R. Mallahzadeh, "Quad ridged horn antenna for UWB applications," *Progress In Electromagnetics Research,* vol. 79, pp. 23-38, 2008.
[121] W. Y. Ali-Ahmad and G. M. Rebeiz, "92 GHz dual-polarized integrated horn antennas," *IEEE Transactions on Antennas and Propagation,* vol. 39, no. 6, pp. 820-825, 1991.
[122] L. J. Foged and A. Giacomini, "Wide-band dual polarized probes for near field antenna measurements," in *Antennas and Propagation Society International Symposium, 2007 IEEE*, 2007, pp. 1645-1648: IEEE.
[123] D. M. Pozar, "Microstrip antenna aperture-coupled to a microstripline," *Electronics Letters,* vol. 21, no. 2, pp. 49-50, 1985.
[124] Y. Wang, Y. Bo, and D. Ben, "Wideband aperture coupled microstrip antenna with stubs," in *The 2006 4th Asia-Pacific Conference on Environmental Electromagnetics*, 2006, pp. 682-684.
[125] D. M. Pozar and S. D. Targonski, "Improved coupling for aperture coupled microstrip antennas," *Electronics Letters,* vol. 27, no. 13, pp. 1129-1131, 1991.
[126] F. Croq and D. M. Pozar, "Millimeter-wave design of wide-band aperture-coupled stacked microstrip antennas," *IEEE Transactions on Antennas and Propagation,* vol. 39, no. 12, pp. 1770-1776, 1991.
[127] F. Croq and A. Papiernik, "Stacked slot-coupled printed antenna," *IEEE Microwave and Guided Wave Letters,* vol. 1, no. 10, pp. 288-290, 1991.
[128] S. D. Targonski and R. B. Waterhouse, "An aperture coupled stacked patch antenna with 50% bandwidth," in *IEEE Antennas and Propagation Society International Symposium. 1996 Digest*, 1996, vol. 1, pp. 18-21 vol.1.
[129] H. Alias, M. T. Ali, S. S. N. Ramli, M. A. Sulaiman, and S. Kayat, "A back lobe reduction of aperture coupled microstrip antenna using DGS," in *2013 10th International Conference on Electrical Engineering/Electronics, Computer, Telecommunications and Information Technology*, 2013, pp. 1-5.
[130] M. A. Aris, A. H. M. T, N. H. A. Rahman, N. Ramli, and I. Pasya, "Frequency reconfigurable aperture-coupled microstrip patch antenna using periodic Defected Ground Structures," in *2015 IEEE Conference on Antenna Measurements & Applications (CAMA)*, 2015, pp. 1-4.
[131] H. Alias, M. T. Ali, S. Subahir, N. Ya'acob, and M. A. Sulaiman, "Aperture coupled microstrip antenna array integrated with DGS and parasitic elements," in *2013 IEEE Symposium on Wireless Technology & Applications (ISWTA)*, 2013, pp. 259-263.
[132] R. Qinjiang and R. H. Johnston, "Modified aperture coupled microstrip antenna," *IEEE Transactions on Antennas and Propagation,* vol. 52, no. 12, pp. 3397-3401, 2004.

[133] C. Liao, Y. Lin, C. Chen, S. Kao, and H. Chen, "A novel aperture-coupled circularly polarized square-ring patch antenna for wireless communication systems," in *2016 IEEE 5th Asia-Pacific Conference on Antennas and Propagation (APCAP)*, 2016, pp. 57-58.
[134] M. Clenet, D. Roy, and D. Lee, "Arrays of 4 circularly polarised aperture-coupled-fed stacked patch antennas for GPS interference mitigation," in *2009 13th International Symposium on Antenna Technology and Applied Electromagnetics and the Canadian Radio Science Meeting*, 2009, pp. 1-4.
[135] V. Balusa, V. S. K. P. Kumar, and B. T. P. Madhav, "Aperture coupled feed circularly polarized antenna," in *2015 International Conference on Signal Processing and Communication Engineering Systems*, 2015, pp. 240-244.
[136] S. D. Targonski and D. M. Pozar, "Design of wideband circularly polarized aperture-coupled microstrip antennas," *IEEE Transactions on Antennas and Propagation,* vol. 41, no. 2, pp. 214-220, 1993.
[137] J. Patin and S. Sharma, "Single Feed Aperture-Coupled Wideband Dielectric Resonator Antenna with Circular Polarization for Ku-Band Applications," *International Journal of Antennas and Propagation,* vol. 2012, no. 2012, 2012.
[138] J. Wang, Z. Wang, B. Yan, and M. Zhan, "A Ka-band aperture-coupled patch antenna with stacked rectangular rings based on LTCC technology," in *2009 Asia Pacific Microwave Conference*, 2009, pp. 1946-1949.
[139] A. Adrian and D. Schaubert, "Dual aperture-coupled microstrip antenna for dual or circular polarisation," *Electronics Letters,* vol. 23, no. 23, pp. 1226-1228, 1987.
[140] C. Tsao, Y. Hwang, F. Kilburg, and F. Dietrich, "Aperture-coupled patch antennas with wide-bandwidth and dual-polarization capabilities," in *Antennas and Propagation Society International Symposium, 1988. AP-S. Digest*, 1988, pp. 936-939: IEEE.
[141] S. K. Padhi, N. C. Karmakar, C. L. Law, and S. Aditya, "A dual polarized aperture coupled microstrip patch antenna with high isolation for RFID applications," in *Antennas and Propagation Society International Symposium, 2001. IEEE*, 2001, vol. 2, pp. 2-5 vol.2.
[142] S. Chakrabarti, "Development of Shared Aperture Dual Polarized Microstrip Antenna at L-Band," *IEEE Transactions on Antennas and Propagation,* vol. 59, no. 1, pp. 294-297, 2011.
[143] F. Klefenz and A. Dreher, "Aperture-coupled stacked microstrip antenna with dual polarization and low back-radiation for X-band SAR applications," in *Radio and Wireless Conference, 2000. RAWCON 2000. 2000 IEEE*, 2000, pp. 179-182: IEEE.
[144] S. Targonski, R. Waterhouse, and D. M. Pozar, "Wideband aperture coupled stacked patch antenna using thick substrates," *Electronics Letters,* vol. 32, no. 21, pp. 1941-1942, 1996.
[145] K. Ghorbani and R. Waterhouse, "Dual polarized wide-band aperture stacked patch antennas," *IEEE Transactions on Antennas and Propagation,* vol. 52, no. 8, pp. 2171-2175, 2004.
[146] M. Edimo, A. Sharaiha, and C. Terret, "Optimised Feeding of Dual Polarised Broadband Aperture Coupled Printed Antennas," 1992.
[147] A. Serra, P. Nepa, G. Manara, G. Tribellini, and S. Cioci, "A wide-band dual-polarized stacked patch antenna," *IEEE antennas and wireless propagation letters,* vol. 6, pp. 141-143, 2007.
[148] W. Stutzman, "Synthesis of shaped-beam radiation patterns using the iterative sampling method," *Antennas and Propagation, IEEE Transactions on,* vol. 19, no. 1, pp. 36-41, 1971.
[149] A. Waterman and D. Henry, "Stripline strap-on antenna array," *PROCEEDINGS OFRTICE,* p. 11.
[150] T. G. Campbell, "An extremely thin, omnidirectional, microwave antenna array for spacecraft applications," 1969.
[151] R. Munson, "Microstrip phased array antennas," in *Proc. of Twenty-Second Symp. on USAF Antenna Research and Development Program*, 1972.
[152] E. G. Fubini, "Stripline radiators," *Microwave Theory and Techniques, IRE Transactions on,* vol. 3, no. 2, pp. 149-156, 1955.

[153] J. McDonough, R. Malech, and J. Kowalsky, "Recent developments in the study of printed antennas," in *IRE International Convention Record*, 1966, vol. 5, pp. 173-176: IEEE.
[154] J. James and G. Wilson, "Radiation characteristics of stripline antennas," in *4th European Microwave Conference*, 1974, vol. 1, pp. 484-488.
[155] D. M. Pozar, "Microstrip antennas," *Proceedings of the IEEE,* vol. 80, no. 1, pp. 79-91, 1992.
[156] N. K. Das and D. M. Pozar, "Analysis and design of series-fed arrays of printed-dipoles proximity-coupled to a perpendicular microstripline," *Antennas and Propagation, IEEE Transactions on,* vol. 37, no. 4, pp. 435-444, 1989.
[157] H.-Y. Yang, N. G. Alexopoulos, P. M. Lepeltier, and G. J. Stern, "Design of transversely fed EMC microstrip dipole arrays including mutual coupling," *Antennas and Propagation, IEEE Transactions on,* vol. 38, no. 2, pp. 145-151, 1990.
[158] C. Wu, J. Wang, R. Fralich, and J. Litva, "Study on a series-fed aperture-coupled microstrip patch array," in *Antennas and Propagation Society International Symposium, 1990. AP-S. Merging Technologies for the 90's. Digest.*, 1990, pp. 1762-1765: IEEE.
[159] N. K. Das and D. M. Pozar, "A class of enhanced electromagnetically coupled feed geometries for printed antenna applications," in *Antennas and Propagation Society International Symposium, 1990. AP-S. Merging Technologies for the 90's. Digest.*, 1990, pp. 1100-1103: IEEE.
[160] W. L. Stutzman, *Antenna theory and design*, 3rd ed. ed. Hoboken, NJ: Hoboken, NJ : Wiley, 2013.
[161] R. C. Johnson, *Antenna engineering handbook*, 3rd ed. ed. New York: New York : McGraw-Hill, 1993.
[162] J. J. Carr, *Practical antenna handbook*, 5th ed. ed. New York: New York : McGraw-Hill, 2012.
[163] T. T. Taylor, "Design of line-source antennas for narrow beamwidth and low side lobes," *Antennas and Propagation, Transactions of the IRE Professional Group on,* vol. 3, no. 1, pp. 16-28, 1955.
[164] Y. V. Baklanov, "Chebyshev distribution of currents for a plane array of radiators," vol. 11, ed: SCRIPPS CLINIC RES FOUNDATION 476 PROSPECT ST, LA JOLLA, CA 92037, 1966, pp. 640-&.
[165] E. J. Wilkinson, "An N-Way Hybrid Power Divider," *IRE Transactions on Microwave Theory and Techniques,* vol. 8, no. 1, pp. 116-118, 1960.
[166] L. C. Godara, *Smart antennas*. CRC press, 2014.
[167] J. Li and P. Stoica, *Robust adaptive beamforming*. Wiley Online Library, 2006.
[168] J. R. Guerci, *Space-time adaptive processing for radar*. Artech House, 2002.
[169] A. B. U. W. Bandara and E. M. Amin, "Beam forming algorithm with different power distribution for RFID reader," *Chipless and Conventional Radio Frequency Identification: Systems for Ubiquitous Tagging: Systems for Ubiquitous Tagging,* p. 64, 2012.
[170] C. L. Dolph, "A Current Distribution for Broadside Arrays Which Optimizes the Relationship between Beam Width and Side-Lobe Level," *Proceedings of the IRE,* vol. 34, no. 6, pp. 335-348, 1946.
[171] M. Ma and D. Cheng, "A critical study of linear arrays with equal side lobes," in *IRE International Convention Record*, 1966, vol. 9, pp. 110-122: IEEE.
[172] A. Zielinski, "An Efficient Method of Dolph-Chebyshev Beamforming," in *Progress in Underwater Acoustics*, H. Merklinger, Ed.: Springer US, 1987, pp. 759-764.
[173] J. George, N. OCEANOGRAPHIC, and A. R. L. S. S. C. MS., *Beamforming with Dolph-Chebyshev Optimization and Other Conventional Methods*. Defense Technical Information Center, 1991.
[174] I. T. Fung and D. K. Cheng, "Optimum scannable planar arrays with an invariant sidelobe level," *Proceedings of the IEEE,* vol. 56, no. 11, pp. 1771-1778, 1968.
[175] D. Kosloff and H. Tal-Ezer, "A modified Chebyshev pseudospectral method with an O (N-1) time step restriction," *Journal of Computational Physics,* vol. 104, no. 2, pp. 457-469, 1993.

[176] D. Calvetti, G. H. Golub, and L. Reichel, "An adaptive Chebyshev iterative method\ newline for nonsymmetric linear systems based on modified moments," *Numerische Mathematik,* vol. 67, no. 1, pp. 21-40, 1994.
[177] A. Safaai-Jazi, "Modified chebyshev arrays," in *Microwaves, Antennas and Propagation, IEE Proceedings*, 1998, vol. 145, no. 1, pp. 45-48: IET.
[178] A. Baki, N. Shinohara, H. Matsumoto, K. Hashimoto, and T. Mitani, "Study of isosceles trapezoidal edge tapered phased array antenna for solar power station/satellite," *IEICE transactions on communications,* vol. 90, no. 4, pp. 968-977, 2007.
[179] A. Baki, K. Hashimoto, N. Shinohara, T. Mitani, and H. Matsumoto, "Isosceles-trapezoidal-distribution edge tapered array antenna with unequal element spacing for solar power satellite," *IEICE transactions on communications,* vol. 91, no. 2, pp. 527-535, 2008.
[180] A. Baki, K. Hashimoto, N. Shinohara, T. Mitani, and H. Matsumoto, "New and improved method of beam forming with reduced side lobe levels for microwave power transmission," in *Electrical and Computer Engineering, 2008. ICECE 2008. International Conference on*, 2008, pp. 773-777: IEEE.
[181] G. Kumar and K. C. Gupta, "Nonradiating edges and four edges gap-coupled multiple resonator broad-band microstrip antennas," *Antennas and Propagation, IEEE Transactions on,* vol. 33, no. 2, pp. 173-178, 1985.
[182] W. F. Richards, S. Davidson, and S. A. Long, "Dual-band reactively loaded microstrip antenna," *Antennas and Propagation, IEEE Transactions on,* vol. 33, no. 5, pp. 556-561, 1985.
[183] A. Sangiovanni, J. Y. Dauvignac, and C. Pichot, "Stacked dielectric resonator antenna for multifrequency operation," *Microwave and Optical Technology Letters,* vol. 18, no. 4, pp. 303-306, 1998.
[184] K. R. Carver, "Antenna technology requirements for next-generation spaceborne SAR systems," in *Antennas and Propagation Society International Symposium, 1983*, 1983, vol. 21, pp. 365-371.
[185] L. L. Shafai, W. A. Chamma, M. Barakat, P. C. Strickland, and G. Seguin, "Dual-band dual-polarized perforated microstrip antennas for SAR applications," *Antennas and Propagation, IEEE Transactions on,* vol. 48, no. 1, pp. 58-66, 2000.
[186] A. K. Bhattacharyya and L. Shafai, "A wider band microstrip antenna for circular polarization," *Antennas and Propagation, IEEE Transactions on,* vol. 36, no. 2, pp. 157-163, 1988.
[187] R. Pokuls, J. Uher, and D. M. Pozar, "Dual-Frequency and Dual-Polarization Microstrip Antennas for SAR Applications," vol. 46, no. 9, pp. 1289-1296, 1998.
[188] D. M. Pozar and S. D. Targonski, "A Shared-Aperture Dual-Band Dual-Polarized Microstrip Array," vol. 49, no. 2, pp. 150-157, 2001.
[189] F. Ferrero, C. Luxey, G. Jacquemod, and R. Staraj, "Dual-Band Circularly Polarized Microstrip Antenna for Satellite Applications," *Antennas and Wireless Propagation Letters,* vol. 4, no. 1, pp. 13-3, 2005.
[190] Y. Kai-Ping and W. Kin-Lu, "Dual-band circularly-polarized square microstrip antenna," *Antennas and Propagation, IEEE Transactions on,* vol. 49, no. 3, pp. 377-382, 2001.
[191] Z. Shi-Gang and C. Tan-Huat, "Dual-wideband, dual-polarized shared aperture antenna with high isolation and low cross-polarization," *Isape2012,* pp. 30-33, 2012.
[192] M. Wei, H. Deng, H. Sun, and Y. Liu, "Design of an X/Ka dual-band co-aperture broadband microstrip antenna array," *2011 IEEE International Conference on Microwave Technology & Computational Electromagnetics,* pp. 217-220, 2011.
[193] K.-p. Yang, K.-l. Wong, and S. Member, "Dual-Band Circularly-Polarized Square Microstrip," vol. 49, no. 3, pp. 377-382, 2001.
[194] H. Wong, K. L. Lau, and K. M. Luk, "Design of Dual-Polarized L-Probe Patch Antenna Arrays With High Isolation," *IEEE Transactions on Antennas and Propagation,* vol. 52, no. 1, pp. 45-52, 2004.

[195] J. Granholm, K. Woelders, M. Dich, and E. L. Christensen, "Microstrip antenna for polarimetric C-band SAR," in *Antennas and Propagation Society International Symposium, 1994. AP-S. Digest*, 1994, vol. 3, pp. 1844-1847 vol.3.

[196] Z. S. Gang, C. T. Huat, and L. Jian, "A shared-aperture dual-wideband dual-polarized stacked microstrip array," *Microwave and Optical Technology Letters,* vol. 54, no. 2, pp. 486-491, 2012.

[197] W. S. T. Rowe and R. B. Waterhouse, "Investigation of proximity coupled patch antennas suitable for MMIC integration," in *Antennas and Propagation Society International Symposium, 2004. IEEE*, 2004, vol. 2, pp. 1591-1594 Vol.2.

[198] R. B. Waterhouse and W. S. T. Rowe, "MMIC compatible printed antennas," *Electronics Letters,* vol. 39, no. 21, pp. 1493-1495, 2003.

[199] G. C. Topp, J. L. Davis, and A. P. Annan, "Electromagnetic determination of soil water content: Measurements in coaxial transmission lines," *Water Resources Research,* vol. 16, no. 3, pp. 574-582, 1980.

[200] M. T. Hallikainen, F. T. Ulaby, M. C. Dobson, M. A. El-Rayes, and W. Lil-Kun, "Microwave Dielectric Behavior of Wet Soil-Part 1: Empirical Models and Experimental Observations," *Geoscience and Remote Sensing, IEEE Transactions on,* vol. GE-23, no. 1, pp. 25-34, 1985.

[201] J. R. Wang and T. J. Schmugge, "An Empirical Model for the Complex Dielectric Permittivity of Soils as a Function of Water Content," *IEEE Transactions on Geoscience and Remote Sensing,* vol. GE-18, 1980.

[202] M. C. Dobson, F. T. Ulaby, M. T. Hallikainen, and M. A. El-Rayes, "Microwave Dielectric Behavior of Wet Soil-Part II: Dielectric Mixing Models," *IEEE Transactions on Geoscience and Remote Sensing,* vol. GE-23, 1985.

[203] B. J. Choudhury, T. J. Schmugge, R. W. Newton, and A. T. C. Chang, "Effect of surface roughness on the microwave emission from soils," *Journal of Geophysical Research,* vol. 84, pp. 5699--5706, 1978.

[204] J. R. Wang, "Passive microwave sensing of soil moisture content: The effects of soil bulk density and surface roughness," *Remote Sensing of Environment,* vol. 13, no. 4, pp. 329-344, 9// 1983.

[205] T. Mo and T. J. Schmugge, "A parameterization of the effect of surface roughness on microwave emission," *IEEE Transactions on Geoscience and Remote Sensing,* vol. GE-25, pp. 481--486, 1987.

[206] U. Wegmuller and C. Matzler, "Rough bare soil reflectivity model," *Geoscience and Remote Sensing, IEEE Transactions on,* vol. 37, no. 3, pp. 1391-1395, 1999.

[207] J. P. Wigneron, L. Laguerre, and Y. H. Kerr, "A simple parameterization of the L-band microwave emission from rough agricultural soils," *IEEE Transactions on Geoscience and Remote Sensing,* vol. 39, pp. 1697--1707, 2001.

[208] A. K. Fung, *Microwave Scattering and Emission Models and Their Applications*. Artech House, Incorporated, 1994.

[209] A. A. Chukhlantsev, *Microwave radiometry of vegetation canopies*. 2006.

[210] P. O'Neill, S. Chan, E. Njoku, T. Jackson, and R. Bindlish, "Soil Moisture Active Passive (SMAP) algorithm theoretical basis document (ATBD) SMAP level 2 & 3 soil moisture (passive)," *SMAP Project, JPL D-66480,* 2012.

[211] V. Favier, C. Agosta, C. Genthon, L. Arnaud, A. Trouvillez, and H. Gallée, "Journal of Geophysical Research. Earth Surface," 2011.

[212] A. G. Meesters, R. A. De Jeu, and M. Owe, "Analytical derivation of the vegetation optical depth from the microwave polarization difference index," *IEEE Geoscience and Remote Sensing Letters,* vol. 2, no. 2, pp. 121-123, 2005.

[213] D. Chung, R. De Jeu, W. Dorigo, S. Hahn, T. Melzer, and R. Parinussa, "ESA CCI soil moisture algorithm theoretical baseline document version 1," 2013.

[214] K. Saleh, J.-P. Wigneron, P. de Rosnay, J.-C. Calvet, and Y. Kerr, "Semi-empirical regressions at L-band applied to surface soil moisture retrievals over grass," *Remote Sensing of Environment,* vol. 101, no. 3, pp. 415-426, 2006.
[215] C. Mattar *et al.*, "A combined optical–microwave method to retrieve soil moisture over vegetated areas," *IEEE Transactions on Geoscience and Remote Sensing,* vol. 50, no. 5, pp. 1404-1413, 2012.
[216] F. Del Frate, P. Ferrazzoli, and G. Schiavon, "Retrieving soil moisture and agricultural variables by microwave radiometry using neural networks," *Remote Sensing of Environment,* vol. 84, no. 2, pp. 174-183, 2// 2003.
[217] M. Parde *et al.*, "N-parameter retrievals from L-band microwave observations acquired over a variety of crop fields," *IEEE Transactions on Geoscience and Remote Sensing,* vol. 42, pp. 1168--1178, 2004.
[218] D. M. Pozar, "A Review of Aperture Coupled Microstrip Antennas: History, Operation, Development, and Applicatons," *University of Massachusetts at Amherst,* 1996.
[219] M. Hassan and N. Karmakar, *Design considerations of DP ACPA with higher isolation at Ku-band for soil moisture radiometer*. 2017, pp. 1055-1058.
[220] K. J. Russell, "Microwave Power Combining Techniques," *IEEE Transactions on Microwave Theory and Techniques,* vol. 27, no. 5, pp. 472-478, 1979.
[221] Sakakibara, Y. Kimura, A. Akiyama, J. Hirokawa, M. Ando, and N. Goto, "Alternating phase-fed waveguide slot arrays with a single-layer multiple-way power divider," *IEE Proceedings - Microwaves, Antennas and Propagation,* vol. 144, no. 6, pp. 425-430, 1997.
[222] J. Xin, S. Ortiz, and A. Mortazawi, "A novel Ka-band 1 to 8 power divider/combiner," in *2001 IEEE MTT-S International Microwave Sympsoium Digest (Cat. No.01CH37157)*, 2001, vol. 1, pp. 35-38 vol.1.
[223] R. Munson, "Conformal microstrip antennas and microstrip phased arrays," *IEEE Transactions on Antennas and Propagation,* vol. 22, no. 1, pp. 74-78, 1974.
[224] W. Lei, S. Zengguang, H. Yilmaz, and M. Berroth, "A dual-frequency wilkinson power divider," *IEEE Transactions on Microwave Theory and Techniques,* vol. 54, no. 1, pp. 278-284, 2006.
[225] L. Jeng-Sik, L. Sung-Won, K. Chul-Soo, P. Jun-Seek, A. Dal, and N. Sangwook, "A 4.1 unequal Wilkinson power divider," *IEEE Microwave and Wireless Components Letters,* vol. 11, no. 3, pp. 124-126, 2001.
[226] L. I. Parad and R. L. Moynihan, "Split-Tee Power Divider," *IEEE Transactions on Microwave Theory and Techniques,* vol. 13, no. 1, pp. 91-95, 1965.
[227] K. Song and Q. Xue, "Novel Ultra-Wideband (UWB) Multilayer Slotline Power Divider With Bandpass Response," *IEEE Microwave and Wireless Components Letters,* vol. 20, no. 1, pp. 13-15, 2010.
[228] R. Mailloux, J. McIlvenna, and N. Kernweis, "Microstrip array technology," *IEEE Transactions on Antennas and Propagation,* vol. 29, no. 1, pp. 25-37, 1981.
[229] D. Nascimento and J. d. S. Lacava, "Design of Arrays of Linearly Polarized Patch Antennas on an FR4 Substrate: Design of a probe-fed electrically equivalent microstrip radiator," *IEEE Antennas and Propagation Magazine,* vol. 57, no. 4, pp. 12-22, 2015.
[230] Y.-M. Yoon, J.-H. Kim, and B.-G. Kim, "Radiation characteristics of an H-plane linear microstrip array antenna on a finite substrate," in *Antennas and Propagation Society International Symposium (APSURSI), 2013 IEEE*, 2013, pp. 1584-1585: IEEE.
[231] S. Farzaneh and A.-R. Sebak, "Microwave sampling beamformer—Prototype verification and switch design," *IEEE Transactions on Microwave Theory and Techniques,* vol. 57, no. 1, pp. 36-44, 2009.
[232] L. Peng, J. Xie, X. Li, and X. Jiang, "Front to Back Ratio Bandwidth Enhancement of Resonance Based Reflector Antenna by Using a Ring-Shape Director and Its Time-Domain Analysis," *IEEE Access,* vol. 5, pp. 15318-15325, 2017.

[233] W. Lim, H. Jang, and J. Yu, "New method for back lobe suppression of microstrip patch antenna for GPS," in *The 40th European Microwave Conference*, 2010, pp. 679-682.
[234] N. C. Karmakar, "Back radiation suppression of aperture coupled microstrip antennas using photonic bandgap back shield," in *IEEE Antennas and Propagation Society International Symposium. Digest. Held in conjunction with: USNC/CNC/URSI North American Radio Sci. Meeting (Cat. No.03CH37450)*, 2003, vol. 4, pp. 863-866 vol.4.
[235] K. Klionovski and A. Shamim, "Back Radiation Suppression Through a Semitransparent Ground Plane for a Millimeter-Wave Patch Antenna," *IEEE Transactions on Antennas and Propagation,* vol. 65, no. 8, pp. 3935-3941, 2017.
[236] E. Rajo-Iglesias, O. Quevedo-Teruel, B. Cabanillas-Fernandez, and L. Inclan-Sanchez, "Practical applications of planar soft surfaces to patch antennas," in *2008 IEEE Antennas and Propagation Society International Symposium*, 2008, pp. 1-4.
[237] M. Hassan, S. Dey, and N. Karmakar, "Ka-band complementary reflector backed slot antenna array for soil moisture radiometer," ed.
[238] T. Namiki, Y. Murayama, and K. Ito, "Improving radiation-pattern distortion of a patch antenna having a finite ground plane," *IEEE Transactions on Antennas and Propagation,* vol. 51, no. 3, pp. 478-482, 2003.
[239] B. Allen and M. Ghavami, *Adaptive array systems: fundamentals and applications*. John Wiley & Sons, 2006.
[240] M. Brandstein and D. Ward, *Microphone arrays: signal processing techniques and applications*. Springer Science & Business Media, 2013.
[241] N. Fourikis, *Advanced array systems, applications and RF technologies*. Academic Press, 2000.
[242] S. Haykin, J. H. Justice, N. L. Owsley, J. Yen, and A. C. Kak, "Array signal processing," 1985.
[243] J. Hudson, *Adaptive array principles*. IET, 1981.
[244] D. H. Johnson and D. E. Dudgeon, *Array signal processing: concepts and techniques*. Simon & Schuster, 1992.
[245] R. A. Monzingo and T. W. Miller, *Introduction to adaptive arrays*. SciTech Publishing, 1980.
[246] A. A. M. Nicol, *Normal Distribution. Encyclopedia of Research Design. SAGE Publications, Inc*. Thousand Oaks, CA: SAGE Publications, Inc., pp. 927-932.
[247] R. S. Elliot, *ANTENNA THEORY AND DESIGN, REVISED ED*. Wiley India Pvt. Limited, 2006.
[248] B. C. Brock, "The application of taylor weighting, digital phase shifters, and digital attenuators to phased-array antennas," SAND2008-1687; TRN: US200814%%676 United States10.2172/932884TRN: US200814%%676Thu Aug 07 07:14:23 EDT 2008SNLEnglish, 2008, Available: http://www.osti.gov/scitech//servlets/purl/932884-T5tKjg/.
[249] A. K. M. Baki and N. C. Karmakar, "Performance comparison of RFID tag at UHF band and millimeter-wave band," *Journal of Networks,* vol. 9, no. 12, p. 3215, 2014.
[250] A. K. M. Baki and N. C. Karmakar, "60 GHz array antenna with new method of beam forming," ed, 2012, pp. 638-641.
[251] R. L. Jordan, B. L. Huneycutt, and M. Werner, "The SIR-C/X-SAR synthetic aperture radar system," *Proceedings of the IEEE,* vol. 79, no. 6, pp. 827-838, 1991.
[252] L. L. Shafai, W. A. Chamma, M. Barakat, P. C. Strickland, and G. Seguin, "Dual-band dual-polarized perforated microstrip antennas for SAR applications," *IEEE Transactions on Antennas and Propagation,* vol. 48, no. 1, pp. 58-66, 2000.
[253] D. Isleifson and L. Shafai, "A study on the design of dual-band perforated microstrip antennas for SAR applications," in *2012 15 International Symposium on Antenna Technology and Applied Electromagnetics*, 2012, pp. 1-3.
[254] L. Shafai and W. Chamma, "Bandwidth and polarization characteristics of perforated patch antennas," in *Tenth International Conference on Antennas and Propagation (Conf. Publ. No. 436)*, 1997, vol. 1, pp. 43-46 vol.1.

[255] D. M. Pozar and S. D. Targonski, "A shared-aperture dual-band dual-polarized microstrip array," *IEEE Transactions on Antennas and Propagation,* vol. 49, no. 2, pp. 150-157, 2001.
[256] H. Schippers *et al.*, "Development of dual-frequency airborne Satcom antenna with optical beamforming," in *2009 IEEE Aerospace conference*, 2009, pp. 1-16.
[257] H. Shih-Hsun, R. Yu-Jiun, and C. Kai, "A Dual-Polarized Planar-Array Antenna for S-Band and X-Band Airborne Applications," *IEEE Antennas and Propagation Magazine,* vol. 51, no. 4, pp. 70-78, 2009.
[258] K. Wincza, S. Gruszczynski, and J. Grzegorz, "Integrated dual-band dual-polarized antenna element for SAR applications," in *2009 IEEE 10th Annual Wireless and Microwave Technology Conference*, 2009, pp. 1-4.
[259] A. Vallecchi, G. B. Gentili, and M. Calamia, "Dual-band dual polarization microstrip antenna," in *IEEE Antennas and Propagation Society International Symposium. Digest. Held in conjunction with: USNC/CNC/URSI North American Radio Sci. Meeting (Cat. No.03CH37450)*, 2003, vol. 4, pp. 134-137 vol.4.
[260] G. Jaworski, T. Maleszka, S. Gruszczynski, and K. Wincza, "Dual frequency & dual-linear polarization integrated Antenna array for application in Synthetic Aperture Radar," in *The 40th European Microwave Conference*, 2010, pp. 1714-1717.
[261] D. M. Pozar and S. D. Targonski, "A shared-aperture dual-band dual-polarized microstrip array," *Antennas and Propagation, IEEE Transactions on,* vol. 49, no. 2, pp. 150-157, 2001.
[262] Z. Sun, S. S. Zhong, K. P. Esselle, J. Guo, and Y. Cai, "Broadband dual-band dual-polarized overlapped antenna element," in *2012 IEEE-APS Topical Conference on Antennas and Propagation in Wireless Communications (APWC)*, 2012, pp. 223-226.
[263] M. Kaboli, M. S. Abrishamian, S. A. Mirtaheri, and S. M. Aboutorab, "High isolation dual band dual polarized antenna," in *6th International Symposium on Telecommunications (IST)*, 2012, pp. 1-6.
[264] M. Mira, E. Valor, R. Boluda, V. Caselles, and C. Coll, "Influence of soil water content on the thermal infrared emissivity of bare soils: Implication for land surface temperature determination," *Journal of Geophysical Research: Earth Surface,* vol. 112, no. F4, 2007.
[265] J. O. Curtis, "Moisture effects on the dielectric properties of soils," *IEEE Transactions on Geoscience and Remote Sensing,* vol. 39, no. 1, pp. 125-128, 2001.
[266] J. O. Curtis, C. A. Weiss Jr, and J. B. Everett, "Effect of Soil Composition on Complex Dielectric Properties," ARMY ENGINEER WATERWAYS EXPERIMENT STATION VICKSBURG MS ENVIRONMENTAL LAB1995.
[267] W. Fano and V. Trainotti, "Dielectric properties of soils," in *2001 Annual Report Conference on Electrical Insulation and Dielectric Phenomena (Cat. No. 01CH37225)*, 2001, pp. 75-78: IEEE.
[268] J. E. Hipp, "Soil electromagnetic parameters as functions of frequency, soil density, and soil moisture," *Proceedings of the IEEE,* vol. 62, no. 1, pp. 98-103, 1974.
[269] Z. Sipus, S. Skokic, and J. Bartolic, "Measurements of electromagnetic parameters of soil," in *17th International Conference on Applied Electromagnetics and Communications, 2003. ICECom 2003.*, 2003, pp. 56-59: IEEE.
[270] W. R. Scott and G. S. Smith, "Measured electrical constitutive parameters of soil as functions of frequency and moisture content," *IEEE Transactions on Geoscience and Remote Sensing,* vol. 30, no. 3, pp. 621-623, 1992.
[271] R. Zajicek, L. Oppl, and J. Vrba, "Broadband measurement of complex permittivity using reflection method and coaxial probes," *Radioengineering,* vol. 17, no. 1, pp. 14-19, 2008.
[272] Z. Alex and J. Behari, "Laboratory evaluation of emissivity of soils," *International Journal of Remote Sensing,* vol. 19, no. 7, pp. 1335-1340, 1998.